Experimental Evaluation and Simulations of Fiber Orientation in Injection Molding of Polymers Containing Short Glass Fibers

Gregorio Manuel Vélez-García

Dissertation submitted to the faculty of the Virginia Polytechnic Institute and State University in partial fulfillment of the requirements for the degree of

Doctor of Philosophy
In
Macromolecular Science and Engineering

Peter Wapperom, Chair
Donald G. Baird Co-Chair
Audrey Zink-Sharp
Yuriko Renardy

January 31, 2012
Blacksburg, VA

Keywords: short glass fiber composites, image analysis, sample preparation, enhanced method of ellipses, fiber orientation, injection molding, finite element simulation

Experimental Evaluation and Simulations of Fiber Orientation in Injection Molding of Polymers Containing Short Glass Fibers

Gregorio Manuel Vélez-García

ABSTRACT

Injection molded short fiber reinforced composites have generated commercial interest in the manufacturing of lightweight parts used in semi-structural applications. Predicting these materials' fiber orientation with quantitative accuracy is crucial for technological advancement, but the task is difficult because of the effect of inter-particle interactions at high concentrations of fiber found in parts of commercial interest.

A complete sample preparation procedure was developed to obtain optical micrographs with optimal definition of elliptical and non-elliptical footprint borders. Two novel aspects in this procedure were the use of tridimensional markers to identify specific locations for analysis and the use of controlled-etching to produce small shadows where fibers recede into the matrix. These images were used to measure fiber orientation with a customized image analysis tool. This tool contains several modifications that we introduced in the method of ellipses which allow us to determine tridimensional fiber orientation and to obtain measurements in regions with fast changes in orientation. The tool uses the location of the shadow to eliminate the ambiguity problem in orientation and characterizes non-elliptical footprints to obtain the orientation in small sampling areas.

Cavitywise measurements in two thin center-gated disks showed the existence of an asymmetric profile of orientation at the gate and an orientation profile that washed out gradually at the entry region until disappearing at about 32 gap widths. This data was used to assess the prediction of cavitywise orientation using a delay model for fiber orientation with model parameters obtained from rheometrical experiments. Model predictions combining slip correction and experimentally determined orientation at the gate are in agreement with experimental data for the core layers near the end-of-fill region.

Radialwise measurements of orientation at the shell, transition and core layer, and microtextural description of the advancing front are included in this dissertation. The analysis and assessment of the radial evolution of fiber orientation and advancing front based on comparing the experimental data with simulation results are under ongoing investigation.

Format of Dissertation-

The work in this thesis has been done as part of a PhD program at the Department of Macromolecular Science and Engineering, Virginia Polytechnic Institute and State University, Blacksburg, Virginia, United States.

This dissertation is written in journal format. Chapters 3, 4, and 5 are self-contained papers that have been submitted for journal publication. Each paper separately describes the methods, experimental and numerical results and discussion, and conclusions relevant to that paper. The figures and tables in all chapters are distributed in the text. Figures are in color to provide better detail to the description of concepts presented in those figures.

Dedication

Commitment, effort, and dedication were fundamental elements for the completion of my doctoral dissertation, but even more necessary was the support of my family and friends. To my teachers, today I dedicate to them this important professional achievement because without their presence, support, and comprehension I would not have achieved my goal. Thank you!

Acknowledgements

First of all, I want to thank my supervisors, Drs. Peter Wapperom and Donald G. Baird, for their patience, help, and constructive criticism of my work during my PhD project. I offer special thanks to my primary supervisor, Dr. Peter Wapperom, for his guidance, constant encouragement, and for being a great example of how to conduct serious, ethical research during my doctoral studies. I hope that one day I would become as good an advisor to my students as Dr. Wapperom has been to me. I am also very grateful to Dr. Audrey Zink-Sharp and Vlastimil Kunc for their help and encouragement during this work. Additionally, I wish to express my gratitude to Dr. Carlos Suchicital and Dr Alex Aning of the Department of Material Science and Engineering; their help and assistance, as well as the support of their department, were significant during the experimental portion of this thesis.

The summer internship at Oak Ridge National Laboratories was important to my progress as a PhD candidate and was critical for providing me with a foundation in the experimental elements I used at Virginia Tech. My internship there also provided me with the opportunity to improve my communication skills, it allowed me to establish contacts in the field and it helped me to gain new insights in my research.

In addition, I want to thank the University of Puerto Rico – Mayaguez and the NSF-IGERT program for funding my PhD. I also want to thank Aaron Eberle, Kevin Ortman, and Syed Mazahir, members of the polymer processing group at Virginia Tech for the beneficial discussions, comments and exchange of ideas during my progress towards the PhD. I want to express my gratitude to Kenneth Dilorenzo who was extremely helpful and offered invaluable assistance in redacting the last chapter of this document.

Last, but by no means the least, I want to thank my roommate, Dr. Keith Ray. His patience and support in helping me overcome many crisis situations and finish this dissertation. I will always be grateful to him.

Gregorio M. Vélez-García

Blacksburg, January 2012

Original Contributions

The following are considered to be the significant original contributions of this research:

- Development and implementation of a complete sample preparation procedure to obtain optical micrographs. This procedure allows for both obtaining optimal definition of footprints and recognizing the direction of the fibers coming out of the polished plane. The use of tridimensional markers to precisely indicate locations for analysis and controlled-etching used in the sample preparation are innovations in the procedure introduced in our research.
- Unambiguous orientation and measurements in small sampling areas suitable for regions exhibiting fast changes in orientation can be obtained with modifications introduced to the method of ellipses. Development of customized image analysis tool containing these modifications and the use of a shadow to identify the correct in-plane angle for every fiber allow for the evaluation of orientation from non-elliptical footprints. The recognition of the shadow by optical microscopy is an innovation in the literature of fiber composites.
- The modified method of ellipses was used to obtain information of fiber orientation not available in the literature. These are, measurement of the 6 components of the tensor of orientation which provides a tridimensional orientation; measurement of orientation in mutually perpendicular planes; determination of the minimum sampling width required for obtaining reliable measurement of fiber orientation; and estimation of the particle migration through the cavity thickness based on orientation data.
- Novel information of orientation obtained for center-gated disks. These are, cavitywise measurements of orientation in critical regions such as the inlet and near the advancing front; radialwise measurements of orientation for the shell, transition and core layers; cavity wise orientation obtained from independent center-gated disks showing high reproducibility in the lubrication and the critical regions. The accuracy in the experimental fiber orientation in critical regions is attributed to the high-quality images and the additional information obtained with the characterization of the non-elliptical footprints. The small thickness of the center-gated disk used

in this study provides relevant orientation data which is suitable in evaluating simulation results based on the Hele-Shaw approximation. Such data is unavailable in the literature

- Assessment of a delay model, with model parameters obtained from simple shear flow experiments, for predicting fiber orientation in a center-gated disk. The use of experimentally determined orientation at the gate as inlet orientation for simulations used to predict fiber orientation for a center-gated disk is a novelty in the literature of fiber composites.

Attribution

Several colleagues aided in the writing and research behind three of my chapters presented as part of this dissertation. A brief description of their contribution is included here

Chapter 3 Sample preparation and image acquisition using optical-reflective microscopy in the measurement of fiber orientation in thermoplastic composites

Chapter 3 was submitted to Journal of Microscopy

Vlastimil Kunc, MS, Oak Ridge National Laboratory, P.O. Box 2009, Oak Ridge, TN 37831, USA. Mr. Kunc is a researcher in the Polymer Matrix Composites Group Materials Science & Technology Division and co-author on this paper. In addition, Mr. Kunc provided technical support during the start-up of the sample preparation in our facilities in Virginia Tech, and contributed in editorial comments.

Chapter 4 Unambiguous orientation in short fiber composites over small sampling area in a center-gated disk

Chapter 4 was publisehed in Composites Part A

Vlastimil Kunc, MS, Oak Ridge National Laboratory, P.O. Box 2009, Oak Ridge, TN 37831, USA. Mr. Kunc is a researcher in the Polymer Matrix Composites Group Materials Science & Technology Division and co-author on this paper. In addition, Mr. Kunc supervised the initial phase of the image analysis tool developed during my internship in Oak Ridge National Laboratories, provided initial samples used in the analysis of fiber orientation, and contributed in editorial comments.

Alex O. Aning, PhD, Department of Material Science and Engineering, Virginia Tech, Blacksburg, VA 24061, USA is currently an associate professor at Virginia Tech and co-author on this paper. Dr. Aning was my faculty sponsor to get access to the polishing facilities at Material Science and Engineering. H allowed the use of his optical microscope used to image the samples employed in this study.

Chapter 5 Simulation of injection molding using a model with delayed fiber orientation

Chapter 5 was published in International Polymer Processing

Syed M. Mazahir, MA, Department of Chemical Engineering, Virginia Tech, Blacksburg, VA 24061, USA is currently doctoral student at Virginia Tech and co-author on this paper. Mr. Mazahir helped with the simulations performed in this publication and contributed editorial comments.

Table of contents

List of figures

Chapter 1

Chapter 2

Chapter 3

Chapter 5

Chapter 6

List of tables

Chapter 1

Chapter 2

Chapter 3

Chapter 4

Chapter 1 Introduction

The continued development of industrial countries is threatened by present-day crises related to energy use and the environment. Many services, such as transportation, which are vital to the maintenance of technological and commercial growth, are directly responsible for these problems due to high consumption of energy resources and the generation of pollution. In the USA, the Department of Energy (DOE) is leading a national initiative oriented toward developing more energy efficient and environmentally friendly highway transportation technologies that will enable Americans to use less petroleum. Known as the FreedomCAR and Vehicle Technologies (FCVT) Program [1], this office sponsors a variety of activities aimed at making advances in fields such as materials technology. The objective of this program is to foster the development of lightweight, high-performance materials that can play an important role in improving the efficiency of transportation engines and vehicles.

The development of lightweight materials is an attractive idea for two reasons. First, if we consider current transportation technologies, weight reduction is one of the most practical ways to increase the fuel economy of vehicles while reducing exhaust emissions. Second, if we see the problem in terms of alternative sources of energy, such as fuel cells, which provide a lower output of energy per unit of mass, then we need to reduce the weight of the cars to compensate for the reduction in power obtained from these alternate sources.

1. Introduction

In the research presented herein, the development of lightweight composite materials made by the injection molding process will be explored. This popular polymer processing method is widely used to manufacture intricate molded parts and can be used for mass production of composites without major modifications. Lightweight molded composites consist of a polymeric matrix reinforced with high aspect ratio (length/diameter) particles, chosen because of the excellent mechanical properties obtained in the final product, the high throughput, and cost reduction. The typical high aspect ratio particles used to reinforce the composites are glass fibers classified as short and long, with a length of 1 mm as the threshold value for this classification. Although our main interest is fibers, the discussion in the justification and literature review will include nanoparticles, *e.g.* nanoclays and nanotubes, which are also high aspect ratio particles.

The improvement in mechanical properties is dependent on the particle orientation through the whole part. The greatest increase in such properties occurs when the fibers are aligned in the direction of mechanical interest. However, the particle orientation varies through the part as a consequence of flow-induced orientation within the mold during the forming stage. This can lead to local variation in the part's mechanical properties. This means that mechanical properties such as strength will be dependent on both the local stress state and fiber orientation [2]. In order to optimize the technology, a predictive tool should be developed using a computer model capable of designing the correct molding machinery, mold, and process conditions, which are capable of controlling fiber orientation. The objective of this work is to develop experimental and numerical tools capable of predicting the flow-induced orientation of glass fiber.

1.1 Background of reinforcement materials in thermoplastic composites

Composite materials are engineering materials with improved mechanical or electrical properties such as strength, stiffness, and conductivity, relative to properties of the main component. This improvement is obtained by incorporating the properties of constituents to develop a hybrid material possessing the desired properties. This is a broad field in engineering where several different technologies have been developed to manufacture these materials. Figure 1.1 shows a summary of the different alternatives used to classify composites [2], depending on the reinforcing material and the internal structure developed during their manufacture. From the spectrum of technologies shown in Figure 1.1, our main interest is discontinuous high-

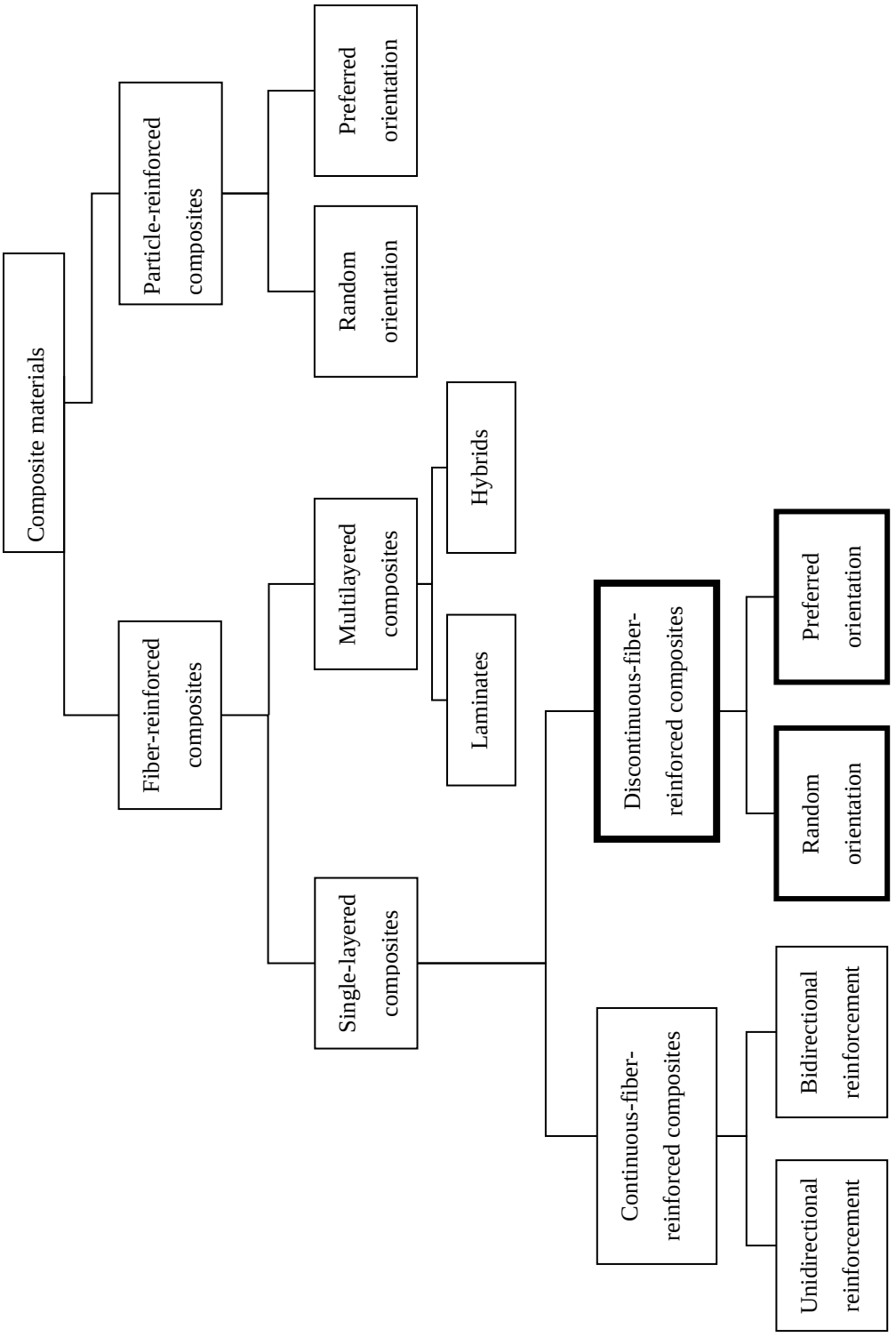

Figure. 1.1 Classification of composite materials[9]

1. Introduction

aspect-ratio-reinforced composites, *e.g.* discontinuous fiber composites and nanoparticles-reinforced composites. The discontinuous fiber composites are composed of chopped strands of reinforcing particles and are used in general purpose applications of moderate strength. The larger length of continuous fiber composites causes these materials to have the greatest improvement in properties compared to the matrix and other types of composites. For this reason, they are mostly used in high performance applications such as aerospace structures or sporting goods. However, the advantage of discontinuous- over continuous-fiber composites is the reduction of the cost of manufacturing parts and manufacturing time. Particle reinforced composites have the lowest enhancement properties of the various types of composites because the reinforcing agent consists of particles having roughly equal dimensions in all directions. In this chapter, we will refer to the discontinuous fiber composites and nanoparticle-reinforced composites as fiber composites and nanocomposites, respectively.

The constituents of composites, irrespective of the technology employed, are the matrix, the reinforcement materials, and the coupling agent. The matrix is the material of major concentration that gives the support to the composite and transmits the force to the reinforcement. A commonly used matrix for composites in the automotive industry is polypropylene, due to its low cost, its low density, its moisture resistance, its acceptable mechanical properties, and its low melting temperature compared to engineering resins [3]. The reader is referred to Sehanobish [4], where an recent description of polymer composites used in the automotive industry is provided.

Fibers and nanoparticles are discontinuous high aspect ratio particles of interest which can enhance thermal, electrical and mechanical properties relative to the neat matrix. Materials in the form of filaments can have better mechanical properties than bulk materials due to the reduction of intermolecular defects [5]. For example, Bunsell and Renard [5] indicate that an assembly of glass fibers making up a given volume can be much stronger than the same volume of the same glass in bulk form. The properties of glass fiber and other high strength fibers typically used in composites are summarized in Table 1.1. As one moves down in the table, the improvement in mechanical properties increases, but so does the cost. The E-glass fiber has gained popularity due to its good balance of mechanical properties and low cost [3]. On the other hand, the

Table 1.1 Properties of high strength fibers [2].

Type of fiber	Tensile strength (MPa)	Tensile modulus (GPa)	Elongation at Failure (%)	Density (g/cm^3)	Coefficient of thermal expansion (10^{-6}/K)	Fiber diameter (μm)
Glass						
E-Glass	3447	75.8	4.7	2.58	4.9-6.0	5-20
S-2-Glass	4482	86.9	5.6	2.48	2.9	5-10
Quartz	3378	68.9	5.0	2.15	0.5	9
Organic						
Kevlar 29	3620	82.7	4.0	1.44	-2.0	12
Kevlar 49	3792	131.0	2.8	1.44	-2.0	12
Kevlar 149	3447	186.2	2.0	1.47	-2.0	12
Spectra 1000	3103	172.4	0.7	0.97	- - - - -	27
Pan Based Carbon						
Standard modulus	3447-4826	221-241	1.5-2.2	1.80	-0.4	6-8
Intermediate modulus	4137-6205	276-296	1.3-2.0	1.80	-0.6	5-6
High modulus	4137-5516	345-448	0.7-1.0	1.90	-0.75	5-8
Pitch based Carbon						
Low modulus	1379-3103	172-241	0.9	1.9	- - - - -	11
High modulus	1896-2758	379-621	0.5	2.0	-0.9	11
Ultra high modulus	2413	689-965	0.3	2.2	-1.6	10

.

outstanding mechanical, thermal, and electrical properties of the nanoparticles has drawn the attention of researchers and industry to consider them as reinforcement material for polymer nanocomposites [6]. Fibers and several types of nanoparticles differ in their absolute dimensions. Fibers have dimensions in a range of micrometers to several millimeters, while nanoparticles have dimensions in a range of nanometers to micrometers. Figure 1.2 illustrates the dimensions and shape of fibers, carbon nanotubes and nanoclays. As we can see in Figs. 1.2(a) and (b), the fibers and carbon nanotubes are rod-like particles but have differences in lengths and diameter, while the nanoclays (Fig. 1.2. (c)) are platelets in the same range of aspect ratio as the

1. Introduction

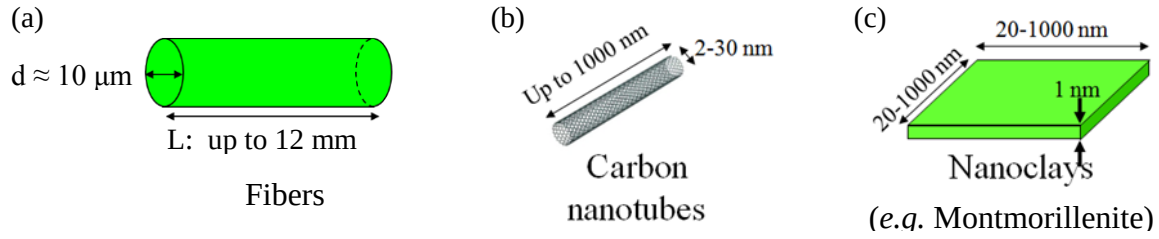

Figure 1.2 Dimensions and shape of high aspect ratio particles (a) discontinuous fibers (b) carbon nanotubes and (c) nanoclays.

carbon nanotubes, *i.e.* $(\text{diameter/thickness})_{\text{nanoclays}} \approx (\text{length/diameter})_{\text{nanotubes}}$. One of the drawbacks of composites that has been surmounted is the affinity between the matrix and the reinforcement materials. The particle-to-matrix bond is critical for the transmission of force in the composite; for this reason a coupling agent is added. They have an end-group that is compatible with the surface of the particle and another end group that is compatible with the polymeric matrix. Organosilane and maleic anhydride are coupling agents used in commercial fiber-composites and nanocomposites, respectively. Campbell [3] indicates that organosilanes improve the tensile, flexural, and compression strength in fiber composites by over 100%. He also indicates that the coupling agent helps to protect the glass fiber from attack by water.

Control of the particle orientation during processing is one of the most important factors in obtaining a consistent and reliable property of interest, *e.g.* electrical, thermal, and mechanical properties, in composites. The problem arises from the flow induced orientation causing local variation of the properties of interest in the part. This anisotropy of properties of interest depends on the volume fraction, orientation and aspect ratio of the particles [7]. The uncontrollability of the orientation is accentuated for parts containing longer particles and higher volume fractions. Therefore, in order to optimize and control the injection molding of thermoplastic composites, it is crucial to understand and to be able to predict the dynamics of flow and particle orientation as a function of process conditions and material parameters.

1.2 Injection molding process for thermoplastic composites

In this section, the description of the injection molding process is summarized. A detailed description can be found elsewhere [8-10]. In general terms, the injection molding process of a fiber composite consists of

melting plastic pellets containing the reinforcement material and injecting the molten material into a cooled mold, which remains closed until the part is solidified enough to maintain its shape without distortion. Knowing key aspects of the injection molding machinery and of the molding cycle are important for understanding the effects of the process which will be in part responsible for the final orientation in the molded parts. Fig. 1.3 illustrates the main components of an injection molding machine, *i.e.* the injection unit (also called a plasticizing unit), the clamping unit, and the mold. The purpose of the injection unit is to melt and inject the melt, while the clamping unit holds the mold closed during the forming and solidification of the part. The heart of the injection molding process is the mold because this is the place where the suspension flows and gives shape to the part (Fig. 1.3(b)). All of these parts directly interact in the molding cycle illustrated in Fig. 1.4. The cycle is divided into the stages of plastication, filling, packing, hold, cooling, and part ejection [11]. The plastication occurs in the injection unit, while the filling, packing and cooling happen in the mold. The part ejection is mainly due to the action of the clamping unit. An important aspect of the molding cycle shown in

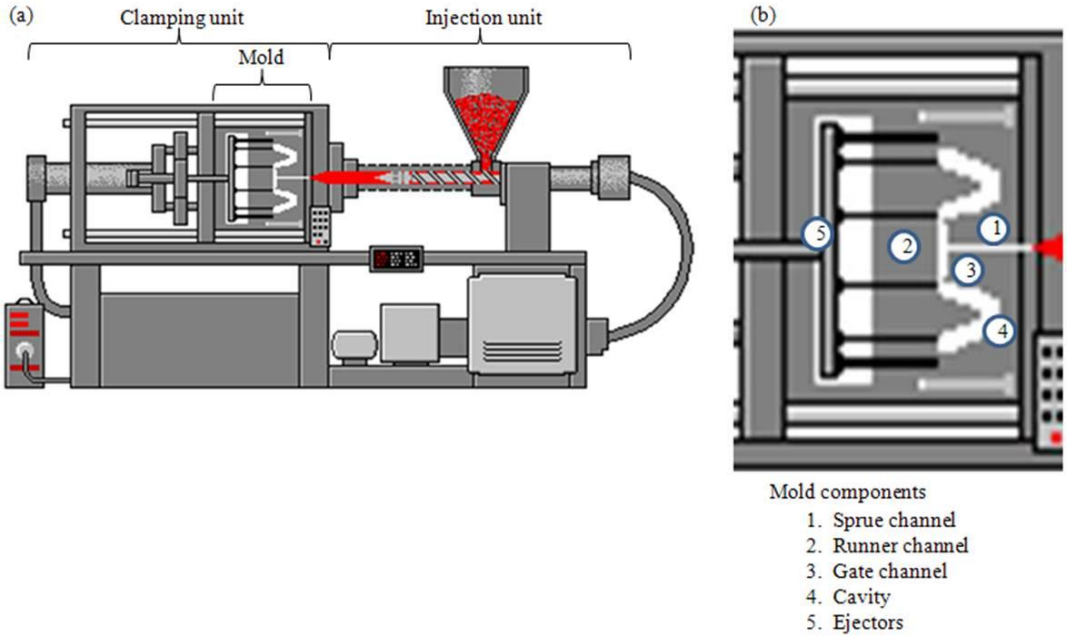

Figure .1.3 Injection molding components. (a) Injection molding machine and (b) mold. Image obtained from Ref. [12].

1. Introduction

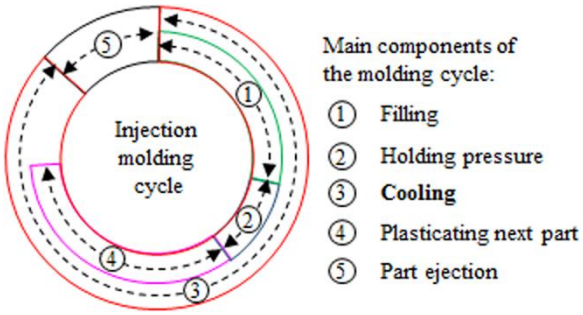

Figure .1.4 Main components of the molding cycle.

Fig. 1.4 is that the cooling stage overlaps the mold filling, packing, and holding stages. The plastication and the mold filling are the most relevant steps to the orientation pattern through the molded part. The contribution of packing and cooling has secondary implications in the orientation and their contribution has not been investigated in detail [7].

Plastication is crucial for obtaining a uniformly molten suspension in the case of glass fiber composites and to exfoliate nanoparticles in the case of nanocomposites. About 70% of the energy required to melt the pellets is provided by shearing action [8]. However, the use of shearing heating is detrimental to the fibers because it causes a gradual breakage, known as fiber attrition. Indeed, the fiber attrition is attributed to fiber-fiber interaction, fiber-polymer interaction, and fiber contact with surfaces of processing [13]. The impact of differences in fiber length, mostly caused by the plastication of plastics, is typically ignored in the estimation of fiber orientation, but understanding how the breakage occurs is important [14, 15]. Experimental measurements have shown fiber length distribution (FLD) in the molten material having an asymmetric profile with a peak skewed toward small fiber lengths [16]. The FLD is determined by original fiber length, fiber concentration, mold geometry, and process conditions. However, it is common to assume uniform length of fibers due to the inability to measure individual length of the fibers during orientation analysis.

In the filling stage, the screw moves axially by ram-advancement of the screw pushing approximately 95% of molten material (called shot size) to the mold within a few seconds, causing relatively high shear rates in the fluid. In the case of neat polymers, these shear rates are 100-10000s^{-1} [8]. When a melt containing fillers

such as fibers is injected, the filling of the part is more difficult because the viscosity of the suspension increases. As expected, processing difficulty increases with increased reinforcement loading [17]. In a general case, the molten dispersion is forced to pass through the different components of the mold: sprue, runner, gate, and cavity, as seen in Figure 1.3(b). Some molds are absent of these components, *e.g.* center-gated disks have not runners. The sprue is a tapered cylindrical conduit that directs the melt from the injection unit into the channels of distribution known as runners. The diverging shape of the sprue causes complex kinematics in which both shear and elongational flow define the orientation of fibers [7]. Orientation in the sprue is mainly parallel to the flow direction [18]. Usually, the flow changes direction when it passes from the sprue to the runners. Then the suspension meets a constriction followed by expansion at the gate. The changes in geometries and direction, as well as contraction/expansion flow, significantly affect the particle orientation in the cavity and can be responsible for additional fiber attrition.

Finally, the fluid enters into the cavity, where the material acquires the shape of the part. For a neat polymer, Tadmor and Gogos [19] indicate that the melt flowing into the cavity encounters three regions of flow: the entry region, the fully developed region, and the frontal region. At the entry region, the fluid experiences three-dimensional flows and a combination of elongational and shear flows. As the polymer melt continues flowing through the cavity, the flow character changes due to a strong shear effects due to predominant axial velocity. The frontal part of the fluid, in contact with the air, has a free surface that modifies the flow phenomena as compared to the bulk flow. The center of the fluid is moving at a maximum velocity but the borders of the fluid always have zero (or low) velocity due to fast cooling when the polymer melt touches the surface at the borders. Therefore, the fluid elements experience a fast deceleration as they approach the wall. As a result of incompressibility, in a Lagrangian reference frame, the fluid elements acquire a transverse velocity, spilling out towards the wall, developing a fountain-like profile, known as fountain-flow [7, 19]. Papathanasiou [7] indicates that fountain flow is the most important feature of the filling process, contributing to the development of certain fiber orientation in a region close to the wall of the cavity.

The flow field in the cavity induces the orientation of the fibers, creating a layered structure. Papathanasiou [7] gives a very detailed description of the filling pattern in the cavity and the effects on the final

structure in the cavity. The key consequence of the flow field is the formation of distinct laminate structures across the thickness influenced by the flow kinematics in the cavity. The formation of a skin containing a random planar fiber orientation determined by the frontal flow surrounds a multilayer structure. This multilayer structure has been named the "shell-core structure," and it has been attributed to the formation of parallel and transverse fiber alignment due to shear and extensional flow, respectively. Papathanasiou [7] indicates that the following factors define the orientation in the core: the kind of injection gate, injection speed, wall solidification, cavity thickness, cavity wall temperature, and melt rheology. Other factors that also affect orientation are wall-effects, regions with inhomogeneous fiber concentration, fiber orientation in the sprue, effect of packing, weldlines, fiber length and concentration [7].

1.3 Weaknesses in the current simulation of thermoplastic composites

Enhancement of simulation capabilities for thermoplastic composites is required to develop reliable design analysis and control of molding operations to meet the quality and performance requirements of the automotive industry. Commercial simulation packages available, *e.g.* Moldflow, Moldex 3D, and Sigma Soft, provide just a qualitative prediction of particle orientation due to limitations in mathematical models describing the orientation and numerical capabilities of the software. More specifically, the orientation is only predicted for short fiber composites within a limited range of fiber concentration and the predictions are only valid in regions away from the entrance or near the advancing front of the part. The standard model in commercial simulation software, the Folgar-Tucker model [20], is unable to completely account for all fiber-fiber interactions for concentrated suspensions, thus preventing a precise description of orientation for molded parts within a fiber concentration of commercial interest. Additionally, experimental evidence including rheological measurements [21-23] and measurement of fiber orientation in highly concentrated suspensions [24, 25] indicates that the Folgar-Tucker model predicts a faster evolution of orientation than is observed. Capturing the correct behavior of the orientation evolution of high aspect ratio particles has come to the forefront due to the commercial interest in using long fibers and nanoparticles to improve the mechanical, thermal and electrical properties of composites. An additional limitation of the modeling of fiber composites is that the model

parameters used for the simulations are typically obtained from empirical relationships or obtained from the injection molding experiment being simulated [26-28].

The numerical strategy used in the simulation of fiber orientation relies on the use of several simplifications which allows solving the problem in reasonable time. The decoupled approach and the Hele-Shaw flow approximation are two common simplifications introduced in the governing equations to simulate the fiber orientation in thermoplastic composites. These simplifications are based on the fact that injection molded parts are thin geometries, *i.e.* the thickness of the mold is much less than other characteristic dimensions of the parts are. The decoupled approach is a simplification for fiber suspensions flowing in narrow gaps in which the extra stress depends only on the velocity gradient but not on the fiber orientation state [29]. This simplification consists of the flow field computation without considering the presence of fibers followed by the post-calculation of the orientation from the velocity profile found in the previous step. The second simplification, the Hele-Shaw flow approximation, is a simplification based on the lubrication approximation, where the balance equations are approximated in such way that the flow is always locally similar to pressure-driven flow between parallel plates [30]. However, the Hele-Shaw flow approximation is limited in that it neglects the entry and the fountain flow regions. The use of these assumptions is not necessarily representative of the physics of the problem, but this numerical strategy is used because its use reduces the simulation time. Two additional numerical limitations in simulating fiber orientation are the prescription of the inlet orientation and simulations that only consider the upper half of the fluid domain. The hyperbolic nature of the Folgar-Tucker model requires the specification of the orientation at the inlet of the geometry.

Obtaining the complete orientation information along the entire domain of a molded part can help to improve the simulation models used in designing parts and process manufacturing. The evaluation of orientation at various locations will provide data to validate simulation results and to optimize simulation tools capable in designing better molding machinery, molds and process conditions. However, the number of publications including orientation measurements on test geometries in which the flow conditions are well known is limited and these experimental characterizations of orientation are incomplete. For example, the center-gated disk is one of these test geometries but there are only a limited number of experimental fiber

orientation studies [31-33]. This geometry has industrial relevance because the radially-divergent flow pattern seen in center-gated disks also commonly occurs near the entry region in complex industrial molds [34]. The assessment of orientation at the gate will provide inlet orientation data rather than assuming inlet orientation as is typically done in existing simulations. Nevertheless, measurements at key locations that affect the orientation state, such as the entry and frontal regions, are not available in the literature. Capturing the 3D nature and fast changes in orientation over these areas is still challenging from an experimental point of view. However, a reliable and cost-effective experimental method to quantify the final three-dimensional orientation state in the parts either to assess the procedure or to validate simulation results is not available.

1.4 Research objectives

The primary goal of this research is the prediction of high aspect ratio particle orientation in injection-molded parts and the experimental validation of these predictions of orientation. With regard to this goal, three objectives have been formulated:

1. The introduction of modifications in the standard method (*i.e.* the method of ellipses) and the development of an image analysis tool to evaluate fiber orientation. The proposed modification considers the evaluation of orientation from non-elliptical footprints observed in optical micrographs, which allows the measurement of orientation in a small sampling region. The modifications also include a special sample preparation which enables identifying the direction of the fibers coming out of the polished plane and eliminating the ambiguity problem in fiber orientation. The modifications require the development of a customized image analysis tool.
2. The development of a 2D numerical simulation tool to predict the flow-induced orientation of high aspect ratio reinforced thermoplastic composites in a decoupled solution scheme. The proposed simulation considers inter-particle interactions and delay in the evolution of the fiber orientation. The numerical tool uses the discontinuous Galerkin method to solve the hyperbolic nature of the constitutive equations and the Arbitrary Langrangian Eulerian method for the moving front problem. Assuming isothermal conditions due to fast filling, the filling process of a short glass fiber

thermoplastic injection molded composite will be solved using a decoupled approach for an approximated solution using a Hele-Shaw flow approximation which excludes the frontal flow.

3. Corroboration of the prediction of fiber orientation with experimental data obtained from the experiments performed. Orientation from incomplete thin center-gated disks is used to validate predictions of orientation for a fast filling operation. The simulations are based on the Folgar-Tucker model with a slip parameter correction using customarily assumed inlet orientation being random and experimentally measured at the gate. The model parameters used in these simulations were obtained from rheometrical experiments which are part of earlier efforts of our research group.

1.5 References

[1] Vehicle Technologies Program. In: USDOE, editor.2012. p. http://www1.eere.energy.gov/vehiclesandfuels/.

[2] Agarwal BD, Broutman LJ, Chandrashekhara K. Analysis and performance of fiber composites 3rd ed. Hoboken, N.J. : John Wiley; 2006.

[3] Campbell FC. Manufacturing processes for advanced composites. Oxford, UK Elsevier; 2004.

[4] Sehanobish K. Engineering plastics and plastics composites in automotive applications. Warrendale, PA, USA: SAE International; 2009.

[5] Bunsell AR, Renard J. Fundamentals of fibre reinforced composite materials. Bristol, UK: Taylor & Francis, Inc; 2005.

[6] Moniruzzaman M, Winey KI. Polymer nanocomposites containing carbon nanotubes. Macromolecules. 2006;39:5194-5205.

[7] Papathanasiou TD. Flow-induced alignment in injection molding of fiber-reinforced polymer composites. In: Papathanasiou TD, Guell DC, editors. Flow-induced alignment in composite materials. Cambridge, England: Woodhead Publishing Limited; 1997. p. 112-165.

[8] Morton-Jones DH. Polymer processing. London, UK: Chapman and Hall; 1989.

[9] Pötsch G, Michaeli, W. Injection molding: An introduction. Munich, Germany: Hanser-Gardner Publications; 1995.

1. Introduction

[10] Rosato DV, Rosato DV, Rosato MG. Injection molding handbook. 3rd ed. Boston, MA, USA: Kluwer Academic Publishers; 2000.

[11] Malloy RA. Plastic part design for injection molding: An introduction. 2nd ed. Munich, Germany: Hanser-Gardner Publications; 2011.

[12] Hill M. Machine Animation. Ferris State University.

[13] vonTurkovich R, Erwin L. Fiber fracture in reinforced thermoplastic processing. Polym Eng Sci. 1983;23:743-749.

[14] Bay RS, Tucker CL. Stereological measurement and error estimates for three-dimensional fiber orientation. Polym Eng Sci. 1992;32:240-253.

[15] Nguyen BN, Kunc V, Frame B, Phelps J, Tucker III C, Bapanapalli S, et al. Fiber length and orientation in long-fiber injection-molded thermoplastics. Part I. Modeling of microstructure and elactic properties. J Compos Mater. 2009;42:1003–1029.

[16] Fu SY, Yue CY, Hu X, Mai YW. Characterization of fiber length distribution of short-fiber reinforced thermoplastics. J Mater Sci Lett. 2001;20:31– 33.

[17] Throne JL. Processing thermoplastic composites. In: Peters ST, editor. Handbook of composites. 2nd ed. London, UK: Chapman and Hall; 1998. p. 525-552.

[18] Bright PF, Crowson RJ, Folkes MJ. A study of the effect of injection speed on fiber orientation in simple mouldings of short glass fibre-filled polypropylene. J Mater Sci. 1978;13:2497-2506.

[19] Tadmor Z, Gogos CG. Principles of polymer processing. Hoboken, NJ, USA: John Wiley; 2006.

[20] Folgar F, Tucker C. Orientation behavior of fibers in concentrated suspensions. J Reinf Plast Comp. 1984;3:98–119.

[21] Sepehr M, Ausias G, Carreau P. Rheological properties of short fiber filled polypropylene in transient shear flow. J Non-Newtonian Fluid Mech. 2004;123: 19-32.

[22] Eberle A, Vélez-García G, Baird D, Wapperom P. Fiber orientation kinetics of a concentrated short glass fiber suspension in startup of simple shear flow. J Non-Newtonian Fluid Mech. 2010;165:110 - 119.

[23] Wang J, O'Gara J, Tucker C. An objective model for slow orientation kinetics in concentrated fiber suspensions: Theory and rheological evidence. J Rheol. 2008;52:1179-1200.

[24] Huynh HM. Improved fiber orientation predictions for injection-molded composites: Master's Thesis, University of Illinois at Urbana-Champaign; 2001.

[25] Vélez-García GM, Mazahir SM, Wapperom P, Baird DG. Simulation of injection molding using a model with delayed fiber orientation. Intern Polym Processing. 2011;26:331-339.

[26] Bay R, Tucker CL. Fiber orientation in simple injection moldings .1. Theory and numerical-methods Polym Composite. 1992;13:317-331.

[27] O'Dowd F, Levesque M, Gilchrist MD. Analysis of fibre orientation effects on injection moulded components. P I Mech Eng B-J Eng. 2006;220:1909-1921.

[28] Phelps J, Tucker C. An anisotropic rotary diffusion model for fiber orientation in short- and long-fiber thermoplastics. J Non-Newtonian Fluid Mech 2009;156:165-176.

[29] Tucker CL. Flow regimes for fiber suspensions in narrow gaps. J Non-Newtonian Fluid Mech. 1991;39:239-269.

[30] Dantzig JA, Tucker, C.L. Modeling in materials processing. Cambridge, UK: Cambridge University Press; 2001.

[31] Vincent M, Agassant, J.F. Experimental study and calculations of short glass fiber orientation in center gated molded disks. Polym Composite. 1986;7:76-83.

[32] Bay RS, Tucker CL. Fiber orientation in simple injection moldings. 2. Experimental results. Polym Composite. 1992;13:332-341.

[33] Neves N, Pontes A, Pouzada A. Experimental validation of morphology simulation in glass fibre reinforced polycarbonate discs. J Reinf Plast Comp. 2001;20:452-465.

[34] Vincent M, Agassant, JF. Predicting fiber orientation in injection molding. In: Utracki LA, editor. Progress in polymer processing: Two phase polymer systems. Munich: Hanser; 1991. p. 277-303.

Chapter 2 Literature review on high aspect ratio particle thermoplastic composites

The simulation of a thermoplastic composite during mold-filling in an injection molding process is a difficult task. During the filling stage the composite is a binary mixture in the fluid state composed of polymeric suspending medium and solid high aspect ratio particles. The behavior of each component in the fluid must be described using a constitutive equation in order to predict the properties of interest of the mixture. However, describing the behavior of the fluid is difficult due to the non-Newtonian nature of the polymeric matrix, i.e. viscoelastic or shear-thinning effects, and the complex rheology introduced by the presence of high aspect ratio particles. In addition, a suitable description of a flow that mimics the real process requires the inclusion of the advancing front. The transient behavior will lead to the development of certain special features observed in the solidified composite such as a distribution of high aspect ratio particles orientations arranged in a layered structure. Therefore, the first section (§2.1) of this review is focused on the equations used to describe the flow during the filling stage. First, the balance equations with the boundary conditions describing the filling flow are described followed by the constitutive equations for the matrix and the high aspect ratio particles.

The challenge in simulating the injection molding of thermoplastic composites can be seen not only as a problem of finding the correct mathematical model to describe the system, but also as a problem in determining the numerical strategy to be used in the solution of the equations. Therefore, in section 2.2 numerical methods to solve the system of equations in a coupled scheme are reviewed. The section begins by reviewing space and time discretization used to solve the governing equations. Then, methods of tracking a moving boundary are reviewed in an effort to determine the location of the flow front. The solution of the problem is a difficult task due to the hyperbolic form of the constitutive equations and advancing front. The discontinuous Galerkin method is reviewed in order to understand how other research groups have been using it to solve similar systems of hyperbolic equations.

The third section of this review is focused on the experimental methods used to evaluate the high aspect ratio particle orientation in 2D and 3D. The objective of this section is to review the tools involved in experimental characterization of particle orientation i.e. fiber orientation of injection molded parts.

Chapter 2

2.1 Governing equations

This section describes the governing equations of the filling stage of an injection molding process. The flow is assumed to be isothermal. The isothermal conditions are justified in the filling phase of injection molding process based on the fact that the injection process occurs very rapidly (fill times of the order of a few seconds) compared to the time required to significantly change the melt temperature (minutes). For the practical point of view, the fountain flow near the advancing front must be captured. For this reason, the full system of balance equations and boundary conditions including the moving front are reviewed in order to develop the physical description of the marching problem that occurs during the mold filling. The constitutive equations for the polymeric matrix are reviewed in the second subsection (§2.1.2) organized in Newtonian, generalized Newtonian and viscoelastic matrix. The third subsection (§2.1.3) describes the Folgar-Tucker equation that model the orientation of high aspect ratio particles. In addition, in section 2.1.3 the different stress or orientation equations to model high aspect ratio particles are reviewed. In order to assess the proposed viscoelastic and high aspect ratio particle models in terms of the commercially accepted method of simulation, the Hele-Shaw approximation is reviewed in section 2.1.4. This approximation is a simplification to the use the balance equations which is used to ease the calculations and reduce the computational demands. A physical impact of the Hele-Shaw approximation is that it ignores the contribution of the frontal flow, which can lead to imprecision in the predicted orientation if the frontal flow has big impact in the behavior of orientation.

2.1.1 Balance equations of a polymeric suspension during the filling stage

The mass and momentum equation for isothermal flow are referred to as the conservation equations and are defined, respectively as:

$$\frac{D\rho}{Dt} = \frac{\partial \rho}{\partial t} + \underline{v} \bullet \underline{\nabla}\rho = -\rho\left(\underline{\nabla} \bullet \underline{v}\right) \tag{2.1}$$

$$\rho \frac{D\underline{v}}{Dt} = \rho \frac{\partial \underline{v}}{\partial t} + \rho \underline{v} \bullet \underline{\nabla}\underline{v} = \underline{\nabla} \bullet \underline{\underline{\sigma}} \tag{2.2}$$

where D/Dt represents the material derivative, the t time, ρ the fluid density, $\underline{\nabla}$ the gradient operator, $\underline{v}$ the velocity, and $\underline{\underline{\sigma}}$ the total stress tensor or Cauchy stress. The conservation of mass (Eq. (2.1)) expresses that the

total mass is conserved, while the conservation of momentum (Eq. (2.2)) expresses that the sum of internal forces (momentum due to molecular transport) is equal to the change in momentum. The Cauchy stress indicates that the internal forces in a fluid are due to the pressure (p) and extra stress ($\underline{\underline{T}}$) that is represented as:

$$\underline{\underline{\sigma}} = -p\underline{\underline{\delta}} + \underline{\underline{T}} \tag{2.3}$$

where $\underline{\underline{\delta}}$ denotes the unit tensor. By definition the pressure is a compressive normal stress, having a negative sign. It implies that the fluid flows from high to low pressure regions. The sign of the extra stress is the opposite because the usual fluid dynamics sign convention takes a tensile stress to be the positive normal stress [1].

In order to adapt the conservation equations combined with Eq. (2.3) to the injection molding process, the following assumptions are made: constant mass, negligible inertia and local acceleration (due to the high viscosity of the polymer melt). The set of equations defining a polymer melt flowing into a cavity during the filling stage of an injection molding process then becomes

$$\underline{\nabla} \bullet \underline{v} = 0 \tag{2.4}$$

$$\underline{\nabla} \bullet \left(-p\underline{\underline{\delta}} + \underline{\underline{T}}\right) = \underline{0} \tag{2.5}$$

Eq. (2.4) is known as the incompressibility condition, meaning that density remains constant [2]. The key to simulate injection molding of composite materials is the specification of the extra stress tensor[2].

The extra stress tensor for a high aspect ratio particle-filled polymeric suspension consists of two components,

$$\underline{\underline{T}} = \underline{\underline{T}}^{particles} + \underline{\underline{T}}^{matrix} \tag{2.6}$$

where $\underline{\underline{T}}^{particles}$ is the stress due to the movement of high aspect ratio particles in the fluid and the $\underline{\underline{T}}^{matrix}$ the contribution of the polymer matrix.

To understand the behavior of the material, it is necessary to develop an equation that relates the flow phenomena to the stress. When a suspension of high aspect ratio particles in a viscoelastic fluid is considered, the stresses due the matrix and high aspect ratio particles have to be considered. One arises from the

deformation due to the kinematics of the fluid and the other from the drag produced by the fluid as it flows past the high aspect ratio particles. Therefore, we need to consider rheological expressions for both sources.

Boundary conditions

The boundary conditions in the cyclic process of injection molding are the result of fluid-solid (melt suspension-wall) or fluid-fluid (i.e melt suspension-air) interactions. Boundary conditions along the 1,3-plane are shown in Fig. 2.1 because the focus of this review is 2-D analysis. Fig. 2.1 depicts the following boundary conditions used to solve the balance equations. They are described as follows [3]:

Inflow: $\underline{v} \bullet \underline{n} = f(x_3), \quad \underline{v} \bullet \underline{t} = 0$ (2.7)

where $f(x_3)$ denotes a velocity profile.

Symmetry: $\left(\underline{\underline{\sigma}} \bullet \underline{n}\right) \bullet \underline{t} = \underline{0}, \quad \underline{v} \bullet \underline{n} = 0$ (2.8)

where $\underline{t}$ the tangent and $\underline{n}$ the normal vector to the axis of symmetry. Along the centerline, Eq. (2.8) indicates the absence of tangential stress and normal velocity components, typical for symmetry boundary.

Free surface: $\left(\underline{\underline{\sigma}} \bullet \underline{n}\right) \bullet \underline{n} = 0$ (2.9)

$\left(\underline{\underline{\sigma}} \bullet \underline{n}\right) \bullet \underline{t} = 0$ (2.10)

Eqs. (2.9) and (2.10) mean that the components of the traction vector normal and tangential to the surface, respectively are zero. The free surface moves with the fluid velocity that is determined from the solution of the balance equations.

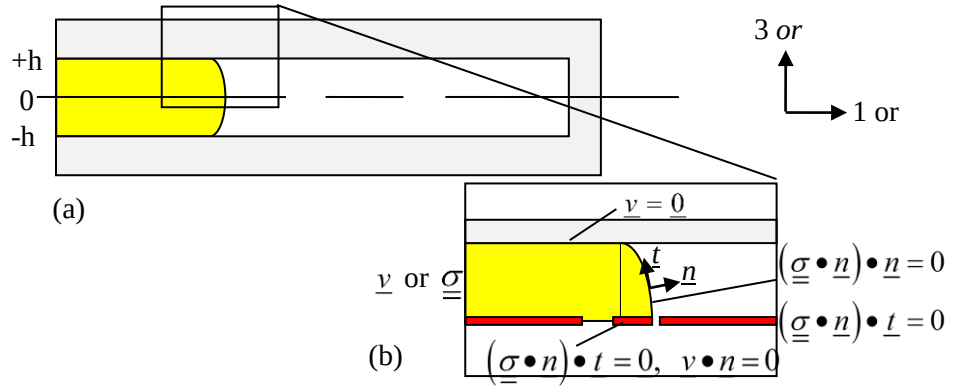

Figure 2.1 Boundary conditions considering no-slip condition at the wall in the injection molding process.

Wall: $\underline{v} = \underline{0}$ (2.11)

Eq (2.11) expresses the typical assumption of no-slip boundary condition at the wall indicating that the normal and tangential components of the fluid velocity are zero. This means that the fluid cannot move through the wall and that no-slip occurs at the boundary. Although the no-slip condition can reproduce the characteristic of flow, there are situations e.g. corner flow and some flow of polymer melts, that lead to singular or unrealistic behavior [4-6]. The existence and degree of slip depend on the structural and dynamic properties of the fluid-solid interface [7]. A wall-slip is described by Navier's slip condition which states a relationship between the tangential component of the momentum flux at the wall and the local slip velocity [8]. This relationship is expressed as

Wall: $\left(\underline{\underline{\sigma}} \bullet \underline{n}\right) \bullet \underline{t} + \varsigma \underline{v} \bullet \underline{t} = 0$ (2.12)

$\underline{v} \bullet \underline{n} = 0$ (2.13)

where ς is the proportionality coefficient representing the slip length. The slip length is defined as the extrapolated distance from the wall where the fluid tangential velocity component vanishes [7]. Eq. (2.13) represents no flow through a solid wall.

2.1.2 Constitutive equations of polymeric matrices

There are several alternatives to the development of a rheological constitutive equation for a polymer melt, however here the continuum approach and molecular approach, will be considered. The continuum approach does not make a distinction between the constituents and consists of empirical modifications to the constitutive equation to fit their response, depending on the terms included in the equations. This approach has been useful to develop constitutive equations for Newtonian and shear-thinning non-Newtonian fluids. This section will review of Newtonian and generalized Newtonian constitutive relations.

2.1.2.1 Newtonian matrix

A Newtonian constitutive equation can be used to describe the behavior of a fluid of low molecular weight molecules and polymeric solutions or disperse system at low polymer or disperse phase concentration, respectively. The extra stress is given as:

$$\underline{\underline{T}}^{matrix} = 2\eta\underline{\underline{d}} \tag{2.14}$$

where η is the Newtonian viscosity and $\underline{\underline{d}}$ the rate of deformation tensor defined as:

$$\underline{\underline{d}} = \frac{1}{2}\left(\underline{\nabla v}^T + \underline{\nabla v}\right) \tag{2.15}$$

where $\underline{\nabla v}$ is the velocity gradient tensor. This constitutive equation indicates that the extra stress tensor is linearly proportional to the rate of deformation tensor. In extension the Newtonian model predicts that $\eta_E = 3\eta$. As the molecular structure of the materials become more complicated, such as for concentrated solutions and polymers melts the fluids deviate from Newtonian behavior. These kinds of fluid are referred to as non-Newtonian fluids. Non-Newtonian fluids can exhibit certain characteristic behaviors among others shear thinning, normal stress differences, and viscoelastic (memory) effects. The characteristic behaviors shown by the fluid have to be described by a different equation to the Newtonian constitutive equation. The Newtonian model can be used to approximate the behavior of Non-Newtonian fluid only at low deformation rates [9].

2.1.2.2 Enhancement of matrix viscosity at high shear rate

The contribution to the total extra stress from an inelastic matrix can be modeled as a viscous fluid which can play the dominant role at very high deformation rates [10]. At low deformation rates, the contribution to the total extra stress due to the matrix accounts for the isotropic contributions from the fluid and the particles, as described by Eq. (2.14) with viscosity (η) defined as the solvent i.e. matrix, viscosity (η_s). However, at high shear rates the typical shear thinning effects affect the values of the suspension viscosity [11]. The viscosity is enhanced by the addition of high aspect ratio particles, as depicted in Fig. 2.2. The amount of displacement is proportional to the relative viscosity (η_r) defined as

$$\eta_r = \frac{\eta_{suspension}}{\eta_{matrix}} \tag{2.16}$$

where the η_r accounts for the effective enhancement of the shear rate in matrix as a result of the large volume fraction occupied by the rods [10]. When the relative viscosity is introduced in the matrix stress, the form of the equation becomes

$$\underline{\underline{T}}^{matrix} = 2\eta_r \eta_s \underline{\underline{d}} \tag{2.17}$$

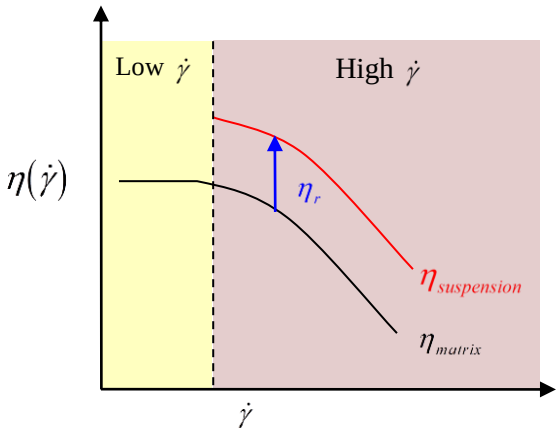

Figure 2.2 Typical enhancement of suspension viscosity at high shear rate.

Two possible empirical expressions that can be used to evaluate the relative viscosity has been indicated by Doraiswamy and Metzner [10]. These empirical expressions depend on the type of flow, i.e. shear or extensional, volume fraction, and aspect ratio. The relative viscosity in shear flows is defined as

$$\eta_r = \left(1 - \frac{\phi_v}{K}\right)^{-2} \tag{2.18}$$

where ϕ_v denotes the volume fraction and K is an experimental constant. The relative viscosity in elongational flow is

$$\eta_r = 1 + \frac{4}{9}\frac{\phi_v a_r^{\,2}}{\ln\left(\pi/\phi_v\right)} \tag{2.19}$$

The structure of these equations can be used to assess the enhancement in shear and extensional flow. In shear flow the enhancement shows exponential growth for concentration in a range below the *K* value while in extensional flow it shows linear growth with concentration and quadratic growth with aspect ratio.

2.1.2.3 Generalized Newtonian matrix

The generalized Newtonian constitutive equation can be used to describe fluids which show only shear thinning behavior, but it does not predict normal stresses in shear and memory effects. The generalized Newtonian constitutive equation is given by

$$\underline{\underline{T}}^{matrix} = 2\eta\left(II_d, III_d\right)\underline{\underline{d}} \tag{2.20}$$

where $\eta\left(II_d, III_d\right)$ is a function that describes the viscosity dependence on the second (II_d) and third (III_d) invariant of the rate of deformation tensor, defined respectively as:

$$II_d = 2\underline{\underline{d}} : \underline{\underline{d}} \tag{2.21}$$

$$III_d = \det(\underline{\underline{d}}) \tag{2.22}$$

For flows dominated by shear flow rather than extensional flow, III_d is not taken into account for the viscosity (η) [12]. When Eqs. (2.20) and (2.14) are compared, it can be seen that the difference between the Newtonian and Generalized Newtonian constitutive equations is based on the description of the viscosity function of shear rate.

Acceptable empirical relations for $\eta(\dot{\gamma})$ (where $\dot{\gamma}$ is scalar magnitude of the rate-of-deformation tensor) have to describe the viscosity for a wide range of shear rates. At low shear rates, the profile must show a plateau, but as the shear rate increases it shows a shear thinning behavior, i.e. a decrease of viscosity. In addition, the curve must include a transition region between the plateau and the shear thinning behavior. The Carreau-Yasuda empiricism is widely used because it describes all of the features of the viscosity curve [12]. It is defined as:

$$\eta = \left(\eta_0 - \eta_\infty\right)\left[1 + \left(\lambda\sqrt{II_d}\right)^{\alpha}\right]^{\left(\frac{n-1}{\alpha}\right)} + \eta_\infty \tag{2.23}$$

where λ is a time constant approximately representing the reciprocal of the shear rate for the onset of shear thinning behavior [12], η_0 the zero-shear viscosity, η_∞ the viscosity as II_d or $dv_1/dx_3 \rightarrow \infty$, α represents the width of the transition region between η_0 and the power law region, and n describes the degree of deviation from Newtonian behavior at higher shear rates.

2.1.3 Constitutive Equations for high aspect ratio particles

The rheological response to deformation of a suspension containing high aspect ratio particles is a function of the particle orientation and its evolution. The orientation of a population of these particles is developed from the description of a single particle using statistical methods combined with the Smoluchowski equation. The use of a statistical description is computationally expensive and has therefore lead to the development of the less costly orientation tensor. As the high aspect ratio particles rotate in the suspending medium, they will affect the local flow field causing an additional extra stress in the system. As a result the stress and associated rheological characteristics are intimately bound to the particle orientation.

This section is divided into two subsections. The first subsection will present the orientation tensor developed from the description of a single particle, while the second subsection will present the orientation of the population of particles is used to determine the stress due to the particles in the suspensions. The continuum and molecular approach will be reviewed for both the orientation and stress for high aspect ratio particles.

2.1.3.1 Particle orientation

Typically, high aspect ratio particles are described by some geometrical characteristics of the particles and the concentration range of the suspension. The particles are assumed to be uniform, axisymmetric, and characterized by the aspect ratio (a_r), which is defined as

$$a_r = \frac{l}{d} \tag{2.24}$$

where the l and d are the length and diameter of the particle, respectively. The particles are assumed to be suspended in a Newtonian solvent. The characteristics of the suspension have been found defined by the

particle volume fraction (ϕ_v) and aspect ratio simultaneously, which let to classify the suspension in three regimes of concentration:

- Dilute regime: $\phi_v << a_r^{-2}$
- Semi-dilute regime: $a_r^{-2} < \phi_v < a_r^{-1}$
- Concentrated regime: $\phi_v > a_r^{-1}$

These concentration regimes can be related to other variables typically used in the rheology of composites such as particle concentration (ν) or particle number (N_p). These additional rheological variables are related to volume fraction using:

$$\phi_v = \frac{\pi d^3}{4a_r}\nu \tag{2.25}$$

$$\phi_v = \frac{\pi d^3 \eta_s}{4a_r \zeta_{str}} N_p \tag{2.26}$$

where η_s denotes solvent viscosity and ζ_{str} viscous drag coefficient. N_p and ζ_{str} will be formally described later in the discussion. An important consideration on composites of commercial interest is that they fall in the concentrated regime classification, and, therefore, they will be our focus of attention. The modeling of concentrated suspensions is based on the inter-particle interactions and a coupled effect between the particle and fluid motion. However, previous work on modeling the motion of high aspect ratio particles has mainly focused on dilute and semi-dilute regimes. The dilute regime defines the particle motion in absence of particle interactions therefore this is the starting point in this section of the review.

The spatial orientation of a single high aspect ratio particle can be described using spherical coordinates with the azimuthal (ϕ) and zenith (θ) angles as is shown in Fig. 2.3. These angles are used to construct an orientation unit vector $\underline{p}$ parallel to the backbone of the particle defined as:

$$\underline{p} = p_1\underline{\delta}_1 + p_2\underline{\delta}_2 + p_3\underline{\delta}_3 \tag{2.27}$$

where the components are defined as:

$$p_1 = \sin\theta\cos\phi \tag{2.28}$$

Chapter 2

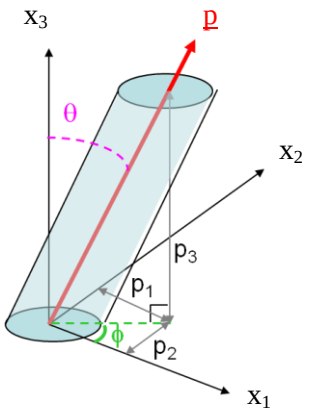

Figure 2.3 Description of high aspect ratio particle orientation in spherical coordinates

$$p_2 = \sin\theta \sin\phi \tag{2.29}$$

$$p_3 = \cos\theta \tag{2.30}$$

However, the description of the orientation of a high aspect ratio particle in a suspension which is flowing in a cavity is still not complete because the particles move with the fluid and change orientation due to the molecules of the suspending medium. Therefore, the orientation unit vector has to be part of an equation that describes the temporal changes of orientation due to the macroscopic flow field.

Jeffery developed an equation of motion for a single ellipsoidal particles immersed in a viscous fluid. The model is based on the following set of assumptions [13]:

1. The particle is rigid, ellipsoidal, neutrally buoyant, axisymmetric, and large enough for Brownian motion to be negligible.
2. The suspension fluid is Newtonian.
3. The matrix is sufficiently viscous that particle inertia and particle buoyancy are negligible so that the fluid motion is determined by Stoke's equation.
4. The velocity gradients are constant over the particle length so that the particle is subject to a homogeneous flow field.
5. There are no external forces or torques acting on the suspension.

The time rate of change of $\underline{p}$ for a dilute concentration of slender particles in a Newtonian solvent, originally described by Jeffery's equation [14] is defined by:

$$\dot{\underline{p}} = \frac{D\underline{p}}{Dt} = \underline{p} \bullet \underline{\underline{\varpi}} + \lambda \left[\underline{p} \bullet \underline{\underline{d}} - \left(\underline{p} \bullet \underline{\underline{d}} \bullet \underline{p} \right) \underline{p} \right] \tag{2.31}$$

where $\underline{\underline{\varpi}}$ is the vorticity tensor and λ_s is a constant that depends on the shape. λ_s is defined as

$$\lambda_s = \frac{a_r^{\,2} - 1}{a_r^{\,2} + 1} \tag{2.32}$$

For high aspect ratio particles $\lambda_s \approx 1$, therefore we will use this value for the rest of the review. The first term indicates the rotational motion of the high aspect ratio particles due to the macroscopic flow field. The second term indicates that the high aspect ratio particle moves as though it were an element of the fluid. The third term accounts for a constant length [15]. In Eq. (2.31) the rate of change of a particle's orientation is unaffected by Brownian motion, sedimentation, or other external forces such as particle-particle interactions [16]. For high aspect ratio particles, in the limiting case $\lambda_s \rightarrow 1$, Eq. (2.31) becomes:

$$\dot{\underline{p}} = \frac{D\underline{p}}{Dt} = \underline{\nabla v} \bullet \underline{p} - \left(\underline{p} \bullet \underline{\nabla v} \bullet \underline{p} \right) \underline{p} \tag{2.33}$$

The rate of change of orientation unit vector ($\dot{\underline{p}}$) to the macroscopic field for dilute particles suspended in a Newtonian solvent described by Eq. (2.31) or Eq. (2.33) is specific to just one high aspect ratio particle. Therefore, they must be extended to a complete population of particles in a suspension using a statistical method. The distribution function $\psi(\theta, \phi)$ or $\psi\left(\underline{p}\right)$ represents the orientation state of high aspect ratio particles with the same length and diameter [17], as long as it fulfills certain conditions explained in detail by Advani and Tucker [18]. From these conditions, the only condition pertinent to this review is Smoluchowski equation [19] defined as:

$$\frac{D\psi\left(\underline{p}\right)}{Dt} = -\frac{\partial}{\partial \underline{p}} \bullet \left(\psi\left(\underline{p}\right) \dot{\underline{p}} \right) \tag{2.34}$$

This condition describes the change in $\psi(\theta, \phi)$ with time when the high aspect ratio particles are changing orientation. The term Smoluchowski equation will be used to refer to Eq. (2.34), instead of the term continuity

condition. If we assume that the high aspect ratio particles move with the bulk motion of the fluid, then $\psi(\theta,\phi)$ may be regarded as a convected quantity [18]. The Smoluchowski equation provides an equation for the evolution of $\psi(\theta,\phi)$ with time when an appropriate expression for $\underline{\dot{p}}$ selected [18].

The background information exposed previously will be used in the following two subsection to develop several model used for suspension containing high aspect ratio particles i.e. Jeffery's, and Folgar-Tucker's [20] model. These subsections indicate the assumptions used to develop the model. Then the orientation tensor and typical predictions for each model will be presented in order to show a computationally effective description of the behavior of the population of particles including certain details about how the Folgar-Tucker model handle the Brownian or Brownian-like motions and closure approximations. Also typical predictions using each model will be discussed.

2.1.3.1.1 Jeffery model

The successful application of Jeffery's model to ellipsoidal suspension influenced the extension of the model to predict the behavior of high aspect ratio particles. However, the use in a single high aspect ratio particle involves modification in the behavior of the model such as the elimination of the periodic rotation. In this case a particle will rotate from its initial orientation toward the flow direction but never completely align or rotate. The orientation of a population of high aspect ratio particles described by Jeffery's model can be predicted using the evolution equation for the second order orientation tensor $\left(\underline{\underline{A}}\right)$, given by:

$$\frac{D\underline{\underline{A}}}{Dt}=\frac{\partial\underline{\underline{A}}}{\partial t}+\underline{v}\bullet\nabla\underline{\underline{A}}=\left(\nabla\underline{v}\right)^{T}\bullet\underline{\underline{A}}+\underline{\underline{A}}\bullet\nabla\underline{v}-2\underline{\underline{d}}:\Re \tag{2.35}$$

$$\underline{\underline{A}}=\left\langle p_i p_j\right\rangle=\int_0^{2\pi}\int_0^{\pi}p_i p_j\psi(\theta,\phi)\sin\theta d\theta d\phi \tag{2.36}$$

$$\Re=\left\langle p_i p_j p_k p_l\right\rangle=\int_0^{2\pi}\int_0^{\pi}p_i p_j p_k p_l\psi(\theta,\phi)\sin\theta d\theta d\phi \tag{2.37}$$

where $\Re$ denotes the fourth (A_{ijkl}) order orientation tensor and A_{ij} the components of the second order orientation tensor. <●> represents the ensemble average of the dyadic product of the unit vectors $\underline{p}$ over all possible orientations at a position *r* and time *t*. An important property of the second order orientation tensor is

$\mathrm{tr}\left(\underline{\underline{A}}\right)=1$. For a more complete description of orientation tensors and their use in representing fiber suspension the reader is referred to Advani & Tucker [18].

The orientation tensor definition is used in (2.35) to avoid the computational high cost involved in the distribution function used by the Smoluchowski equation. The orientation tensor represents the moments of the distribution function distribution function [18] and it is a concise, effective, and convenient for constitutive models [13]. However the levels of description contained in the orientation tensors has lower amount of information. In consequence, there is a loose of considerable amount of information when the orientation tensor is used instead the distribution function. The orientation tensor is computed using the Smoluchowski equation and the even product of the orientation unit vector $\underline{p}$. The resulting expression is then integrated along the azimuthal and zenith domain. The reason for using even products to form the orientation tensor is that the distribution function is even implying the odd-tensors are all zero [21].

The use of orientation tensors provides an alternative to compute the evolution of orientation, however it introduces a closure problem, i.e. higher order orientation tensors (moments of the orientation distribution function) need to be expressed in terms of lower order orientation tensors in order to obtain a closed set of equations [21]. Chung and Kwon [21] recently published a review indicating the various closure approximations that have been proposed. Advani and Tucker [18] indicate that a correct closure approximation is one that the following guidelines:

- The approximation must be constructed only from lower order orientation tensors and the unit tensor.
- The approximation must satisfy normalization conditions, expressed as:

$$\mathrm{tr}\left(\underline{\underline{A}}\right)=A_{ii}=1,\ A_{ijkk}=A_{ij} \tag{2.38}$$

- The approximation must maintain the symmetries of the orientation tensors.

Then if the approximation satisfies the guidelines it is judged on the basis of their accuracy.

Jeffery's model is valid for a suspension in dilute régimes, i.e. when the hydrodynamic interaction among the particles is negligible. For a single fiber the model predicts a periodic rotation along the azimuthal and zenith angle resulting in a 3D orientation termed Jeffery's orbit. Experimental work with high aspect ratio

particles has demonstrated the qualitative agreement for dilute suspensions in simple flow despite the strong assumptions contained in the model [22, 23]. The solutions provide basic features on how the kinematics influences the particle orientation [13] therefore, Jeffery's model is the starting point of almost all the fiber orientation constitutive modeling. Predictions using Jeffery's model for ellipsoidal particles immersed in Newtonian fluid has produced good agreement with experimental results. In shear flow the particles show an unstable nature. Each particle rotates along a Jeffery orbit, spending most time of the period aligned with the flow direction. However, occasionally particles quickly flip and return to its alignment with respect to the flow. This periodic rotation is called Jeffery orbit. This periodical rotation described by the model causes that the properties predicted show undamped oscillations [13]. The particle contribution to shear viscosity at steady state is modest due to the alignment of the particle in the flow direction, however every time that the particle flips it contributes to the viscosity [19]. The model predicts zero normal stresses due to its symmetric alignment with the flow in shearing flow but positive values of N_1 have been reported experimentally.

2.1.3.1.2 Folgar - Tucker model

Folgar and Tucker developed a continuum model for a non-dilute suspension based on Jeffery's model that is used for dilute fiber suspensions, but they included a term that accounts for fiber-fiber interactions [21]. The following are the additional assumptions to those indicated in the section 2.1.3.1.1: [20]:

1. The fibers are rigid cylinders, uniform in length and diameter
2. The fibers are sufficiently large so that Brownian motion is negligible
3. The center of mass of the particles are randomly distributed

These assumptions are used to develop the evolution equation for the second order orientation tensor in the Folgar-Tucker model for high aspect ratio particles:

$$\frac{D\underline{\underline{A}}}{Dt} = \frac{\partial \underline{\underline{A}}}{\partial t} + \underline{v} \bullet \nabla \underline{\underline{A}} = \left(\nabla \underline{v}\right)^T \bullet \underline{\underline{A}} + \underline{\underline{A}} \bullet \nabla \underline{v} - 2\underline{\underline{d}} : \Re - 6D_r \left(\underline{\underline{A}} - \frac{1}{3}\underline{\underline{\delta}} \right) \tag{2.39}$$

where D_r is the rotary diffusivity-like parameter. When Eq. (2.39) is compared with Eq. (2.35), it can be seen that that the Folgar-Tucker model consists of the Jeffery model plus is the isotropic diffusivity term (the last term in Eq. (2.39)). In a non-dilute high aspect ratio particle suspension, the rotation of particles is affected due

to the presence of other particles therefore the isotropic diffusivity, considers the fiber-fiber interactions. Then the objective of the isotropic diffusivity term is to deal with the modification in the particle rotation in a semi-concentrated suspension.

The isotropic diffusivity term acts to randomize the flow induced orientation in an analogous way to Brownian motion. Typically the rotary diffusivity is defined as the rate at which a particle in submicroscopic dimensions changes its orientation with respect to rotational Brownian motion [16]. However Brownian motion is neglected in Folgar-Tucker model because it only considers high aspect ratio particles with micro and macroscopic dimensions i.e. fibers. Therefore, the rotary diffusion term is a Brownian-like term introduced empirically because Folgar and Tucker observed that the suspension exhibits many of the same qualitative features of Brownian motion. When the rotary diffusivity is set equal to zero, the Folgar-Tucker model is reduced to Jeffrey's model [14] which describes non-interacting particle suspensions and is the basis for the theory of dilute suspensions. The Folgar-Tucker model is based on the assumption that the Brownian-like term must vanish when the flow is stopped [24], therefore Folgar and Tucker proposed a constant isotropic rotary diffusivity term having the form

$$D_r = C_I \dot{\gamma} \tag{2.40}$$

where $\dot{\gamma}$ is the scalar magnitude of the rate-of-deformation tensor and the empirical material constant C_I the interaction coefficient. C_I has been evaluated experimentally by fitting predictions to fiber orientation data from injection modeling experiments [24, 25] or steady Couette flow [26]. The values of C_I are in a range of 0.003-0.016 [19], but an established empirical model for the prediction of the interaction coefficient does not exist [21]. As a note, from this point in this subsection, the term fiber will be used instead of high aspect ratio rigid micro- (or macro-) particles.

There have been several attempts to establish an empirical model for the interaction coefficient, but still there is not an accepted method to find this parameter. Bay and Tucker [27] suggested an empirical function depending on fiber volume fraction (ϕ_v) and aspect ratio (a_r) defined as

$$C_I = 0.0184 \exp\left[-0.7148 \phi_v a_r\right] \tag{2.41}$$

This model is valid only for concentrated suspensions and cannot be used for dilute or semi-dilute suspensions [28]. Ranganathan and Advani [29] suggested measuring the interaction coefficient in terms of the inverse of the average inter-fiber spacing:

$$C_I = \frac{K_{ifs}}{a_c / l} \tag{2.42}$$

where K_{ifs} is a proportionality constant, a_c the average inter-fiber distance, and l the length of a fiber. This model represents the tendency of C_I to be variable according to fiber orientation [28].

The closure approximation used in the Folgar-Tucker model has been the subject of many publications. Various closure approximations proposed for the Folgar-Tucker model are reviewed by Chung and Kwon [21]. Orthotropic types and invariant based closure approximations are commonly used to approximate $\mathfrak{R}$ [28, 30-32]. We focus on the invariant-based optimal fitted (IBOF) closure approximation [33]. Chung and Kwon [33] showed two relevant aspects of the IBOF closure in simple and complex flow simulations. First, the use of IBOF in the prediction of orientation, for a wide range of C_I, produced results comparable to the orientation obtained from the direct solution of the probability function for several homogeneous flows, an unsteady combined flow, and a nonhomogeneous radial diverging flow field. Second, IBOF is computationally efficient, compared to other orthotropic types of closures.

In summary, we have seen the development of an expression which describes the evolution of movement of the high aspect ratio particles in a fluid. The key points addressed in the discussion were the of the Jeffery model to describe the orientation of micro and macroparticles in a dilute régime suspension, its extension to describe the orientation of micro and macroparticles in a non-dilute régime suspension using Folgar-Tucker model. Other aspects relevant to the orientation of a population of high aspect ratio particles discussed was the development of a computationally efficient method to compute the evolution of orientation using the orientation tensor. In addition, the problem of closure approximations introduced by the use of orientation tensors was discussed.

2.1.3.2 Extra stress

The stress due to the presence of high aspect ratio particles in the suspension is related to the orientation state of these particles, described by the orientation tensor as discussed in the previous section. The extra stress contribution of the high aspect ratio particle is now subdivided into the elastic and viscous component.

$$\underline{\underline{T}}^{particle} = \underline{\underline{T}}^{particle}\Big|_{elastic} + \underline{\underline{T}}^{particle}\Big|_{viscous} \tag{2.43}$$

The viscous fiber-related extra stress in Eq. (2.43) results from viscous drag of the fluid on the particle, while the elastic fiber-related extra stress is related to the Brownian motion of the particles.

In the reminder of this section, various models for the extra stress for high aspect ratio particles and fibers are indicated will be discussed.

As mentioned before, a formal criterion to determine the importance of Brownian motion in particles is the determination of rotational Péclet number, however the size of the particles used in thermoplastic composite are larger than 10 μm enough to neglect the Brownian contribution. Therefore, when the suspension contains large size aspect ratio particles i.e. fibers, the extra stress become:

$$\underline{\underline{T}}^{particle} = \underline{\underline{T}}^{fiber}\Big|_{viscous} \tag{2.44}$$

The viscous stress in a suspension arises primarily from solvent drag on the particles as the matrix flows past the particle [15]. The general form of the viscous extra stress due to high aspect ratio particles can is:

$$\underline{\underline{T}}^{fiber}\Big|_{viscous} = \nu\zeta_{str}\underline{\underline{d}} : \Re \tag{2.45}$$

where ζ_{str} is the viscous drag coefficient [15]. Some references [34-36] describe the viscous component of the extra stress in terms of the particle number (N_p) and η_s. In those publications N_p is an expression which represents the anisotropic contribution of the fibers, i.e. the effect of the fibers in the rheology [30]. The relation between both forms is given by

$$\eta_s N_p = \nu\zeta_{str} \tag{2.46}$$

Chapter 2

In the next several paragraphs, some of the models for the viscous drag coefficient used for high aspect ratio particle suspensions are reviewed. In general, these different models describe the viscous drag coefficient as a function of the volume fraction of the particles and the aspect ratio.

Viscous drag coefficients for a dilute suspension

Slender particle theory, developed by Batchelor [37], predicts that for high aspect ratio particles in a dilute suspension, ζ_{str} has the form:

$$\zeta_{str} = \frac{\pi \eta_s l^3}{6 \ln(2a_r)} f(\varepsilon) \tag{2.47}$$

with $\varepsilon = \left[\ln(2a_r)\right]^{-1}$. $f(\varepsilon)$ is the correction factor to account for finite fiber thickness [29], given by

$$f(\varepsilon) = \left\{\frac{1+0.64\varepsilon}{1-1.50\varepsilon} + 1.659\varepsilon^2\right\} \tag{2.48}$$

Eq. (2.48) indicates that $f(\varepsilon) \to 1$ as the $a_r \to \infty$. In the onset of high aspect ratio particles ($\lambda \approx 1$, or $a_r = 30$) $f(\varepsilon)$ = 1.924, this is significantly greater than 1, meaning an appreciable correction for fiber thickness. The advantage of this model is that it can predict shear stress contribution when the fibers are aligned with the flow direction in simple shear, due to the correction factor to account for finite fiber thickness. However, this model is not in the concentration régime of interest for commercial composites because it just describes the viscous stress in the dilute regime. The importance of this model for the viscous component of the extra stress tensor is the correction factor for the finite fiber thickness that has been used in the simulation of thermoplastic composites.

Viscous drag coefficient for a semi-dilute suspension

The most popular model used to determine the viscous drag coefficient in the simulation of injection molded thermoplastic composites has been the Dinh and Armstrong [15] model. This model was derived following the work of Batchelor mentioned before, where they followed his cell model approach to estimate the hydrodynamic drag on a fiber from its neighbor. The following assumptions where used by Dinh and Armstrong to develop the model:

1. The suspending fluid is Newtonian
2. The fibers are rigid
3. The fibers are large enough so that the Brownian motion is negligible
4. Inertia effects are negligible
5. The particle is in a homogenous flow field.

Using these assumptions, the viscous drag coefficient for the Dinh-Armstrong model is obtained:

$$\zeta_{str} = \frac{\pi \eta_s l^3}{12 \ln\left(2 a_c / d\right)} \tag{2.49}$$

where a_c is the average inter-fiber distance that depends on the orientation of the fibers. There are two possible values for the inter-fiber distance considered in the original Dinh-Armstrong model depending on the orientation state

$$a_c = a_{c,\,aligned} = \left(\nu l^3\right)^{-1/2} \tag{2.50}$$

$$a_c = a_{c,\,random} = \left(\nu l^3\right)^{-1} \tag{2.51}$$

However, Chung and Kwon [38, 39] defined a modified average inter-fiber distance in simulations of injection molding for fiber reinforced thermoplastic composites. They assumed an averaged inter-fiber distance as a linear combination of terms for the scalar measure of orientation when the number of fibers per unit volume n is less than $1/(dl^2)$. Then the general form of the average inter-particle distance becomes:

$$a_c = (1-f)\, a_{c,\,random} + f a_{c,\,aligned} \quad \text{for} \quad a_r^{-2} < \frac{4}{\pi}\phi_v < a_r^{-1} \tag{2.52}$$

$$a_c = a_{c,\,aligned} \quad \text{for } a_r^{-1} \le \frac{4}{\pi}\phi_v < 1 \tag{2.53}$$

where the scalar measure of orientation (f) is defined as $f = 1 - 27 \det\left[\underline{\underline{A}}\right]$, the $a_{c,\,random}$ and $a_{c,\,aligned}$ are defined by Eqs. (2.50) and (2.51), respectively. The f-parameter varies from zero (in case of a random orientation) to unity (in case of a perfectly aligned orientation). This model has the advantage of its simplicity [21], however,

one of its weaknesses is that this model predicts increased viscosity compared with theoretical value for random suspensions [28].

Shaqfeh and Fredrickson [40] determined the average hydrodynamic stress in a suspension of rigid rods for dilute and semi-concentrated regimes using a diagrammatic representation of the hydrodynamic interactions. Physical interpretation of this model is that the presence of other fibers around a given test fiber creates a rapid decay of any disturbance velocity that it introduces [21]. The viscous drag coefficient for a semi-concentrated suspension was calculated as

$$\zeta_{str} = \frac{\pi \eta_s l^3}{3} \left\{ \frac{1}{\ln\left(1/\phi_v\right) + \ln\left[\ln\left(1/\phi_v\right)\right] + Hs} \right\} \tag{2.54}$$

where *Hs* is a constant that depends on the orientation state

$$Hs = +0.1585 \qquad \text{for aligned orientation} \tag{2.55}$$

$$Hs = -0.6634 \qquad \text{for random orientation} \tag{2.56}$$

A deficiency of the Dinh-Armstrong and the Shaqfeh and Fredrickson model is that they predict a zero shear stress contribution when the fibers are aligned with the flow direction in simple shear [29]. This is due to the fact that it neglects the finite diameter of the fiber contained in the Batchelor's theory [37]. Ranganathan and Advani [29] suggested to solve this weakness modifying the viscous drag coefficient including a correction factor to account for finite fiber thickness (*f(ε)*), that is defined in Eq. (2.48).

Viscous drag coefficient for a concentrated suspension

As we have seen along this section, in the case of modeling high aspect ratio particles, the viscous contribution it is the dominant term. An estimate for the drag coefficient which is valid for modestly concentrated solution, has the form [19]:

$$\zeta_{str} = \frac{\pi \eta_s l^3}{6\left[\ln\left(a_r\right) - \gamma\right]} \tag{2.57}$$

where γ is a small constant that can be taken to be 0.8, or neglected altogether. The model has the same deficiency as the Dinh-Armstrong and the Shaqfeh and Fredrickson model, predicting zero shear stress contribution when the fibers are aligned with the flow direction in simple shear.

2.1.4 Hele-Shaw flow approximation for injection molding

The mathematical complexity of the problem in the balance equations can be simplified reducing the problem from 2D to 1.5D using the Hele-Shaw flow approximation. The use of this simplification is justified by the injection molding design. These guidelines require the molding of parts with uniform and thin walls. Thin walled parts are injection molded because of the poor thermal conductivity of polymers and hence slow cooling rates. The generalized Hele-Shaw flow is a simplification based on the lubrication approximation, where the balance equations are approximated in such way that the flow is always locally similar to pressure-driven flow between parallel plates [2]. When a fluid is moving within a narrow gap cavity at a low Reynolds number, the balance equation can be approximated using Hele-Shaw flow approximation. In a narrow gap geometry, the height of the cavity ($2H$) is assumed much smaller than the length (L) in the in-plane direction. Fig. 2.4 depicts these geometrical dimensions in a 2-D coordinate system. In this figure, the gapwise direction is assumed to run along the 3-direction with while the only in-plane component direction considered is assumed to run along the 1-direction.

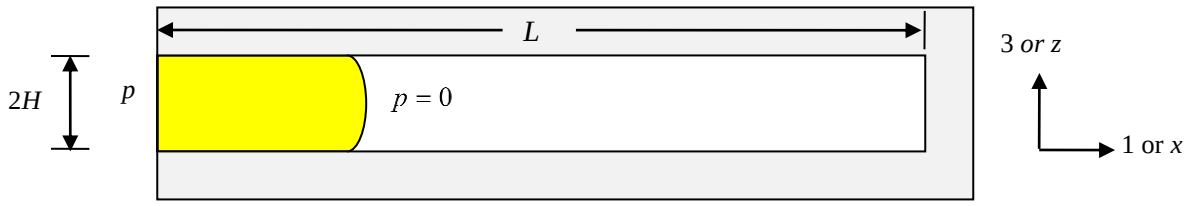

Figure 2.4 Boundary conditions considering no-slip condition at the wall in the injection molding process.

The Hele-Shaw approximation is developed from certain simplifications to the balance equations. The Hele-Shaw approximation typically found in the literature has a formulation developed only for viscous flows. One of the implications of the Hele-Shaw approximation for viscous fluids is that the pressure does not vary in the x_3 direction, and that the velocity in the x_3 direction is negligible compared with the in-plane velocities [2].

This simplification implies a modification in the incompressibility condition because the term $\partial v_3/\partial x_3$ can be neglected, written in mathematical way:

$$\frac{\partial v_1}{\partial x_1}+\frac{\partial v_3}{\partial x_3}\approx\frac{\partial v_1}{\partial x_1}=0 \tag{2.58}$$

Eq. (2.58) satisfies that $\partial v_1/\partial x_1=0$ which implies that $v_1=v_1(x_3)$ and does not satisfy the continuity condition in local sense. The continuity equation in differential form can be replaced by the condition that the volume of the flow in every section must be constant:

$$Q=\int \underline{v}dA=\underline{\bar{v}}\int dA=\text{constant} \tag{2.59}$$

where Q denotes the volumetric flow, $\underline{\bar{v}}$ the vector of average velocity, and dA differential in area. For the 2D problem, one component of the velocity in direction 1 (v_1) is considered and the differential in area is simplified as $dA \approx (1)\, dx_3$. An average velocity in direction 1 ($\bar{v}_1$) expression becomes:

$$\bar{v}_1=\frac{\int_{-h}^{h} v_1 dx_3}{\int_{-h}^{h} dx_3}=\frac{\int_{-h}^{h} v_1 dx_3}{2h} \tag{2.60}$$

A modified version of the incompressibility condition in terms of the average velocity along the gapwise coordinate ($\bar{v}_1$) can be found when Eq. (2.58) is integrated along the gapwise direction, followed by an interchange of the order of differentiation and integration and finally introduce Eq. (2.60). This modified version of the incompressibility condition is sometimes called the integrated continuity equation, having the form [2]:

$$\underline{\nabla}\bullet\left(h\underline{\bar{v}}\right)=0 \tag{2.61}$$

where h is the half gap width. The 2-D velocity field in the fluid consists of a component v_1 which is parallel to the wall and depends primarily on x_3 but not on x_1 (i.e. $\partial v_1/\partial x_1 << \partial v_1/\partial x_3$) [12]. This component varies parabolically between the walls and it is averaged across the height leading to a 1-D problem on the middle of surface [41]. Indeed, this means that in the Hele-Shaw approximation the shearing stresses are the dominant terms while the normal stresses are neglected, therefore the momentum equations become:

$$0 = -\frac{\partial p}{\partial x_1} + \frac{\partial T_{31}}{\partial x_3} \tag{2.62}$$

$$0 = \frac{\partial p}{\partial x_3} \tag{2.63}$$

Eq (2.63) implies that pressure varies in 1-direction only, $p = p(x_1)$. As consequence of Eq. (2.63) the velocity only depends on the pressure gradient in Eq. (2.62). The boundary conditions for the Hele-Shaw approximation problem can be determined from the general boundary conditions indicated in Section 2.1.1. At the inflow the pressure can be prescribed i.e. $p = p_{in}$ while the pressure is typically set to zero at the moving front, i.e. $p = 0$. When the suspension reaches the wall the pressure gradient in the normal direction to the boundary is zero. Therefore

$$\frac{\partial p}{\partial \underline{n}} = 0 \tag{2.64}$$

Eq. (2.64) physically means that material cannot flow through the walls [42]. More details about this the derivation of Hele-Shaw flow approximation, can be found elsewhere [2, 12, 43].

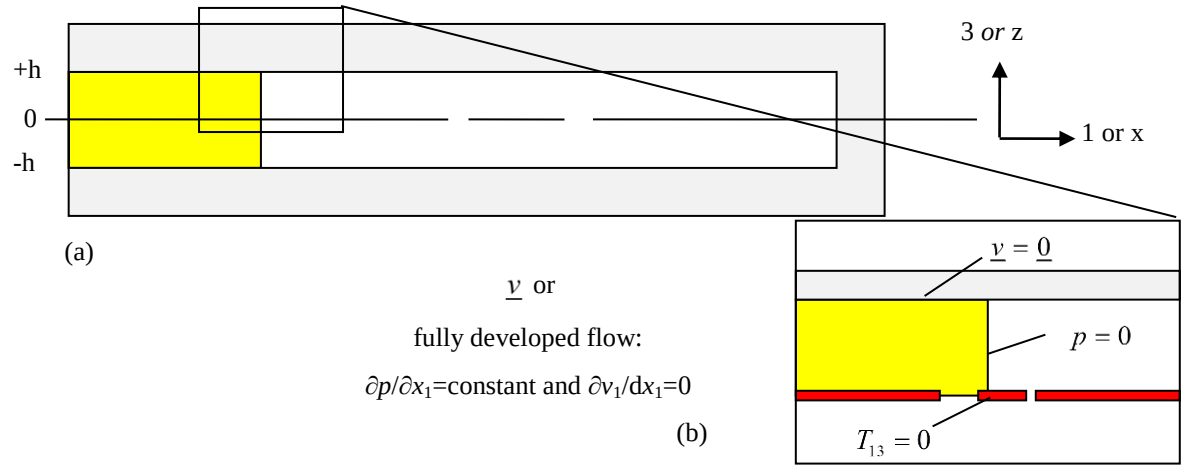

Figure 2.5 Boundary conditions considering no-slip condition at the wall in the injection molding process.

The Hele-Shaw flow approximation for viscoelastic fluids requires modifications due to the possible effects of the normal stress contribution. The Hele-Shaw approximation is valid as long as the shear stress terms are larger than the in-plane stress. This implies that

$$\frac{\partial T_{13}}{\partial x_1} >> \frac{\partial T_{11}}{\partial x_1} \tag{2.65}$$

The suspension can show normal stress differences, therefore the perpendicular stress component in the gapwise direction has to be considered in the momentum equation. Therefore, in order to include this component, Eq. (2.63) is modified to have the form

$$0 = \frac{\partial p}{\partial x_3} + \frac{\partial T_{33}}{\partial x_3} \tag{2.66}$$

More details about the derivation of viscoelastic Hele-Shaw flow approximation, can be found in Baaijens [44] and Im et al. [45].

The Hele-Shaw flow approximation is the method used in commercial simulation programs available on the market, and it has been extensively used by different research groups to simulate the flow induced orientation in injection molding of composites. The main interest developing this strategy in this research is that it gives us the ability to compare results obtained with full balance equations with those obtained using Hele-Shaw flow approximation. When the Hele-Shaw flow approximation is used in simulations for polymer composites, the stresses due to the viscoelastic nature of the polymer matrix and due to the fibers are typically ignored in the balance equations.

The predictions based on Hele-Shaw approximation are restricted to limited number of geometries. Some of the geometries valid to apply Hele-Shaw approximation are geometries with narrow gaps as shown in Fig. 2.4(i), geometries where the gap thickness varies slowly with position and curved geometries in which the radius of curvature is large compared with the gap thickness [2]. Some limitations of the Hele-Shaw flow approximation. indicated in the literature [26, 28, 29] are depicted in Fig. 2.4 (ii)-(vii) and summarized below:

- Inaccurate model for front flow (ii)
- Flow in thick parts or complex geometry (iii)

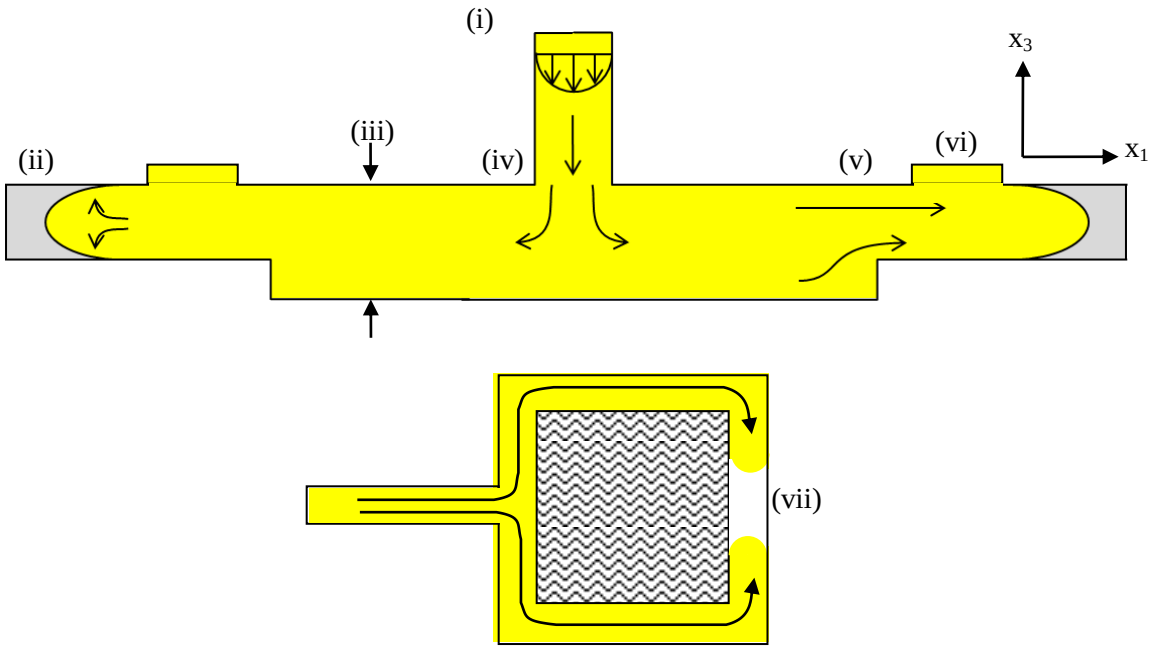

Figure 2.6 Some representative regions of interest in a simulation of a "real" part in injection molding: (i) thin walls, (ii) frontal flow, (iii) thick part, (iv) bifurcation (v) sudden contraction, (vi) boss, (vii) weldlines.

- Flow junctions: e.g. bifurcations, T-junctions (iv)
- Regions where shear or extensional deformation contribute significantly to the stress fields:
    - Sudden changes in thickness e.g. expansion, contractions (v)
    - Special part features e.g. gates, ribs, bosses, corners (vi)
- The merging of two or more melt fronts: e.g. weldlines (vii)

2.2 Numerical methods

The solution of the balance and constitutive equations reviewed in section 2.1 requires numerical methods to solve the system of PDEs. In the specific case of simulating the filling stage of injection molding of a thermoplastic composite, the balance equations are elliptic PDE's, while the constitutive equations are hyperbolic PDE's. A rigorous treatment of this problem requires its solution as a transient problem where the instantaneous bulk stress and fiber orientation state are determined at each time step.

Chapter 2

The elliptic equations can be handled using the Galerkin Finite Element Method (GFEM) without major problems, however, the hyperbolic form of the constitutive equations is not easy to solve due to the convective term. It is known that the solution of transport problems containing a convective term can show non-physical node-to-node oscillations [46]. Then, a different formulation is required in order to avoid these oscillations. The traditional Galerkin and discontinuous Galerkin Method are reviewed in this section as methods to be used for the spatial discretization of the balance and constitutive equations, respectively. The temporal discretization of the balance equation is not included explicitly due to the steady state nature of the balance equations. However the time discretization is important in the constitutive equations due to their transitory nature, which is handled using a multistep finite difference formulation.

In addition the filling of thermoplastic composites involves a moving boundary. A moving boundary problem is a PDE problem which describes how part of the boundary evolves and may undergo severe deformations [47]. Therefore, the surface position and shape of the surface at the boundary must be determined as part of the solution.

2.2.1 Space discretization of the balance equations using Galerkin FEM.

The space discretization involves the approximated solution of $\underline{v}$ and p at prescribed values of $\underline{x}$ on a spatial grid. In the literature of thermoplastic composite simulations, finite elements, finite differences, boundary elements, and spectral methods have been used to discretize the balance equations or Hele-Shaw flow approximation. However, the most widely used method has been the finite element method (FEM) due to its ability to handle complex geometries.

The finite element method is based on the variational form of the equations considered. Recall from section 2.1.1:

$$\underline{\nabla} \bullet \underline{v} = 0 \tag{2.67}$$

$$\underline{\nabla} \bullet \left(-p\underline{\underline{\delta}} + 2\eta_s \underline{\underline{d}} + \underline{\underline{T}} \right) = \underline{0} \tag{2.68}$$

The method is described in detail elsewhere [48]. The differential equations are transformed in a weighted-integral statement by multiplying the entire equation with a test function and integrating over the domain (Ω).

Then the weighted-integral statement is transformed into the weak form by distributing the differentiation among the dependent variable and the weight function, and including the natural boundary conditions of the problem. The exact solution is replaced by its approximation. The approximate solution is assumed to be in the form of a linear combination of suitable approximation functions and undetermined parameters. The governing equations are obtained over each element by algebraic relations among the undetermined coefficients. The undetermined coefficients in the approximate solution are solved from a sufficient number of algebraic equations generated from the weighted-integral statements. There are several variational methods of approximation, but the Galerkin (also known as Bubnov-Galerkin) method (GFEM) works satisfactorily with the elliptic nature of the balance equations. The weak form of the balance equations containing all admissible test functions for q and $\underline{u}$ is defined as

$$\left\langle q, \underline{\nabla} \bullet \underline{v} \right\rangle = 0 \tag{2.69}$$

$$-\left\langle \underline{\nabla} \bullet \underline{u}, p \right\rangle + \left\langle \underline{\nabla} \underline{u}, 2\eta_s \underline{\underline{d}}\left(\underline{v}\right) + \underline{\underline{T}} \right\rangle = \left\langle \underline{u}, \underline{\underline{\sigma}} \bullet \underline{n} \right\rangle_\Gamma \tag{2.70}$$

where $\left\langle \bullet, \bullet \right\rangle$ and $\left\langle \bullet, \bullet \right\rangle_\Gamma$ are the appropriate inner products on the domain Ω and boundary Γ, respectively. and the rate of deformation tensor $\underline{\underline{d}}\left(\underline{v}\right)$ is defined as

$$\underline{\underline{d}}\left(\underline{v}\right) = \frac{1}{2}\left(\underline{\nabla} \underline{v}^T + \underline{\nabla} \underline{v}\right) \tag{2.71}$$

Stabilization of GFEM

Stabilized finite element formulations are used for highly convective flows because a chance of instability exists when the GFEM is used with non-smooth solutions obtained from the constitutive equations. Discrete Elastic Viscous Split Stress (DEVSS) [49] has been introduced in the GFEM formulation to enhance stability. The objective of using GFEM-DEVSS is to retain the elliptic contribution in the weak form of the momentum equation [50] which makes the formulation more robust and accurate [49]. This stabilization technique is particularly important when the pure viscous contribution is small compared to the viscoelastic or fiber contribution [50]. Guénette and Fortin [49] developed a stabilization formulation known as discrete elastic viscous stress splitting (DEVSS) which has been used successfully to increase the stability in viscoelastic

simulations [50-52]. The DEVSS formulation consists of introducing an L_2 projection of the rate of deformation tensor containing all admissible weighting functions for $\underline{\underline{f}}$ along with a stabilizing term in the discrete momentum equation defined as

$$2\bar{\eta}\left(\underline{\underline{d}}(\underline{v})-\underline{\underline{\bar{d}}}\right) \tag{2.72}$$

where $\bar{\eta}$ is the auxiliary viscosity and $\underline{\underline{\bar{d}}}$ denotes the discrete rate of deformation tensor. For Stokes flow, the optimal choice of $\bar{\eta}$ is to be equal to the solvent viscosity, η_s [51]. This typical value has been chosen for viscoelastic flows, giving satisfactory results [49, 51-53]. However it has been indicated that this choice is not the most appropriate selection for $\bar{\eta}$ [51]. Then the problem for the balance equations including the DEVSS formulation is as follows: Find $\left(p, \underline{v}, \underline{\underline{\bar{d}}},\right)$ such that for all admissible weighting functions (q, $\underline{u}$, $\underline{\underline{f}}$)

$$\left\langle q, \underline{\nabla} \bullet \underline{v} \right\rangle = 0 \tag{2.73}$$

$$-\left\langle \underline{\nabla} \bullet \underline{u}, p \right\rangle + \left\langle \underline{\nabla} \underline{u}, 2\eta_s \underline{\underline{d}}(\underline{v}) + 2\bar{\eta}\left(\underline{\underline{d}}(\underline{v})-\underline{\underline{\bar{d}}}\right) + \underline{\underline{T}} \right\rangle = \left\langle \underline{u}, \underline{t} \right\rangle_{\Gamma} \tag{2.74}$$

$$\left\langle \underline{\underline{f}}, \underline{\underline{d}}(\underline{v})-\underline{\underline{\bar{d}}} \right\rangle = 0 \tag{2.75}$$

Eq. (2.75) adds stabilization by smoothing the solution. The spatial discretization is accomplished as follows. The domain Ω is divided into N_e elements such that

$$\Omega = \bigcup_{e=1}^{N_e} \Omega_e \tag{2.76}$$

The flow domain Ω is discretized by means of element shapes such as triangular or quadrilateral elements,

The last step in the discretization in GFEM is the definition of the order of the interpolation polynomials of different variables with respect to each other. The order of the polynomial approximation for the different variables can be crucial in order to avoid issues of convergence. For example, the velocity and pressure polynomial of interpolations cannot be chosen independently because they have to satisfy the Ladyzhenskaya, Babouska and Brezzi (LBB) stability condition [48]. Typical interpolation polynomials and corresponding nodal positions for quadrilaterals considered for the different variables are indicated in Table 2.1.

Table 2.1 Typical nodal positions for the different polynomial interpolation used in GFEM

Variable	Symbol	Representation
Velocity	Biquadratic continuous (Q_2)	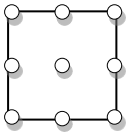
Pressure	Bilinear continuous (Q_1)	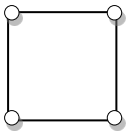
Discrete rate of deformation $\left(\underline{\underline{\bar{d}}}\right)$	Bilinear continuous (Q_1)	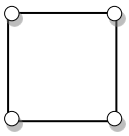

2.2.2 Space discretization for the constitutive equations using Discontinuous Galerkin

Why GFEM is not effective to solve the constitutive equations

The transmission or propagation of information depends on the PDE used to describe the system, therefore it is a criterion that can be used to select the numerical method required to solve system of equations. For example, when elliptic and hyperbolic PDEs are considered, it can be seen that the information travels symmetrically and asymmetrically, respectively. Therefore, this concept can be used in the balance and constitutive equations considered here. If we take a point (x, y) in the plane of flow, in the case of our balance equation, considering only the viscous extra stress, their elliptic form makes that the information propagates symmetrically in all directions. This kind of problem is known as diffusion dominated problem. It contrasts with the situation when our constitutive equations are considered because their hyperbolic form makes that the direction of propagation of information depends on the velocity. Indeed, the convective term in the hyperbolic equations makes that the information is transported by the velocity coming from the upstream direction [54]. This kind of problem is known as convection dominated problem. The directionality of information propagation due to the convection term causes oscillations in the solution. These spurious oscillations cause a failure to provide meaningful solutions beyond a certain range of We [55]. However, the upwinding techniques can be used to stabilize the solution. In general terms an upwind technique considers a minor or zero contribution to the information from elements downstream to the element under consideration if the convective term has significant contribution. In GFEM, the upwinding technique is typically developed using a special kind of weighting function which adapt itself to a major contribution in weighting functions from other than downstream elements when the convective term is dominant. Fig. 2.7 illustrates how the typical linear test functions used in GFEM without upwinding (a) compares with the upwinded weighting functions (b). It can be seen how the contribution of the weighting is higher in the upstream element and lower in the downstream element (b), while the contribution in (a) is exactly the same for upstream and downstream elements

There are several ways to solve systems of equations where the convective term dominates the diffusive one. Within the finite element framework, Streamline Upwinding (SU), Streamline Upwind Petrov Galerkin (SUPG), and discontinuous Galerkin (DGFEM) methods have been used to discretize the hyperbolic

viscoelastic and fiber orientation constitutive equations. DGFEM has never been used to simulate the fiber orientation constitutive equation in an injection molding operation; it has only been used to simulate a fiber suspension in 4:1 contraction [56]. The difference between the methods previously indicated is in the way of implementation of the upwinding technique. The upwinding is used to modify the convective term. In the case of SU, the use of an upwind test function is equivalent to add an additional false diffusion (numerical diffusion) which acts only in the streamline direction [57], and it is proportional to the mesh size [58]. However, this additional diffusion produces a smooth but inaccurate solution. Moreover, the SU scheme cannot be more than first-order accurate [55]. In the case of SUPG, the streamline-upwind test function is applied to all terms in the equation, requiring the use of test functions

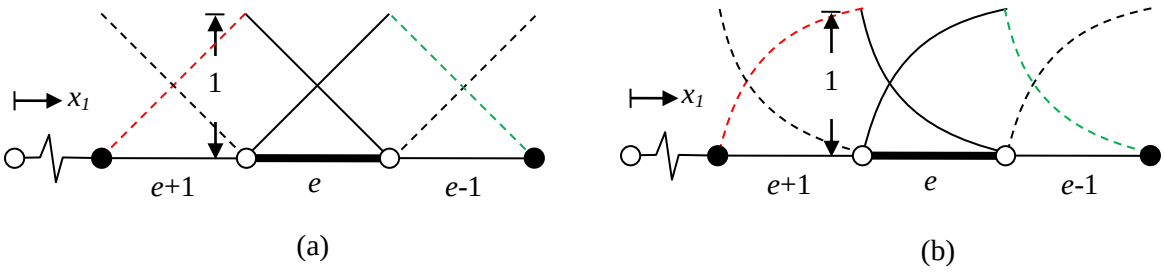

Figure 2.7 Local test functions around the element of consideration, using: (a) typical linear weighting functions and (b) weighting functions for an upwinding scheme. e denotes the element under consideration, e+1 the upstream element, and e-1 the downstream element.

different from the interpolation functions, which has to satisfy the LBB compatibility condition [57]. The SUPG has similar problem of solution inaccuracy due to the artificial diffusion introduced, however it is a popular method to solve the convective problem because it is able to suppress the oscillations to obtain solutions for higher values of We. In terms of order of accuracy, the SUPG has been found to be $O(h^{k+1/2})$ for degree k polynomial basis functions, or half order higher than GFEM [55]. Baaijens et al. [50] indicate that there are limitations of SUPG in problems with geometrical singularities. In regions of the flow near singularities or stress boundary layers, SUPG may produce oscillatory stress fields [55]. An additional

comment about streamlines upwind techniques is that their stabilization terms are added only on the element interiors and not on the element boundaries [57].

In the case of DGFEM, the upwinding is handled by sequential transmission of information coming from the upwind element and entering to the element being analyzed through the inflow boundary of the element, i.e. the boundary in contact with an upwind element. DGFEM and SUPG must be compared as well. Fan [59] showed their differences in performance in the computation of steady viscoelastic flows. The comparative computations showed that DGFEM has, at least the same accuracy as, and a higher stability than SUPG [55, 59]. The results also demonstrated that a key factor for the success of DGFEM is to use a stabilization technique analogous to DEVSS as discussed in Section 2.2.1. When the stabilization technique was not used, the results showed poor performance. The stabilized DG showed to be more expensive than the stabilized SUPG, however it increases robustness [59]. In an axisymmetric abrupt contraction, the stabilized DGFEM reached solutions up to We=21, while the stabilized SUPG attained solutions up to We=10.

If we consider that the orientation equation is a hyperbolic equation with the following general form:

$$\frac{\partial \underline{\underline{A}}}{\partial t} + \underline{v} \bullet \nabla \underline{\underline{A}} = \underline{\underline{f}}\left(\nabla \underline{v}, \underline{\underline{A}}\right) \tag{2.77}$$

The problem is to find $\left(\underline{\underline{A}}\right)$ such that for all admissible weighting functions $\left(\underline{\underline{\phi}}_{\tau}\right)$

$$\left\langle \underline{\underline{\phi}}_{\tau}, \frac{\underline{\underline{A}} - \underline{\underline{A}}_n}{\Delta t} + \underline{v} \bullet \nabla \underline{\underline{A}} + \left(2\left(\Re : \underline{\underline{d}}\right) - 2C_I \sqrt{II_D}\left(\underline{\underline{I}} - 3\underline{\underline{A}}\right) - \nabla \underline{v}^T \bullet \underline{\underline{A}} - \underline{\underline{A}} \bullet \nabla \underline{v}\right)\right\rangle + \tag{2.78}$$

$$\Delta t \sum_{e=1}^{N} \int_{\Gamma^{Inflow}} \underline{\underline{\phi}}_{\tau} : \left(\underline{v} \bullet \underline{n}\right)\left[\underline{\underline{A}}^{-} - \underline{\underline{A}}^{+}\right] d\Gamma = 0$$

where $\left[\underline{\underline{A}}_i^{-} - \underline{\underline{A}}_i^{+}\right]$ is the upwinding or jump operator over the element boundary, *N* are the total number of elements and *i* represents the i^{th} node. The interpolation polynomials used for the orientation tensor is a bilinear polynomial where the nodal positions are shown in Fig. 2.8.

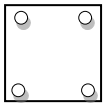

Figure 2.8 Representation of bilinear discontinuous (Q_1^d) nodal position to be used as the interpolation polynomials for the orientation and configuration tensor.

2.2.3 Time discretization for the constitutive equations in a DGFEM scheme

Explicit and implicit integration schemes can be used for time integration in a discontinuous formulation. However, the explicit methods are preferred with discontinuous element formulation whenever possible [60]. One of the reasons for such preference is due to the local formulation involved, because it often leads to standard explicit structures [60]. Another reason justifying the explicit scheme is its very convenient form to produce a global mass matrix which is block diagonal with uncoupled blocks. Then the problem can be solved element by element in one sweep by inverting at very low cost the element mass matrix [61]. Li [60] also indicates that a most efficient time integration can be computed, if the mass matrix is diagonalized when an explicit scheme is used. This positive aspect contrasts with the results obtained using implicit schemes. If the element ordering can not be performed, the use of an implicit scheme results in an even larger global matrix than a GFEM, which eliminates the advantage of localized formulation associated with DGFEM [60]. Therefore, almost all DGFEM the time stepping scheme in the literature [60] use the explicit time integration which has the benefit to facilitate the parallel computation associated with a local formulation [60]. Among others options, four of the commonly used time integration schemes in DGFEM are the first order forward Euler, second, third and fourth order schemes [60]. However in the majority of viscoelastic simulations using DGFEM done by Baaijens group the former alternative is used as the integration scheme. The reader is referred to Baaijens et al. [50] for a more complete description of the steps involved in time integration using explicit methods in a DGFEM scheme to solve constitutive equations.

It should be noted certain precautions dealing with explicit time-stepping schemes in DGFEM. The DGFEM is a conditionally stable method and the explicit methods are prone to numerical instability, appropriate stability analysis is needed for the time integration schemes. Therefore, a stability criterion has to be used in DGFEM schemes. Since these schemes are explicit, the time step has to satisfy the CFL (Courant–Friedrich–Levy) condition for stability [60]. For example Hulsen et al. [62] indicate that the proper step for the discontinuous Galerkin method in space and second order schemes in time is found by trial and error procedure. They recommend initiating this procedure determining and initial estimate of time step (Δt_0). In terms of our specific problem, the initial estimates is computed by using the following condition:

$$\Delta t_0 \left(\frac{v_1}{\Delta x_1} + \frac{v_3}{\Delta x_3} \right) \leq \frac{1}{6} \tag{2.79}$$

where is the convection velocity $\underline{v}$, and grid spacing $\Delta \underline{x}$. It should be noted that the velocity and grid spacing are position dependent.

2.2.4 Moving front

In many problems of practical importance, a fluid flows within well-defined wall boundaries and acquires a defined shape. In this section, we will be focusing on moving boundary problems which consider moving fluids having a boundary with an unconstrained surface shape or free surface, *i.e.* changing in position with respect to time. Finding the location of the free surface is crucial in moving boundary problems. Free surface flow occurs during the filling stage of the injection molding process, when the incompressible polymer suspension moves through the cavity.

A free surface moves according to certain kinematics and dynamic conditions that complicate the solution of the equations mainly because it is not an easy task to accurately track the melt front. The kinematics boundary conditions at the free surface are defined by Eqs. (2.9) and (2.10). One way to describe the motion of a free surface is

$$\frac{DF}{Dt} = \frac{\partial F}{\partial t} + \underline{v} \bullet \left(\underline{\nabla} F \right) = 0 \tag{2.80}$$

where F is defined as a material density function [8] or a color function [63] used to represent and track the interface. The interface is a thin region which separates two immiscible fluids, *i.e.* suspension and air in a filling stage of injection molding [64]. F has values of 1 at the filled section, zero outside of the free surface, and a value between 0 and 1 at the free boundary which implicitly defines the location of the flow front (interface). The interface plays a major role in defining the system and must be determined as part of the solution. The boundary condition described by Eq. (2.80) results from the conservation of mass and corresponds to the free boundary condition (the position of the flow front is unknown) [41].

In fluid dynamics, there are two classical frames of reference for observing the motion of a fluid: Lagrangian and Eulerian. In the Lagrangian reference frame, the observer follows an individual fluid particle as

it moves through time and space. In the Eulerian reference frame, the frame is fixed to a specific location in space through which the fluid flows. These reference frames are used to define Lagrangian and Eulerian methods. In the Lagrangian method each node of the mesh follows the associated material particle during motion; in other words, a particular region of flow is identified and followed. This method is preferred for problems with small deformation [65]. In the Eulerian description, the mesh is fixed and the material moves with respect to the grid, implying that a location of certain volume is fixed in the fluid and a continuously renewed fluid is studied as it passes through the volume. The Eulerian description has the advantage of preserving the mesh regularity.

In the remaining part of this section, the Arbitrary-Lagrangian Eulerian (ALE) method will be reviewed. The ALE is a hybrid method that combines characteristics of Lagrangian and Eulerian methods. It is used to analyze fluid motions if the material strain rate is large the ALE method has been advantageous in analyzing problems of a very flexible structure. ALE has been used in abrupt contractions for viscoelastic flows [66], cold roll forming [67], free surface flows of viscous [68] and viscoelastic flows [69]. In metal forming simulations, ALE has gained popularity in applications where interaction between flow and fluid structure are important.

The Arbitrary Lagrangian-Eulerian method is a hybrid method that combines the advantages of the Lagrangian and Eulerian methods while minimizing their respective drawbacks insofar as possible [70, 71]. ALE description is a valuable tool for moving boundary problems because it allows the mesh to follow the moving boundaries [65]. When ALE is used, the nodes can move with the material, or be held fixed, or move with a mesh velocity different from the fluid velocity to give a continuous rezoning (remeshing) capability [70, 72]. Then it is possible both to maintain reasonably shaped meshes and to describe the boundaries accurately at the same time [68].

The general idea of ALE is shown below; however the reader is referred to Donea *et. al.* [70] for a complete description and details of the method. The ALE formulation requires the modification of the convective terms in the governing equations; therefore in the case of isothermal filling of fiber composites, it is only used in the orientation equation. The ALE transformation for the orientation is

$$\frac{D\underline{\underline{A}}}{Dt} = \left.\frac{\partial \underline{\underline{A}}}{\partial t}\right|_x + \underline{v}_c \bullet \underline{\nabla}\underline{\underline{A}} \tag{2.81}$$

where $\underline{v}_c$ denotes the convective velocity, defined as

$$\underline{v}_c = \underline{v} - \underline{v}_m \tag{2.82}$$

where $\underline{v}$ is the fluid velocity and $\underline{v}_m$ is the mesh velocity. Eq. (2.81) reflects the motion of the mesh in the orientation equation, while the convective velocity (Eq. (2.82)) accounts for the motion of the mesh.

ALE methods require a mesh-update procedure that assigns mesh-node velocities at each time step of a calculation. The mesh-update procedure involves two steps. In the first step, the relevant boundary conditions are used to compute the location of the boundaries. The material surface at the moving surface always moves with prescribed kinematic and dynamic conditions, while the mesh at the inflow never moves. In the second step, the mesh velocities in the interior of the domain are determined using a mesh regularization method. The mesh nodes rezoning consists of solving a Laplace (or Poisson) equation for each component of the mesh velocity so that in a logically regular region of mesh, equal lines are formed based on

$$\underline{\nabla} \bullet \underline{\nabla} \underline{v}_m = 0 \tag{2.83}$$

2.3 Experimental evaluation of particle orientation

The experimental characterization of the orientation of the reinforcing particles in a thermoplastic composite is important for validating the predictions of orientation obtained from simulations. However, the tridimensional characterization of the orientation has not been an easy task to accomplish, due to physical and technological limitations of the experimental methods developed. In addition, the degree of difficulty depends on the aspect ratio particle. The experimental analysis of orientation will treat three high-aspect ratio particles, namely, nanoparticles, short glass fibers and long glass fibers.

In the case of nanoparticles, it has been found that the use of transmission electron microscopy (TEM) and X-ray diffraction is effective in the study of dispersion of nanoparticles in the matrix [73, 74]. There are several publications [73, 75] where X-ray diffraction techniques are used to obtain qualitative insight concerning the particle orientation. TEM also provides qualitative information about the orientation, due to the

nanoparticles' small size. In the case of long glass fiber, flexibility or semi-flexibility of the particles requires the use of 3D techniques in order to capture the changes in fiber direction. Some techniques that can provide the 3D structure of the composites are confocal laser scanning microscopy (CLSM), micro X-ray computerized tomography (μ-XCT), and scanning acoustic microscopy (SAM). Although these techniques are relatively recent, having been developed in the late 1990's or early 2000's, they still have several limitations. For example, the CLSM analysis depends on the transparency of the composite, while the μ-XCT and SAM can only handle small-sized samples. The publications reviewed, deal with the feasibility of 3D microscopy techniques for evaluating the orientation of short or long glass fiber in thermoplastic composites. In addition, there are few studies using these techniques to validate predictions given by simulation.

For short glass fiber thermoplastic composites, the standard method used to determine orientation of the particles is known as the method of ellipses (MoE). In this method, the 3D orientation is based on application of 2D information, combined with some geometrical assumptions. The microscopes involved in this 2D technique have typically been optical microscopy (OM) and scanning electron microscopy (SEM). An alternative method used in the early stages of simulation of thermoplastic composites was microradiography. However, this method has fallen out of use since about 1990 for reasons that are somewhat unclear. The characterization of fiber composites is tied to the incorporation of image analysis in order to reduce the delivery time, to increase the area inspected, and to reduce the error of the measurements.

2.3.1 2D orientation measurement techniques

The measurement of orientation in 2D techniques is based on the method of ellipses. The parameters developed to characterize the fibers are based on the assumption that the fibers are perfect rigid cylinders that are smooth, straight, and circular cross-sectioned particles [76]. These assumptions apply to short fibers, but this is not necessarily the case for long fibers, carbon fibers and Kevlar fibers, which are semi-flexible fibers. In 2D techniques, a specimen is cut and embedded in epoxy and then the sample is metallographically polished. In order to increase the contrast between the matrix and fibers, the polished surface is acid- or plasma-etched and then gold sputtered. Typically, a reflective optical microscope is used to acquire the sample's surface image. The images obtained from the surface show elliptical objects illustrated in Fig. 2.9. Each rounded object in the

figure represents a fiber cut by a surface plane of the polished sample. Objects showing circular shape represent a fiber perpendicular to the plane while elliptical shapes represent fibers oriented at any other angle. In some pictures rectangular-like shapes can be seen, representing fibers cut longitudinally. The ellipses are used to characterize the position and orientation of the fibers. Fig. 2.10 illustrates a fiber embedded in a sample using solid lines with their complementary section removed during the cutting and polishing of the fiber (depicted with dashed lines). The fiber position is determined from the center of mass ($\bar{x}_1$, $\bar{x}_2$) of the ellipse, while the fiber orientation at this location can be determined from the minor (m) and major (M) axis of the ellipses and the in-plane angle (ϕ) defined with respect to the x_1-axis and M. The out-of-plane or zenith angle (θ) is given by:

$$\theta = \cos^{-1}\left(\frac{M}{m}\right) \tag{2.84}$$

However, this method does not give the complete information about the fiber orientation [77]. The in-plane angle is ambiguous because there is not a geometrical certainty if the angle is (ϕ) or ($\phi + \pi$) [2]. Fig. 2.11 illustrates the ambiguity in differentiating between the red and black color fibers because their cross sections are identical at the surface of measurement.

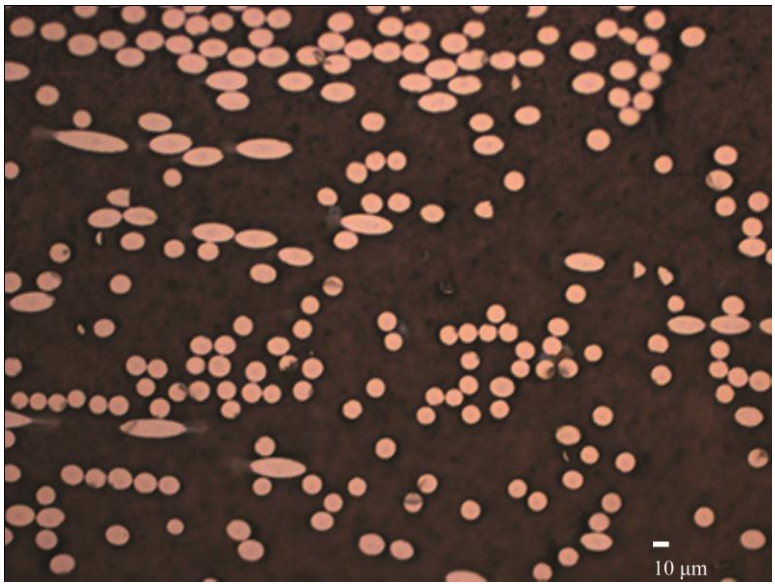

Figure 2.9 Ellipses seen in an optical microscope micrograph for polypropylene reinforced with short glass fiber. The sample was prepared at Oak Ridge National Laboratories.

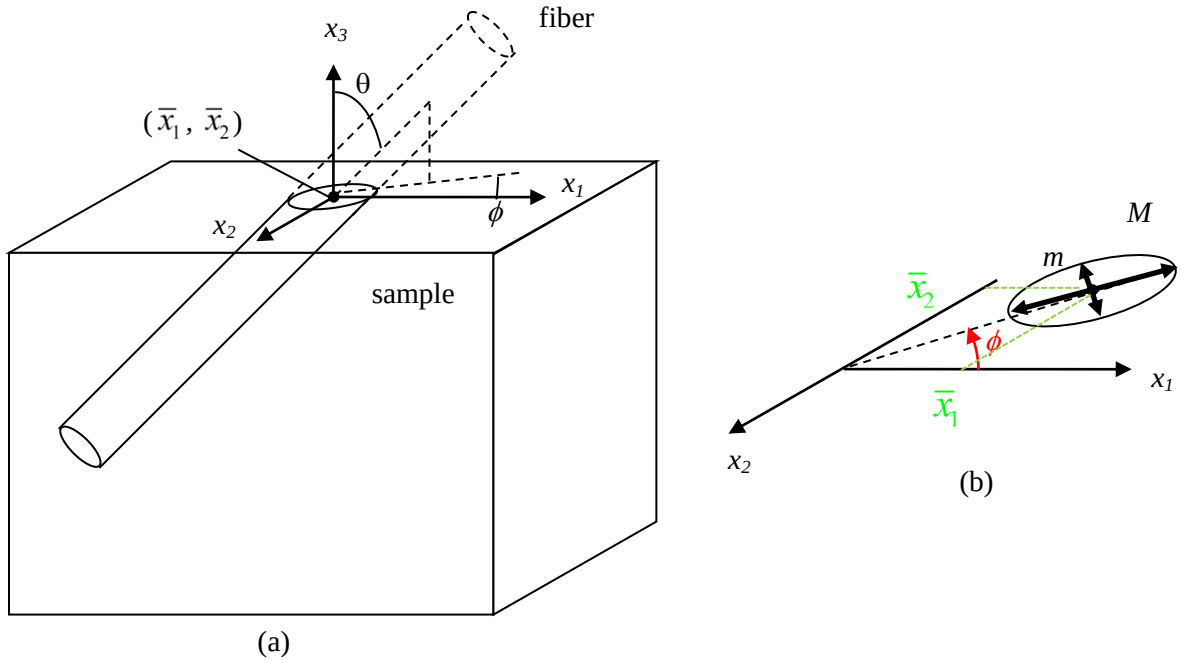

Figure 2.10 Fiber embedded in the sample illustrating the experimental parameters required to characterize the fiber orientation: (a) perspective view (b) definition of in-plane parameters.

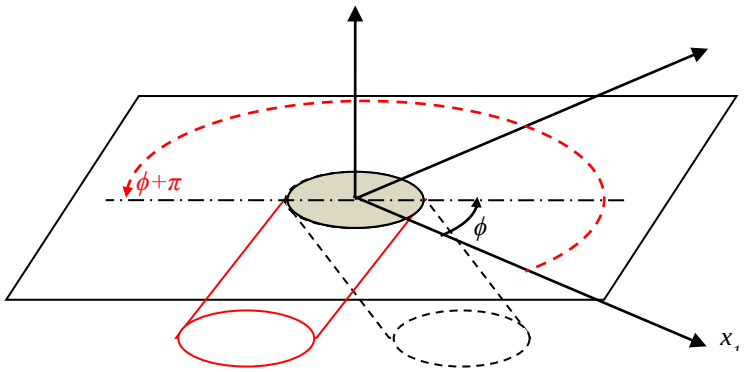

Figure 2.11 Ambiguity in fiber orientation in the method of ellipses. The fibers drawn in black and red color haves the same elliptical image but have different in-plane angles, ϕ and $\phi + \pi$, respectively.

The orientation angles of each fiber can be transformed into components of second-order orientation (A_{ij}) as shown in section 2.1. The orientation components for a single fiber *n* determined experimentally for an image taken on the plane 1-2 are given by the following set of equations [77]:

$$\left(A_{11}\right)_n = \sin^2\theta\cos^2\phi \tag{2.85}$$

$$\left(A_{12}\right)_n = \sin^2\theta\cos\phi\sin\phi \tag{2.86}$$

$$\left(A_{22}\right)_n = \sin^2\theta\sin^2\phi \tag{2.87}$$

$$\left(A_{33}\right)_n = \cos^2\theta \tag{2.88}$$

$$\left(A_{13}\right)_n = \sin\theta\cos\theta\cos\phi \tag{2.89}$$

$$\left(A_{23}\right)_n = \sin\theta\cos\theta\sin\phi \tag{2.90}$$

The ambiguity of ϕ only affects the odd functions of ϕ, A_{13} and A_{23}.

Typically, the values of orientation components reported in the literature are based on the volumetric average of orientation. Stereological principles are required in the estimation of this quantity because the objective is to obtain volumetric information based on information obtained from an arbitrary plane. The transformation of information requires an inclination-dependent correction factor which accounts for the probability of a randomly placed section plane intersecting each fiber. A fiber aligned perpendicular to the sectioning plane has a higher probability of being intersected by the plane than those oriented parallel to the plane. Konicek [78] derived an equation for estimating the probability for the intermediate cases and found that the inclination-dependent correction factor is the inverse of the probability.

The unbiased weighted-average orientation is obtained by [77]

$$\bar{A}_{ij} = \frac{\sum\left(A_{ij}\right)_n L_n F_n}{\sum L_n F_n} \tag{2.91}$$

where *n* denotes the *n-th*, L_n is the length of the fiber, and F_n is the weighting function which depends on the out-of-plane angle of the fiber. The most general weighting function was defined by Konicek [78] as:

$$F_n = \frac{1}{L_n \cos\left(\theta_f\right)_n + d_n \sin\left(\theta_f\right)_n} \tag{2.92}$$

where d_n is the diameter of the *n-th* fiber. The Konicek weighting function is suitable in analyses considering complete and partial ellipses of any size. Bay and Tucker [77] defined an alternative model that can be used when complete and partial ellipses greater than half ellipse are considered in the analysis of orientation. The Bay weighting function neglects the term $d_n \sin\left(\theta_f\right)_n$ in Eq. (2.92) and becomes singular before the out-of plane angle reaches π/2. To avoid this limitation, F_n is modified above a certain cutoff angle (θ_c) to:

$$F_n = \frac{1}{d_n} \qquad \theta_c > \cos^{-1}\left(d/L\right) \tag{2.93}$$

where d_n is the diameter of the *n-th* fiber, θ_c is the cut-off angle and d and L are the average diameter and average length of the fibers, respectively. The cut-off angle is introduced to avoid a singularity of F_n when θ_n approaches π/2. A detailed description of this transformation can found elsewhere [78, 79].

The measurements of the 5 parameters, *i.e.* $\overline{x}_1$, $\overline{x}_2$, *m*, *M*, ϕ, required to characterize the fiber orientation are carried out using image analysis software. Within this software, built-in algorithms are used to recognize the borders of ellipses and to measure the characteristics of each ellipse, *i.e.* centroid, in-plane angle, and major and minor axis. Then these data are used to compute the out-of-plane angle and the orientation components. The main advantages of using these software programs is the reduction in time employed to recognize the ellipses in the images and to measure the ellipses' dimensions accurately. However, a concern about using the image analysis programs is the reliability of recognizing objects as ellipses. Sometimes the polished samples show objects with distorted shapes instead of perfect ellipses, or rectangular shapes when the fibers are cut longitudinally. These non-elliptical shapes cause significant error in recognition, affecting the orientation results. Other sources of error of recognition are caused when two or more ellipses are very close or touching, because the software recognizes the objects as one single ellipse.

The method of ellipses has been proven to be effective for rigid short fibers, becoming the standard method of measurement. Its consistency led the material science microscopy group in the University of Leeds, UK to commercialize a method known as Leeds Analyzer [80]. However the main disadvantage of the method

is its potential for ambiguity in the in-plane angle. It should be noted that several options have been suggested to eliminate those limitations [77, 81].

2.3.2 3D orientation measurement techniques

There are relatively few instances in which recently developed 3D techniques have been employed in thermoplastic composite analysis. Confocal laser scanning microscopy (CLSM) in fluorescence mode (CLSM-FM) and X-ray micro computerized tomography (μ-XCT) are two of the most promising 3D techniques indicated in the literature [81]. CLSM-FM consists of a collection of 2D fluorescent images taken from different focal planes. The depth of each focal plane is modulated using the power of a laser. This microscopy can be seen analogous to taking optical microscopy images of consecutively microtomed samples. The advantage of this technique is its ability to render 3D information in a non-destructive way. However, laser penetration is limited to several micrometers below the surface, depending on the sample transparency. The μ-XCT is able to take a perpendicular image of a sample up to a certain sample depth. Then the sample is rotated in order to capture the information from multiple angles. The procedure is repeated until the whole height of the sample is scanned. The volume is computationally reconstructed from the overlapping graphical information taken at heights. Three of the advantages of μ-XCT are that this technique allows for fast 3D analysis of the samples in a non-destructive fashion; it has a high spatial resolution; and it does not require polishing, etching and gold sputtering steps. Its disadvantage is the small dimension of the sample perpendicular to the laser and penetration depth. Currently, technology only allows the inspection of small samples. For example, the instrument at Oak Ridge National Laboratories can use samples around 1 x 1 mm in the cross section and a height of up to 25 mm [82].

2.4 Numerical simulation of discontinuous fiber reinforced thermoplastic composites

The following is a review of literature pertaining to the approaches of simulating high aspect ratio thermoplastic composites. During the last 30 years, prediction of high aspect ratio particle orientation in thermoplastic composites has been focused on the orientation of fibers in inelastic polymeric matrices. These

simulations have been performed assuming that the change of orientation of the fiber during mold filling does not alter the rheological behavior of the melt composite. This assumption is known as decoupled flow-orientation approach. However, the velocity profile developed during the filling stage of a melt composite deviates from the velocity profile expected for the filling of a neat polymer. Therefore, the presence of fiber has influences on the rheology of the suspension. Indeed when simulations take into account this point, it is known as coupled approach. The first simulation assuming coupled approach was publish in 1993, however since then, there have been a limited number of simulations following such approach.

Irrespective of the approach used to solve the system of equations, the method used to compute the flow kinematic has been other controversial area in thermoplastic simulations. The two methods used to evaluate the kinematic of the suspension are the full system of the governing equations and the Hele-Shaw flow approximation. The Hele-Shaw flow approximation has been successfully used to predict qualitatively the orientation state of the fibers in the molded part, but it ignores one of the most important features during the filling state, the fountain flow. Indeed, the fountain flow has been found to play a major role in the fiber orientation in molded parts [25].

The equations describing the discontinuous fiber-reinforced thermoplastic composites can be too complicated to solve in injection molding geometries. Therefore, analytical results are limited to a few simplified problems and hence the researchers use numerical simulations as a powerful tool to solve more complex problems and verify the existing experimental results and theoretical predictions. The typical test geometries simulated have been end gated rectangular channels and center gated disks, cavities as shown in Fig. 2.12 (a) and (b), respectively. The specification of the dimensions of such geometries is limited to a few numbers of publications. For example Bay and Tucker used a disk with inner radius R_i = 3.81 mm, outer radios R_o=76.2 mm, and thickness $2b$ = 3.18 mm; and a film-gated rectangular plaque L = 203.2 mm, width w = 25.4 mm, and thickness $2b$ = 3.18 mm. Indeed, this publication has been commonly used for validation purposes and comparison of results, in several papers dealing with the simulation thermoplastic composites. Another interesting aspect in literature focused on simulations of thermoplastic composites is the flow domains that have been used in each one of typical geometries.

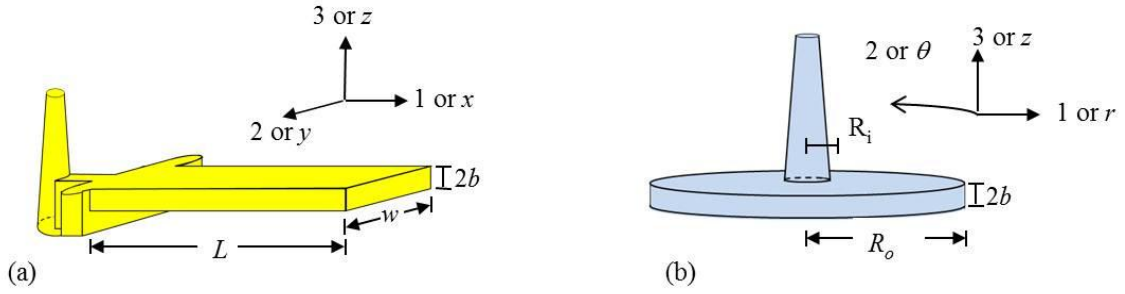

Figure 2.12 Typical geometries used simulations in (a) end gated plaque and (b) center-gated disk.

Fig. 2.13 depicts the flow domains more commonly used in center-gated disk and end-gated plaque geometries. The most common plane used for the both geometry is the plane 1,3 shown in Fig. 2.13 (a) and (c), for the center-gated disk and end-gated plaque respectively. However recently, there have several publications which have included the runner as part of the flow domain of simulations as shown on Fig. 2.13 (b) and (d), for the center-gated disk and end-gated plaque respectively. Fig. 2.13 (e) depicts the plane 1,2 which also have been simulated in several publications. The inflow position and the flow direction through the geometry are indicated in each plane using the word *inflow* and the arrow, respectively. It should be noted that the initial condition of orientation has been specified at the inflow in all simulations.

2.4.1 Decoupled flow-orientation simulations

The decoupled approach has been used to reproduce flow induced orientation in molded parts in at least 20 publications, when increases further if including publications that use commercial software to simulate the process. This assumption lets us compute the fiber orientation sequentially. First, the velocity field is computed without considering the fibers, then the orientation is post-calculated using this calculation. The flow kinematic is computed using the full balanced equations or Hele-Shaw flow approximation (HSA). Independent of the computational method, the decoupled approach simulations can predict orientation qualitatively, but fail to indicate the orientation quantitatively [83]. Therefore, this section will be focused on reviewing the key publications that define the basis of the accepted knowledge on fiber orientation, in terms of the method employed to compute the kinematics, full balance equations and Hele-Shaw flow approximation.

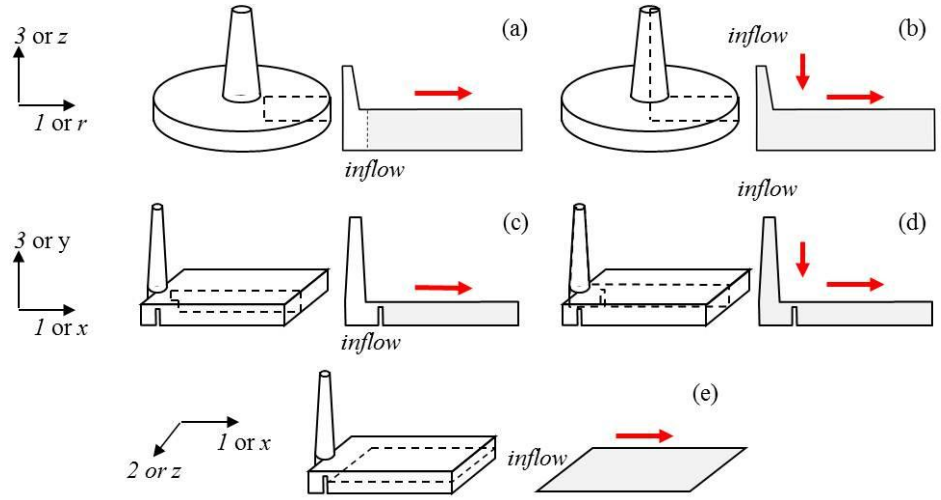

Figure 2.13 Typical planes used as domain for simulations in (a, b) axisymmetric disk and (c-e) rectangular plaque geometries. The arrow indicates the flow direction through the domain and the inflow indicate the location where the initial conditions have been imposed.

2.4.1.1 Balance equations

Vincent and Agassant [84] performed a decoupled simulation to predict the orientation of a 30% fiber suspension flowing in a center gated disk without a sprue and compared them with experimental results. The constitutive equations used to represent the matrix and the fiber orientation was Newtonian and Jeffreys model, respectively. They solved the Jeffrey's model integrating along the streamlines to predict the shape of the orientation along the cavity. They used a planar orientation function to describe the orientation defined as:

$$f = \frac{2\langle \cos^2\theta \rangle - 1}{2} \tag{2.94}$$

$$\langle \cos^2\theta \rangle = \frac{\sum_i N_i \cos^2\theta}{\sum_i N_i} \tag{2.95}$$

with N_i the number of fiber with and angle θ_i relative to a reference direction (usually the local flow direction). The use of initial conditions as a function of the height is a relevant aspect of this publication. Fig. 2.14(a) shows the orientation at the mold entrance observed experimentally. The provenance of this orientation is not specified in the original paper. However, they published a review of the flow induced orientation on 1991 [22]

where they indicate explicitly its experimental origin. Fig. 2.14 (b) shows the function of orientation along the cavity thickness at a certain position in *r*-direction not indicated. The orientation function in the disk thickness showed the formation of 3 layers of orientation in the disk with the following characteristics:

- The borders of the curve describe the skin layer: fibers only slightly oriented in flow direction.
- The top of the humps represent the sub skin layer: marked fiber orientation in flow direction
- Convex area around *z*=0 represents the core of the disk: orientation is transverse to the flow direction.

The shape and characteristics of the orientation function described the experimental results qualitatively.

In order to determine the influence of fountain flow on the fiber orientation, Devilers and Vincent [85] developed a finite element decoupled simulation for a dilute fiber suspension with a moving mesh based on ALE. The approach used in this publication is to track individual groups of fibers along their trajectory through the mold in order to understand the history orientation, with special interest on the orientation at the fountain flow. The flow kinematics in either disk with and without sprue, was computed in base of a method developed by Magnin *et al.* [86]. In this method, the boundary conditions are fully developed Poiseuille flow at the inflow, no slip conditions at the wall, no stress at the free surface. The initial orientation is always set

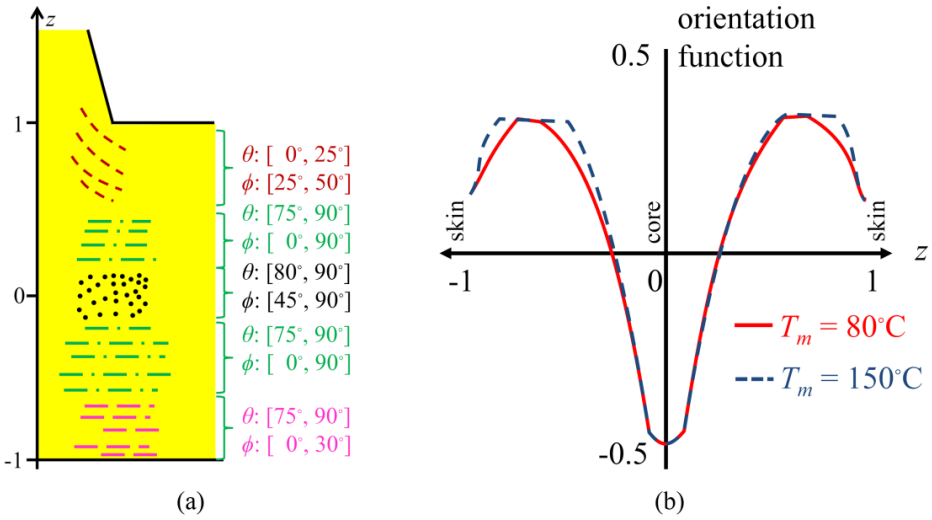

Figure 2.14 Fiber orientation experimentally measured in a disk for PA-6,6 30wt% short glass fiber adapted from [22]: (a) Initial orientation at the mold entrance (b) Orientation within the cavity (r position is not specified).

random conditions. In the case of the geometry without sprue the results indicates that the displacement of the fibers depends on the gapwise position. Fibers moving at a position close to the axis of symmetry, keep its position constant with respect to the wall, but having a velocity higher than average. When they reach the fountain flow region, the fibers change direction, moving towards the wall until reach a constant gapwise position very close to the wall, but this time moving more slowly. The fibers moving in the sprue show a different behavior than the previously described. The simulations in the sprue regions close to the axis of symmetry of the sprue indicate that the fibers get oriented perpendicular to the sprue axis and to the radial direction. The authors indicate that this behavior is in agreement with experiments. At the junction with the disk the fibers move towards the opposite mold wall where they tend to orient in the flow direction. However fibers moving in the sprue far from the axis of symmetry get aligned with the flow direction. At the junction with the disk they move away from the midplane, and they are oriented nearly perpendicular to the flow direction.

In a subsequent paper, Vincent *et al.* [87] extends the simulation to a semi-concentrated regime using the Folgar-Tucker model instead Jeffery's model, but only considering tube and sprueless disk geometries. They found that in a tube filling, fibers near the center reach the front region at about the same axial position. Fibers initially closer the surfaces maintain its position from the wall and reach the fountain flow later because their velocity is lower. The tube filling is also computed using Jeffery's model. It indicates that the fibers orient in the flow direction in the shear region, however when they reach the fountain flow, the fibers orient perpendicular to the flow along the 2-direction. When the fibers are close to the wall, they reorient in the flow direction. In the disk the fibers orient transverse to the radial flow in the extensional flow region, when they enter in the fountain flow region, a complex behavior is observed. The A_{11} increases followed by a decrease and finally increase due to the shear flow near the wall, while the A_{33} show exactly the opposing profile. The authors conclude that the introduction of fiber interaction leads to slight disorient the fibers with respect to the plane of the part, which makes shear flows efficient to orient fibers in the flow direction.

2.4.1.2 Hele-Shaw flow approximation

Altan *et al.* [88] simulated the flow of a polymeric suspension in rectangular and planar converging cavities using quasi-steady state isothermal Hele-Shaw. The matrix was treated as a Newtonian fluid with a dilute concentration of fibers. The fiber orientation is post-calculated at every time step for every fiber using a fourth order orientation tensor described by the Jeffery's equation. The method developed by Altan *et al.* [88] was the prediction of fiber orientation after each time step developed in a moving front algorithm, using fourth order orientation tensors departing from the Dinh-Armstrong [15] model. The authors employed a decoupled approach using the Livermore Solver for Ordinary Differential Equations (LSODE) algorithm in a predictor-corrector scheme. The boundary condition at walls as taken under non-slip condition and the inflow and free surface were set assuming uniform velocity and zero shear stress condition, respectively. The results showed a complete analysis of orientation in several directions (planar, transversal and longitudinal) along the part. This paper contains the most illustrative representation of fiber orientation in the literature reviewed.

Bay and Tucker [27] developed a simulation where two numerical procedures were solved consecutively, where in the first numerical procedure, a finite difference scheme was used to predict the velocities of a viscous matrix using a non-isothermal Hele-Shaw flow approximation, and these results were the initial conditions of a secondary method to compute the velocity profile in frontal region. This secondary simulation performed in the frontal region under assumptions different from the lubrication region simulation and using a finite element scheme solved by FIDAP element package. The fiber orientation was post-calculated using the Folgar-Tucker model, and the polymeric matrix was assumed to be a generalized Newtonian fluid described by a power-law and Arrhenius model [25]. A rectangular plaque and center gated disk were simulated using a suspension composed 43 wt% glass fiber and Nylon. The initial orientation at the mold entrance varied depending on the geometry simulated. In the case of the plaque they used average orientation results obtained experimentally (A_{11}=0.5, A_{22}=0.2, A_{33}=0.3, A_{12}=A_{13}=A_{23}=0.0) while in the disk they used random orientation (A_{11}=1/3, A_{22}=1/3, A_{33}=1/3, A_{12}=A_{13}=A_{23}=0.0). In all of these cases the predictions around the midplane were overestimated. Fig. 2.15 illustrates the differing experimental (circles) / numerical (lines) results are for A_{11} near the gate and close to the end of the fill. Close to the gate the difference predicted and

measured orientation is small. In addition, it can be seen in Fig. 2.15(a) thick core region. However, close to the end of fill, there is a discrepancy between the predictions and experimental observations as shown in Fig. 2.15(b). The simulation predicts a thin core region, while the experimental orientation indicates a thicker core region. It is recognized in Bay and Tucker [25] that the simulation cannot accurately predict the fiber orientation outside of the lubrication region.

The fill time was the most significant processing condition because it can be used to control the layer thickness. A short fill time implies high fill speed, resulting in near-absence of a skin layer, which reflects the fountain flow because it is formed by fibers moving from the center of flow to the walls. Higher levels of Graetz number (*Gz*) indicate a thinner layer and above *Gz* = 100, there is no skin formation. The *Gz* is defined as the ratio of characteristic time for heat conduction to the characteristic time for molding [83]:

$$Gz = \frac{4h^2}{\alpha \cdot t_{fill}} \tag{2.96}$$

where h is the half-cavity thickness, α the melt thermal diffusivity and t_{fill} the mold filling time. The effect of matrix properties on orientation is based on shear thinning and heat of fusion. For example, polypropylene (PP) was selected because it is shear-thinning and sensitive to temperature. The absence of skin formation in this simulation was attributed to the absence of fountain flow effects in PP due to the interaction of its large heat of

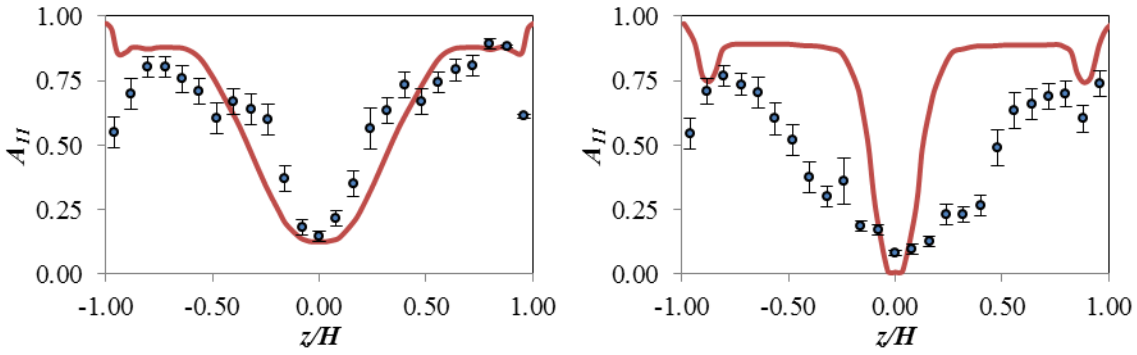

Figure 2.15 Experimental and numerical results for 43 wt% glass fiber reinforced Nylon at a position (a) near the gate (b) Close to end of fill. Adapted from [25].

fusion and shear flow. The authors indicate in the case of PP its large heat of fusion delays the frozen layer formation, and then the shear flow behind the front erases the effect of frontal flow in the orientation structure.

2.4.2 Coupled simulations

The coupled approach has been used in at least 7 publications which have given a better understanding of flow-induced orientation, but still are not able to predict quantitatively the orientation in the molded parts. In contrast with decoupled approach, the solution of coupled simulations of involves the simultaneous computation of the flow kinematics and the fiber orientation. However, like in decoupled simulations, the flow kinematic has been expressed in terms of full balance equations or Hele-Shaw flow approximation. The coupling of flow kinematics to fiber orientation may semi-quantitatively predict fiber orientation and segregation in the molded parts [83]. Therefore, in this section the publications dealing with coupled approach will be reviewed. It should be mentioned, that this section has been organized following the scheme used for the decoupled simulations.

2.4.2.1 Balance equation

Ranganathan and Advani [29] used a finite difference formulation to develop a steady state simulation for a semi-concentrated suspension of rigid fibers with a Newtonian suspending in an axisymmetric cavity. They used the orientation evolution results predicted by Folgar-Tucker model, in combination with the Shaqfeh-Fredrickson model to determine the fiber's stress contribution. The boundary conditions used were uniform radial velocity through the gap at the inflow, no slip condition at the wall, symmetric at the centerline, and the velocity through the gap and its derivative with respect to the radial direction specified to be zero at the outflow boundary. In addition, random and aligned orientations were used at the inflow boundary conditions to explore the effects of initial orientation. In this simulation, the flow field results were used to compute the streamlines passing through each node; then the orientation equations was integrated along the streamline to compute the orientation at each node at every time step assuming aligned orientation along the wall. In the subsequent paragraphs, the discussion will be focused on the kinematics and orientation effects obtained using random initial orientation, unless otherwise indicated.

The kinematic results indicate that the radial velocity along the cavity has a blunt velocity profile in the region dominated by the gate effects. This is attributed to the effect of the high viscosity of the suspension close to the wall [29]. However, as the flow progresses in the cavity, shear aligns the fibers close to the wall and this alignment moves from the wall to the center of the flow, making the velocity profile more Newtonian-like at positions far from the gate. Fig. 2.16(a) qualitatively depicts the velocity profile in the regions close and far from the gate, where different velocity profiles have been seen in simulations of disk without sprue. In Fig. 2.16 (b) the blunt shape radial velocity close to the gate is depicted while Fig. 2.16 (c) shows the parabolic radial velocity far from the gate. Ranganathan and Adavani [29] showed qualitatively the kinematics through the whole domain using streamlines analysis depicted in Fig. 2.17. The reduction in the rate of decay in streamlines with respect to the radial position close to the gate is evident between the decoupled and coupled simulations, as well as the reduction of decay in streamlines increases with concentration.

In the decoupled case, where the fluid behaves as a Newtonian fluid, the streamlines show a short distance decay of the radial velocity to reach a steady velocity that is maintained along the radial distance (Fig. 2.17(a)). The coupled case with low volume fraction shows a longer distance decaying behavior of radial

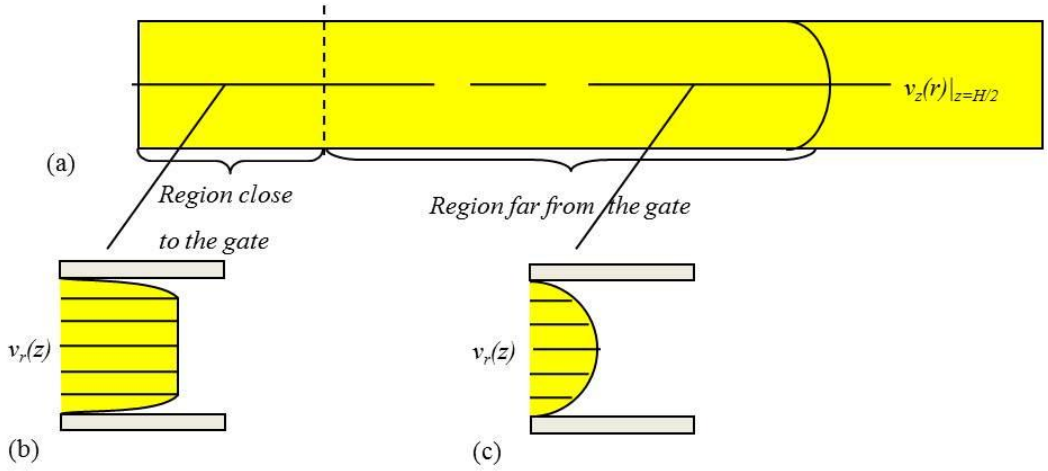

Figure 2.16 Kinematic seen in coupled simulations of a disk without sprue. (a) There have seen two regions with different kinematics located at positions close to the gate and far from the gate. The shape of the velocity profiles are (b) a blunt velocity profile at a region close to the gate and (c) a parabolic velocity profile at a region far from the gate.

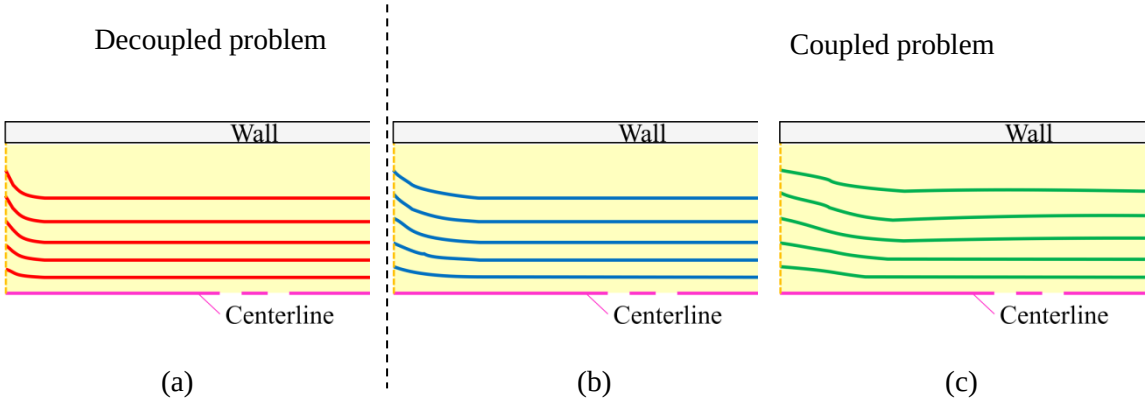

Figure 2.17 Streamline rearrangements (a) decoupled approach (b) coupled approach with ϕ_v = 0.01 (c) coupled approach with ϕ_v=0.05. Adapted from [29].

velocity until reaching a relatively steady radial velocity (Fig. 2.17(b)). However, when the volume fraction increases to 0.05, the decaying in the streamlines is harder and the radial velocity along the radial distance shows a non-steady value (Fig. 2.17 (c)). These reductions in the rate of decay of the streamlines close to the gate are caused by the high shear viscosity close to the wall, which increases with fiber concentration and causes flow deceleration [29]. While the streamline tending towards the centerline after the rearrangement, which is attributed to the low shear viscosity in the centerline, accelerates the flow [29].

Ranganathan and Advani [29] compared the modified dimensionless centerline velocity for a Newtonian matrix without fibers and suspensions having different concentration of fibers. The modified dimensionless velocity ($\overline{v}_1$) is defined as,

$$\overline{v}_1\left(x_1, x_3\right) = \frac{x_1 v_1\left(x_1, x_3\right)}{x_{1,i} v_{1,i}} \tag{2.97}$$

where $x_{1,i}$ is the radial position of the inlet and $v_{1,i}$ is the inlet velocity. This modified dimensionless velocity arises from a volumetric flow rate balance at any radial position due to the axisymmetric geometry [29]. Each concentration reflects different degrees of particle interactions, where both parameters increase in the same direction. Fig. 2.18 depicts the profile of centerline velocity $\left(\overline{v}_1\left(x_1, 0\right)\right)$ along the radial position for the

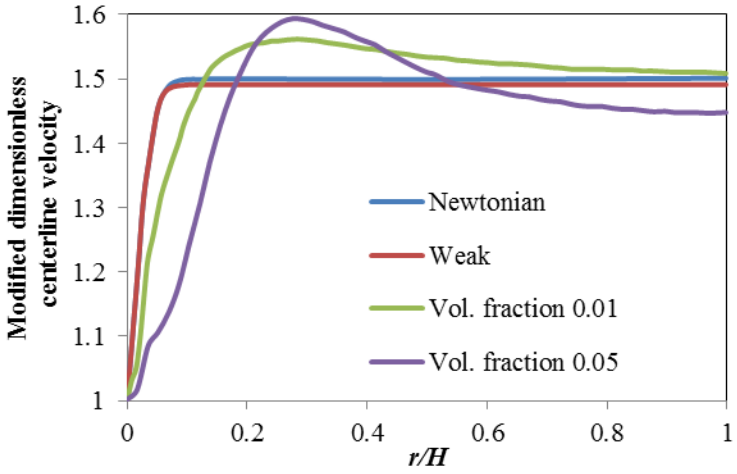

Figure 2.18 Modified dimensionless centerline velocity along radial positions for different coupling levels in coupled simulations for disk for a sprueless cavity. Adapted from [29].

different cases assuming random initial orientation. The Newtonian matrix and weak interaction suspension shows similar behavior, a steep increase in the velocity close to the gate is developed until it reaches a plateau, characteristic of Newtonian fluids. However, this profile showed an overshoot that gradually disappeared until it converges to a plateau far from the gate, as the interactions increase in the suspension. It can be seen in Fig. 2.18 that the following effects exist in the centerline velocity profile with an increase in interactions:

- The reduction of the slope of centerline velocity as function of radial position
- Increase of the overshoot

Ranganathan and Advani [29] analyzed the effect of orientation in the flow domain starting from initial random orientation, using the same criteria discussed for the kinematics. Fig. 2.19 shows a qualitative analysis of the orientation through the domain using orientation plot, where the circles indicate random in-plane orientation, the lines depict the alignment in the direction it lies in, and the dots denote alignment out of plane. The orientation plots for decoupled (Fig. 2.19(a)) and coupled simulations (Fig. 2.19(b) and (c)) shows similar structure without evident differences, as occurred in the kinematic analysis. Using the orientation plots the authors describe three regions:

- Near the wall where fibers align along the flow direction due to the shear dominant region,

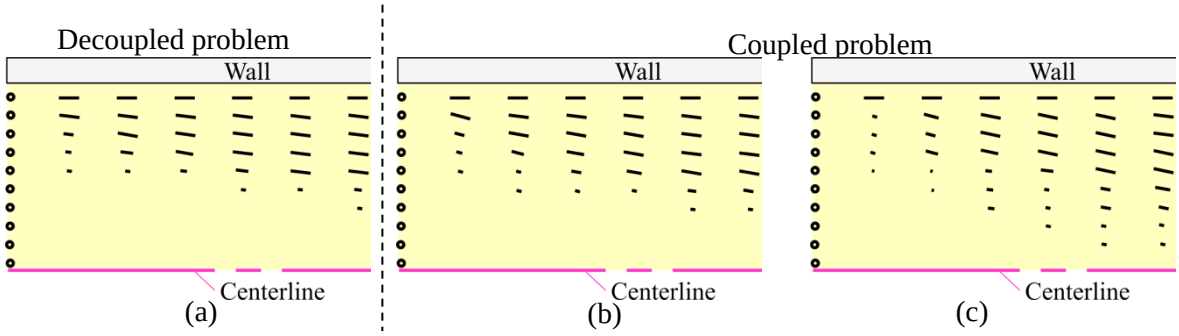

Figure 2.19 Orientation plots (a) decoupled problem (b) coupled problem with ϕ_v = 0.01 (c) coupled problem with ϕ_v=0.05. Adapted from [29].

- Above the centerline where the fibers orient transverse to the flow direction due to the elongational dominant region in the centerline
- Between the wall and centerline where the fibers orient in the flow direction as the radial distance from the inlet increases due to the shear dominant regions extending away from the wall as the radial distance increases.

The quantitative analysis of the orientation was performed plotting the A_{11} component at the z/H =0.5, along different radial positions, shown on Figure 2.20. It should be noted that z/H corresponds to the transition layer. Using the orientation plots the authors describe three regions:

- A_{11} increases initially due to the shear in the 1,3-plane
- A_{11} decreases due to the elongation in the 1,2- plane
- A_{11} increases monotonically after a certain radial location because the flow at z/H=0.5 becomes shear dominant

Ranganathan and Advani [29] also evaluated the effect of the concentration in the orientation along the radial position for a suspension with ϕ_v=0.05. It is seen that a faster and increasing orientation exists in the transition layer with a reduction in concentration [29]. The authors conclude that the differences between the predicted orientation results using the coupled and decoupled approaches are apparent and also it is manifests

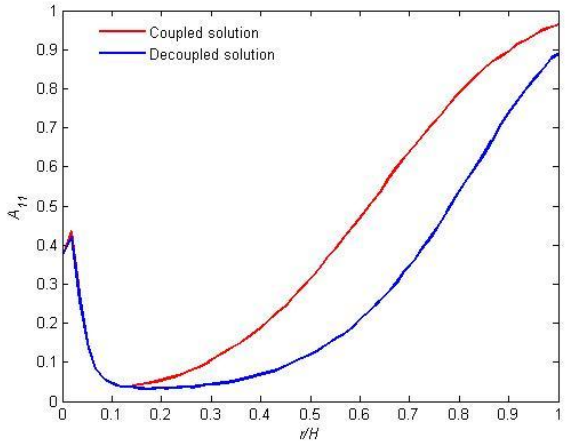

Figure 2.20 Orientation component A_{11} along the radial distance for a suspension with ϕ_v=0.01. Adapted from [29].

itself in the form of the different velocity solution. Another conclusion mentioned by authors but never probed was that the orientation would reach stead state value at a larger radial.

The last result shown in this paper explains the effect of the initial orientation in the evolution of the flow induced orientation. As establish at the beginning of this section, all previous results where done assuming random alignment at the inlet, however they also tried a simulation where fibers enter perfectly aligned in the gapwise direction. The justification involved in the selection of this new condition is to evaluate the potential alignment orientation developed in the sprue before to enter in the cavity. The results of the simulations show a maximum difference in the orientation prediction in that region, as it is shown in the Fig. 2.21. This is an expected behavior because in this intermediate region there is not a shear- or elongational-dominant flow. Ranganathan and Advani [29] showed the importance of the inlet orientation condition, at least in the transition region.

VerWeyst and Tucker [30] qualitatively evaluated the flow-induced orientation using streamlines and orientation plot analyses for both coupled and decoupled simulations, and they found some features which were not seen by Ranganathan and Advani [29]. Fig. 2.22 shows simultaneously the streamlines and orientation plots for a suspension with ϕ_v = 0.2, flowing through a disk with a sprue for decoupled (a) and coupled simulations

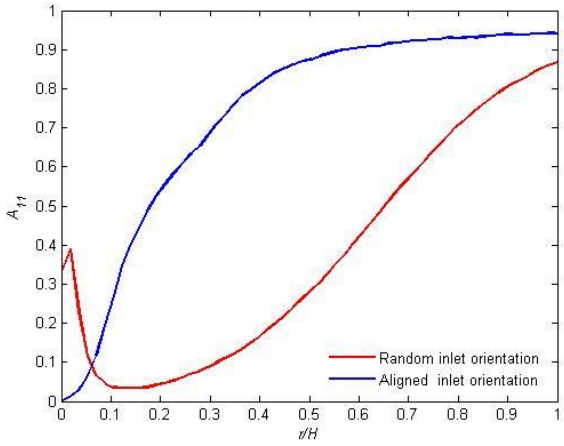

Figure 2.21 Orientation component A_{11} along the radial distance for a simulation of a suspension with ϕ_v=0.01, using random initial orientation and aligned initial orientation. Adapted from [29].

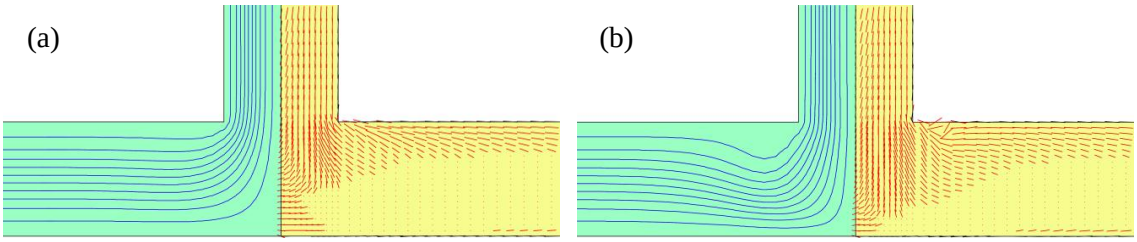

Figure 2.22 Streamlines and fiber orientation vector in a center-gated disk with sprue for (a) decoupled and (b) coupled simulations(ϕ_v= 0.2) performed in Newtonian matrix under steady state conditions assuming random initial orientation at the inlet of a sprue. Adapted from [30].

(b). The streamlines for the decoupled simulation corroborated the finding of Ranganathan and Advani [29], however the coupled simulations show explicitly the effects due to the presence of the sprue at a region close to the gate. The left hand side of Fig. 2.22b shows how the streamlines in the coupled simulations exhibit an undershoot in a region close to the gate, but far from the gate region these streamlines reach the arrangement predicted in decoupled simulations. Changes in the orientation pattern are evident when comparing the decoupled and couple simulations (right hand side of Fig. 2.22a and Fig. 2.22b, respectively). The contrast indicates differences in orientation at the junction and the entrance of the cavity. The difference in orientation

is mainly reflected in the lower half of the junction and upper part of the cavity close to the gate, with a reduction of the out of plane orientation as a result of extensional effects [30].

VerWeyst and Tucker [30] indicate two discrepancies in the kinematic results with respect to Ranganathan and Advani [29] results. The blunt velocity profile in the region close to the gate is not seen in their results and they found a different result for the modified dimensionless centerline velocity. It should be noted that VerWeyst and Tucker [30] used a different formula for the modified dimensionless velocity ($\overline{v}_1$) and is defined as

$$\overline{v}_1(x_1, x_3) = \frac{4\pi h x_1 \left[v_1(x_1, z) \right]}{Q} \tag{2.98}$$

where Q denotes the volumetric flow rate. Fig. 2.23 depicts the modified dimensionless centerline velocity profile along the radial position. The distinctive features seen in $\overline{v}_1$ are: a small overshoot with a narrow breath in the decoupled simulation and lower magnitude and different shape of $\overline{v}_1$ in coupled simulations. It should be noticed that the suspension used by VerWeyst and Tucker [30] are two and four times more concentrated than the highest concentration used by Ranganathan and Advani [29]. The authors attributed these differences to the boundary conditions, constitutive models and C_I parameter used by Ranganathan and Advani [29].

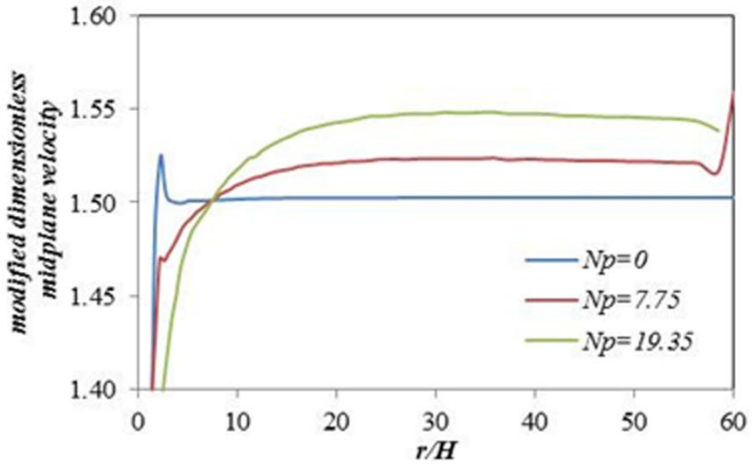

Figure 2.23 Modify dimensionless centerline velocity along radial positions for different coupling levels in coupled simulations for center-gated with a sprue. Adapted from [30].

In addition, VerWeyst and Tucker [30] indicated that the effects of the asymmetric profile of the orientation at the entrance of the cavity might influence these differences.

VerWeyst and Tucker [30] noticed that the initial orientation along the gapwise direction vanishes gradually from gate to the end of the cavity. Fig. 2.24 shows the profile of gapwise orientation at a radial position close to the gate (a) and far from the gate (b). In Fig. 2.24(a), the asymmetry of orientation along gapwise direction can be seen in the region close to the gate with small differences in the magnitude of A_{11} for coupled and decoupled simulations. In contrast, Fig. 2.24(b) shows that the asymmetry practically vanished in the region far from the gate and the small differences in the magnitude of A_{11} for coupled and decoupled simulations are still present. The authors explained that there is a washout of the coupling effects; therefore, the asymmetry disappears in a radial position far from the gate. However, they do not explain why the difference in magnitude of A_{11} is practically insensitive to the simulation conditions.

VerWyest and Tucker's [30] also found non-physical orientation results in their predictions when the flow and orientation equations were coupled. They mention that their FEM results sometimes gave solutions where the tensor components A_{ii} falls outside of the physical range 0 to 1. These non-physical values are "typically associated with a stagnation point on the wall, where the flow is moving away from the wall." It is

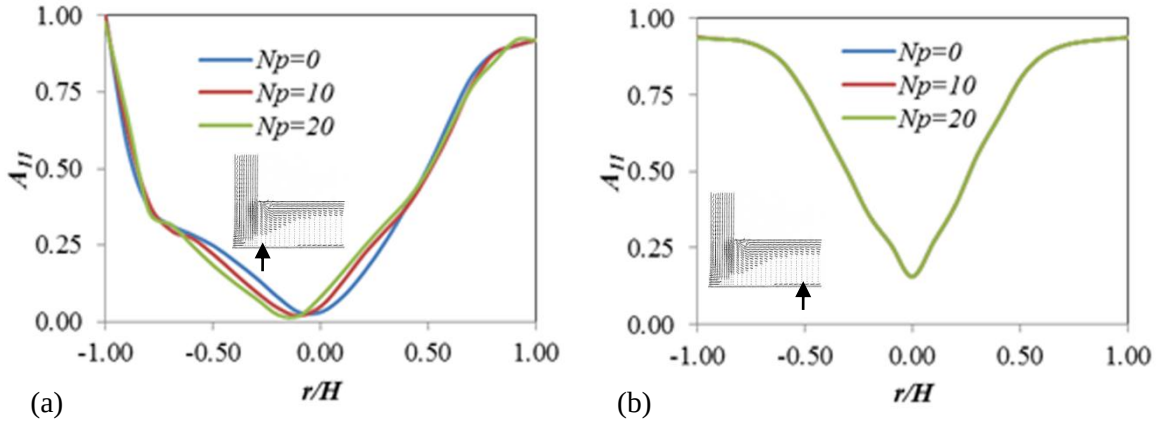

Figure 2.24 Orientation along gapwise direction for several interaction conditions in coupled simulations for disk with sprue at a position (a) close to the gate and (b) far from the gate. These simulations were performed in Newtonian matrix under steady state conditions. Adapted from [30].

very illustrative to show the non-physical results in VerWeyst and Tucker paper, which are exemplified in Fig. 2.25. The stagnation near the lower wall of the entrance region in the center gated disk causes some fibers to have projections out of the limits of the domain as shown in Fig. 2.25(a). While, quantitatively speaking the effect of negative A_{ij} values meaning the a non-physical orientation are shown in Fig. 2.25(b). VerWyest and Tucker, describe a mathematical manipulation that can be used to correct the values before the use of them in the constitutive equation. The readers are invited to read this section in the original paper to understand how deal with this problem in the coupled flow-fiber simulations.

Chung and Kwon [28] used a finite element formulation to develop a transient simulation for a non-Newtonian matrix containing a semi-concentrated regime of fibers (ϕ_v = 0.23) in an axisymmetric with and without a sprue and in planar cavity without a sprue. The evolution of fiber orientation was modeled using the Folger-Tucker model while the stress contribution due to the fibers was described by Dinh-Armstrong model. The frontal flow position is captured using a pseudo-concentration method (PCM). The boundary conditions used are: velocity prescribed at the inflow, no slip condition at the wall, the free slip condition at the front, and the transverse velocity and stress component in the longitudinal direction are zero along symmetry lines.

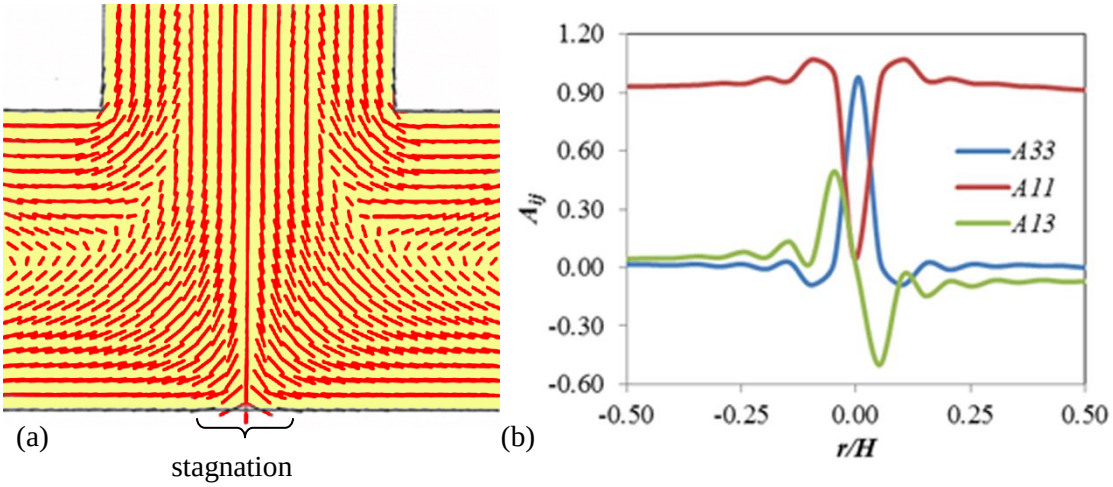

Figure 2.25 Examples of non-physical orientation state Adapted from VerWeyst and Tucker [30] *for (a) vector plot of orientation near a stagnation point and (b) the orientation components around the stagnation point showing the negative values of* A_{ij}.

Chapter 2

Random initial orientation was used for the center-gated disk, at the entrance of the cavity for the sprueless geometry or at the entrance of the sprue. When an end gated rectangular geometry is considered, average result of experimental orientation determined by Bay and Tucker [27] is prescribed. In the simulations, both the governing equations and moving front equation are solved using a Galerkin formulation and the orientation evolution and moving front equations are handled with are Streamline Upwinding Petrov-Galerkin (SUPG) formulation. The Crank–Nicholson implicit finite difference method is used for the temporal discretization.

Chung and Kwon [28] corroborated the kinematic effects on the radial velocity in a disk along the thickness of the part for a spureless cavity found by Ranganathan and Advani [29]. They found that an increase in the bluntness of the radial velocity profile can be seen close to the gate when the decoupled approach is used, while there was an overlapping of results in the region beyond the influences of the gate. Chung and Kwon [28] also showed the effect of the sprue as part of the center gated disk on the radial velocity for the decoupled simulations. When the sprue is considered the maximum radial velocity in a region near to the gate is located above the axis of symmetry of the cavity. However, in a region far from the gate, the radial velocity profile considering and ignoring the sprue are the same.

Chung and Kwon [28] used the multilayer structure approach to analyze the results of orientation for coupled simulations. In all of these cases they analyze the results in terms of multilayer structures. They used the 7 layer approach along the gapwise height consisting of 2 skins, 2 shells, 2 transitions, and 1 core zone. The analysis was focused in the shell, transition, and core zones defined in term of a normalized gapwise height (z/H) defined as 0.833, 0.500, and 0.167, respectively. Fig. 2.26 depicts the A_{11} orientation along the radial position in coupled and decoupled simulation developed in the different layers structures. This figure helps to visualize the following key points seen in the orientation for a suspension flowing a center gated disk, indicated by Chung and Kwon [28]:

- The coupling effect on the orientation state is significant in the core and transition layers, even far downstream especially when the fountain-flow effect is incorporated
- The fountain-flow affected region could be identified by sudden decrease of A_{11} far downstream, and it corresponds to melt-front region when the melt-front reaches the outer radius

- The fountain-flow affected region is larger for shell layers compared with other layers
- The decoupled flow-directional fiber orientation is more aligned (higher values of A_{11}) than the coupled one, irrespective of the layers
- The coupling effect diminishes rapidly for shell layers near the wall. As the dimensionless gapwise location decreases (close to core layers), the effect persists farther downstream. Therefore, the coupling effect is important near the core and transition layers, even for large *r*.

It should be noted that Chung and Kwon [28] qualitatively corroborated the profile of A_{11} for the transition layer along the radial locations originally predicted in the steady state simulations [29].

Chung and Kwon [28] corroborated the asymmetry in orientation at the entrance of the cavity for simulation considering a disk with a sprue. Fig. 2.27 shows the location of random initial orientation for the two center-gated geometries considered, the domain of simulation, and profile of the orientation along the gapwise direction at the entrance of the cavity. Fig.2.27c shows the orientation at the entrance of the cavity assuming the random orientation at the inflow of the sprue (asymmetric curve) or at the inflow of the cavity

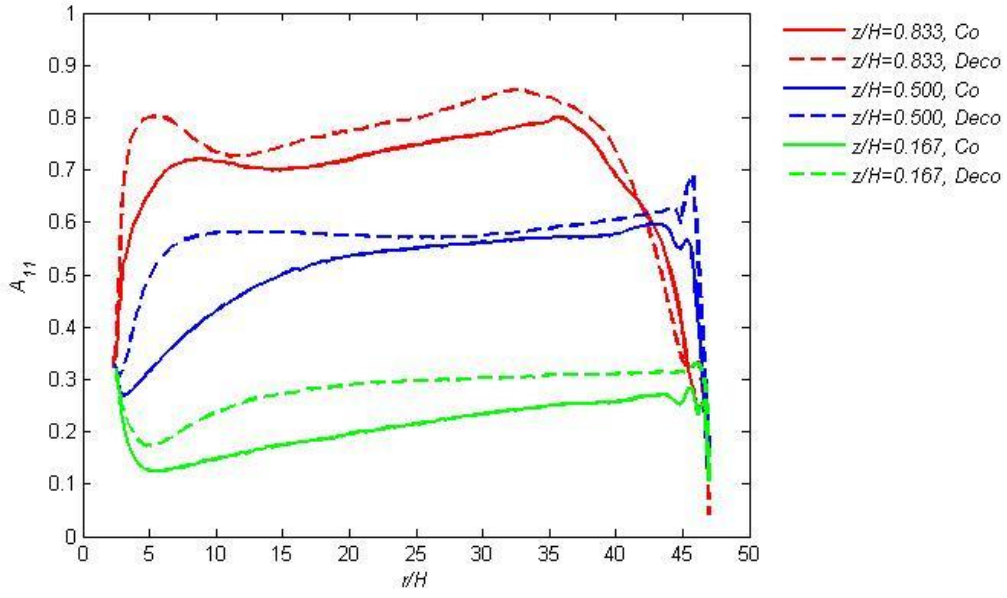

Figure 2.26 A_{11} orientation component along the radial position for a coupled simulation for a center-gated disk. Adapted from [28].

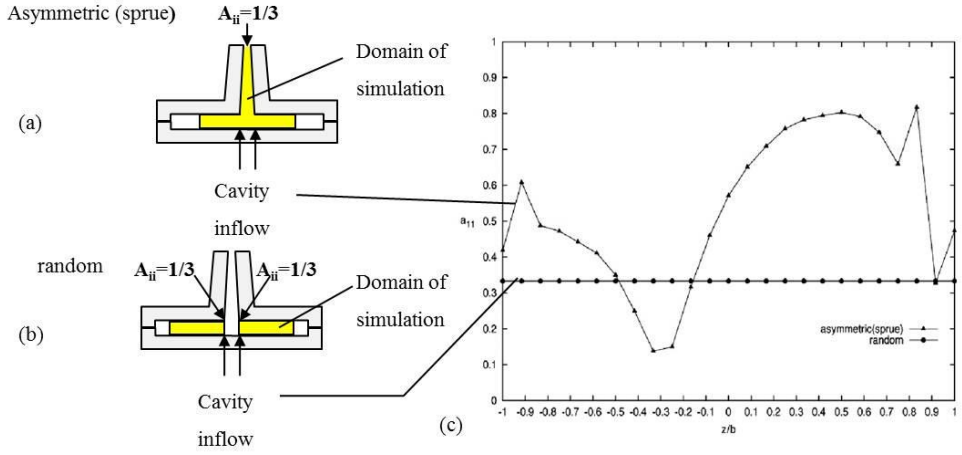

Figure 2.27 Initial conditions at the inlet of the cavity as result of different disk geometries considered. (a) Random orientation prescribed at the inflow the sprue and (b) random orientation prescribed at the inflow of the cavity. The profile of the orientation as result of the geometries previously indicated: the triangles indicate the profile of (a) and the circles the profile of (b). The z/H=1 indicate the top wall and z/H=-1 the lower wall [28]. *(c) Flat orientation profile at the gate region due to the prescription of random orientation an asymmetric orientation profile due to the presence the sprue.*

(straight line). The asymmetric curve indicates that the fibers are more aligned with respect to the flow in the upper half of the entrance of the cavity than the lower half. It should be noted that the asymmetry shown in Fig.2.27 shows a different profile compared to Figure 2.24(a) (predicted steady state simulation) [30].

Chung and Kwon [28] predicted the orientation for the upper and lower half of the cavity in a center-gate geometry with sprue in order to evaluate the asymmetrical effects at the entrance of the cavity. Fig. 2.28 show the gapwise locations used to evaluate the orientation components in both halves of the cavity. It is useful to understand the results on the different layers of orientation at each half of the cavity. Fig. 2.29 shows the initial condition effect on the A_{11} orientation component at each half thickness, upper (a) and lower (b) for different layers of orientation. From Fig. 2.29 it was found that the entrance effects remain near the core and transition regions for upper and lower surface and that the entrance effects persist even near the shell layers. In the original publications there are plots for the components A_{13} and A_{22}, but these plot are not included in this review, what will be included are the following findings indicated by the authors:

- The component of orientation A_{13} is significantly affected by the presence of sprue, especially in the core regions. However, this component shows a "rapid flip-over phenomenon" close to the shell layer around.
- The component A_{22} shows a fiber alignment transversely to the flow direction in the core layer, a decreasing in the transition layer and a more rapid flip over phenomenon than A_{13}. The authors says the presence of sprue affects the A_{22} value in the transition and core but not in the shell layer

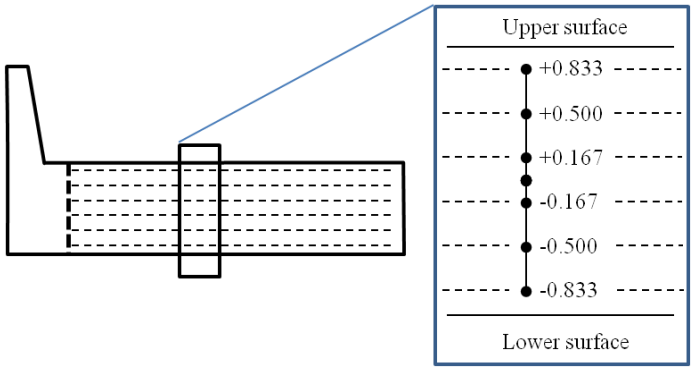

Figure 2.28 Gapwise height used to evaluate the results of orientation components.

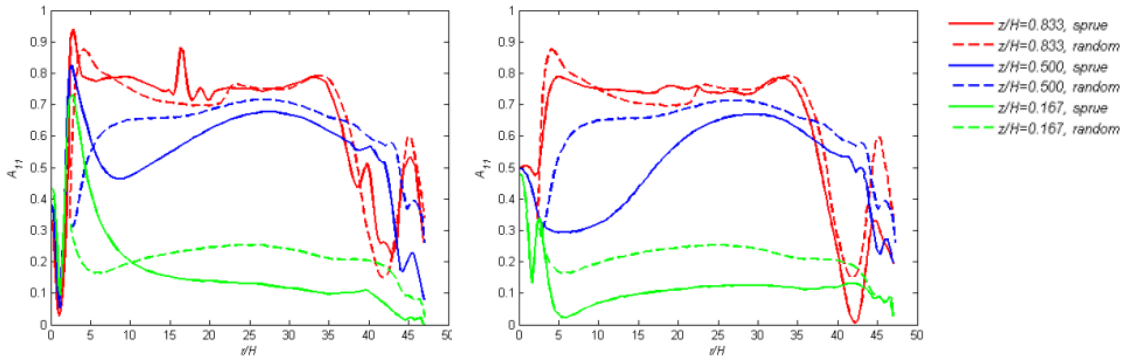

(a) (b)

Figure 2.29 Effect of initial orientation in the A_{11} component along the radial distance for: (a) upper half thickness (b) lower half thickness. Adapted from [28].

Chung and Kwon [28] analysis of initial orientation in the prediction of orientation along the length of flow for a rectangular plaque. When they compared these results with results from the disk, they indicate that the orientation of the disk is more susceptible to initial conditions than the plaque[28].

2.4.2.2 Hele-Shaw flow approximation simulations

Chung and Kwon [39] used a finite element formulation for a Newtonian matrix containing a semi-concentrated regime of fibers (ϕ_v = 0.1 and 0.2) in an axisymmetric without a sprue, featuring a coupled analysis of Hele-Shaw approximation and fiber orientation including in-plane velocity gradient effects. Fiber orientation evolution was modeled using the Folgar-Tucker model while the fibers' stress contribution was described by Dinh-Armstrong model. The boundary conditions used are: pressure prescribed at the gate, no slip condition at the wall, and pressure set zero at the front, with an implied indication of symmetry. The orientation at the inflow was obtained from the orientation evolution equation at steady state with Newtonian velocity field, C_I = 0.002, and hybrid closure. The governing equations were solved using a Galerkin formulation and the orientation evolution equations were computed at the centroid of the finite elements by a time integration.

Chung and Kwon [39] indicate that the in-plane velocity gradient has to be included in the coupled analysis to determine the correct stress. The in-plane stresses are significant to predict the orientation in radial positions near the gate, but not the cavity pressure [39]. The results disagree with the results of Ranganathan and others, which were attributed to the boundary condition dealing with the steady state orientation at the wall.

Chung and Kwon [28] used the multilayer structures approach to analyze the results of orientation for coupled simulations using Hele-Shaw flow approximation, with the formulations described in section 2.4.3.1. Fig. 2.30 shows the multilayer prediction of orientation using Hele-Shaw flow approximation for both simulations, which unlike Fig 2.26 does not show a sudden decrease in A_{11} far downstream but has a broad reduction of the coupling effects. The coupling effect becomes significant as the dimensionless gapwise direction decreases. According to Chung and Kwon [39], the increase in coupling for near-transition layers is due to the in-plane stretching equal to or greater than the gapwise shearing, in the region close to the gate [28]. Some interesting new features left out by Chung and Kwon [28] can be seen in Fig 2.26 and Fig. 2.30.

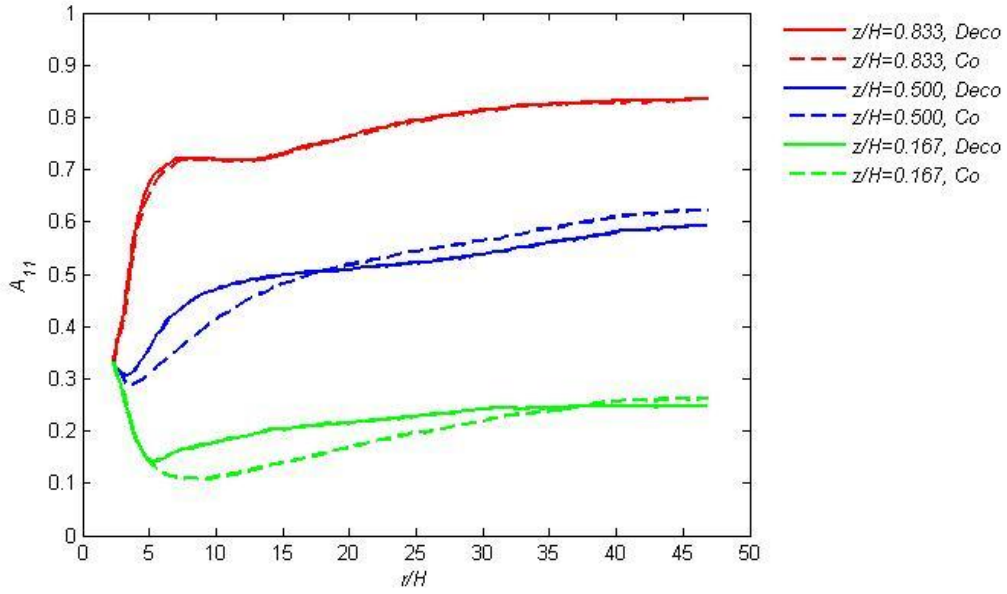

Figure 2.30 A_{11} orientation component along the radial position for a decoupled simulation for a center-gated disk. . Adapted from [28].

Fig. 2.31 shows the orientation component A_{11} along the radial position obtained using Hele-Shaw flow approximation (HAS) and governing equations (Full) for coupled (a) and decoupled (b) simulations. In Fig. 2.31 it can be seen upstream, a qualitative agreement in orientation profile irrespective of the transport equation. The quantitative differences affect the decoupled simulations results, and simulations with the full balance equations overpredict the A_{11} orientation except for the upstream shell layer for coupled simulations.

2.4.2.3 Experimental comparison

Chung and Kwon [28] compared the prediction of decoupled simulation using Hele-Shaw and full balance equations with the Bay and Tucker [25] experimental results. Chung and Kwon [28] indicate that they

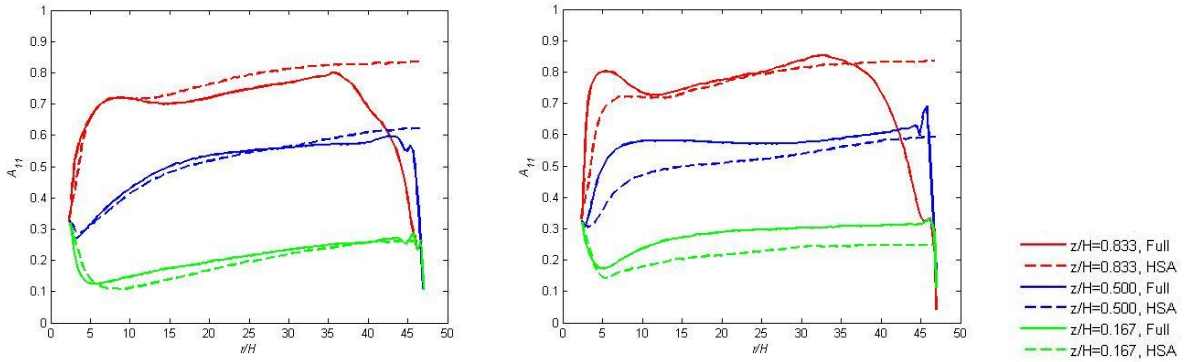

Figure 2.31 Orientation results for simulations using full balance equations (Full) and Hele-Shaw flow approximation (HSA) for different layers using (a) couple flow-orientation strategy (b) decoupled flow-orientation strategy.

could not perform the analysis using a coupled simulation due to the limited amount of material parameters in Bay and Tucker [25]. Figure 2.32 show the experimental result and predictions of decoupled simulations using the governing equations (Full) or Hele-Shaw flow approximation (HSA) for A_{11} orientation component along the gapwise direction in a center-gated disk at several dimensionless radial location (r/H): (a) 5.68, (b) 22.8, and (c) 40.4. The authors point out that the predictions based upon governing equations almost match the experimental data, irrespective of layers. However, it can be seen in Figure 2.32(a) and 2.32(c) that the simulations fail to predict the core layer in a region close to the gate and the shell layer in a region close to the end of fill, respectively. The authors remark poor performance of simulation using Hele-Shaw approximation to validate the experimental result in the center-gated disk indicating that "the fountain-flow effect is very crucial for the exact prediction of the orientation state and the Hele–Shaw model should be discarded" [28]. However, it should be noted that a similar analysis was done with the rectangular plaque show that simulations using Hele-Shaw Approximation and the governing equations have similar performance to predict the shear layer. In addition, both approaches fail trying to predict the core layer.

Chung and Kwon [28] evaluated the sprue effects in decoupled simulations validating their results with Bay and Tucker [25] experimental results for a center-gated disk. Figure 2.33 shows the experimental result and predictions of decoupled simulations using the governing equations and random or asymmetric orientation,

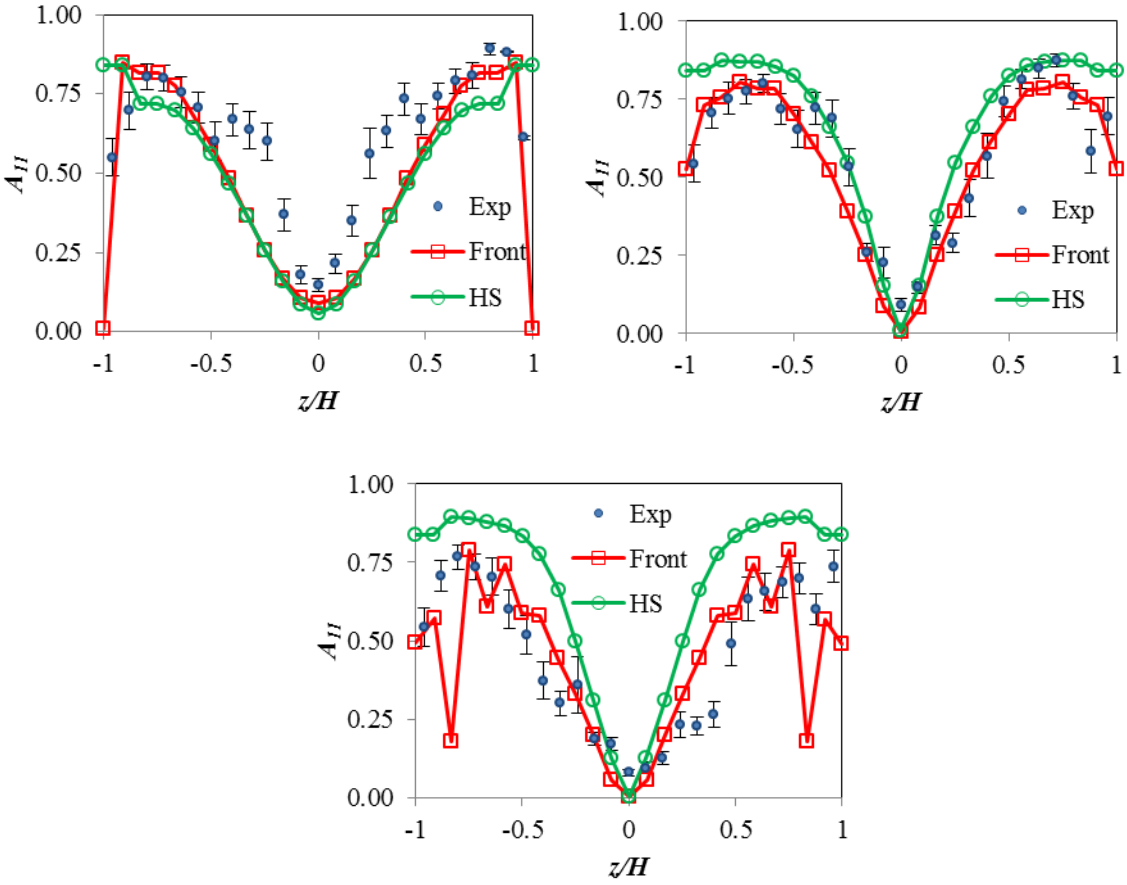

Figure 2.32 Comparison of experimental results with the prediction of orientation calculated in decoupled simulations using full balance equations (labeled as fountain flow) and Hele-Shaw flow approximation at several dimensionless radial location (r/H): (a) 5.68, (b) 22.4, and (c) 40.4. Adapted from [28].

for A_{11} orientation component along the gapwise direction in a center-gated disk at several dimensionless radial location (*r/H*): (a) 22.4 and (b) 40.4. The simulations were performed imposing random initial conditions at the entrance of cavity of a center-gated disk or asymmetric orientation at the same place due to the inclusion of the sprue as part of the flow domain. The following findings indicated were indicated [28]:

- The sprue effects are evident.
- For the shell layers: sprue effects are negligible.

Chapter 2

- For core and transition layers: predictions including sprue region consistently under-predict A_{11} compared with those neglecting sprue
- The predictions including the sprue region more approach the experimental data, except at the lower part of the thickness around gate regions.
- Results including the sprue seem to be in better agreements with experimental data than those without the sprue.
- Including the sprue region is important because it influences orientation state still far downstream.

The authors indicate as a conclusion of this study that the effects of the initial conditions are important for the accurate prediction of orientation state because steady state is seldom reached for center-gated disk geometry [28].

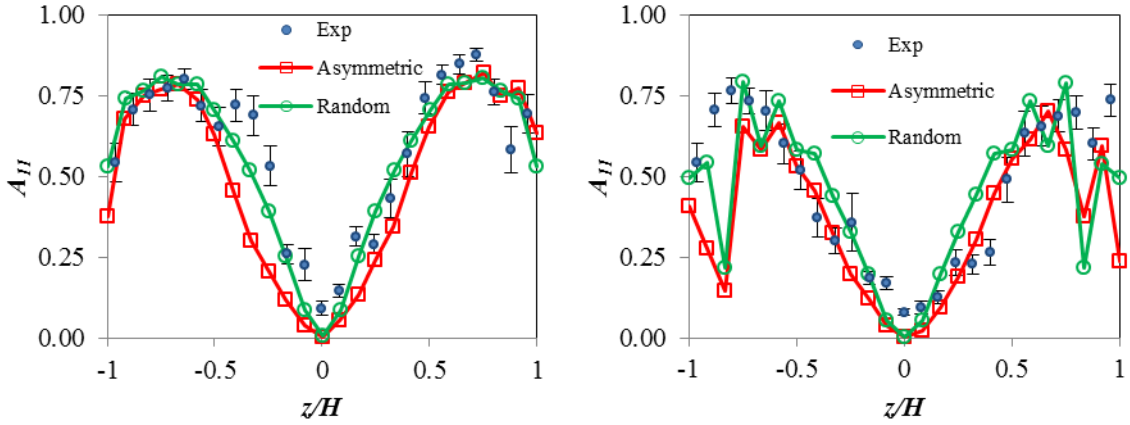

Figure 2.33 Corroboration of the effect of initial orientation with the experimental results of Bay and Tucker at several dimensionless radial location (r/H): (a) 22.8 and (b) 40.4. Adapted from [28].

2.5 Nomenclature

Latin letter symbols

Symbol	Definition
a_r	Aspect ratio
A	Area
$\underline{\underline{A}}$	Second order orientation tensor
C_I	Interaction coefficient
d	Diameter of the particle
$\underline{\underline{d}}$	Rate of deformation tensor
$\overline{\underline{\underline{d}}}$	Discrete rate of deformation tensor
D_r	Rotary diffusivity-like parameter
f	Scalar measure of orientation
$f(\varepsilon)$	Correction factor to account for finite fiber thickness
$\underline{\underline{f}}$	Finite element weighting function for the discrete deformation tensor projection
F	Material density function
F_n	Weighting function for orientation
H	Half gap width
a_c	Average inter-fiber distance
Hs	Constant that depends on the orientation state for Shaqfeh and Fredrickson model
II_d	Second invariant of the rate of deformation tensor
III_d	Third invariant of the rate of deformation tensor
K_{ifs}	Proportionality constant used in the interaction coefficient
K	Experimental constant used in the relative viscosity
l	Length of the particle
m	Minor axis of the ellipse
M	Major axis of the ellipse
n	Power-law index
$\underline{n}$	Outward pointing unit normal vector
N_i	Number of fiber
N_p	Particle number

Chapter 2

Symbol	Definition
p	Pressure
$\underline{p}$	Orientation unit vector parallel to the backbone of the particle
Q	Volumetric flow rate
q	Finite element weighting function for continuity equation
$\mathfrak{R}$	Fourth order orientation tensor
t_{fill}	Mold filling time
t	Time
$\underline{t}$	Tangent vector to the surface
$\underline{\underline{T}}$	Extra stress tensor
$\underline{\underline{T}}^{particle}$	Extra stress due to the movement of particles
$\underline{\underline{T}}^{fiber}$	Extra stress due to the movement of fibers
$\underline{\underline{T}}^{matrix}$	Extra Stress contribution due to polymer matrix
$\underline{\underline{T}}^{viscous}$	Extra stress due to viscous contribution or fast relaxation
$\underline{u}$	Finite element weighting function for momentum equation
$\underline{v}$	Velocity
$\overline{\underline{v}}$	Average velocity along the gapwise coordinate
$\underline{v}_m$	Mesh velocity

Greek letter symbols

Symbol	Definition
α	Width of the transition region between η_0 and the power law region
$\dot{\gamma}$	Scalar magnitude of the rate of deformation or simply strain rate
$\underline{\underline{\delta}}$	Unit tensor
$\Delta\underline{x}$	Grid spacing
Δt_0	Initial estimate of time step
ε	Function of aspect ratio in Batchelor model
ς	Proportionality coefficient representing the slip length

Symbol	Definition
ζ_{str}	Viscous drag coefficient
η	Newtonian viscosity
η_0	Zero-shear viscosity
η_s	Solvent viscosity
η_r	Relative viscosity
λ	Time constant approximately representing the reciprocal of the shear rate for the onset of shear thinning behavior
λ_s	Constant that depend on the shape
θ	Out-of-plane angle
θ_c	Cut off angle
ρ	Density
$\underline{\underline{\sigma}}$	Total stress
ϕ	In-plane angle
$\underline{\underline{\phi}}_{\tau}$	Finite element weighting function for orientation equation
ϕ_v	Particle volume fraction
$\psi(\phi,\theta)=\psi(\underline{p})$	Distribution function for orientation
$\underline{\underline{\varpi}}$	Vorticity tensor

Special character symbols

Symbol	Definition
D/Dt	Material derivative
$\underline{\nabla}$	Gradient operator
$\underline{\nabla}\underline{v}$	Velocity gradient tensor
<●>	Ensemble average of the dyadic product of the unit vectors p over all possible orientations
$(\ldots)^T$	Transpose
$\begin{pmatrix}\cdot\\ \ldots\end{pmatrix}$	Time derivative

Chapter 2

2.6 Rererences

[1] Versteeg HK, Malalasekera, W. An introduction to computational fluid dynamics: The finite volume method. Essex, England: Longman Scientific & Technical; 1995.

[2] Dantzig JA, Tucker, C.L. Modeling in materials processing. Cambridge, UK: Cambridge University Press; 2001.

[3] Cuvelier C, Segal, A., vanSteenhoven, A.A. Finite element methods and Navier-Stokes equations. Dordrecht: D. Reidel Publishing Co; 1986.

[4] Koplik J, Banavar, J. R. Corner flow in the sliding plate problem. Phys Fluids. 1995;7:3118-3125.

[5] Thompson PA, Troian, S.M. A general boundary condition for liquid flow at solid surfaces. Nature (London). 1997;389-362:360.

[6] Zhu Y, Granick, S. . Rate-dependent slip of Newtonian liquid at smooth surfaces. Phys Rev Lett. 2001;87:0961051-0961054.

[7] Priezjev NV. Rate-dependent slip boundary conditions for simple fluids. Phys Rev E. 2007;75:0516051-0516057.

[8] Nassehi V. Practical aspects of finite element modeling of polymer processing Chichester, West Sussex, England ; New York, NY Wiley; 2002.

[9] Lapasin R, Pricl, S. Rheology of industrial polysaccharides: Theory and applications Springer; 1995.

[10] Doraiswamy D, Metzner, A.B. . The rheology of polymeric liquids crystals. Rheol Acta. 1986;25.

[11] Metzner AB. Rheology of Suspensions in Polymeric Liquids. J Rheol. 1985;26:739-775.

[12] Baird D, Collias D. Polymer processing: Principles and design: Wiley, John & Sons, Incorporated; 1995.

[13] Altan MC. A review of fiber-reinforced injection molding: Flow kinematics and particle orientation. J Thermoplast Compos. 1990;3:275-313.

[14] Jeffery GB. The motion of ellipsoidal particles immersed in a viscous fluid. Proc R Soc A. 1922;102:161-179.

[15] Dinh SM, Armstrong, R. C. A rheological equation of state for semi-concentrated fiber suspensions. Journal of Rheology. 1984;28:207-227.

[16] Eberle APR. Modeling the Rheology and Orientation Distribution of High Aspect Ratio Particles Suspended in Polymeric Melts: Nanoclays and Glass Fibers [Proposal]. Blacksburg: Virginia Polytechnic Institute; 2007.

[17] Ranganathan S, Advani, S.G. Fiber-fiber and fiber-wall interactions during the flow of non-dilute suspensions. In: Papathanasiou TD, Guell, D.C., editor. Flow-induced alignment in composite materials. Cambridge, England: Woodhead Publishing Limited; 1997. p. 43-76.

[18] Advani S, Tucker C. The use of tensors to describe and predict fiber orientation in short fiber composites. J Rheol. 1987;31:751-784.

[19] Larson RG. The structure and rheology of complex fluids. New York: Oxford University Press; 1999.

[20] Folgar F, Tucker C. Orientation behavior of fibers in concentrated suspensions. J Reinf Plast Comp. 1984;3:98–119.

[21] Chung D, Kwon T. Fiber orientation in the processing of polymer composites. Korea-Aust Rheol J. 2002;14:175-188.

[22] Vincent M, Agassant, JF. Predicting fiber orientation in injection molding. In: Utracki LA, editor. Progress in polymer processing: Two phase polymer systems. Munich: Hanser; 1991. p. 277-303.

Chapter 2

[23] Henry_de_Frahan H, Verleye, V., Dupret, F., Crochet, M. J. Numerical prediction of fiber orientation in injection-molding. Polym Eng Sci. 1992;32:254-266.

[24] Tucker CL, Advani, S.G. Processing of short-fiber systems. In: Advani SG, editor. Flow and rheology in polymer composites manufacturing. Amstendarm: Elsevier; 1994. p. 147-197.

[25] Bay RS, Tucker CL. Fiber orientation in simple injection moldings. 2. Experimental results. Polym Composite. 1992;13:332-341.

[26] Fan X. Numerical study on some rheological problems of fibre suspensions. Sydney: The University of Sydney; 2006.

[27] Bay R, Tucker CL. Fiber orientation in simple injection moldings .1. Theory and numerical-methods Polym Composite. 1992;13:317-331.

[28] Chung D, Kwon T. Numerical studies of fiber suspensions in an axisymmetric radial diverging flow: the effects of modeling and numerical assumptions. J Non-Newtonian Fluid Mech. 2002;107:67-96.

[29] Ranganathan S, Advani, S.G. . A simultaneous solution for flow and fiber orientation in axisymmetric diverging radial flow. J Non-Newtonian Fluid Mech. 1993;47:107-136.

[30] VerWeyst B, Tucker C. Fiber suspensions in complex geometries flow/orientation coupling. Can J Chem Eng. 2002;80:1093-1106.

[31] Wang J, Silva C, Viana J, van Hattum F, Cunha A, Tucker C. Prediction of fiber orientation in a rotating compressing and expanding mold. Polym Eng Sci. 2008;48:1405-1413.

[32] Phelps J, Tucker C. An anisotropic rotary diffusion model for fiber orientation in short- and long-fiber thermoplastics. J Non-Newtonian Fluid Mech 2009;156:165-176.

[33] Chung S, Kwon T. Invariant-based optimal fitting closure approximation for the numerical prediction of flow-induced fiber orientation. J Rheol. 2002;46:169-194.

[34] Phan-Thien N, Tanner, R. T. A new constitutive equation derived from network theory. J Non-Newtonian Fluid Mech. 1977;2:353-365.

[35] Quinzani L, Armstrong, R.C., Brown, R.A. . Use of coupled birefringence and LDV studies of flow through a planar contraction to test constitutive equations for concentrated polymer solutions. J Rheol. 1995;39:1201–1228.

[36] Cruz DOA, Pinho, F.T., Oliveira, P.J. . Analytical solutions for fully developed laminar flow of some viscoelastic liquids with a Newtonian solvent contribution. J Non-Newtonian Fluid Mech. 2005;132 28–35.

[37] Batchelor GK. The stress generated in a non-dilute suspension of elongated particles by pure straining motion. J Fluid Mech. 1971;46:813-829.

[38] Chung ST, Kwon, T.H. . Numerical simulation of fiber orientation in injection molding of short-fiber-reinforced thermoplastics. Polym Eng Sci. 1995;35:604-618.

[39] Chung S, Kwon T. Coupled analysis of injection molding filling and fiber orientation, including in-plane velocity gradient effect. Polym Composite. 1996;17:859-872.

[40] Shaqfeh ESG, Fredrickson, G. H. The hydrodynamic stress in a suspension of rods. Phys Fluids A-Fluid. 1990;2:7-24.

[41] Almeida A, Faria, L., Febra, R. Refined two-dimensional models for the analysis of free boundary flows between parallel plates. Comput Methods Appl Mech Engrg. 1998;151 163-180.

[42] Kennedy P. Flow analysis of injection molds. New York: Hanser-Gardner Publications; 1995.

[43] Crochet MJ, Dupret, F., Verleye, V. Injection molding. In: Advani SG, editor. Flow and rheology in polymer composites manufacturing. Amsterdam: Elsevier Science; 1994. p. 415-463.

[44] Baaijens FPT. Calculation of residual stresses in injection molded products Rheol Acta. 1991;30:284-299.

Chapter 2

[45] Kim IM, Park, S.J., Chung, S.T., Kwon,T. H. Numerical modeling of injection/compression molding for center-gated disk: Part I. Injection molding with viscoelastic compressible fluid model. Polym Eng Sci. 1999;39:1930-1942.

[46] Pittnam JPT. Finite elements for field problems. In: Tucker CL, editor. Fundamentals of computer modeling for polymer processing. Munich: Hanser Publishers; 1989. p. 237-334.

[47] Li J, Hesse, M., Ziegler, J., Woods, A.W. An arbitrary Lagrangian Eulerian method for moving-boundary problems and its application to jumping over water. J Comput Phys. 2005;208 289–314.

[48] Reddy JN. An introduction to finite element methods. New York: McGraw-Hill, Inc; 1993.

[49] Guénette R, Fortin, M. A new mixed finite-element method for computing viscoelastic flows. J Non-Newton Fluid. 1995;60:27-52.

[50] Baaijens FPT, Hulsen, M.A, Anderson, P.D. The use of mixed finite element methods for viscoelastic fluid flow analysis. In: Stein E, de Borst, R., Hughes, T.J.R., editor. Encyclopedia Of Computational Mechanics. Chichester,: John Wiley & Sons; 2004. p. 480-498.

[51] Baaijens FPT, Selen, S.H.A., Baaijens, H.P.W., Peters, G.W.M., Meijer, H.E.H. Viscoelastic flow past a confined cylinder of a low density polyethylene melt. J Non-Newton Fluid 1997;68:173-203.

[52] Baaijens FPT. An iterative solver for the DEVSS/DG method with application to smooth and non-smooth flows of the upper convected Maxwell fluid J Non-Newtonian Fluid Mech,. 1998;75:119-138.

[53] Bogaerds ACB, Verbeeten, W.M.H., Peters, G.W.M., Baaijens, F.P.T. 3D Viscoelastic analysis of a polymer solution in a complex flow. Comput Method Appl M 1999;180:413-430.

[54] Osswald TA, Hernández-Ortiz, J.P. Polymer processing: Modeling and simulation: Hanser-Gardner Publications; 2006.

[55] Owens RG, Phillips, T.N. Computational rheology. 1 ed. London: Imperial College Press; 2002.

[56] Reddy BD, Mitchell GP. Finite element analysis of fibre suspension flows. Comput Methods Appl Mech Engrg. 2001;190:2349-2367.

[57] Ilinca F, Hétu, J. -F., Pelletier, D. . On stabilized finite element formulations for incompressible advective–diffusive transport and fluid flow problems. Comput Methods Appl Mech Engrg. 2000;188:235-255.

[58] Keunings R. Simulation of viscoelastic fluid flow. In: Tucker CL, editor. Fundamentals of computer modeling for polymer processing. Munich, Vienna, New York: Carl Hanser Verlag; 1989.

[59] Fan YR. A comparative study of the discontinuous Galerkin and continuous SUPG finite element methods for computation of viscoelastic flows Comput Methods Appl Mech Engrg. 1997;141:47-65.

[60] Li BQ. Discontinuous Finite Elements in Fluid Dynamics and Heat Transfer. Berlin: Springer; 2006.

[61] Donea J, Huerta,A. Finite element methods for flow problems Chichester ; Hoboken, NJ John Wiley & Sons., Ltd; 2003.

[62] Hulsen M, Peters, EAJF, van den Brule, BHAA. A new approach to the deformation fields method for solving complex flows using integral constitutive equations. J Non-Newton Fluid Mech 2001;98:201-221.

[63] Khismatullin D, Renardy, Y., Renardy, M. . Development and implementation of VOF-PROST for 3D viscoelastic liquid–liquid simulations J Non-Netonian Fluid Mech. 2006;149:120-131

[64] Scardovelli R, Zaleski, S. Direct numerical simulation of free surface and interfacial flow. Annu Rev Fluid Mech. 1999;31:567–603.

[65] Souli M, Zolesio, J.P. Arbitrary Lagrangian-Eulerian and free surface methods in fluid mechanics. Comput Method Appl Mech Eng. 2001;191:451-466.

Chapter 2

[66] Ganvir V, Lele, A., Thaokar, R., Gautham, B.P. Simulation of viscoelastic flows of polymer solutions in abrupt contractions using an arbitrary Lagrangian Eulerian (ALE) based finite element method. J Non-Netonian Fluid Mech. 2007;143:157-169.

[67] Boman R, Papeleux, L., Bui, Q.V., Ponthot, J.P. Application of the Arbitrary Lagrangian Eulerian formulation to the numerical simulation of cold roll forming process. Journal of Materials Processing Technology. 2006;177 621–625.

[68] Braess H, Wriggers, P. Arbitrary Lagrangian Eulerian finite element analysis of free surface flow. Comput Method Appl Mech Eng. 2000;190:95-109.

[69] Baaijens FPT. Numerical analysis of start-up planar and axisymmetric contraction flows using multi-mode differential constitutive models. J Non-Newton Fluid Mech. 1993;48:147-180.

[70] Donea J, Huerta, A., Ponthot, J.-Ph., Rodríguez-Ferran, A. Arbitrary Lagrangian–Eulerian methods. In: Stein E, de_Borst, R., Hughes, T.J.R., editor. Encyclopedia of computational mechanics: John Wiley & Sons, Ltd; 2004.

[71] Stoker C. Developments of the Arbitrary Lagrangian-Eulerian method in non-linear solid mechanics: Applications to forming processes: Universiteit Twente; 1999.

[72] Roels S, Carmeliet,J., Hens, H. . Mesh adaptative finite element formulation for moisture transfer in materials with a critical moisture content. Int J Numer Meth Engng. 1999;46:1001-1016

[73] Cser F, Bhattacharya SN. Study of the orientation and the degree of Exfoliation of nanopartilces in Poly(ethylene-vinyl acetate) nanocomposites. J Appl Polym Sci. 2003;90:3026-3031.

[74] Jinnai H, Spontak RJ, Nishi T. Transmision electron mirotomography and Polymer Nanostructures. Macromolecules. 2010;43:1675-1688.

[75] Drummy LF, Wang YC, Shoenmakers R, May K, Jackson M, Koerner H, et al. Morphology of layered silicate- (nanoclay-) polymer nanocomposites by electron tomography and small-angle x-ray scattering. Macromolecules. 2008;41:2135-2143.

[76] Clarke AR, Davidson, N.C., Arhenhold, G. Mesostructrural characterization of aligned fibre composites. In: Papathanasious TD, Guell DC, editors. Flow-induced alignment in composite materials. Cambridge: Woodhead Publishing Limited; 1997. p. 230-292.

[77] Bay RS, Tucker CL. Stereological measurement and error estimates for three-dimensional fiber orientation. Polym Eng Sci. 1992;32:240-253.

[78] Konicek TS. A method to determine three-dimensional fiber orientation in fiber reinforced polymers: Master's thesis, University of Illinois at Urbana-Champaign; 1987.

[79] Clarke AR, Eberhardt CN. Microscopy techniques for materials science. Boca Raton, FL, USA: CRC; 2002.

[80] Kawamura M IS, Morita S, et al. Unambiguous determination of 3D fiber orientation distribution in thermoplastic composites using SAM image of elliptical mark and interference fringe JOURNAL OF COMPOSITE MATERIALS. 2005;39:287-299.

[81] Clarke AR, Eberhardt, C.N. Microscopy techniques for materials science Boca Raton, FL: CRC Press 2002.

[82] Kunc V. Personal communication. 2008.

[83] Papathanasiou TD. Flow-induced alignment in injection molding of fiber-reinforced polymer composites. In: Papathanasiou TD, Guell DC, editors. Flow-induced alignment in composite materials. Cambridge, England: Woodhead Publishing Limited; 1997. p. 112-165.

[84] Vincent M, Agassant, J.F. Experimental study and calculations of short glass fiber orientation in center gated molded disks. Polym Composite. 1986;7:76-83.

[85] Devilers. E. V, M. Fibre orientation in injection moulding of a disk. In: Blain WR, De Wilde, W. P., editor. Computer aided design in composite material technology (CADCOMP/94). Southampton, UK: Computational Mechanics; 1994. p. 264-272.

Chapter 2

[86] Magnin B, Couplez, T., Vincent, M., Agassant, J.F. Numerical modeling of injection mold-filling with an accurate description of the frontal flow. In: Chenot JL, Wood, R.D., Zienkiewick, O.C., editor. Proceedings of Numiform 1992: Numerical methods in Industrial forming processes. Valbonne, France1992. p. 365-370.

[87] Vincent M, Devilers, E., Agassant, J.F. Fibre orientation calculation in injection moulding of reinforced thermoplastics J Non-Newtonian Fluid Mech. 1997;73:317-326.

[88] Altan MC, Subbiah, S., Guceri, S.I., Pipes, R.B. Numerical prediction of three-dimensional fiber in Hele-Shaw flows. Polym Eng Sci. 1990;30:848-859.

Chapter 3 Sample preparation and image acquisition using optical-reflective microscopy in the measurement of fiber orientation in thermoplastic composites

Gregorio M. Vélez-García[1], Peter Wapperom[2], Vlastimil Kunc[3], Donald G Baird[4], Audrey Zink-Sharp[5].

[1]Macromolecules and Interfaces Institute, Virginia Tech, Blacksburg, VA 24061, USA

[2]Department of Mathematics, Virginia Tech, Blacksburg, VA 24061, USA

[3]Oak Ridge National Laboratory, P.O. Box 2009, Oak Ridge, TN 37831, USA

[4]Department of Chemical Engineering, Virginia Tech, Blacksburg, VA 24061, USA

[5]Department of Wood Science and Forest Products, Virginia Tech, Blacksburg, VA 24061, USA

Manuscript submitted to the Journal of Microscopy: Vélez-García GM, Wapperom P, Kunc V, Baird DG, Zink-Sharp A. Sample preparation and image acquisition using optical-reflective microscopy in the measurement of fiber orientation in thermoplastic composites. J Microsc-Oxford. 2012 (Submitted).

3.1 Abstract

A complete sample preparation procedure used to determine three-dimensional fiber orientation from optical micrographs of glass fiber-reinforced thermoplastic composites is presented. Considerations for elimination of irregularities in the elliptical footprints, contrast enhancement between fibers and surrounding polymer matrix, controlled-etching that allows the identification of small shadows where fiber recedes into the matrix, and topographical reconstruction of the elliptical footprint are described in the procedure. This procedure has produced high-quality optical micrographs employed to obtain accurate fiber orientation data for thermoplastic composites using the method of ellipses. The optimal definition of the non-elliptical footprints' borders allows an accurate measurement of orientation in small sampling areas.

3.2 Introduction

Fiber-reinforced composites have enhanced physical properties relative to the polymer matrix. However, the physical properties, *e.g.* thermal and mechanical, of these materials are dependent on the local orientation of fibers in the parts, which varies with position. Therefore, obtaining reliable measurements of orientation is important for estimating the properties of these materials.

Chapter 3

The method of ellipses (MoE) is the standard method used to determine the orientation in polymer composites, due to its low cost and simplicity. In the MoE, the orientation of fibers is obtained from the characteristic values of complete or incomplete elliptical footprints and rectangular footprints seen in micrographs [1, 2]. Characteristic values for elliptical footprints are the center position, the minor (m) and major (M) axes lengths, and the angle between the horizontal and the major axis. In the case of rectangles, the axis lengths are substituted by the footprints' height and length. Each footprint represents a cylindrical rod with fiber orientation expressed by the angles of orientation, *i.e.* in-plane (ϕ_f) and out-of-plane angles (θ_f). Fig. 3.1 illustrates the angles of orientation for a single fiber.

The problem of determining fiber orientation reduces to obtaining accurate measurement of the footprints' characteristic values. For this, it is essential to procure high-quality images showing footprints with well-defined edges as well as excellent contrast between the fibers and the surrounding polymer matrix. Moreover, the use of high-quality images is a crucial element for automatic detection of footprints based on image analysis tools [3]. Corroboration of automatically detected footprint borders via manual measurement is time consuming and it is at odds with the purpose of image analysis tools. Therefore, the imprecisions detected in footprint borders automatically cause inaccurate measurements of fiber orientation which are consequently accepted as correct results.

Measurement of orientation in small sampling regions can be obtained by considering the contribution of fractional footprints as demonstrated by Vélez-García, et al. [2]. This is particularly important for regions with rapidly evolving orientation or with low fiber concentration. Fractional footprints seen in the polished plane may arise when the polished plane intersect the tip of a fiber. However, inappropriate sample preparation can cause fiber breakage which also produces fractional objects. Therefore, a good experimental procedure is critical in order to avoid undesired footprints.

The ambiguity problem is one of the major limitations of the MoE and arises from the fact that every elliptical footprint has two possible values, ϕ_f or $\phi_f + \pi$ [4]. Recently, Vélez-García, et al. [2] developed a method in which the tips of the fibers underneath the polished plane of a footprint are exposed by the plasma etching treatment. This results in a dark region in the optical reflection micrograph next to the major axis of

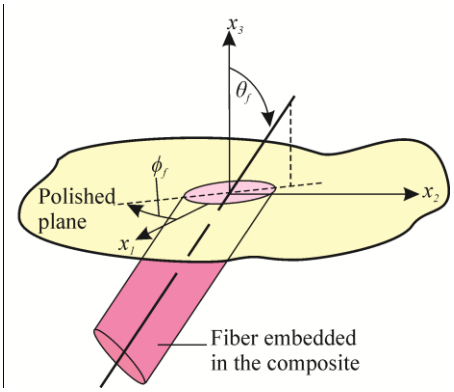

Figure 3.1 In-plane angle (ϕ_f) and out-of-plane angle (θ_f) describing the orientation of a single fiber.

footprints for inclined fibers and can be used to determine unambiguously the in-plane angle. The correct sign of the in-plane angle is determined from the position of the dark region (shadow). An effective visualization of the shadow depends on the controlled excavation of the polymer matrix during the etching step, the quality of the in-focus image, and the inclination of the fiber. The identification of this new parameter requires a distinctive sample etching procedure.

The sample preparation procedure has a direct impact on the production of high-quality images for obtaining reliable and complete fiber orientation in thermoplastic composites. A standardized method, however, is not available in the literature which can lead to the use of low-quality images for evaluating fiber orientation. These low-quality images show low contrast and poor footprint edge definition, *e.g.* irregular or diffuse edges, which prevent obtaining the footprints' characteristic values correctly. Imprecision in elliptical footprint dimensions may increase the systematic error significantly [5].

There are three reasons for the absence of guidelines encompassing sample preparation of fiber composites for orientation analysis. First, the American Society for Testing and Materials (ASTM) standards, *i.e.* ASTM E3 and ASTM E 2015, are only for metals and neat polymers. Second, very few publications encompass all steps of sample preparation for fiber composites. Typically, the only sample preparation step mentioned is sample polishing, referred to as metallographic polishing [2, 6-8]. Third, literature considering fiber composites provides only general aspects involved in sample preparation for fiber thermoplastic composites, *e.g.* Sawyer, et al. [9] and Hayes and Gammon [10], but these references lack sufficient details.

The objective of this paper is to provide a sample preparation procedure that will serve as guidance for obtaining optimal definition of the footprints' border and appropriate contrast enhancement. This experimental procedure attempts to provide sufficient detail in all steps involved in the sample preparation of fiber composites. In addition, we consider modifications in the etching procedure that allow identifying an additional parameter in the image used to unambiguously determine the fibers orientation. As a result of the sample preparation, high-quality images suitable for image analysis in a small sampling area are obtained.

3.3 Sample preparation

Sample preparation steps include cutting, marking, mounting, grinding, polishing, etching, and sputtering. The procedure presented in this paper has been applied to several commercially available resins containing short and long glass fibers, *e.g.* 30 wt% short glass fiber filled polybutylene terephthalate (SF-PBT, Valox 420, Sabic, Co.), 30 wt% short fiber polypropylene (SF-PP, RTP-105, RTP Co.), 30 wt% long fiber polypropylene (LF-PP, LNP Verton MV006S, Sabic Co.) and 30 wt% long fiber polyamide 6 (LF-PA6, LNP Verton PX00700, Sabic Co.). A detailed description that can be readily adapted to other composites is presented below.

3.3.1 Sample Cutting

Appropriate cuttings are critical to avoid both fiber breakage and changes in the fiber orientation. First, aggressive cutting causes fractures and surface irregularities of fibers. This results in distorted shapes of fiber footprints in the final polished plane which increases the imprecision in their characteristic values. Second, the deformation and rise in temperature related to the cutting operation can change the orientation of the fibers. Especially for circular and nearly circular footprints, errors in characteristic values of the order of several pixels, significantly increase the systematic error in orientation analysis [2]. Setting a margin between the line denoting the measurement plane and the cutting lines, as well as performing the cut by abrasion using low speed, prevent effects of fiber breakage and alteration of orientation on the polished plane [10, 11]. The material in the margin region is subsequently removed during the grinding step to prevent effects related to the cutting operation. If cuts by abrasion are not possible, cuts using a band saw combined with larger margins are

necessary. Cuts using a band saw have the advantage of reducing the cutting time considerably with respect to the low-speed abrasive cutter. However, the dimensions of the margins related to band saw cutting must be set judiciously. Small margins would suffer from the problems described above, while large margins as recommended by Sawyer, et al. [9], *i.e.* 25 to 50 mm, are impractical and would increase the grinding time by as much as 12 times. The dimensions of the sample are important in order to avoid problems if compression molding is used for sample mounting. Large samples cause vertical inclination and deformation of the sample during compression molding.

The following procedure considers a careful cutting operation that has been proven to produce polished surfaces without irregular footprints caused by fiber breakage created during this step. Fig. 3.2 summarizes the relevant aspects of the cuts made to obtain a mounting sample. Fig. 3.2(a) illustrates the line indicating the plane of interest, the line indicating a sampling location, and the cutting lines. In addition, this figure depicts

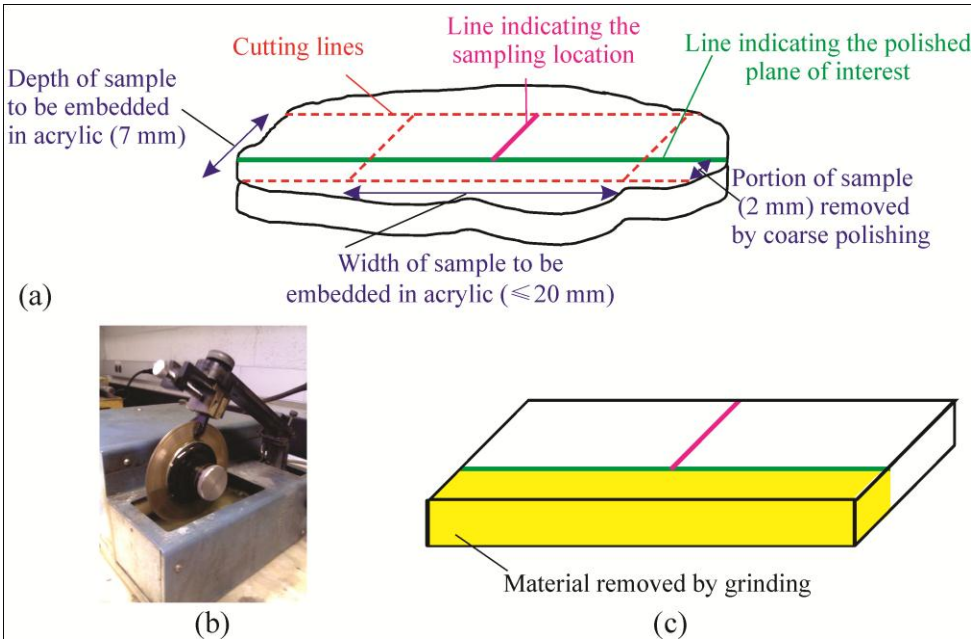

Figure 3.2 Sample in molded part: (a) Lines indicating the location of polished plane, sampling location and cutting lines considering the distances away from the polished plane and width of the sample, (b) abrasive cut of sample, and (c) mounting sample with the yellow area used to denote the material to be extracted by sample grinding.

the dimensions, *i.e.* 20 x 7 mm, of a rectangular mounting sample appropriate for a mounting mold of 25.4 mm. The 7 mm in final depth includes a margin of 2 mm of material removed during the grinding step. Increasing the margin from 2 to 5 mm showed no significant differences in footprints' shape. Also, our results indicate that a depth of 7 mm does not cause problems of sample tilting or deformation during the hot mounting. The mounting sample is cut using a low-speed diamond wheel saw (South Bay Technology, Inc.; San Clemente, CA, USA), as shown in Fig. 3.2(b), with cutting oil used as a cooling agent. At the end of the cutting operation, a mounting sample similar to the one shown in Fig. 3.2 (c) is obtained. In Fig. 3.2(c), the gray color denotes the portion of material to be removed during the grinding step.

In the case of large samples, an initial sample cut around the region of interest is necessary and is illustrated in Fig. 3.3. Fig. 3.3 (a) shows two samples of interest located in the interior of a large part and the cutting-lines' distance from the line of interest for cuts made with a band saw. Our results indicate that at least 10 mm margins between the line of interest and cutting lines do not cause fractures or promote changes in the polished samples. In Fig. 3.3(b) an initial sample of ≈ 20 mm in depth with the important lines on it is shown. The dimensions of this sample are suitable for abrasive cutting using the low-speed diamond wheel saw.

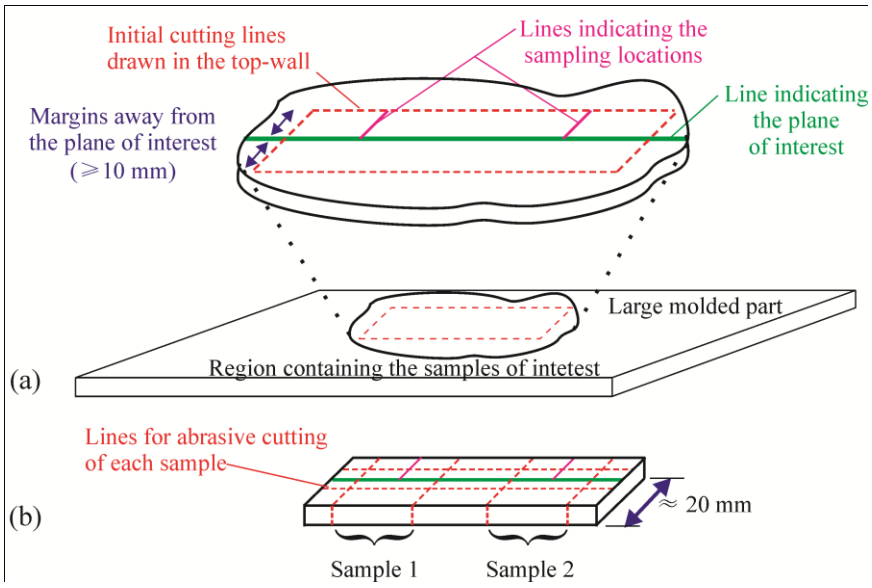

Figure 3.3 Sampling cut in large samples: (a) Lines indicating precut of initial sample containing two sampling locations of interest (b) Lines for abrasive cuts in the initial sample for obtaining two mounting samples.

Chapter 3

3.3.2 Sample Marking

Identifying precise locations for measuring the fiber orientation is important in studies in which information of local orientation is relevant. However, sample marking on locations of interest is an aspect that has not yet been described in the literature. Tridimensional sample markers made of polymeric material are a feasible option for identifying specific locations during image acquisition. However, the polymer must be selected carefully to avoid problems in subsequent steps of sample preparation. For example, the polymer has to be softer than the composite material which is to be grinded and polished, and it must resist deformation due to the heating operation if compression molding is used for sample mounting.

Tridimensional sample markers made of squared and colored polymeric pieces bonded on the mounting sample provide a means of identifying locations of interest during image acquisition. The idea is to use one side of the marker to stop the grinding step and to use the other side as a reference of the location of interest during the image acquisition as shown in Fig. 3.4. Tridimensional markers based on red-colored polyethylene terephthalate (PET), and bonded with a commercially available cyanoacrylate adhesive (Krazy Glue, Columbus, OH, USA) are feasible options. This material resists the mounting temperature and is softer than the composites considered in this study.

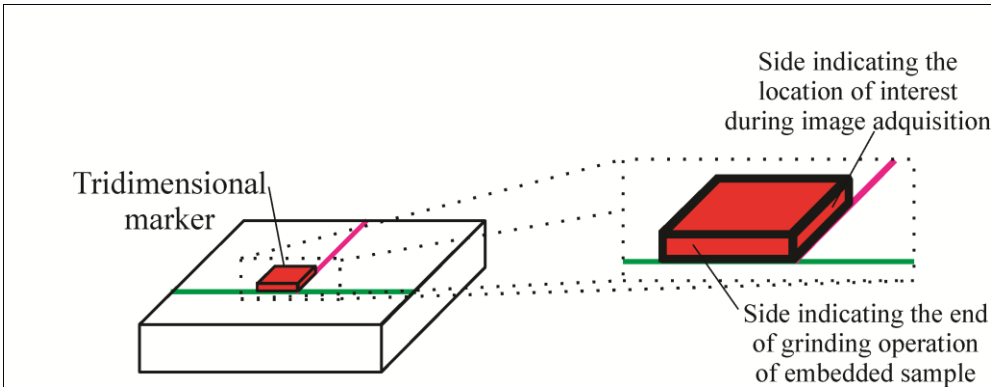

Figure 3.4 Mounting sample with a tridimensional marker indicating the position where the location of interest and line indicating the polished plane meet.

3.3.3 Sample mounting

Appropriate sample mounting is essential because this step influences the sample preparation resources and time and keeps the sample in correct position during the mounting. Description of sample mounting of fiber-reinforced composites in the literature is limited to using epoxies [9, 10]. Compression molding is a less expensive and faster option for fiber composites. However, it requires that the thermal and structural characteristics of the fiber composite remain intact at the mounting temperature and pressure. Notably, the compression pressure required to mount fiber thermoplastic composite samples is much lower, *i.e.* ≈ 1 kPa, than that required for metals and ceramics [12]. To reduce the time required for sample preparation and in order to save resources, multiple samples can be mounted in the same puck.

A consistent mounting operation with low values of compression pressure requires an appropriate control of the heating and cooling cycles. An effective heating cycle consists of compacting the sample with approximately 20 ml of acrylic powder (thermoplastic powder; Precision Surfaces International, Inc., Houston, TX, USA) and preheating for 7 min at 458 K to melt the mounting material, slowing the application of compression pressure until the material sustains 1 kPa, and maintaining the heat for 7 min. Subsequently, a transparent puck is obtained by allowing the sample to cool for 15 min while maintaining 1 kPa pressure. Our results indicate that the use of this cycle prevents the tilting of the sample during mounting and that the samples must be located away from the edges of the puck, *e.g.* 1 or 2 mm, in order to avoid potential problems of uneven light intensity during image acquisition. We found that SF-PBT and LF-PA6 are able to resist the heating conditions with few problems, but materials like SF- and LF-PP can be negatively affected by the heating conditions. Fig. 3.5 shows the deformation near the surface of LF-PP samples induced by the strong grip of support clips (UniClip; Buehler, Lake Bluff, IL, USA). This deformation can cause errors in the evaluation of orientation near the surface of the sample if the clips are near the sampling region. To avoid any distortion in the sample, soft clips (spring clips; Precision Surfaces International, Inc., Houston, TX, USA) with reduced heating time are recommended. Reduction in heating time can cause the "cotton ball" effect, *i.e.* partially melted acrylic in the middle of the puck, but we observed no adverse impact of this cosmetic imperfection.

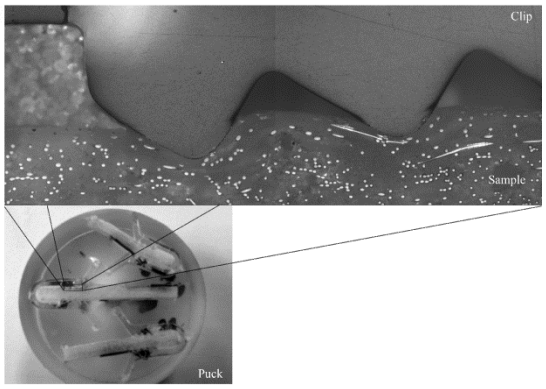

Figure 3.5 Deformation of a sample of 30 wt % long fiber polypropylene (LNP Verton MV006S) due to the indentation of mounting clips illustrates the sensitivity of fiber-reinforced composites to hot mounting conditions.

3.3.4 Sample grinding

Sample grinding is critical for removing material damaged by the cutting operation. The purpose of this section is to provide guidance for sample grinding specifically tailored for fiber composites that will be helpful in extrapolating the procedure for other composites. Factors inherent to the composite, *i.e.* fiber type, fiber concentration, polymer type, glass transition temperature and crystallinity, all make it challenging to derive a distinctive procedure capable of meeting the above objective. Indeed, an adapted version of metallographic grinding suitable for fiber thermoplastic composites requires a set of experimental considerations and personal skills and judgment to tackle these factors. In contrast with recent literature focused on general experimental considerations, *i.e.* Sawyer, et al. [9] and Hayes and Gammon [10], in this section we provide a specific procedure that can be used as a starting point for sample grinding. During the grinding operation, it is important to maintain wet conditions in order to avoid excessive fiber breakage caused by using dry grinding and simultaneously eliminating the debris. Periodic rotation of the sample is essential to keep the even height of the puck as well as to erase the grooves in the direction of the previous grinding step.

Effective sample grinding of fiber thermoplastic composites consists of a two-stage process which is summarized in Table 3.1. The objectives of these two stages are material removal from the margin region and gradual reduction of the grooves from previous grinding steps, respectively. The first stage consists of a semi-

Table 3.1 Sample grinding procedure for fiber orientation studies in thermoplastic composites.

Stage (instrument)	**CAMI Grit designation (average sizes of the abrasive material in μm)**	**Time (min)**	**Interval for 90° Rotation (s)**	**Objective**
I (wet belt grinder)	120 (115)	1-2 (until blurry marker is perceived)	10	Removal of material until plane of interest is reached
	180 (82)	1-2 (until clear marker is seen)	10	
II (wet hand grinder)	240 (53)	2	30	Gradual removal of surface layers to eliminate grooves
	320 (36)	2	30	
	400 (23)	2	30	
	600 (16)	2	30	

manual operation in which a wet-belt grinder (BG-32 dual belt grinder; LECO, St. Joseph, MI, USA) is used to remove material quickly, but its use requires careful operation due to safety and control issues. We have found that using 120– followed by 180–grit abrasive paper for the wet-belt grinder helps to provide control of material removal in the first stage. We also explored a fully manual execution for the first stage, using 120–grit abrasive paper, but it increases the grinding time for this stage from 4 min to at least 30 min. The second stage for the sample grinding involves manual operation using a wet hand grinder (HandiMet® 2 Roll Grinder; Buehler Co, Lake Bluff, IL, USA), while taking into account the considerations indicated in Table 3.1. It is critical to reach the plane of interest, defined by the border of the marker embedded in the puck, especially when multiple

samples are embedded in a single puck. Uneven sample grinding affects the performance of the subsequent sample preparation steps as well as causes images to be acquired over a non-desired plane. To ensure even removal of material at each step of the sample grinding, the height of the puck is measured at a minimum of 4 locations after every complete puck rotation. Regions exhibiting greater height than others are targeted for additional grinding. A careful and systematic 90° rotation of the puck, as indicated Table 3.1, showed no significant variation in the height of the puck, *i.e.* less than 0.010 mm. The purpose of the values and conditions indicated in Table 3.1 is to provide a basic procedure for implementing the grinding operation. This information may be easily adapted and implemented to any other composite. For example, Fig. 3.6 shows a linear change in the height of the puck after the different grinding steps for fiber composites with different polymeric matrices. The amount of material removed depends on the polymeric matrix and its morphological characteristics assuming that E-glass with the same dimensions and composition is used as reinforcing material.

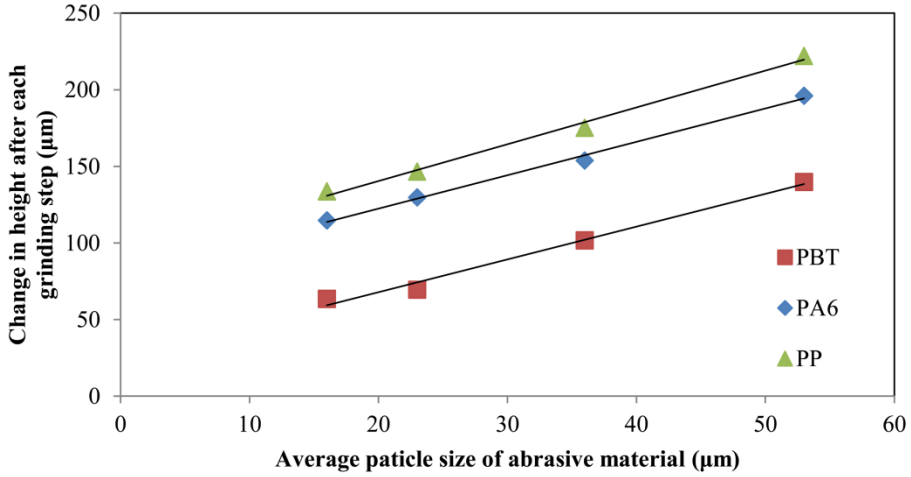

Figure 3.6 Removal of material by abrasion during the second stage of sample grinding based on change in height after each grinding step. Sandpapers with average abrasive material sizes of 53, 36, 23, and 16 µm were used to remove the material. The material removed consisted of either polybutylene terephthalate (PBT), nylon 6 (PA6), or polypropylene (PP) composites embedded in acrylic. The concentration of glass fiber in the composites was 30 wt%.

3.3.5 Sample polishing

Sample polishing is critical for obtaining optimal footprint borders in the polished surface. At the end of the polishing step, the surface exposes the microstructure of the composite at the plane of interest. Factors inherent to the composite, *i.e.* fiber type, fiber concentration, polymer type, glass transition temperature and crystallinity, all make it challenging to derive a distinctive procedure capable of meeting the sample polishing objective**.** The purpose of this section is to develop a procedure which can be extrapolated to other composites. During polishing, there are four experimental considerations in this step that promote obtaining optimal footprint borders in the polished surface [9, 10]. First, automatic polishing provides precise control of the polishing conditions. Second, avoiding extreme pressure levels prevents undesired artifacts on the polished surface. Third, avoiding excessive amount of suspension prevents the surface from slipping over the particles rather than polishing the surface. Fourth, removing the debris after each polishing step by putting the sample in an ultrasonic bath for 30 sec. In addition we have found that repeating the polishing steps, based on visual inspection of the polished surface and checking the footprint border, are essential for obtaining a high-quality polished surface.

Adequate sample polishing that allows obtaining the polished surface with optimal footprint borders for the composites is presented. Table 3.2 summarizes the sample polishing based on the use of a semi-automatic single mount grinder/polisher (MiniMet® 1000 grinder/polisher; Buehler Co, Lake Bluff, IL, USA). The use of this type of instrument is crucial for providing precise control in polishing conditions and for obtaining the desired footprint borders indicated in the last column of Table 3.2. This column is included because we have found that tracking the elimination of holes and reduction in irregularities of footprint borders are better indicators than time for the purpose of gauging the polishing progress. In contrast with a typical automatic polisher, the use of the MiniMet® 1000 requires a hole drilled perpendicular to the upper side of the puck to hold the sample in place and to avoid uneven polishing. We have found that the use of a single type of cloth, *e.g.* synthetic nap cloth (Final finish cloth; Precision Surface International Inc., Houston, TX, USA), is capable of producing satisfactory results for the different polishing steps. However, changes in cloth every 15

Table 3.2 Sample polishing procedure for fiber orientation studies in thermoplastic composites using a MiniMet® 1000 grinder-polisher.

Alumina particle size (μm)	Speed (rpm)	Vertical force (N)	Time (min)	Typical fiber border at the end of polishing step
5	40 - 50	22.2	60	Repeat step if there are holes near or inside fiber: 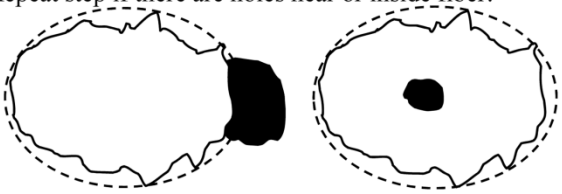 Acceptable: Irregularities at the edge of footprints allow ≈ 90% final footprint dimensions to be seen. 
1	40 - 50	22.2	30	Repeat step if the irregularities at the edge of the footprints are similar to previous step: Acceptable: Irregularities at the edge of footprints allow > 95% final footprint dimensions to be seen. 
0.05	40 - 50	22.2	30	Acceptable: No irregularities at the edge of footprints 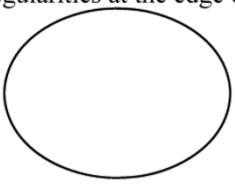

to 30 min are necessary because of the moderate pressure levels dictated by the vertical force indicated in Table 3.2. To prevent excessive dryness in the polish cloth, three drops of the polishing suspension must be added every 10 min. Removal of debris from the polishing step by putting the sample in an ultrasonic bath for 30 sec keeps undesired artifacts from the polished surface. We have observed that sample polishing performance depends more significantly on the local fiber concentration than on other factors inherent to the composites. For example, a good polishing quality of a region having a large concentration of fibers is achieved much later than in regions of moderate concentration. Regions having large numbers of fibers require careful visual inspection and may require some modifications to the polishing procedure indicated in Table 3.2.

3.3.6 Plasma etching and gold sputtering

When optical microscopy is used to image the sample, the etching of the polished surface with oxygen plasma is necessary to provide contrast enhancement between the fiber and polymer matrix. The contrast between the glass fibers and the polymer matrix in the polished surface is insufficient for producing quality images used to determine accurately the fiber orientation by image analysis. To overcome this limitation, oxygen plasma is used to excavate and to uniformly roughen the polymer matrix, causing the fibers to rise over the matrix producing a clear distinction between the fibers and polymer [3, 8]. However, determining the etching time is important for reaching an appropriate depth of surface erosion that allows differentiating the direction of the fibers coming out of the polished plane. The rate of volatilization of the polymer roughening the surface depends on the polymer type and microstructure. Junkar, et al. [13] have found that the etching time increases with crystallinity because the rate of surface erosion is reduced due to the molecular arrangement in this morphological state. A detailed description of the mechanism and volatilization of resin surface due to the interaction of plasma and structural groups of different families of polymers is given by Egitto [14]. As a result of appropriate plasma treatment, the images of the surface allow for fast and reliable recognition of the elliptical footprints during image analysis and for identification of fiber direction.

Optimum etching times for different composites were determined from the analysis of surface erosion as a function of time. This analysis consists of tracking the sharpening of the footprints' edges, the increasing

appearance of light-dark regions, and the lengthening of shadows from samples etched with oxygen plasma in 5 minute increments. Here the optimum etching time is defined as the minimum time required for both contrast enhancement and reliable identification of shadows. In Fig. 3.7, the progression of contrast enhancement and increase in shadow size for SF-PBT at different etching times is shown. Also observed in Fig. 3.7 is that the PBT acquires a mid-tone gray color but not black as suggested in the literature [3]. On the other hand, PA6 is the only material that becomes practically black in about 4 min, but without showing appreciable surface erosion. These observations suggest that contrast enhancement is strongly dependent on the chemical reaction and not on the change in fiber height above the matrix background as suggested in Mlekusch, et al. [3]. Fig. 3.8 shows the impact of the material on the rate of the surface erosion. The difference in height between the polished surface of the glass fiber and the surface of the polymer matrix seen in Fig. 3.8 was estimated from fibers having inclinations between 77 and 82°. Based on visual inspection, the optimum etching time for PBT and PP samples was determined to be 40 minutes while that for PA6 was found to be 60 minutes. The plasma etching was performed using a radio frequency (RF) plasma cleaner (Plasma Prep™ II; SPI Supplies, West Chester, PA). Our results demonstrate that this commonly available instrument is a feasible alternative to the more expensive, direct current (DC) plasma etcher used by Mlekusch, et al. [3] and Clarke and Eberhardt [4]. To obtain a uniform etching, it was observed that only 2 or 3 pucks placed near the open end of the inner chamber of the Plasma Prep II should be used.

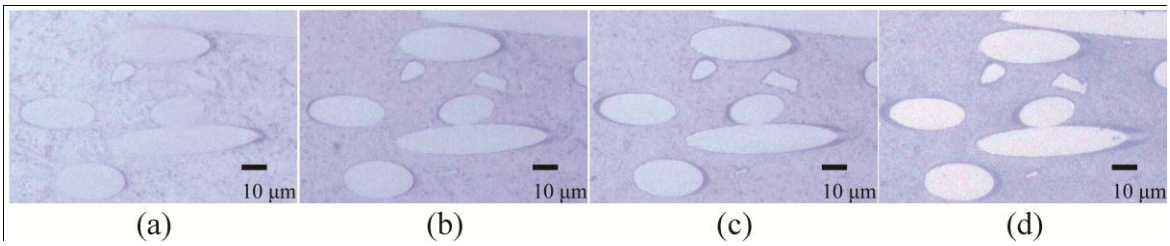

Figure 3.7 Reflective-optical microscope images (objective 20x) showing the growth of shadows for footprints in the polished surface of 30 wt % short fiber-PBT during plasma etching: (a) 0, (b) 20, (c) 40, and (d) 60 min of plasma etching.

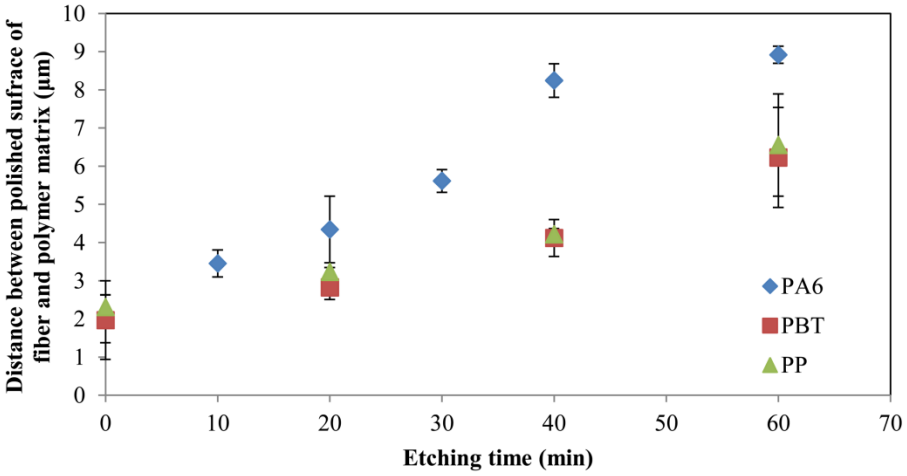

Figure 3.8 Difference in height between the polymer matrix and the polished surface of fiber for three polymer composites as a result of varying exposure time to oxygen plasma. The polymer matrices consisted of polybutylene terephthalate (PBT), nylon 6 (PA6), and polypropylene (PP).

Gold sputtering after plasma etching may be used as a secondary means for contrast enhancement. A 30-sec gold sputtering step has been used as part of the sample preparation following standard polishing procedures. However, our results did not show the need for gold sputtering in any of the composites considered, due to the satisfactory contrast enhancement obtained with the plasma etching.

3.4 Image acquisition

Image acquisition requires setting appropriate magnification and uniform illumination and use of topographical correction to reduce systematic errors in fiber orientation analysis. Clarke and Eberhardt [4] indicate that approximately 20x objective magnification provides sufficient resolution to reduce errors related to the pixilation of the digital image. A higher magnification can be used, but it increases the scanning time for and the noise in the images [5, 15]. Use of uniform illumination avoids changes in appearance across the image. These changes alter the information during the image processing and cause imprecise measurement of orientation [4]. Clarke and Eberhardt [4] indicate that the use of autofocusing algorithms is essential to obtain a sharp contrast for large areas because the flatness of the polished surfaces cannot be guaranteed to be within the depth of field of the microscope objectives. The use of a motorized stage is also important for efficiently

scanning the region of interest in the sample [15]. Precise displacement of the stage is required in order to acquire multiple images with partial overlap. At the end of this step, a single image is reconstructed from multiple high quality images that are stitched together. Advanced microscopes have software that performs the autofocusing and stitching automatically. However, these steps may be done manually by using commercially available software.

Microscopes with advanced features, *e.g.* modules for scanning, stitching of images, and autofocusing correction, are able to produce the single global image automatically. Unlike recommendations provided by Clarke and Eberhardt [4], our results indicate that the topographical corrections given by the autofocusing algorithm are important for obtaining high-quality images even for scans over small regions. The advanced features in the microscope indicated above are suitable for scanning the large areas required for determining orientation in long-fiber composites. If the microscope does not have these advanced features, image acquisition using a semi-manual procedure permits fiber orientation measurement with acceptable precision [2]. An optical-reflection microscope (*e.g.* Axiovert 40 MAT; Carl Zeiss LLC, Thornwood, NY, USA) with a motorized stage allows for precise displacement between image frames. A scan over the region of interest must include images taken with 20x objective magnification, partial overlap, and uniform illumination. Each image has to be taken at different focus levels (depending on the irregularity of the topography) to capture the fiber detail from the matrix to the polished footprint with good resolution and to compensate for any variation in surface flatness. Subsequently, a single in-focus image is created from partially-focused images using Helicon Focus (Helicon Soft Ltd., Kharkov, Ukraine) software. Finally, the multiple in-focus local images are stitched together using Photoshop (Adobe, San Jose, CA, USA) to form a single global image.

3.5 Conclusions

We present a detailed sample preparation and image acquisition procedure for obtaining high-quality images from carefully prepared polished surfaces. The optimal footprint borders and contrast enhancement in those images allow accurate measurement of footprint characteristic values at locations of interest. The excellent definitions of the non-elliptical footprints allow us to include these shapes in the analysis of orientation, which reduces the sampling region. In addition, the described procedure of controlled etching

enables the identification of small shadows where fiber recedes into the matrix. This allows eliminating the ambiguity in the value of the in-plane angle of orientation. Subsequently, these values are used to compute reliable three-dimensional fiber orientation. This paper provides detailed yet simple guidelines specifically developed for the complete sample preparation procedure including cutting, marking, mounting, grinding, polishing, etching, and sputtering, as well as image acquisition used in the analysis of orientation for fiber composites. These guidelines take into consideration efficiency and time and cost reduction in every step. We indicated a number of aspects of sample preparation, not yet described in the literature, which should prove useful in further studies of fiber composites. The sample marking based on 3D markers presented here provides a simple but effective alternative for identifying specific regions of interest in the samples. Also, we demonstrated that compression mounting can be used to embed samples of thermoplastic composites as a less expensive and expedient alternative to cold mounting. The procedure outlined in this paper should be applicable to other composites, as well as to other means of image acquisition such as scanning electron or confocal laser scanning microscopy.

3.6 Acknowledgements

The financial support from the National Science Foundation through grant numbers DMI-052918 and CMMI-085353 are gratefully appreciated The research was also partially sponsored by the US Department of Energy, Assistant Secretary for Energy Efficiency and Renewable Energy, Office of Vehicle Technologies, as part of the Lightweight Materials Program. The authors also wish to thank SABIC Americas, Inc. for supplying the Valox 420, LNP Verton MV006S, and LNP Verton PX00700, and RTP Company for supplying the RTP-105 used in this work. They also gratefully thank the Department of Materials Science and Engineering (Dr. Carlos Suchicital, facilities manager) for allowing us to use the facilities for sample preparation. Gregorio M. Vélez-García also acknowledges support from NSF-IGERT: DGE-0548783 and the University of Puerto Rico-Mayagüez. We wish to thank Dr. Garth L. Wilkes, Dr. Alex Aning and John Hofmann for the helpful comments.

Chapter 3

3.7 Nomenclature

Latin letters symbols

Symbol	Definition
$\boldsymbol{x}$	Spatial coordinates

Greek letter symbols

Symbol	Definition
θ_f	Out-of-plane angle of a cross-section in the polished plane
ϕ_f	In-plane angle of a cross-section in the polished plane

Acronyms

Acronym	Definition
ASTM	American Society for Testing and Materials
DC	Direct current
MoE	Method of ellipses
LF	Long fiber
PA	Polyamide 6 (Nylon 6)
PBT	Polybutylene Terephtalate
PET	Polyethylene Terephthalate
PP	polypropylene
RF	Radio frecuency
SF	Short fiber

3.8 References

[1] Zhu YT, Blumenthal WR, Lowe TC. Determination of non-symmetric 3-D fiber-orientation distribution and average fiber length in short-fiber composites. J Compos Mater. 1997;31:1287-1301.

[2] Vélez-García GM, Wapperom P, Baird DG, Anning AO, Kunc V. Unambiguous orientation in short fiber composites over small sampling area in a center-gated disk. Compos Part A-Appl. 2012;43:104-113.

[3] Mlekusch B, Lehner E, Geymayer W. Fibre orientation in short-fibre-reinforced thermoplastics - I. Contrast enhancement for image analysis. Compos Sci Technol. 1999;59:543-545.

[4] Clarke AR, Eberhardt CN. Microscopy techniques for materials science. Boca Raton, FL, USA: CRC; 2002.

[5] Bay RS, Tucker CL. Stereological measurement and error estimates for three-dimensional fiber orientation. Polym Eng Sci. 1992;32:240-253.

[6] Bay RS, Tucker CL. Fiber orientation in simple injection moldings. 2. Experimental results. Polym Composite. 1992;13:332-341.

[7] Lee KS, Lee S, Chung K, Kang T, Youn J. Measurement and numerical simulation of three-dimensional fiber orientation states in injection-molded short-fiber-reinforced plastics. J Appl Polym Sci. 2003;88:500–509.

[8] Hine PJ, Duckett R. Fiber orientation structures and mechanical properties of injection molded short glass fiber reinforced ribbed plates. Polym Composite. 2004;25:237-254.

[9] Sawyer LC, Grubb DT, Meyers GF. Polymer Microscopy. 3rd ed. New York: Springer Science+Business Media, LLC; 2008.

[10] Hayes BS, Gammon LM. Optical microscopy of fiber-reinforced composites. Materials Park, OH, USA: ASM International; 2010.

[11] Bates PJ, Wang CY. The effect of sample preparation on the mechanical properties of nylon 66. Polym Eng Sci. 2003;43:759-773.

[12] LECO Corporation. Metallography principles and procedures. Form No: 200-860. St. Joseph, MI, USA: Leco Corporation; 2001.

[13] Junkar I, Cvelbar U, Vesel A, Hauptman N, Mozetic M. The role of crystallinity on polymer interaction with oxygen plasma. Plasma Process Polym. 2009;6:667-675.

[14] Egitto FD. Plasma etching and modification of organic polymers. Pure & Appl Chem. 1990;62:1699-1708.

[15] Davidson NC, Clarke A, Archenhold G. Large-area, high-resolution image analysis of composite materials. Meeting of Microscopy of Composite Materials III. Oxford, England1996. p. 233-242.

Chapter 4 Unambiguous orientation in short fiber composites over small sampling area in a center-gated disk

G.M. Vélez-García, Macromolecules and Interfaces Institute, Virginia Tech, Blacksburg, VA 24061, USA

P. Wapperom, Department of Mathematics, Virginia Tech, Blacksburg, VA 24061-0123, USA

D. Baird, Department of Chemical Engineering, Virginia Tech, Blacksburg, VA 24061, USA

A.O. Aning, Department of Material Science and Engineering, Virginia Tech, Blacksburg, VA 24061, USA

V. Kunc, Oak Ridge National Laboratory, P.O. Box 2009, Oak Ridge, TN 37831, USA

Use with permission of Elsevier: Vélez-García GM, Wapperom P, Baird DG, Anning AO, Kunc V. "Unambiguous orientation in short fiber composites over small sampling area in a center-gated disk". Compos Part A-Appl. 2012; 43: 104-13

4.1 Abstract

A modified version of the method of ellipses was successfully developed, validated, and implemented to characterize short fiber orientation. Unambiguous orientation and a small sampling area were obtained by distinguishing between in-plane angles of ϕ and $\phi+\pi$ for every fiber and characterizing non-elliptical footprints, respectively. Measurements in two thin center-gated disks showed the existence of an asymmetric profile of orientation at the gate, which differs from the 3D random orientation commonly assumed in simulations. This profile washed out gradually at the entry region until disappearing at about 40% of flow length. A detailed set of orientation data for comparing fiber orientation to calculated values was obtained.

4.2 Introduction

Short fiber reinforced composites have generated commercial interest in the manufacturing of lightweight parts used in semi-structural applications. The improvement in mechanical properties is obtained when, in an average sense, the fibers are oriented parallel to the direction of mechanical demand. However, obtaining the desired orientation is a challenging task due to the impact of flow on fiber orientation during the forming stage, referred to as flow-induced orientation. A common engineering strategy, used in industrial applications to manage the flow-induced orientation effects, has been to control the final microstructure based on a trial-and-error of the processing conditions. On the other hand, a scientific approach based on a computer

simulation can be used to understand the effect of some critical process variables on the predicted final microstructure. However, regardless of the approach used to control the process, a reliable and cost-effective experimental method to quantify the final three-dimensional (3D) orientation state in the parts to either assess the procedure or validate simulation results, is not available.

Optical [1-3], acoustic [4], irradiation [5-8], and electromagnetic [9-11] methods have been used to evaluate fiber orientation. Acoustic methods and some irradiation methods are non-destructive techniques able to give a complete 3D representation of the orientation. However, these methods require extremely expensive equipment, which has limited their applications in detailed and complete studies [12]. On the contrary, electromagnetic and optical methods use two-dimensional (2D) data and stereological principles to obtain an incomplete 3D description of orientation within the part. This incompleteness in orientation can be attributed to the geometrical limitations inherent to the 2D method used to quantify the orientation, known as the method of ellipses [13]. There are two problems, commonly indicated in the literature, intrinsic to this method. First, one of the angles used to describe the fiber orientation cannot be determined unambiguously [13], while second, the method does not account for non-elliptical objects [14]. In spite of these limitations, the simplicity and reduced cost has made it the preferred method to evaluate fiber orientation.

Several test geometries for which the flow information is well understood have been used to elucidate the short fiber orientation in composites [15]. The center-gated disk is one of these geometries but there is only a limited number of experimental fiber orientation studies [16, 17]. This geometry has industrial relevance because the radially divergent flow pattern seen in center-gated disks also occurs commonly near the entry region in complex industrial molds [18]. A qualitative understanding about the pattern of fiber orientation and its distinctive layering structure across the thickness has been established from irradiation studies [19]. However, the quantitative description about the thickness, evolution, and conformation of the layering structure in center-gated disks is limited. Bay and Tucker [17] quantified the cavity-wise fiber orientation at several radial locations in a center-gated disk. They used the method of ellipses to obtain the orientation of 40 wt% short-glass fiber reinforced Nylon in a center-gated disk of 3 mm thickness. Nevertheless, measurements at key

locations that affect the orientation state such as the gate and frontal regions, was not performed. Capturing the 3D nature and fast changes in orientation over these areas is still challenging from an experimental point of view.

Obtaining the complete orientation information along the whole domain of a center-gated disk can help to improve the simulation models used to design parts and process manufacturing. The assessment of orientation at the gate will provide inlet orientation data rather than making the assumption of random inlet orientation typically done in existing simulations. The evaluation of orientation at various radial locations will provide data to validate simulation results and to optimize simulation tools capable to design better molding machinery, mold and process conditions.

The objective of this paper is to develop a simple and unambiguous method to obtain the 3D fiber orientation in a small sampling region. The novelty of the proposed method is the reduction in sampling area based on the evaluation of elliptical and non-elliptical footprints. This approach is desirable in regions having fast evolution of orientation or areas having a high number of incomplete footprints. The elimination of the ambiguity problem in order to obtain a 3D description of the orientation state is addressed by introducing simple and inexpensive modifications to the method of ellipses. Subsequently this procedure is used to determine experimentally the inlet fiber orientation at the mold entry of a thin center-gated disk and to obtain a complete set of data for assessing fiber orientation over a range of radial positions.

4.3 Determination of orientation in short fiber in composites using the method of ellipses

4.3.1 Characterization

The method of ellipses (MoE) is the most commonly used technique to evaluate the orientation in short fiber composites because of its simplicity and reliability [13]. The method has been commercialized and is referenced to as Leeds Analyzer [13]. In the method of ellipses, elliptical footprints of a fiber in a polished cross section are used to reconstruct the three-dimensional orientation of a fiber. A good quality of these footprints is crucial for fast and reliable measurements, which is determined mainly by the neatness of the metallographic polishing plane [20] and an excellent contrast between fiber and matrix after etching and

sputtering steps [1]. Fig. 4.1 illustrates high quality elliptical footprints in a reflective optical micrograph for a polypropylene composite. In this image, circles represent fibers perpendicular to the plane while ellipses represent fibers at an angle with the plane. Typically, reflective optical microscopes are used to acquire the images, but scanning election microscopes (SEM) also have been used [9, 20, 21].

Five geometrical parameters are measured from each elliptical footprint. Fig. 4.2(a) depicts these parameters: the center of the ellipse (x_c, y_c), the minor (m) and major (M) axes of the ellipse, and the in-plane angle (ϕ_f) between the x_1-axis and M. A second directional angle commonly referred to as the out-of-plane angle (θ_f) is determined from geometrical principles, and is defined by:

$$\theta_f = \cos^{-1}\left(\frac{m}{M}\right) \tag{4.1}$$

Fig. 4.2(b) illustrates ϕ_f and θ_f for a single fiber. The directional angles ϕ_f and θ_f can be used to create a vector of orientation. An orientation unit vector **p** parallel to the axis of the fiber has components:

$$p_1 = \sin\theta_f \cos\phi_f \qquad p_2 = \sin\theta_f \sin\phi_f \qquad p_3 = \cos\theta_f \tag{4.2}$$

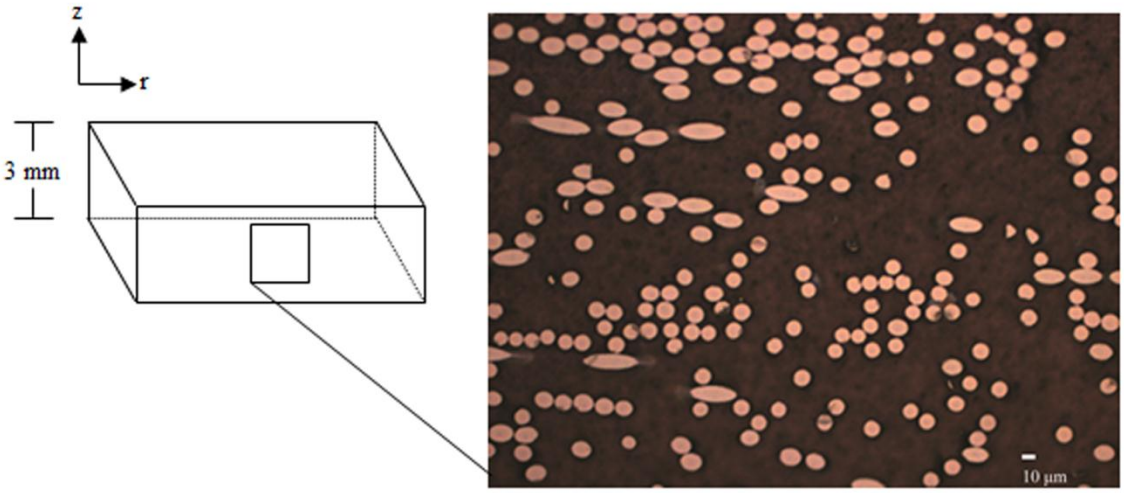

Figure 4.1 Optical microscope image (objective 20x) showing elliptical footprints at the center of a 3 mm thick specimen of polypropylene reinforced with short glass fiber. The sample was prepared at Oak Ridge National Laboratories.

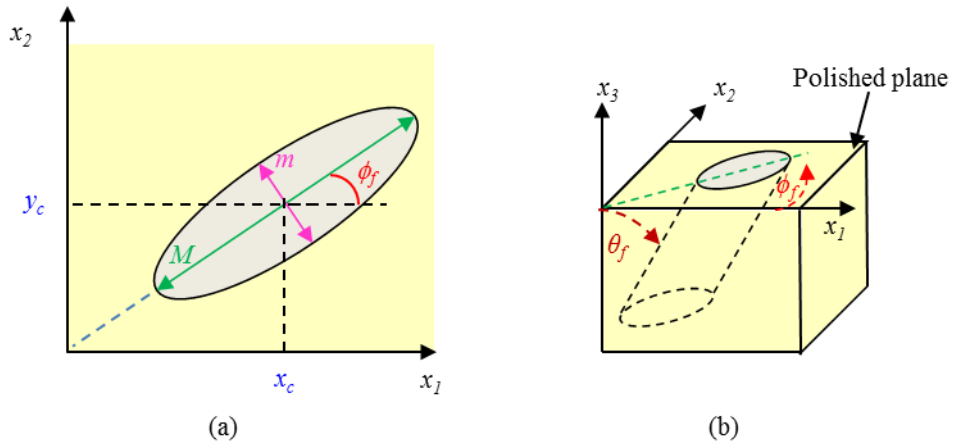

Figure 4.2 (a) Definition of geometrical parameters measured in the method of ellipses: coordinates of the center of the ellipse (x_c, y_c), minor axis (m), major axis (M), and in-plane angle (ϕ_f). (b) Definitions of the in-plane (ϕ_f) and out-of-plane (θ_f) angles used to describe the orientation of a single fiber.

Orientation tensors represent an average orientation for a group of fibers evaluated from the information of individual fibers [22]. For this reason, they are commonly used to describe the local orientation in a molded part. The second order orientation tensor (**A** = <**pp**>) is the most widely used tensor representation in the literature on composites, where $\langle \_ \rangle$ represents the ensemble average. These orientation tensors can be expressed in terms of the directional angles by using Eq. (4.2). Experimentally, the components of the tensor **A** per unit volume of material in the area inspected are obtained using a weighted average [10]:

$$A_{ij} = \frac{\sum_n \left(p_i p_j\right)_n L_n F_n}{\sum_n L_n F_n} \tag{4.3}$$

where *n* denotes the *n-th* fiber with the center of the elliptical footprint in the area inspected, L_n is the length of the fiber, and F_n is the weighting function that relates the orientation per unit area to the orientation per unit volume. F_n is based on purely geometric probabilities and depends on the type of footprint that intersects on the polished plane [10, 23]. The most general weighting function was defined by Konicek [24] as:

$$F_n = \frac{1}{L_n \cos\left(\theta_f\right)_n + d_n \sin\left(\theta_f\right)_n} \tag{4.4}$$

where d_n is the diameter of the *n-th* fiber. The Konicek weighting function is suitable in analyses considering complete and partial ellipses of any size. Bay and Tucker [10] defined an alternative model that can be used when complete and partial ellipses greater than half ellipse are considered in the analysis of orientation. The Bay weighting function neglects the term $d_n \sin\left(\theta_f\right)_n$ in Eq. (4.4) and becomes singular before the out-of plane angle reaches π/2. To avoid this limitation, F_n is modified above a certain cutoff angle (θ_c) to:

$$F_n = \frac{1}{d_n} \qquad \theta_c > \cos^{-1}\left(d/L\right) \tag{4.5}$$

where *d* and *L* are the average diameter and average length of the fibers, respectively. The weighting functions commonly used in the literature are the Bay and the Konicek weighting functions, with L_n replaced by *L* [11, 17, 20, 25]. The Bay weighting function is the default option used in the Leeds Analyzer [26].

4.3.2 Limitations

Several experimental and geometrical limitations related to the method of ellipses can cause inaccurate measurements and interpretations about the orientation in short fiber composites. Some of these limitations are: the bias in the selection of footprints in the polished plane, the ambiguity problem [13], and small angle problem [13]. In the following paragraphs we define those limitations and explain their significance.

To capture a rapid evolution in fiber orientation, *i.e.* near the entry and frontal regions, it is important to obtain a reliable orientation in a minimum sampling area. In the current method, numerous footprints are acquired from a large sampling area and several filters are used to discard non-elliptical footprints. Therefore, a large sampling area becomes essential to obtain a sufficient number of elliptical footprints. However, the non-elliptical footprints contain valuable information capable to reduce the need for a large sampling area. Non-elliptical footprints can be classified as rectangular or partially elliptical cross-sections [10, 14, 27]. Rectangular footprints are cross sections of fibers parallel to the polished plane while partially elliptical footprints are cross-sections through fiber ends [28] or broken fragments due to attrition during processing [29].

Every detected ellipse can represent a fiber inclined in two possible directions causing the ambiguity problem [10], which is a main concern in using the method of ellipses [13]. Fig. 4.3 depicts the problem of ambiguity. The two fibers with orientations ϕ_f and $\phi_f + \pi$ have identical cross sections in the x_1-x_2 plane. The ambiguous angle causes uncertainty in the off-diagonal components containing the neutral direction, *i.e.* A_{13} and A_{23}. However, the major orientation components A_{11}, A_{22}, A_{33} and the off-diagonal component explicitly measured in the x_1-x_2 plane, A_{12}, are the same for values of ϕ_f and $\phi_f + \pi$.

Large measurement errors have been found for fibers crossing the polished plane nearly perpendicularly. At small out-of-plane angles, the difference in dimensions of *m* and *M* can be of the same order as the experimental error, causing some inaccuracy in the estimation of θ_f for a single fiber [13, 30]. For cylindrical fibers, the lower limit of resolution of θ_f, *i.e.* $\theta_{\min}$, can be determined from the following geometrical relation $\theta_{\min} = \cos^{-1}(1-e)$, where *e* denotes the degree of ellipticity of the fiber. O'Connell and Duckett [31], experimentally measured the ellipticity of carbon fibers and found an angular resolution of approximately 8°.

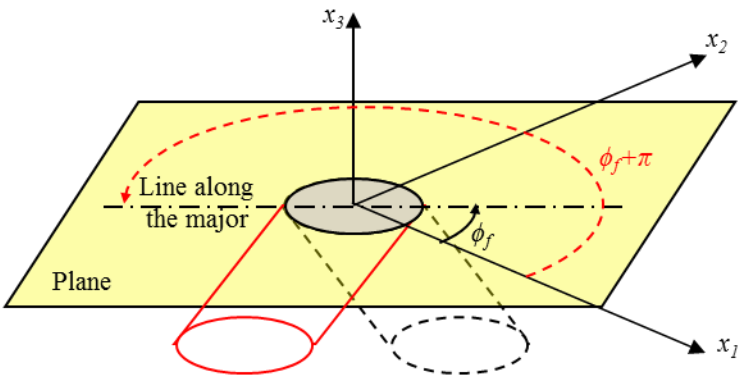

Figure 4.3 Ambiguity in fiber orientation. A fiber with in-plane angle ϕ_f (solid lines) has identical elliptical footprint in the x_1, x_2 - plane and out-of-plane angle as a fiber with in-plane angle $\phi_f + \pi$ (dashed lines).

4.4 Experimental

4.4.1 Materials and sample preparation

Resin data: For this work a commercially available 30wt% (volume fraction $\phi_v = 0.1766$) short glass fiber filled polybutylene terephthalate (Valox 420, Sabic, Co.) was used. Over a wide range of shear rates the PBT matrix behaves like a Newtonian fluid with viscosity $\eta = 350$ Pa·s [32]. From a burn-off process, the number average fiber length of fibers for 949 fibers was found to be L = 362.8 ± 5.4 μm. The average measured diameter for 1000 fibers was determined as 12.9 ± 0.05 μm.

Sample preparation: Samples were obtained along a line of constant θ in a 90% incomplete molded center-gated disk. Four sampling regions were considered in this study: gate, 10%, 40%, and 90% of the flow length (R). Each sample was cut, mounted, and metallographically polished following standard procedures [13]. Subsequently, each sample was plasma etched and gold sputtered.

4.4.2 Image acquisition

Each sampling region was captured from a single column of four images having a partial overlap. These images were taken at 20× objective magnification using an inverted optical-reflection microscope with a motorized stage. Each micrograph has a dimension of 700 × 525 μm (2310 × 1731 pixels) and contains a variable amount of fiber, depending on the region inspected. The roughness of the surface due to matrix excavation caused by the plasma etching [1] required several pictures (depending on the irregularity of the surface) at different focus levels to capture the details of the fibers from the matrix to the polished footprint. A single in-focus image was created from partially focused images, followed the improvement of brightness, contrast, and level of colors. Finally, the four in-focus local images were stitched to form a single global image.

4.4.3 Image processing and analysis

The image processing and image analysis were done by using an in-house program developed with Matlab® and the image processing toolbox (IPT). A detection scheme based on a manual or semi-manual selection was implemented to measure elliptical and non-elliptical footprints. The algorithm implemented

consisted of the following general steps: selection, classification and characterization of footprints, correction of in-plane angles, and computation of average fiber orientation.

4.4.3.1 Selection, classification and characterization of footprints

The acquisition of the maximum number of footprints in a small sampling area involved the development of a semiautomatic selection algorithm combined with a manual classification procedure. A large number of footprints were automatically selected from the single-column color image by using algorithms for binarization, thresholding, and image-acquisition, built-in in the IPT subroutines from Matlab. This automatic selection algorithm used many steps indicated in [2]. The main differences between our method and standard methods are: the absence of automatic filters, color of the microscopic image, and a sampling region of a single column [17, 33]. The parameters of interest were verified and adjusted for the automatically selected footprints and were obtained manually for the manually selected footprints, by using interactive tools. A complete description can be found in [34].

4.4.3.2 Shadow detection

The tips of the fibers underneath the polished plane of a footprint are exposed by the plasma etching treatment. This results in a dark region next to the major axis of footprints for inclined fibers in the optical reflection micrograph as shown in Fig. 4.4(a) and can be used to correct the in-plane angle. The correct sign of the in-plane angle was determined from the position of the dark region. An efficient visualization of the dark region depends on the controlled excavation of polymer matrix during the etching step, quality of in-focus image, and inclination of the fiber. In the proposed method, the term "shadow" is used to describe this dark region to follow the idea introduced by Bay and Tucker [10], and Averous et. al. [9] in scanning electron microscopy (SEM) images. However, the nature of the shadow in SEM is totally different than for the proposed method because it is caused by the backscattered electrons from the polymer matrix between the polished plane and the fiber. In addition, use of SEM involves higher cost than optical microscopy [35].

A correction of the in-plane angle was implemented based on the presence of a shadow and its location for elliptical and partially elliptical footprints. Representative images of elliptical footprints with shadow are

shown in Fig. 4.4(a). The way these shadows are related to a fiber and the correction methodology of the in-plane angle are shown using a perspective and top view in Fig. 4.4(b and c). If the shadow is located at a shift of π with respect to the measured in-plane angle ($\phi_{f,m}$), no correction is required (Fig. 4.4(b)). A correction $\phi_f = \phi_{f,m} + \pi$ is applied when the shadow and the measured in-plane angle are at the same location (Fig. 4.4(c)). This correction is based on the fact that when a shadow is present, it represents a portion of fiber underneath the polished plane. These shadows are seen in the majority of the footprints (2/3 to 3/4 of the total footprints) and in practically all large elliptical and partially elliptical footprints which have a high contribution in the calculation of the volumetric average orientation. The small shadows seen in nearly circular ellipses are sometimes difficult to recognize. However values of $\phi_{f,m}$ or $\phi_{f,m} + \pi$ in these footprints will results in nearly the same **p**-components and have a low contribution in the calculation of volumetric average of orientation. Therefore, the impact of the shadow correction in the volumetric average of orientation of the nearly circular ellipses is typically small. The in-plane angle was not corrected for the following cases: rectangles, footprints

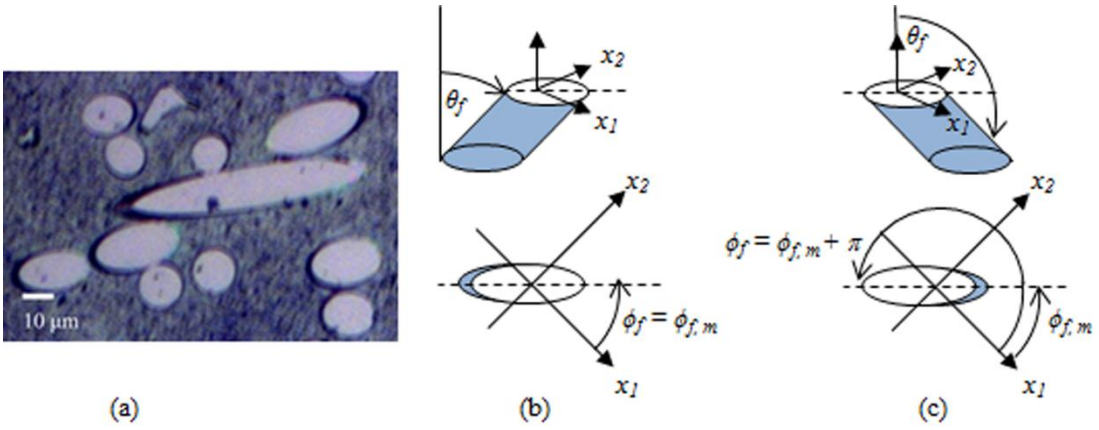

Figure 4.4 (a) Optical micrograph showing a shadow at one of the ends of the major axis for elliptical objects. Correction of in-plane angle for fiber inclined toward (b) left and (c) right hand side. The correct in-plane (ϕ_f) angle for each case is displayed in a projection in the x_1,x_2 - plane.

without a shadow, footprints showing a very small shadow, or in footprints showing two sha--dows or a dark halo that may be observed for by non-perfectly cylindrical fibers.

4.4.3.3 Volumetric average orientation tensor

Every stitched image for a center-gated disk was divided in rectangular bins of dimension *H*/6 in the *z*-direction and *H* in the *r*-direction. Then, the orientation tensor **A** was computed using a weighted average of orientations of all individual particles within each bin. The number of detected objects within each bin depends on the radial and cavity-wise location. The unbiased weighted-average second-rank orientation tensor is computed by:

$$A_{ij} = \frac{\sum_n \left(p_i p_j\right)_n G_n LF_n}{\sum_n G_n LF_n} \tag{4.6}$$

where G_n denotes the fractional area of the n^{th} footprint in the bin. Eq. (4.6) reduces to Eq. (4.3) if all objects are completely inside the bin (G_n =1). Fractional values of G_n were specified for footprints that were only partially in the bin. The fraction was determined based on the pixel-ratio of area inside of the bin of interest and area of the complete cross-section of the object. The weighting function F_n defined by Eq. (4.4) was used for all objects. The weighted average orientation was computed using $\left\langle A_{ij} \right\rangle = \sum_{k=1}^{N_{disk}} N_{v,k} A_{ij,k} \Big/ \sum_{k=1}^{N_{disk}} N_{v,k}$ with the weighting factor defined as the number of fibers per unit volume, $N_v = (\Sigma G_n F_n)/A_s$, where A_s denotes the sampling area. The averaging of orientation from identical and independent disks represents a unique contribution, since previous studies used only a single disk [17, 36].

The error analysis for orientation was computed within every single bin and between bins from the two disks. For every bin, the single-bin-sampling error and the single-bin-measurement error were evaluated using the procedures outlined in [10] and [30], respectively. As part of these analyses, the standard error was computed based on the total number of fibers in every bin, $N_{fib} = \Sigma G_n$. Additionally, the multiple disk sampling error was computed between bins from two disks based on the indications in [10]. For every bin, the variance for independent samples was defined as $V\left(\left\langle A_{ij} \right\rangle\right) = \left(\sum_{k=1}^{N_{disk}} {N_{v,k}}^2 \Big/ Q^2 \right) \sum_{k=1}^{N_{disk}} N_{v,k} \left(A_{ij,k} - \left\langle A_{ij} \right\rangle \right)^2 \Big/ Q$ where $Q = \sum_{k=1}^{N_{disk}} N_{v,k}$.

4.5 Results and discussion

The capability to obtain the correct data of orientation and evaluation of measurement error was first evaluated for the proposed method, referred to as VWB. The tensor orientation **A** was then computed from the footprint's data using VWB approach and two standard approaches described by Bay and Tucker [10] and the Leeds analyzer [13] referred to as LA. In these standard approaches, the in-plane angle is ambiguous. The contrasts of A_{rr} and $A_{r\theta}$ computed from different approaches were used to validate the assumptions and to compare the approaches. The analysis for the LA approach includes only elliptical footprints. For the Bay and Tucker (BT) approach, the contribution of partially elliptical footprints with area greater-than-half-ellipse and rectangles were considered in the analysis. In the last section, the VWB approach was used to characterize the fiber orientation at four radial locations in a center-gated disk: 0.5%, 10%, 40%, and 90% of flow length, related respectively to the gate, entry, lubrication, and frontal regions.

4.5.1 Error analysis and assessment of orientation in test samples

The systematic error related to the measurement technique was evaluated by assessing the ability of the image processing and analysis program to measure ϕ_f and θ_f for elliptical footprints and to compute **A** correctly from a test sample. An image containing a test distribution of 20 ellipses consisting of two objects having ϕ_f = -10° and θ_f = 1, 5, 10, 15, 20, 25, 30, 40, 60, and 75°, was created using Matlab. Based on this test distribution and the Konicek weighting function, the components of **A** are:

$$\boldsymbol{A} = \begin{bmatrix} 0.42 & 0.25 & -0.07 \\ 0.25 & 0.57 & -0.04 \\ -0.07 & -0.04 & 0.01 \end{bmatrix} \tag{4.7}$$

Only measured values of orientation of A_{11} = 0.41 and A_{22} = 0.58 were slightly different while the other components were identical demonstrating the ability of the image analysis tool to obtain the correct orientation for elliptical objects.

Small θ angles cannot be measured accurately [10, 13]. The smallest θ angles that could be measured had values of θ_{min} = 5 and 18° for analyses based on the pixel dimensions and on the fiber diameter, respectively. For frequency distributions, containing peaks above θ_{min} = 18°, as found in our experiments, no

significant differences in orientation were found due to the small number of fibers with angles below θ_{min}. The large number of inter-particle interactions related to the high concentration of fibers in the suspension is the most likely cause in preventing that a large number of fibers had small θ values.

The precision of measured ϕ_f and θ_f for every elliptical footprint was evaluated using an approach described in the literature [10, 30, 35]. The analytical functions used to obtain the measurement error for each elliptical and partially elliptical footprint were determined and used in the calculation of the measurement error of **A** following the procedure outlined in [30]. For all radial, cavity-wise positions and approaches considered in this study, most standard errors for measurements of **A** were below 0.01 and a maximum value of 0.02 was observed.

Obtaining a consistent evaluation of orientation as we reduce the sampling width is critical to measure orientation in regions where the fiber orientation changes rapidly. The orientation represented by the A_{rr} component approaches for the distribution of fibers considering different non-dimensional sampling widths, *i.e.* 1, 0.75, 0.675, 0.50, 0.375, and 0.25, and representative drawings are shown in Table 3.1. For all sampling widths considered, the A_{rr} values obtained based on the VWB approach showed to remain closer to the original value, indicating the consistency of the method. The results based on the BT approach were as good as the ones from VWB when sampling widths were above or equal to 0.5. However, below this sampling width, the BT approach under predicts the orientation due to the presence of large ellipses having areas less-than-half-ellipse. As expected, the A_{rr} values obtained by the LA approach deviates as smaller area is considered due to the inability of the method to handle partial ellipses.

4.5.2 Mutually perpendicular planes to assess fiber orientation per unit volume

Data collected on mutually perpendicular planes were used to check the consistency of the orientation data, validate the chosen volumetric weighting function, and perform a dispersion analysis. The mutually perpendicular planes used in the analysis were the *rz*-plane normally used in the analyses and the $\theta_p z$– plane which denotes a tangent plane perpendicular to *r*-direction. The orientation analysis from mutually

Table 4.1 Orientation represented by A_{rr} components evaluated by different approaches from a different sampling width for a random distribution of footprints having different degrees of alignment.

	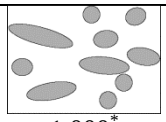 1.000*	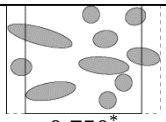 0.750*	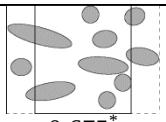 0.675*	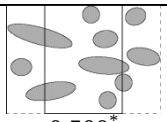 0.500*	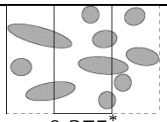 0.375*	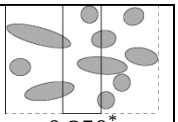 0.250*
LA	0.61	0.57	0.52	0.22	0.00	0.00
BT	0.61	0.62	0.65	0.63	0.52	0.00
VWB	0.60	0.60	0.59	0.60	0.58	0.55

*Non-dimensional sampling width

perpendicular planes was performed at two radial locations with different flow characteristics, the entry and lubrication regions, *i.e.* 2.16% *R* and 50% *R*.

The VWB approach was found to be a consistent method for obtaining orientation independent of the cross section analyzed and to improve orientation results measured in the *rz*-plane near the walls. The following discussion is focused on the orientation near the entry region shown in Figs. 4.5 and 4.6, however similar findings were obtained in the lubrication region. The orientation from VWB and LA approaches are shown in Figs. 4.5(a) and (b), respectively, evaluated on the *rz*- and $\theta_p z$-planes. Similar A_{rr} values are observed

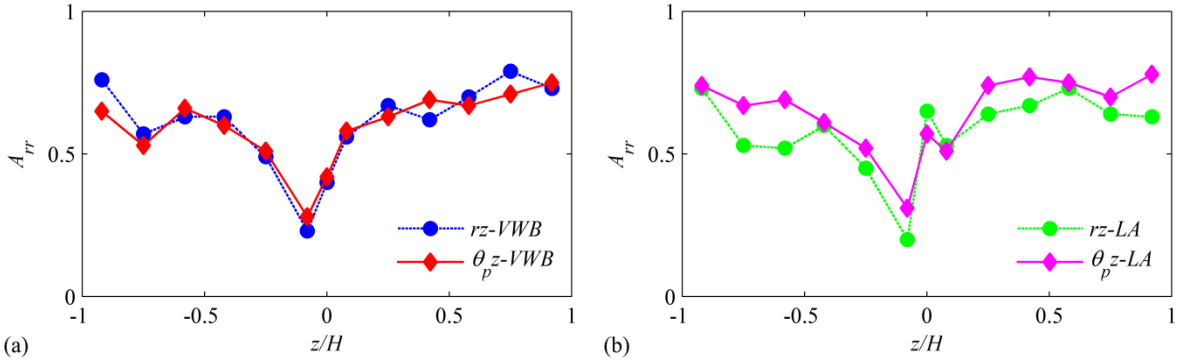

Figure 4.5 Profile of A_{rr} from mutually perpendicular planes in a center-gated disk in the entry region evaluated using (a) VWB and (b) LA. The rz and $\theta_p z$ denote the planes perpendicular to the θ and r direction, respectively.

on the mutually perpendicular planes for both methods. Only local discrepancies were found at few *z/H* positions resulting in an average deviation of 8% and 11% and maximum deviation of 22% and 35% for VWB and LA approaches, respectively. Difficulties of the standard method of ellipses, *i.e.* LA approach, to closely match the orientation from mutually perpendicular planes was also observed by Mlekusch [30], although discrepancies were attributed to experimental variation. Results shown here suggest that ignoring non-elliptical footprints is also a factor.

The importance of the contribution of non-elliptical footprints in correctly assessing the orientation was confirmed by re-plotting the data keeping the plane constant and comparing the approaches. Figs. 4.6(a) and (b) depict the A_{rr} profiles evaluated at the $\theta_p z$- and *rz*-planes, respectively, using both VWB and LA approaches. Both approaches agree very well in regions having many small ellipses and few non-elliptical objects as seen in Fig. 4.6(a) and around the midplane in Fig. 4.6(b). The presence of several large non-elliptical objects explains the differences seen in Fig. 4.6(b), between the VWB and LA approaches for *rz*-plane. In Fig. 4.7 the selection of the footprints used in the approaches (a) LA and (b) VWB is illustrated in a zone near the wall. The large non-elliptical objects that are ignored in the LA approach have a large contribution in the volumetric average, due to their dimensions and inclinations.

For every bin, a fiber dispersion analysis was performed in the *rz*- and $\theta_p z$-planes. The volume fraction of fibers (ϕ_v) was estimated, using $\phi_v := \Sigma N_{v,n} V_{fiber,n}$. This estimation was checked in a test case with 100

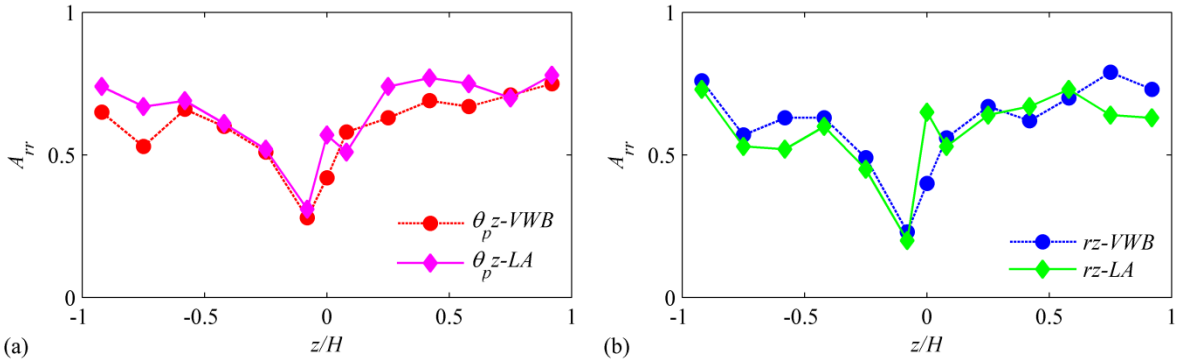

Figure 4.6 Profile of A_{rr} from mutually perpendicular planes: (a) $\theta_p z$-plane, and (b) rz-plane. The orientation was evaluated in the entry region of a center-gated disk using the VWB and LA approaches.

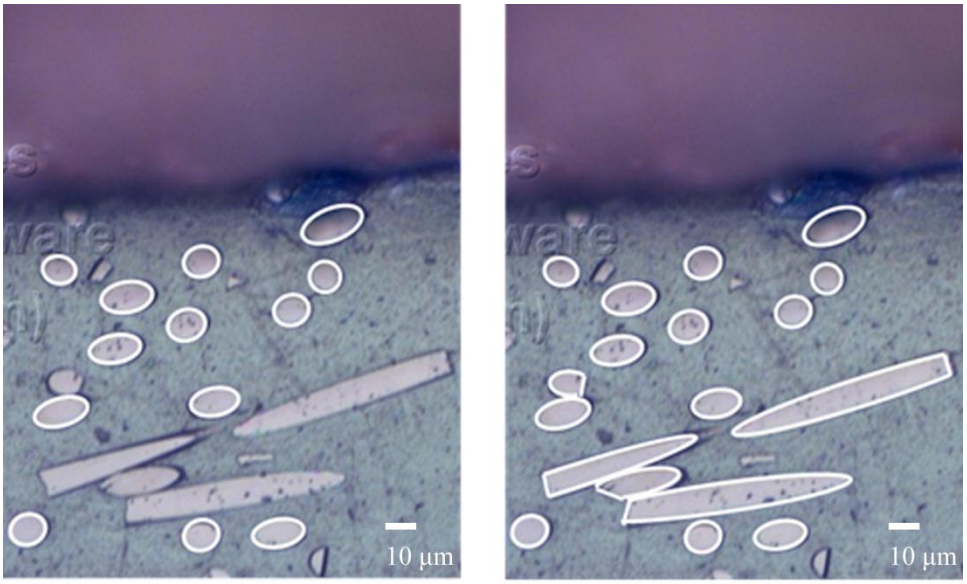

Figure 4.7 Non-elliptical objects close to the walls of a center-gated disk that are (a) ignored in the LA approach and (b) selected in the VWB approach. The shadow can be easily seen for large elliptical and partially elliptical footprints.

randomly selected cross-section of a fiber with out-of-plane angle θ. For all θ values considered the maximum difference was 0.01 for $\phi_v = 0.17$ and the difference decreased with increasing number of cross-sections. Figs. 4.8(a) and (b) show the distribution of average ϕ_v along the cavity height at the entry and lubrication region, respectively. The cavitywise averaged ϕ_v from the VWB approximately captures the volume fraction estimated from the resin manufacturer's data, $\phi_v = 0.177$. The cavitywise averaged $\phi_v = 0.15$ at the gate is slightly lower, but the $\phi_v = 0.18$ in the lubrication region agrees very well. The cavity-wise averaged ϕ_v for the LA approach, 0.13 at the gate and 0.15 in the lubrication region, is lower than for the VWB approach, since the non-elliptical footprints are ignored. These results show that this method is feasible to evaluate particle dispersion in a simple way. Two noticeable observations from Fig. 4.8 are the increase in volume fraction at the core region as the flow progresses and a constant low concentration of fibers is seen near the walls. This

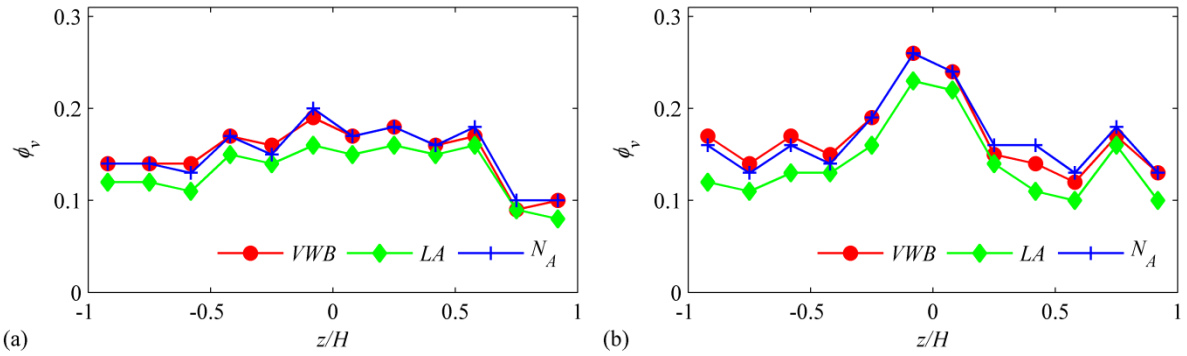

Figure 4.8 Average volume fraction obtained from mutual perpendicular planes at (a) entry and (b) lubrication regions of a center-gated disk. Volume fractions estimated based on all footprints (VWB), complete elliptical footprints (LA) and stereological principles using the fractional area of footprints (N_A) are shown.

quantification of cavity-wise ϕ_v corroborates observations commonly found in the literature [15], where the ϕ_v variations have been attributed to fiber packing and migration. These results are corroborated with volume fraction obtained stereologically using the fractional area of the cross-sections as shown in Fig. 4.8.

4.5.3 Orientation in small sampling area

The minimum sample size giving reliable orientation for the proposed method (VWB) was determined using the A_{rr} profile obtained from the mutually perpendicular planes at the entry region. Since this region has different types and fast changes in orientation, it is a reliable region to evaluate the smallest sample area for the whole disk. The smallest sampling area used in center-gated disks found in the literature was measured on the *rz*-plane at radial locations away from the entry region with a sample height dh = 0.1272 mm and sample width ds = 0.41 mm [17]. Nevertheless, the chosen plane and the sampling dimensions were selected arbitrarily, therefore an appropriate sample size was defined by obtaining A_{rr} from mutually perpendicular plane at the entry region based on a dh = 0.1150 mm and different ds. For orientation from VWB and LA approaches, the smallest sampling widths for $\theta_p z$- and *rz*-plane were found to be 0.30 and 0.69 mm, respectively, using the following analysis. In Fig. 4.9(a), A_{rr} values from the *rz*-plane measured in the gate region are compared using

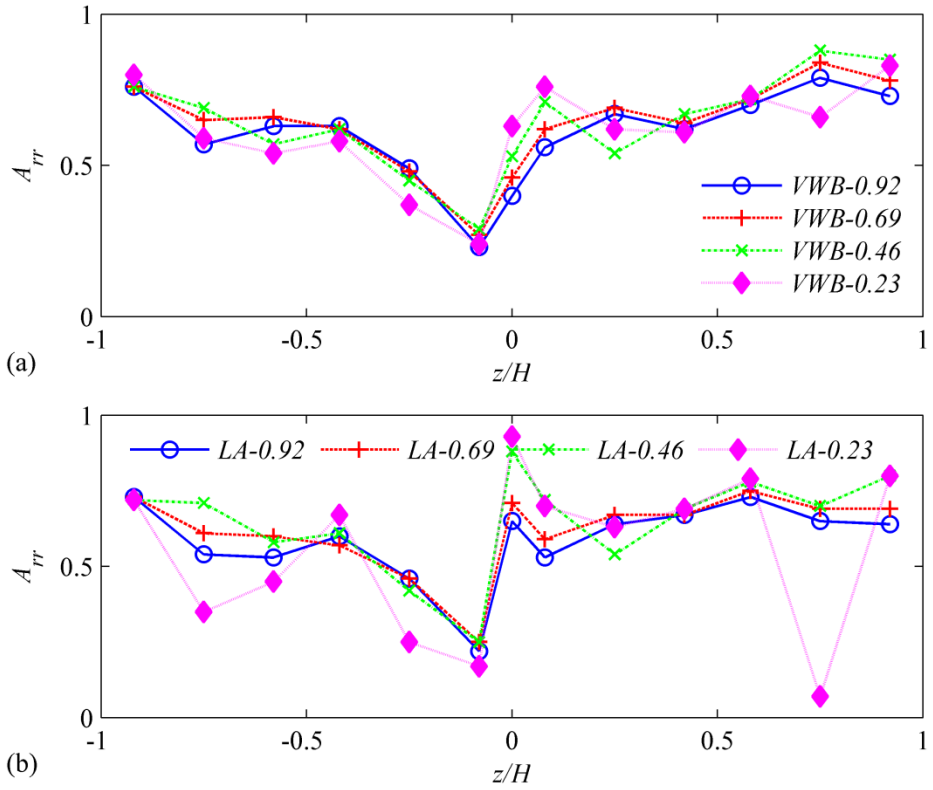

Figure 4.9 Comparison of A_{rr} measured over several sampling widths (ds): 0.23, 0.46, 0.69, and 0.92 mm. Orientation was evaluated at the entry region of a center-gated disk using: (a) VWB and (b) LA.

the VWB approach and various values of *ds*: 0.23, 0.46, 0.69, and 0.92 mm. The A_{rr} values from *ds* = 0.46, 0.69 and 0.92 mm have similar profiles and they practically overlap for many *z*/*H* positions. In particular the A_{rr} values of *ds* = 0.69 and 0.92 mm match closely at nearly all positions. When the LA approach is used, A_{rr} values may be severely underpredicted, when the sampling area contains fractional objects as can be seen in Fig. 4.9(b). In particular, large discrepancies close to the wall are observed for *ds* = 0.23 mm. Henceforth, the orientation analysis is performed on the *rz*-plane with *ds* = 0.69 mm.

For the VWB method, the minimum number of fibers which gives a consistent orientation was determined for the slowly evolving orientation in the lubrication region. For all bins, a consistent orientation was obtained when $\Sigma G_n F_n$ was 100 ± 10 fibers/mm. This quantity has less variation than the number of fibers seen in a cross-section which vary between 14 fibers in regions having large objects and 25 fibers in regions

having mainly circular objects. The $\Sigma G_n F_n \approx 100$ is a quantity that can be extended to other composites and part dimensions.

4.5.4 Elimination of the ambiguity problem

Unambiguous determination of the off-diagonal components containing the neutral direction is important to completely describe the 3D fiber orientation. The correct assessment of all components of **A** has gained relevance because their value is essential to correctly compute the eigenvalues and eigenvectors for inlet orientation used in recent simulation models [37]. When the orientation is evaluated at the *rz*-plane of a center-gated disk, the $A_{r\theta}$ and $A_{\theta z}$ are the ambiguous components. However, since $A_{\theta z} \approx 0$ for a center-gated disk, only $A_{r\theta}$ is discussed. The off-diagonal component $A_{r\theta}$ represents the average tilt of the fibers projected on the $r\theta$-plane. In structural terms, the values of these off-diagonal terms can indicate three possible conditions. Considering the $A_{r\theta}$ component, these possible values of $A_{r\theta} \approx 0$, $A_{r\theta} > 0$, and $A_{r\theta} < 0$ denoting no tilting, tilting in counter-clockwise direction, and tilting in clockwise direction, respectively.

The MoE produces only an upper and lower bound for the values of ambiguous components. Fig. 4.10 shows the unambiguous $A_{r\theta}$ and the bounding limits for the ambiguous $A_{r\theta}$ component obtained with $\phi_f = \phi_{f,m}$ or

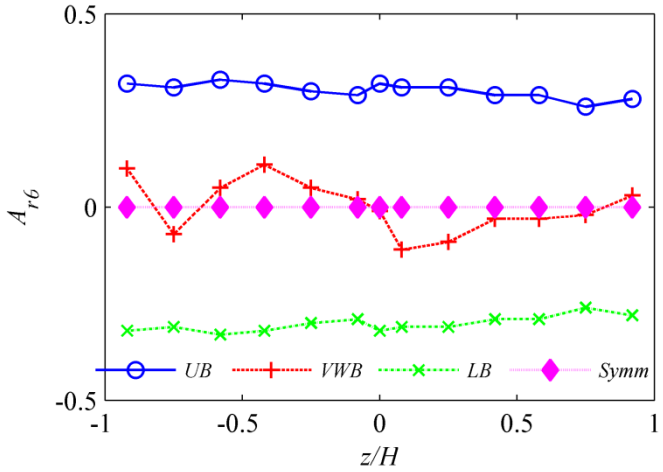

Figure 4.10 Effects of ambiguity in $A_{r\theta}$ evaluated based on the proposed (VWB) approaches at the gate (r = 0% R) of a center-gated disk. Profiles of $A_{r\theta}$ for the upper bound (UB), lower bound (LB), and symmetric conditions are shown.

$\phi_f = \phi_{f,m} + \pi$, at the gate region. It can be noticed from this figure that the unambiguous $A_{r\theta}$ through the cavity thickness which is well within the bounding limits and the profile of $A_{r\theta}$ shows oscillations around $A_{r\theta} = 0$ (symmetry condition [17]). These results suggest that the fibers try to reach an orientation state where they are equally tilted with respect the θz-plane but the inter-particle interaction prevents this. Similar $A_{r\theta}$ profiles were in the $\theta_p z$-plane discussed in Section 3.5.2.

4.5.5 Assessment of orientation in a thin center-gated disk

In the simulation of injection molding it is usually assumed that inlet orientation is random *i.e.* $A_{ii} = 1/3$ and $A_{ij}=0$, and symmetric about $z = 0$. In this section we evaluated whether this assumption is correct. Figs. 4.11(a) and (b) depict profiles for diagonal and off-diagonal orientation components in the gate region, respectively. The standard error from two independent disks is shown in Fig. 4.11. The figure shows two characteristics of the orientation in the gate region: the fast formation of planar structure of orientation *i.e.* $A_{zz} \approx A_{rz} \approx A_{z\theta} \approx 0$, and an asymmetric profile for A_{rr}, $A_{\theta\theta}$, and $A_{r\theta}$. Therefore, the complete information of orientation at the gate can be described by A_{rr} and $A_{r\theta}$, because $A_{\theta\theta} \approx 1 - A_{rr}$. The fast formation of planar orientation at the gate indicates a rapid change of A_{zz} from being dominant in the sprue to nearly 0 at the gate. A planar orientation was consistently found at all radial positions. One important aspect of the

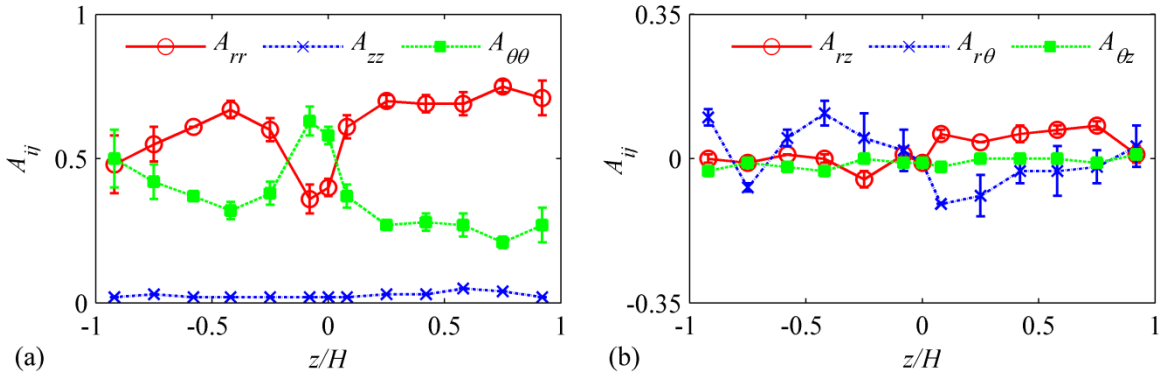

Figure 4.11 Profile of A_{ij} evaluated by proposed approach (VWB) at the gate (r = 0% R) of a center-gated disk: (a) diagonal and (b) off-diagonal orientation tensor components. Error bars denote the multiple-disk-sampling error.

asymmetric profile for A_{rr} seen in Fig. 4.11(a) is that this profile corroborates the asymmetric shape of A_{rr} at the gate predicted from numerical simulation but never validated [38, 39].

Fig. 4.12 illustrates the changes in A_{rr} seen as the flow progressed by measuring orientation along the thickness. The washout in inlet asymmetry between the gate (0.5 %*R*) and 40%*R* and the expansion-contraction-expansion of the core region are the distinctive characteristics of the orientation seen in Fig. 4.12 for the A_{rr} evaluated by the VWB method. On the other hand, the changes in the core can be related to the forces experienced by the suspension as the flow advances. The expansion between the gate and 10% *R* as seen in Fig. 4.12(a) can be related to the strong extensional stretching in the entry region. The influence of shear forces is evident in the lubrication region causing the contraction between 10 %*R* and 40 %*R*. The expansion between 40 %*R* and 90 %*R* can be attributed to flow effects due to the advancing front. The qualitative nature of the profiles of orientation in the lubrication region described above is similar to the Bay and Tucker data [17], which is for a different molding compound. However, our data shows thinner core layers for most radial locations, higher values for the minimum A_{rr} through the cavity thickness, and a steeper orientation profile near the wall.

The relatively small experimental errors observed when two independent samples are compared (Figs. 4.12 a-d) demonstrates that consistent and reproducible measurements of orientation can be obtained from multiple samples. The good reproducibility of results from multiple disks allows us to obtain orientation over smaller sampling areas than found in Section 3.5.3. in regions showing rapid changes without sacrificing theaccuracy of the results. For our experiments, a larger variability in the experimental error was observed at the gate (Fig. 4.12(a)), particularly for the lower half of the cavity. The increased variability can be attributed to the presence of void spaces of different sizes and shapes found in the vicinity of the junction of the sprue and the cavity of the disk.

4.6 Conclusions

The method of ellipses (MoE) is the common approach to obtain fiber orientation in injection molded parts, but, several geometrical limitations restrict the feasibility of obtaining a tridimensional description of

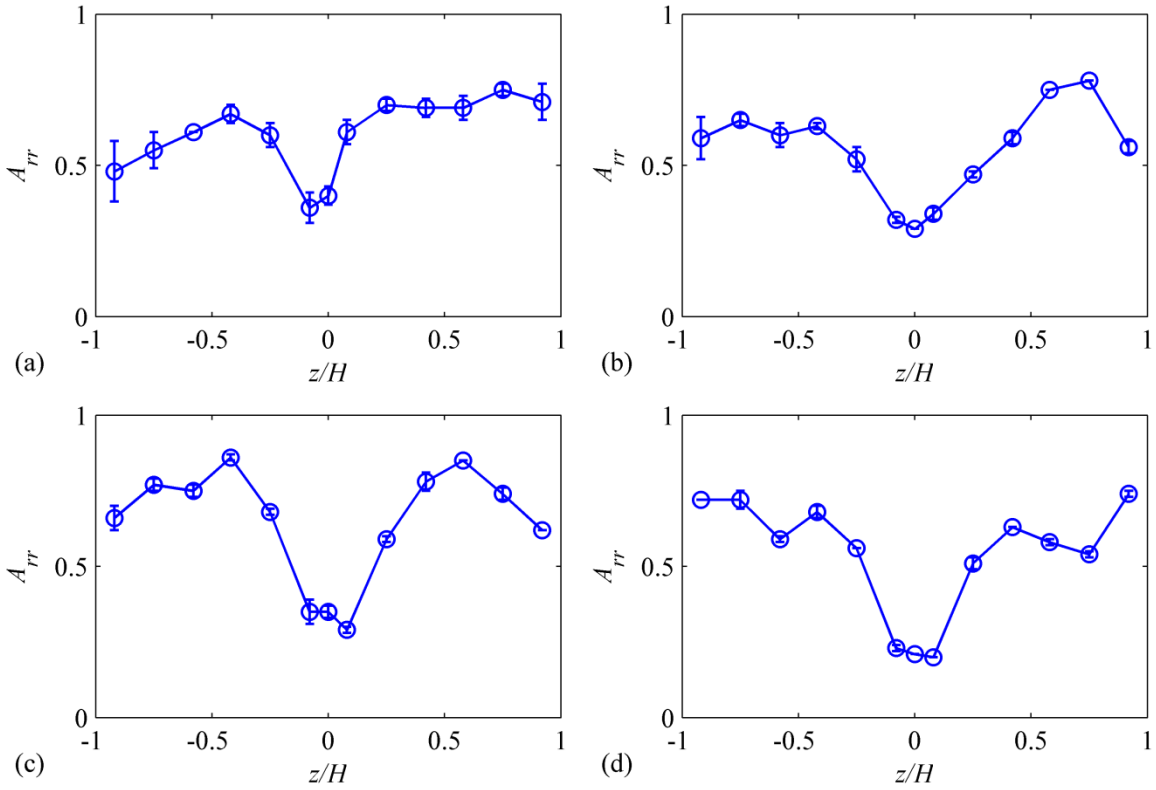

Figure 4.12 A_{rr} obtained from the proposed approach (VWB) at several radial positions in center-gated disk representative of: (a) the gate (0.5 %R), (b) entry region (10 %R), (c) lubrication region (40 %R), and (d) near the advancing front (90 %R). Error bars denote the multiple-disk-sampling error.

orientation. Additionally, minimum sampling dimensions giving a local estimate of orientation has not been reported in the literature. In this work, we were able to obtain an unambiguous orientation evaluated over a small sampling area introducing several modifications in the MoE. The method was validated using orientation results from mutually perpendicular planes and subsequently used to characterize the orientation in a thin center-gated disk. Therefore, we developed a reliable and low cost method capable of capturing the 3-D orientation in molded parts, including regions having fast changes in orientation.

The modifications introduced in the proposed method (VWB) did not show an increase of the systematic error related to the measurement technique and the measurement errors remained small at all regions analyzed in a center-gated disk. Similar orientation from mutually perpendicular planes evidenced that the use

of partially elliptical objects allows us to obtain orientation independent of the direction of analysis and validated the use of the weighting function described by Eq. (4.4) for the VWB method. The VWB method has similar efficiency as the standard method of ellipses in regions highly populated by small ellipses, however the measurements of large non-elliptical footprints using the VWB method improves the assessment of orientation in critical regions such as near the walls. The VWB method provides a simple way to evaluate fiber dispersion. We observed a redistribution of fibers from the walls towards the center of the cavity as the flow progressed. The smallest sampling area giving a reliable orientation near the gate on planes parallel and perpendicular to the flow was found to have a height of 0.11 mm and a width of 0.69 and 0.30 mm, respectively. However, the good reproducibility of orientation in multiple independent disks allows further reduction of the sampling width. This is important to obtain accurate measurement in regions having fast evolution of orientation.

The VWB method was used to obtain the orientation in two thin center-gated disks including the evaluation at the gate, a critical region typically neglected in the literature. Fibers near the gate were found to be planarly oriented and having an asymmetry in A_{rr} trough the cavity thickness. This result contrasts with the assumption of 3-D random orientation typically assumed in numerical simulations. Most of the inlet asymmetry in A_{rr} washed out at radial locations of about 40% of the flow length of the disk (r/H = 32.4). The A_{rr} profiles at radial locations within the lubrication region and near the advancing front region are similar to the ones found in the literature for a thick disk. In addition, changing dimensions of core layer in a thin center-gated disk along the radial direction were more evident than the progressively expanding core seen in the literature. For all radial locations, the elimination of the ambiguity showed that the $A_{r\theta}$ has small values fluctuating around 0 which are different from $A_{r\theta}$ = 0.0 obtained with the standard method of ellipses. The orientation data can be used to better understand the fiber orientation and to improve numerical simulations.

4.7 Acknowledgements

The financial support of NSF/DOE: DMI-052918 is gratefully acknowledged. Research sponsored by the US Department of Energy, Assistant Secretary for Energy Efficiency and Renewable Energy, Office of Vehicle Technologies, as part of the Lightweight Materials Program. The authors also wish to thank Sabic Americas Inc. for supplying the Valox 420 used in this work. They also gratefully thank Dr. Audrey Zink-

Sharp for providing helpful discussions about the image acquisition procedure. Gregorio M. Vélez-García also acknowledges support from NSF-IGERT: DGE-0548783 and University of Puerto Rico-Mayagüez.

4.8 Nomenclature

Latin letters symbols

Symbol	Definition
A_s	Sampling area
$\mathbf{A}$	Second order orientation tensor
$\langle A_{ij} \rangle$	Average of *ij*-component of orientation tensor
d_n	Diameter of the *n-th* fiber
ds	Sampling width
d	Average diameter of the fibers
dh	Sampling height
e	Degree of ellipticity of a fiber
F_n	Weighting function used to determine the volumetric orientation from 2D-data
G_n	Fractional area of the *n-th* footprint in a bin
H	Half gap width
L	Average fiber length
L_n	Length of the *n-th* fiber
m	Minor of an ellipse
M	Major of an ellipse
N_v	Number of fibers per unit volume
N_{fib}	Number of fibers in a rectangular sampling region of $dh \times ds$
N_{disk}	Number of independent disks
$\boldsymbol{p}$	Orientation unit vector parallel to the backbone of the fiber
Q	Total number of fibers per unit volume in a bin
r	Radial direction
R	Flow length of a disk
x_c	Center location in x_1-direction of a fiber cross-section
y_c	Center of mass in x_2-direction of a fiber cross-section
V_{fiber}	Volume of a fiber
$V\left(\langle A_{ij} \rangle\right)$	Variance of the mean for orientation

Chapter 4

Symbol	Definition
$\boldsymbol{x}$	Spatial coordinates
z	Gapwise direction

Greek letter symbols

Symbol	Definition
η	Steady-state shear viscosity
θ	Circumferential direction
θ_f	Out-of-plane angle of cross-sections in the polished plane
θ_c	Cut off angle
$\theta_{\min}$	Lower limit for out-of-plane angle measurements
θ_p	Direction tangent to θ-dir
ϕ_f	In-plane angle of a cross-section in the polished plane
$\phi_{f,\,m}$	In-plane angle measured in a micrograph without shadow correction
ϕ_v	Particle volume fraction

Special character symbols

Symbol	Definition
$\langle\_\rangle$	Ensemble average of the dyadic product of the unit vectors **p** over all possible orientations

Acronyms

Acronym	Definition
BT	Bay and Tucker approach: complete ellipses and incomplete footprints greater than half ellipses
IPT	Image processing toolbox of Matlab©
LA	Leeds Analyzer approach: only complete ellipses
MoE	Method of ellipses
PBT	Polybutylene Terephthalate

Acronym	Definition
SEM	Scanning electron microscopy
VWB	Vélez-Wapperom-Baird approach: complete ellipses and incomplete footprints of any size

4.9 References

[1] Mlekusch B, Lehner E, Geymayer W. Fibre orientation in short-fibre-reinforced thermoplastics - I. Contrast enhancement for image analysis. Compos Sci Technol. 1999;59:543-545.

[2] Hine PJ, Duckett R. Fiber orientation structures and mechanical properties of injection molded short glass fiber reinforced ribbed plates. Polym Composite. 2004;25:237-254.

[3] Silva CA, Viana, JC, van Hattum, FWJ, Cunha, AM. Fiber orientation in injection molding with rotating flow. Polym Eng Sci. 2008;48:395-404.

[4] Kawamura M, Ikeda, S, Morita, S, Sanomura, Y. Unambiguous determination of 3D fiber orientation distribution in thermoplastic composites using SAM image of elliptical mark and interference fringe. J Compos Mater. 2005;39:287-299.

[5] Bright PF, Crowson RJ, Folkes MJ. A study of the effect of injection speed on fiber orientation in simple mouldings of short glass fibre-filled polypropylene. J Mater Sci. 1978;13:2497-2506.

[6] Darlington MW, Smith, GR. Some features of the injection-molding of short fiber reinforced thermoplastics in center sprue-gated cavities. Polym Composite. 1987;8:16-21.

[7] Shen H, Nutt, S, Hull, D. Direct observation and measurement of fiber architecture in short fiber-polymer composite foam through micro-CT imaging. Compos Sci Technol. 2004;64:2113-2120.

[8] Bernasconi A, Cosmi, F, Dreossi, D. Local anisotropy analysis of injection moulded fibre reinforced polymer composites. Compos Sci Technol. 2008;65:1931-1940.

[9] Avérous L, Quantin JC, Lafon D, Crespy A. Determination of 3D fiber orientations in reinforced thermoplastics, using scanning electron microscopy. Acta Stereol. 1995;14:69-74.

[10] Bay RS, Tucker CL. Stereological measurement and error estimates for three-dimensional fiber orientation. Polym Eng Sci. 1992;32:240-253.

Chapter 4

[11] Lee KS, Lee S, Chung K, Kang T, Youn J. Measurement and numerical simulation of three-dimensional fiber orientation states in injection-molded short-fiber-reinforced plastics. J Appl Polym Sci. 2003;88:500–509.

[12] Blanc R, Germain C, Da Costa J, Baylou P, Cataldi M. Fiber orientation measurements in composite materials. Compos Part A-Appl S. 2006;37:197-206.

[13] Clarke AR, Eberhardt CN. Microscopy techniques for materials science. Boca Raton, FL, USA: CRC; 2002.

[14] Zhu YT, Blumenthal WR, Lowe TC. Determination of non-symmetric 3-D fiber-orientation distribution and average fiber length in short-fiber composites. J Compos Mater. 1997;31:1287-1301.

[15] Papathanasiou TD. Flow-induced alignment in injection molding of fiber-reinforced polymer composites. In: Papathanasiou TD, Guell DC, editors. Flow-induced alignment in composite materials. Cambridge, England: Woodhead Publishing Limited; 1997. p. 112-165.

[16] Vincent M, Agassant, J.F. Experimental study and calculations of short glass fiber orientation in center gated molded disks. Polym Composite. 1986;7:76-83.

[17] Bay RS, Tucker CL. Fiber orientation in simple injection moldings. 2. Experimental results. Polym Composite. 1992;13:332-341.

[18] Vincent M, Agassant, JF. Predicting fiber orientation in injection molding. In: Utracki LA, editor. Progress in polymer processing: Two phase polymer systems. Munich: Hanser; 1991. p. 277-303.

[19] Woebcken W. Experience gained during the quality-control and quality assurance testing of plastic products, particularly with respect to deformation of the molding. Kunststoffe. 1981;71:229-233.

[20] Regnier G, Dray D, Jourdain E, Le Roux S, Schmidt FM. A simplified method to determine the 3D orientation of an injection molded fiber-filled polymer. Polym Eng Sci. 2008;48:2159-2168.

[21] Avérous L, Quantin JC, Crespy A, Lafon D. Evolution of the three-dimensional orientation distribution of glass fibers in injected isotactic polypropylene. Polym Eng Sci. 1997;37:329-337.

[22] Advani S, Tucker C. The use of tensors to describe and predict fiber orientation in short fiber composites. J Rheol. 1987;31:751-784.

[23] Yurgartis SW. Measurement of small angle fiber misalignment in continuous fiber composites. Compos Sci Technol. 1987;30:279-293.

[24] Konicek TS. A method to determine three-dimensional fiber orientation in fiber reinforced polymers: Master's thesis, University of Illinois at Urbana-Champaign; 1987.

[25] Phelps J, Tucker C. An anisotropic rotary diffusion model for fiber orientation in short- and long-fiber thermoplastics. J Non-Newtonian Fluid Mech 2009;156:165-176.

[26] Hine PJ. Personal communication. 2011.

[27] Zak G, Park C, Benhabib B. Estimation of three-dimensional fibre-orientation distribution in short-fibre composites by a two-section method. J Compos Mater. 2001;35:316-339.

[28] Fischer G, Eyerer P. Measuring spatial orientation of short fiber reinforced thermoplastics by image-analysis. Polymer Composites. 1988;9:297-304.

[29] Eberhardt C, Clarke, A. Fibre-orientation measurements in short-glass-fibre composites. Part I: automated, high-angular-resolution measurement by confocal microscopy. Compos Sci Technol. 2001;61:1389–1400.

[30] Mlekusch B. Fibre orientation in short-fibre-reinforced thermoplastics - II. Quantitative measurements by image analysis. Compos Sci Technol. 1999;59:547-560.

[31] O'Connell EA, Duckett, RA. Measurements of fiber orientation in short-fiber-reinforced thermoplastics. Compos Sci Technol. 1991;42:329-347.

[32] Eberle A, Vélez-García G, Baird D, Wapperom P. Fiber orientation kinetics of a concentrated short glass fiber suspension in startup of simple shear flow. J Non-Newtonian Fluid Mech. 2010;165:110 - 119.

[33] Davidson NC, Clarke A, Archenhold G. Large-area, high-resolution image analysis of composite materials. Meeting of Microscopy of Composite Materials III. Oxford, England1996. p. 233-242.

[34] Vélez-García GM. Complex flow simulation of short fibers suspendend in polymeric melts. Blacksburg, VA: PhD thesis, Viginia Polytechnic Institute and State University; 2011.

[35] Eberhardt C, Clarke, A., Vincent, M., Giroud, T., Flouret, S. Fibre-orientation measurement in short-glass-fibre composites II: a quantitative error estimate of the 2D image analysis technique. Compos Sci Technol. 2001;61:1961-1974.

Chapter 4

[36] VerWeyst B, Tucker C, Foss P, O'Gara J. Fiber orientation in 3-D injection molded features - Prediction and experiment. Int Polym Proc. 1999;14:409-420.

[37] Wang J, O'Gara J, Tucker C. An objective model for slow orientation kinetics in concentrated fiber suspensions: Theory and rheological evidence. J Rheol. 2008;52:1179-1200.

[38] VerWeyst B, Tucker C. Fiber suspensions in complex geometries flow/orientation coupling. Can J Chem Eng. 2002;80:1093-1106.

[39] Chung D, Kwon T. Numerical studies of fiber suspensions in an axisymmetric radial diverging flow: the effects of modeling and numerical assumptions. J Non-Newtonian Fluid Mech. 2002;107:67-96.

Chapter 5 Simulation of injection molding using a model with delayed fiber orientation

G.M. Vélez-García[1], S.M. Mazahir[2], P. Wapperom[3], and D. Baird[2]*

[1] Macromolecules and Interfaces Institute, Virginia Tech, [2] Department of Chemical Engineering, [3] Department of Mathematics, Blacksburg, VA, 24061

Use with permission of Carl Hanser Verlag GmbH & Co: Vélez-García GM, Mazahir SM, Wapperom P, Baird DG. "Simulation of injection molding using a model with delayed fiber orientation". Intern Polym Processing. 2011;26:331-9.

5.1 Abstract

Delay in fiber orientation evolution based on the Folgar-Tucker model with a slip parameter correction has been proposed as a simple alternative to improve predictions of fiber orientation in injection molded parts. Predictions based on this model and model parameters fitted to data from simple shear experiments were compared with experimentally determined fiber orientation in a center-gated disk. Three methods of fitting to simple shear data were assessed to obtain the isotropic diffusivity and the slip parameter. The model parameters and orientation data evaluated at the entry, lubrication and near-end-of fill regions in a center-gated disk for 30 wt% short glass fiber-filled polybutylene terephthalate (PBT) were obtained from earlier efforts in our laboratory. Simulation results based on the Folgar-Tucker model with the slip correction using customarily assumed inlet orientation being random and experimentally measured at the gate disagreed with measured orientation values at certain positions along the disk. However, improvement in the prediction of orientation due the slip correction was found at the core and transition layers in the lubrication region. The use of inlet conditions washes out quickly in the absence of the slip correction and induced a general reduction of orientation towards the center of the sample causing underestimation of orientation at the entry and lubrication region. Model predictions combining the slip correction and experimentally determined orientation at the gate are in agreement with the experimental data for the core layers near the end-of-fill region.

5.2 Introduction

The variation in the properties of injection-molded thermoplastics composites is due to the local variation of fiber orientation through the part and is attributed to flow-induced orientation during the forming stage of the part. Therefore, to advance this technology it is essential to control the fiber orientation during molding operations by means of processing conditions and mold design as predicted by means of a model that describes the flow behavior of the suspension during the filling stage.

Modeling of fiber orientation in molded parts of commercial interest is a challenging task due to the complex behavior arising from the high concentration of fibers in the suspension. The Folgar-Tucker model [1] has been successful in qualitatively predicting the experimentally measured orientation in molded parts [2-5]. For this reason, it has been the standard model used to predict fiber orientation in commercial simulation packages. The Folgar-Tucker model considers an orientation state where the fibers move with the bulk of fluid and the influence of fiber-fiber interactions on the orientation state. However, the inability to completely account for all fiber-fiber interactions for concentrated suspensions ($\phi_v > a_r^{-1}$ where ϕ_v is the fiber volume fraction and a_r is the fiber aspect ratio), prevents precise description of orientation for molded parts within a fiber concentration of commercial interest. Comparisons of model predictions of stress growth in the startup of shear flow using the Folgar-Tucker model with experimental data have suggested that the rate of orientation evolution is slower than the theory predicts [6-8]. Two modifications to the Folgar-Tucker model have been proposed to slow down the orientation evolution in concentrated suspensions. One modification is the addition of a strain reduction factor (SRF) [9] or slip parameter [10] to the Folgar-Tucker model to delay the evolution of orientation as seen experimentally. Irrespective of the name, the SRF and slip parameters represent the retardation in orientation evolution due to the additional fiber-fiber interactions in a concentrated suspension. However, this additional factor in the Folgar-Tucker model renders the equation for fiber orientation nonobjective. Wang *et al.* [11] proposed the reduced strain closure (RSC) model, which is a modified Folgar-Tucker model, where the slowdown in orientation evolution is added keeping the non-objectivity in the original Folgar-Tucker model. The reduced strain closure (RSC) involves a modification in the closure approximation eliminating the objectivity problem and keeping the delay effects in the evolution of orientation[11]. In spite of

the objectivity problem, the Folgar-Tucker model with slip parameter can be useful to describe evolution of orientation in simple flow [6-8, 10] or in general flows when this model is used in conjunction with the Hele-Shaw approximation. Tucker [12] and Wang *et al.* [13] showed that the SRF model with Hele-Shaw simulation was able to reproduce qualitatively most of the experimental observations in an end-gated plaque and a disk made in a rotating-compressing-expanding mold, respectively.

Simulations for composites generated by means of injection molding use the Folgar-Tucker model. The model parameters used for the simulations are typically obtained from empirical relationships or obtained from the injection molding experiment being simulated [13-15]. In an effort to develop a consistent procedure for the estimation of model parameters, it has been proposed to obtain model parameters from simple flow experiments having well controlled flow conditions [8, 16]. Wang *et al.* [11] and Eberle *et al.* [8, 10] have considered this approach in the Folgar-Tucker model containing the RSC and the slip parameter correction, respectively. We will focus here on the model parameter estimation introduced by Eberle *et al.* [8, 10] as a method for obtaining model parameters.

Eberle *et al.* [8, 10] introduced two experimental approaches to obtain model parameters for the Folgar-Tucker model with the slip correction based on simple shear flow experiments. In these methods, a "donut" shape sample was used to determine model parameters for the Folgar-Tucker model with a slip parameter correction based on (a) a direct fitting from rheometrical experiments in shear flow [8] or (b) fitting the steady state model predictions to orientation data measured on the sheared "donut" samples at a strain (γ) of 200 [10]. We will refer to both methods as "fitting to rheometry" or "fitting to steady orientation", respectively. Eberle *et al.* [8, 10] showed that model predictions from rheometrical simulations were capable of predicting experimentally determined orientation from donut shape samples deformed with different values of strains (γ). However, the proposed methods to determine model parameters provided different sets of model parameters. The experimentally determined orientation in the "donut" shape sample was measured mainly at relatively small strains ($\gamma < 100$) and contains no measurement of values between $\gamma = 100$ and 200. This gives the impression that the orientation may never reach steady state, but in Eberle et al [10] considered the orientation at $\gamma = 200$ as a steady state. Irrespective of the reasons for discrepancies between both approaches, experimental validation

of orientation obtained from a complex flow geometry using model predictions based on these model parameters is required. These results are essential to assess the effect of the slip parameter in a complex flow. Additionally, we will be able to confirm if at least one of the proposed methods is useful to obtain a set of model parameters suitable to predict orientation based on the Folgar-Tucker model with the slip correction for a highly concentrated suspension.

The objective of this paper is to assess the model parameters determined from the simple shear flow experiment and used in a numerical simulation scheme to predict the evolution of fiber orientation of a concentrated short glass fiber suspension in center-gated disks. In particular, model parameters obtained from rheometrical experiments [8] and from fitting orientation measurements in simple shear flow geometries are compared in the simulation of the filling of a center-gated disk using a 30 wt% short glass fiber PBT (Polybutylene Terephthalate) [17, 18]. Effects of inlet orientation used for the simulations are also investigated using a decoupled simulation scheme. The simulations are contrasted with the original Folgar-Tucker model to assess the impact of the model and the model parameters.

5.3 Evolution of fiber orientation and model parameters

The evolution of orientation for a semi-dilute fiber suspension is represented by the Folgar-Tucker model (Folgar and Tucker, 1984), and is described by

$$\frac{\partial \boldsymbol{A}}{\partial t} + \boldsymbol{v} \bullet \nabla \boldsymbol{A} = \left(\nabla \boldsymbol{v}\right)^{T} \bullet \boldsymbol{A} + \boldsymbol{A} \bullet \nabla \boldsymbol{v} - 2\boldsymbol{D} : \boldsymbol{A}_4 + 2C_I \sqrt{II_D}\left(I - 3\boldsymbol{A}\right) \tag{5.1}$$

where $\boldsymbol{A}$ and $\boldsymbol{A}_4$ represent the second and fourth order orientation tensors, respectively. Additionally, $\boldsymbol{v}$ represents the velocity, $\nabla \boldsymbol{v}$ the velocity gradient tensor, $\boldsymbol{D}$ the rate of deformation tensor, and II_D the second invariant of $\boldsymbol{D}$. The last term is the isotropic diffusivity which introduces a randomizing effect in the model and is used to account for the semi-dilute-regime interaction contributions to the orientation. This term is governed by the interaction coefficient, C_I, which is typically determined by fitting simulation results to experimentally determined fiber orientation. When C_I is set to zero in Eq. (5.1), a highly flow-aligned orientation state is predicted and the model is known as the Jeffery model [19]. The values of C_I are typically in a range of 0.003-

0.016 [20]. But recently, Phelps and Tucker [15] have suggested a typical range for short fiber composites of C_I = 0.006 to 0.01. Bay [21] found that C_I increased for non-concentrated suspensions ($\phi_v \leq a_r^{-1}$), but for concentrated suspensions C_I decreased and could be described by the following empirical function

$$C_I = 0.0184 \exp\left[-0.7148 \phi_v a_r\right] \tag{5.2}$$

However, an established empirical model for the prediction of the interaction coefficient does not exist [22] Now VerWeyst *et al.* [23] noted that values of C_I were dependent on the closure approximation used to express $\boldsymbol{A}_4$ in terms of $\boldsymbol{A}$.

Chung and Kwon [22] have reviewed the most commonly used closure approximations. Orthotropic types and invariant-based closure approximations are commonly used to approximate $\boldsymbol{A}_4$ [5, 13, 15, 24]. We use the invariant-based optimal fitted (IBOF) closure approximation [25]. Chung and Kwon [25] showed two relevant aspects of the IBOF closure in simple and complex flow simulations. First, the use of IBOF in the prediction of orientation, for a wide range of C_I, produced results comparable to the orientation obtained from the direct solution of the probability function for several homogeneous flows, an unsteady combined flow, and a nonhomogeneous radial diverging flow field. Second, IBOF is computationally efficient, compared to other orthotropic types of closures.

The evolution of fiber orientation in concentrated suspensions is slower than predicted by the Folgar-Tucker model due to inter-particle interactions. A scaling factor has been used to multiply the right hand side terms of Eq. (5.1), *i.e.* kinematic and diffusivity terms, to reduce the evolution of fiber orientation predicted by the Folgar-Tucker model:

$$\frac{\partial \boldsymbol{A}}{\partial t} + \boldsymbol{v} \bullet \nabla \boldsymbol{A} = \alpha \left[\left(\nabla \boldsymbol{v} \right)^T \bullet \boldsymbol{A} + \boldsymbol{A} \bullet \nabla \boldsymbol{v} - 2 \boldsymbol{D} : \boldsymbol{A}_4 + 2 C_I \sqrt{II_D} \left(I - 3 \boldsymbol{A} \right) \right] \tag{5.3}$$

where α denotes the slip parameter which is a fractional factor representing the effect of inter-particle interactions in a concentrated suspension [6-8]. The slip parameter accounts for the non-affine motion of the particles during the deformation and is used to slow down the orientation evolution. Eq. (5.3) reduces to the Folgar-Tucker model for α = 1. A similar modification was proposed by Huynh [9] by introducing the strain reduction factor based on the argument that the fibers form clusters and during deformation experience less

strain than the bulk. The strain reduction factor is the reciprocal of the slip parameter. A typical range for the slip parameter in short fiber composites is α = 0.30 to 0.40 [6-8].

Eberle *et al.* [8, 10] introduced two approaches to determine model parameter pairs, (C_I, α), for the Folgar-Tucker model with the slip correction obtained using donut shape samples in a cone-and-plate geometry. In one of the approaches values of (C_I, α) were obtained from fitting model predictions using the Folgar-Tucker model with a slip parameter (Eq. (5.3)) combined with the Lipscomb model for the stress, to the transient viscosity at the startup of shear (η^+) and the first normal stress growth function (N_1^+). The value of C_I was obtained from the steady state values of η^+ and N_1^+ measured in the startup of flow at $\dot{\gamma} = 6\ s^{-1}$. Using the same shear rate, the value of α was determined by simultaneously fitting the transient behavior of η^+ and N_1^+. The fit parameters obtained by this approach had values of (0.002, 0.30) [8].

In the second approach, the values (C_I, α) were obtained from fitting model predictions using Eq. (5.3) to measured orientation data obtained at different strain (γ) values at shear rate $\dot{\gamma} = 1\ s^{-1}$ ([10]). The orientation data was observed to level off between γ = 50 and 200 which was assumed as an indicator that the steady state was contained within this region. Eberle *et al.* [10] assumed the orientation at γ = 200 was steady state orientation and used it as a reference point to determine model parameters (C_I, α) fitted to the steady state orientation. The fit parameters obtained based on this assumption had values of (0.006, 0.40). This C_I value is very close to the C_I obtained from Eq. (5.2) based on ϕ_v and a_r for Valox 420, *i.e.* 0.005 and can be considered a typical value for orientation in injection molding as indicated in Wang *et al.* [13]. The C_I = 0.006 is close to the lower limit of typical C_I values given in Larson [20], *i.e.* 0.003, or in Phelps and Tucker [15], *i.e.* 0.006.

A new set of model parameters was determined by fitting model predictions from rheometrical simulations to orientation data measured on the sheared "donut" sample data of Eberle [26] assuming that steady state was reached at γ = 50. It should be noticed that γ = 50, is the strain where the orientation data begins to level off. The new set of model parameters (C_I, α) = (0.012, 0.40) was obtained using the following algorithm. The C_I = 0.012 is close to the upper limit of typical C_I values given in Larson [20], *i.e.* 0.016, or in Phelps and Tucker [15], *i.e.* 0.010. Values of (C_I, α) = (0.002, 1) and (0.02, 1) were used to obtain the profiles of orientation bounding the accepted range in the literature and compared with the experimental profile for the

A_{rr} component of orientation tensor vs. strain determined from the "donut" samples. Then, keeping the value of α =1, C_I was methodically changed, until the difference between the steady portion of the data and predicted values was a minimum as observed by visual inspection. At the end of this step, the fitted C_I value was obtained. Subsequently, keeping the fitted value of C_I, α was methodically changed until the profile passed through the majority of the experimental data points at the transient region. Fig. 5.1 shows the model predictions for the A_{rr} component in startup of simple shear at $\dot{\gamma}$ = 1 based on model parameters determined by fitting from rheometry (0.002, 0.40 [8]), steady state orientation at γ = 200 (0.006, 0.30 [10]), and steady state orientation at γ=50 (0.012, 0.40) data. This new value of C_I is similar to C_I = 0.0112 obtained by Wang *et al.* [11] for the same polymer suspension, *i.e.* Valox 420. The three sets of model parameters used in this study have acceptable values with respect to the typical theory for fiber composites because they are close to the typical limits for C_I defined by Larson [20] and to C_I obtained from Eq. (5.2).

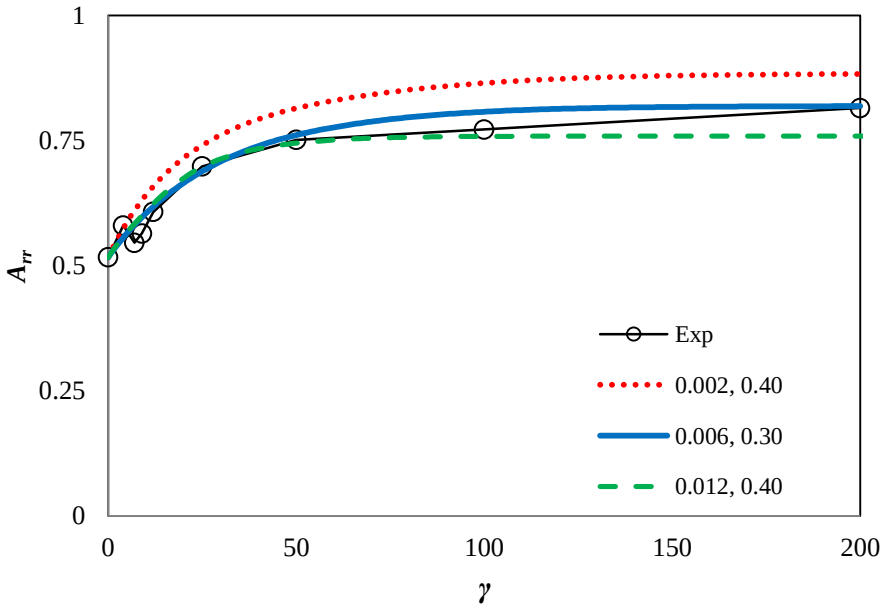

Figure 5.1 *Experimental and predicted fiber orientation represented through the A_{rr} component in startup of simple shear flow at $\dot{\gamma}$ = 1 s^{-1}, using model parameters determined by fitting from rheometry (0.002, 0.40 [8]), steady orientation (0.006, 0.30 [10]) and transient orientation (0.012, 0.40).*

5.4 Problem Description

A center-gated mold having internal radius r_{in} of 2.97 mm, outer disk radius r_{mold} of 57 mm, and thickness $2H$ of 1.38 mm, was used to make an injection molded disk of 30wt% short glass fiber PBT (Valox 420). The number average fiber length L_n = 362.8 μm and average fiber diameter d = 12.9 μm were determined from a burn-off process (approx. 1000 fibers). The viscosity of the suspension was determined on a Rheometrics Mechanical Spectrometer (RMS-800) at 533K from steady shear and dynamic oscillatory measurements [10]. Over a wide range of shear rates the PBT matrix behaves like a Newtonian fluid with viscosity η = 350 Pa·s. Fig. 5.2 shows the complex viscosity η^* versus angular frequency ω used to calculate the shear viscosity by means of the Cox and Merz empirical relation, *i.e.* $\eta(\dot{\gamma}) = |\eta^*(\varpi)|_{\dot{\gamma}=\varpi}$.

An injection-molding machine (Arburg Allrounder® Model 221-55-250) was used to mold center-gated disks. The resin in pellet form was dried overnight at 393 K in a vacuum oven at a pressure less than 1.35 kPa. The dried resin was fed to the hopper under nitrogen atmosphere and plasticated to obtain a melt at 533 K as recommended by the resin manufacturer. The plastication parameters were a screw speed of 200 RPMs and the following profile of temperature: 533, 533, 533, and 513 K. The suspension was injected into the mold, which was kept at 363 K using an injection pressure of approximately 20 MPa, in approximately one second at

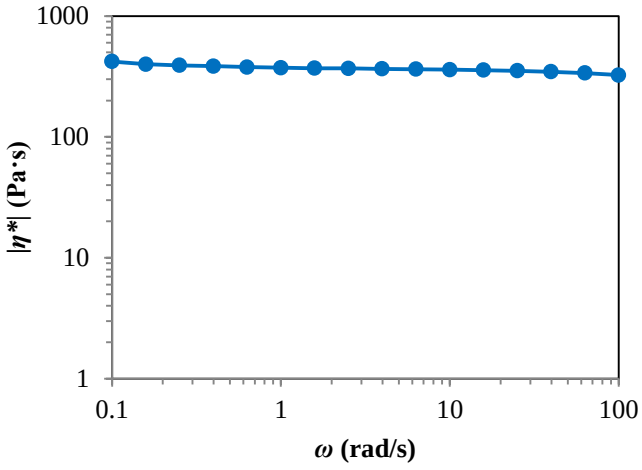

Figure 5.2 *Viscosity (complex) versus angular frequency (ln-ln plot) for neat polybutylene terephthalate (PBT) at 533 K. Values of η* were obtained by means of a cone-and-plate rheometer and reported in Eberle [26].*

a flow rate $q \approx 11.8$ cm^3/s. The part was let to cool and completely solidify in the mold for approximately 1 min. The molded part obtained was an incomplete disk having radial outer diameter, r_{out}, of 51.53 mm equivalent to about 90% of the mold radius. The purpose of obtaining an incomplete part was to account only for the flow effects during the filling stage on the orientation. The first 5 molded disks during a molding run were discarded to allow the mold to reach an equilibrium temperature. It should be indicated that no-warpage was observed in the molded part even several months after molding. Fig. 5.3 shows the radial dimensions of the incomplete disk normalized by the half thickness of the disk, *i.e.* $r_{in}/H = 4.53$ and $r_{out}/H = 75.68$. To capture the asymmetric evolution of orientation seen experimentally, the full thickness of the disk was considered as part of the flow domain, as shown in Fig. 5.3.

Simplifications of the extra-stress tensor and conservation equations are commonly used in fiber composites based on the fact that injection molded parts are thin geometries, *i.e.* the thickness of the mold is much less than other characteristic dimensions of the parts. Tucker [27] introduced a simplification for fiber suspensions flowing in narrow gaps where the extra stress only depends on the velocity gradient but not on the fiber orientation state. This simplification is known as decoupled approach and is commonly used in the

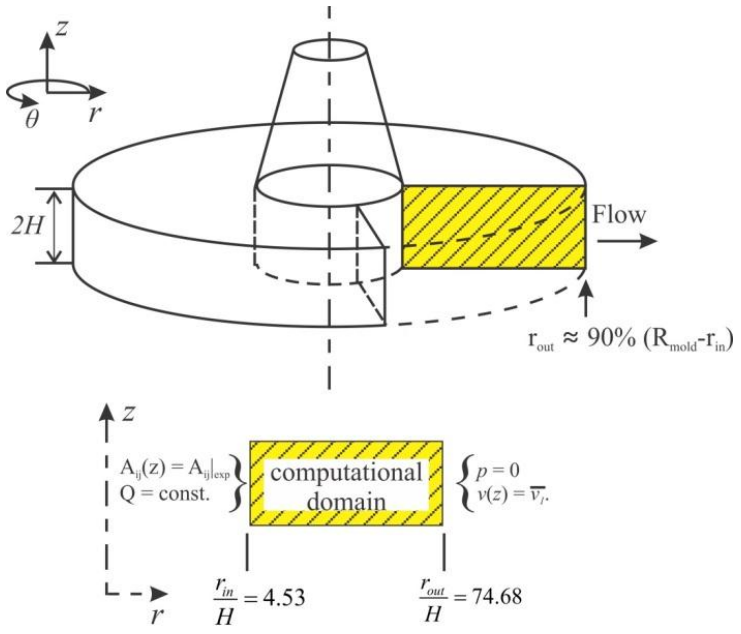

Figure 5.3 *Schematic diagram of the flow problem used in this study.*

simulation of fiber reinforced molded parts [13, 15, 28]. The decoupled approximation, in conjunction with the lubrication approximation, allowed us to solve analytically for the velocity field of an isothermal and incompressible Newtonian fluid (such as the PBT suspension used here) flowing in a thin center-gated disk [29]:

$$v_r(r,z) = \frac{1}{r}\frac{3q}{8\pi H}\left(1-\frac{z^2}{H^2}\right) \tag{5.4}$$

$$v_z(r,z) = 0 \tag{5.5}$$

where r represents the radial direction (*i.e.* flow direction), z the gapwise direction, H the half gap width, v_r and v_z the radial and gapwise velocities, respectively. The short injection time of one second used in the molding of the disks allows us to assume an isothermal filling condition which is in agreement with finds of Wu *et al.* [30]. The isothermicity assumption is valid because in fast filling the viscous dissipation and the rate of heat loss by conduction through the walls are roughly equal. The maximum rise in temperature due to viscous dissipation for our filling conditions was estimated to be approximately 3.5 K. Therefore, we do not expect a large variation in velocities due to thermal effects.

The flow characteristics in a center-gated disk make this geometry useful to understand the fiber orientation in molded parts. Three flow regions having different types of deformation have been identified for this geometry: entry, lubrication and frontal flow region [28]. The shearing and extensional deformations are present along all of these regions but due to their magnitudes are dependent on the radial and through-the-thickness locations considered. The shear deformation arises from small thickness of the molded parts while the radial divergence of the disk causes the extensional deformation. At the entry region of a center-gated disk, the fiber orientation is influenced by extensional deformation in the $r\theta$-plane. This flow region has been assumed to have a few gap heights width [28]**.** Non-significant gapwise velocities are assumed at radial locations away from the gate and end-of-fill regions. This flow region is known as the lubrication region and is dominated by shear deformation that strongly influences the fiber orientation. It is commonly assumed in simulations that the lubrication region covers the majority of the flow length of the geometry [28]. At the flow front, the fountain flow has a dominant effect on the deformation that is not captured by the lubrication approximation. Similar inability of the lubrication approximation to reproduce the flow occurs at the junction

region between the sprue and the gate. Therefore, this region is excluded from the analysis considered here. In order to compensate the possible impact of the flow at the junction in the evolution of orientation downstream, the experimentally determined orientation at the gate of a center-gated disk from Vélez-García *et al.* [17] was used at inlet conditions. Additionally, experimentally determined orientations along the cavity thickness at three radial locations inside the center-gated disk from Vélez-García *et al.* [17] were used to validate the model predictions of orientation based on the different model parameters. The three radial locations were 10, 40, and 90% of r_{out} - r_{in}, that are positions representative of the entry, lubrication, and near end-of-fill for the center-gated disk. Measurements of orientation at the gate were also considered by Vélez-García *et al.* [17]. In these characterizations a modified version of the method of ellipses was adapted to obtain unambiguous orientation over small sampling area. Additionally, the modified method of ellipses used by Vélez-García et al. [17] to evaluate the fiber orientation includes the information of orientation from elliptical and partial elliptical footprints in the polished plane. This consideration maximizes the number of fibers and information on each location analyzed, and therefore guarantees the collection of a statistically significant amount of data. Additionally, the micrographs were taken at high magnification (20x objective) as recommended by Davidson *et al.* [31] to reduce the measurement error. Orientations from two identical and independent molded parts were used to evaluate the error in a robust way as recommended by Bay and Tucker [21]. The error analysis was performed following the procedure described by Bay and Tucker [21] and Mlekusch [32]. It was found that the maximum absolute sampling error based on unequal sample size and unequal variance was approximately ± 0.07. However, the average absolute sampling error is reduced to ± 0.02 assuming unequal sample size and equal variance.

Steady state simulations were performed on a fixed mesh using a decoupled approach. A mesh refinement of the domain was performed in the *r*- and *z*-directions to ensure the convergence of the numerical solution. Fig. 5.4 illustrates the mesh used in the simulations consisting of quadrangle elements arranged with 96 elements along the radial direction and 48 elements along the thickness. The purpose of the smaller mesh at the inlet was to capture the orientation over radial locations near the entry region because in this region, fast changes in orientation are expected. The velocity field was determined by using Eqs. (5.4) and (5.5) while

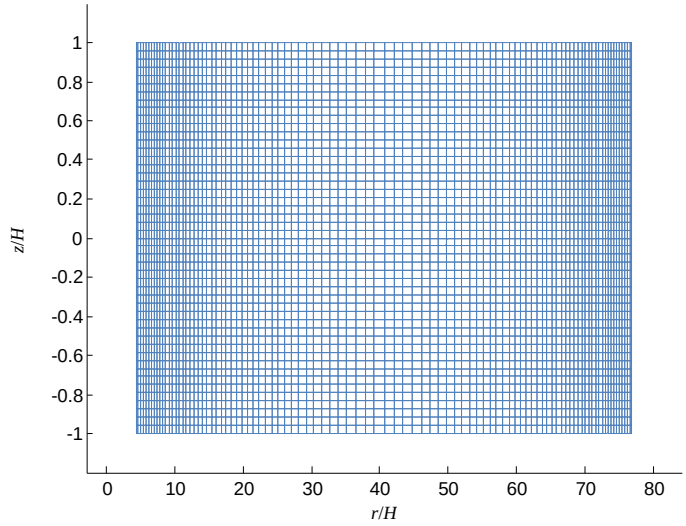

Figure 5.4 *Mesh structure used in this study consisting of quadrangular elements of variable size with smaller elements located at the inlet and outlet and larger element at the center. The elements were arranged in 48 elements along cavity thickness and 96 elements along radial direction.*

the discontinuous Galerkin method (DGFEM) was used to discretize the evolution equations shown in Eqs. (5.1) or (5.3) with $\boldsymbol{A}_4$ approximated by the IBOF closure. The three sets of model parameters (C_I, α) obtained by using different methods of fitting to the simple shear flow data described in Section 5.3 were used in Eq. (5.1) or (5.3). The hyperbolic nature of the Folgar-Tucker model requires the specification of the orientation tensor at the inlet. Typical inlet orientation conditions for a center-gated disk reported in the literature have been assumed as random orientation, *i.e.* $\mathbf{A}(r_{in}, z) = (1/3)\mathbf{I}$, where $\mathbf{I}$ is the unit tensor. The use of random inlet conditions was found to give reasonably good predictions of orientation compared with experimental results away from the gate and advancing front for the center-gated disk [2]. Therefore, they have been the standard inlet orientation conditions used in simulations for this geometry. The random orientation profile along the cavity thickness represented through the A_{rr} component is depicted in Fig. 5.5. However, orientation measured at the gate of a center-gated disk that can be used as experimentally determined inlet condition, has become available recently [17, 18]. This experimental inlet condition is also shown in Fig. 5.5 and the expression "gate orientation" will be used to refer to this orientation profile. The asymmetry of the orientation profile and

component of orientation in flow direction, A_{rr}, having values of $A_{rr} \approx 1 - A_{\theta\theta}$, are the main characteristics of this data. The random orientation and gate orientation shown in Fig. 5.5 were used as inlet orientation conditions in the simulations.

Fig. 5.6 depicts the convention used to describe the multilayer structure obtained from the simulations for a center-gated disk. The typical orientation profile predicted by the Folgar-Tucker model consists of high values of A_{rr} near the walls and an abrupt reduction in orientation towards the midplane of the cavity. To delineate the general shape of the A_{rr} profile, two dashed lines labeled ① and ② were drawn and the interception of the predicted A_{rr} values with these lines was used to define the layering structure as shown in Fig. 5.6. The location of the horizontal lines ① were set at 95% of the maximum value of A_{rr} while the lines ② were defined based on line up of A_{rr} values typically seen between $z/H \approx 0.50$ to 0.08. For the upper and lower half cavity, intersections of the A_{rr} values with lines ① and ② denote the changes from shell-to-transition layers and from transition-to-core layers, respectively. The relative positions of each layer, *i.e.* shell, transition and core, are also indicated in Fig. 5.5 for the lower and upper half cavity. From this point, the expression "width of the core" will be used to denote the abrupt reductions of A_{rr} values towards the midplane. Additionally, the expression "orientation near the walls" will be used to indicate the A_{rr} values at $z/H > 0.90$.

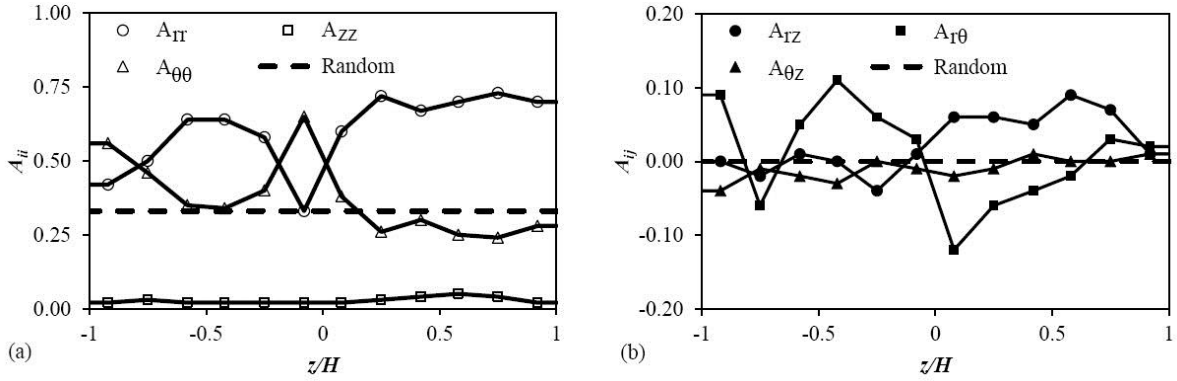

Figure 5.5 *Inlet orientation profiles at the gate (a) diagonal and (b) off-diagonal, reported by Vélez-García et al. [17] and Vélez-García [18]. The symbols denote the experimentally determined orientation, the dashed line represents the profile of random inlet orientation. The lower and upper wall corresponds to z/H = -1 and 1, respectively.*

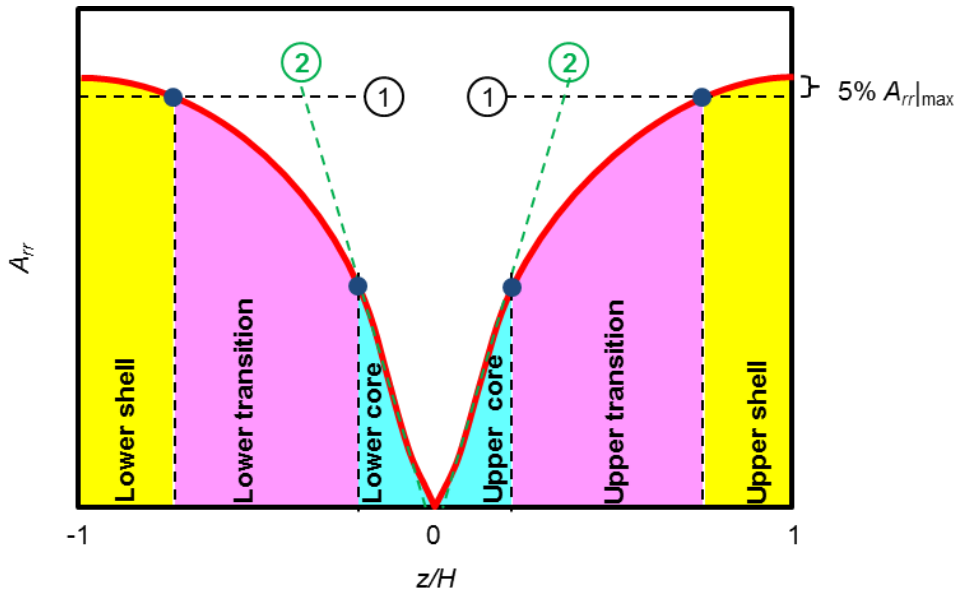

Figure 5.6 *Definition of multilayer structure obtained from the typical A_{rr} orientation profile.*

5.5 Results and Discussion

Experimentally determined orientation in a center-gated disk evaluated at several radial locations represented through component of orientation in flow direction, A_{rr}, was compared with model predictions based on the Folgar-Tucker model, Eq. (5.1), and Folgar-Tucker with slip correction, Eq. (5.3), for both random and gate inlet orientation conditions. The model parameters (C_I, α) used in the simulations were obtained from simple shear flow experiments indicated in Section 5.4 and the inlet orientation conditions are illustrated in Fig. 5.5. Estimation of the multilayer structure based on the convention previously defined and the evaluation of discrepancies between the predicted and experimental orientation for each layer were used to assess the model parameters and the effect of inlet orientation conditions.

Fig. 5.7 illustrates the ability of the Folgar-Tucker model using a random inlet orientation to qualitatively predict the experimentally determined orientation but quantitative discrepancies are evident. When the predicted and experimental A_{rr} values were compared, it was found that model predictions based on different C_I values were capable of validating the experimental results on small portions of the experimental orientation profile. For example, when Figs. 5.7 (a-b) are considered, model predictions based on the smallest

value of C_I, *i.e.* 0.002, were capable of approaching the experimental data reasonably well for the upper transition layers in the entry and lubrication regions. Simulations based on a C_I value of 0.012 predicted A_{rr} values closer to the experimental data for the lower shell layer at these radial locations. Large underestimation of orientation near the center, *i.e.* $z/H \approx 0$ and drastic overestimation of the experimental A_{rr} near the walls are observed in Fig. 5.7(a) and the other radial locations, irrespective of the C_I values used in the simulations. We do not expect good agreement in between predicted and experimental orientation near to the walls, since the formation of the frozen layer was not included in the simulations. At the lubrication region, the dominant

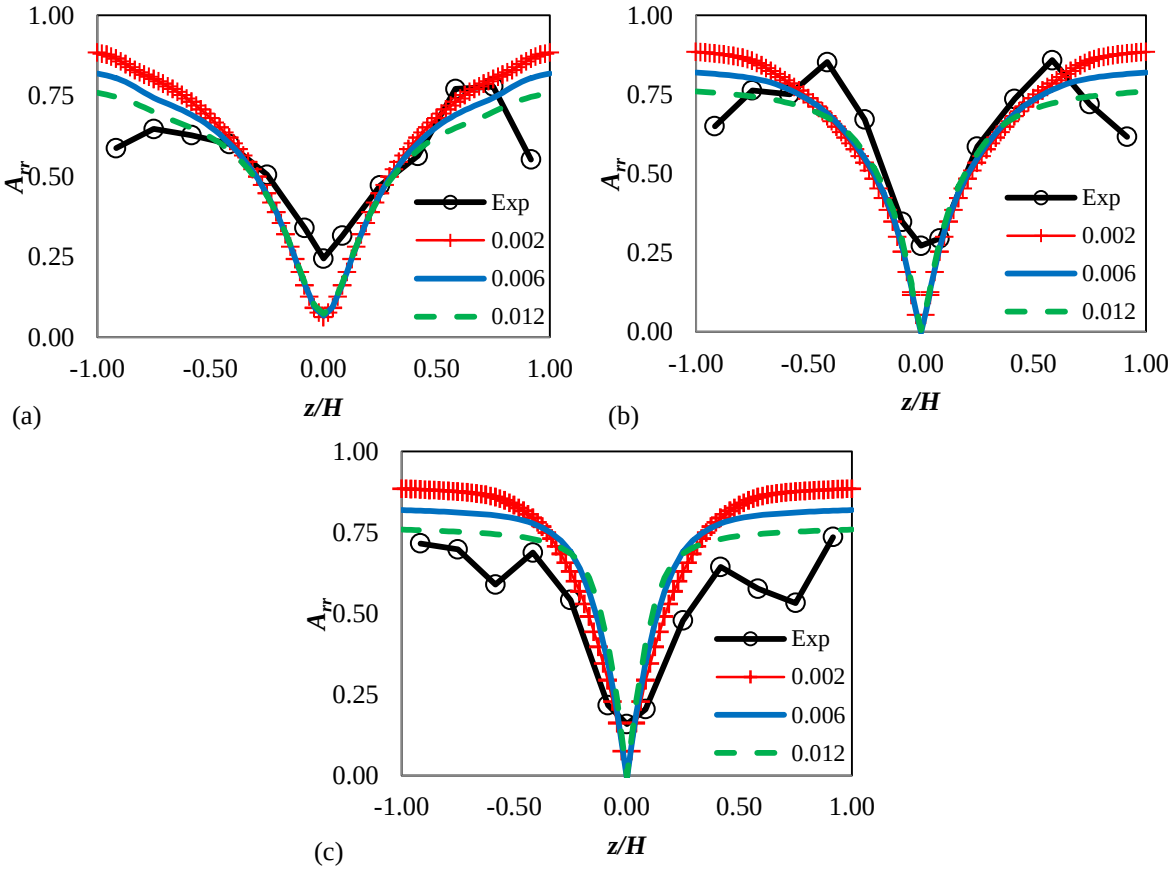

Figure 5.7 *Experimental and predicted fiber orientation represented through the A_{rr} component in a center-gated disk, evaluated at different flow regions (r/H): (a) entry (11.3), (b) lubrication (32.5), and (c) near-end-of-fill (67.5). The simulations were performed using the Folgar-Tucker model, Eq. (5.1), with the C_I values shown in the figure. Inlet orientation was assumed as random.*

effects of shear flow were extended towards the center of the cavity causing the increase in A_{rr} values as seen in Fig. 5.7(b). The higher A_{rr} values in model predictions for all C_I values cause smaller differences between the experimental and predicted orientation at the transition layer. However, the perfect alignment perpendicular to the flow predicted at z/H =0, does not agree with the experimental orientation at this location. When the orientation near the end-of-fill region illustrated in Fig. 5.6(c) was evaluated, model predictions based on the largest value of C_I, *i.e.* 0.012, produced A_{rr} values in agreement with the experimental data right near the walls and for a portion of the lower transition layers. However, simulations based on all C_I values overestimated the orientation for the other layers, especially at the shell layers where local drops in A_{rr} values are observed in the experimental data. It also was observed that the narrow core predicted at the near-end-of-fill region contrasts with the good agreement between the predicted and experimental width of the core at the lubrication region.

The addition of the slip parameter produced changes in orientation, mainly in the transition and core layers for all regions of flow. Fig. 5.8 depicts the experimentally determined orientation and simulation results based on the Folgar-Tucker model with slip parameter and random inlet orientation. It is shown in Fig. 5.8(a) that the most noticeable effect of the slip parameter seen at the entry region for all model predictions is the increase in the width of the core, a reduction in the transition layer and no changes in the shell layer. Concurrently, the orientation near the center remained close to A_{rr} = 1/3, which was imposed as inlet orientation, causing small differences between predicted and experimentally determined orientations. The core for model predictions based on a value of α = 0.30 was not significantly wider than the ones based on values of α = 0.40. When the lubrication region shown in Fig. 5.8(b) was considered, the slight increment in A_{rr} values due to the slip parameter caused that the model predictions agreed with the experimentally determined orientation for large portion of the core and transition layers. This improvement is observed especially for the model parameter (0.002, 0.40). We also observed that the effects of slip parameter vanished for shell layers, causing model predictions similar to the ones obtained based on α =1. Other difference with respect to model predictions using α =1 observed in Fig. 5.8(b), were the larger values of A_{rr} at z/H = 0. The narrow core of the near-end-of-fill region seen in Fig. 5.8(c), caused larger discrepancies between experimental data and model predictions than seen for α = 1 in Fig. 5.7(c). Additionally, a thicker transition layer and a slightly thinner shell

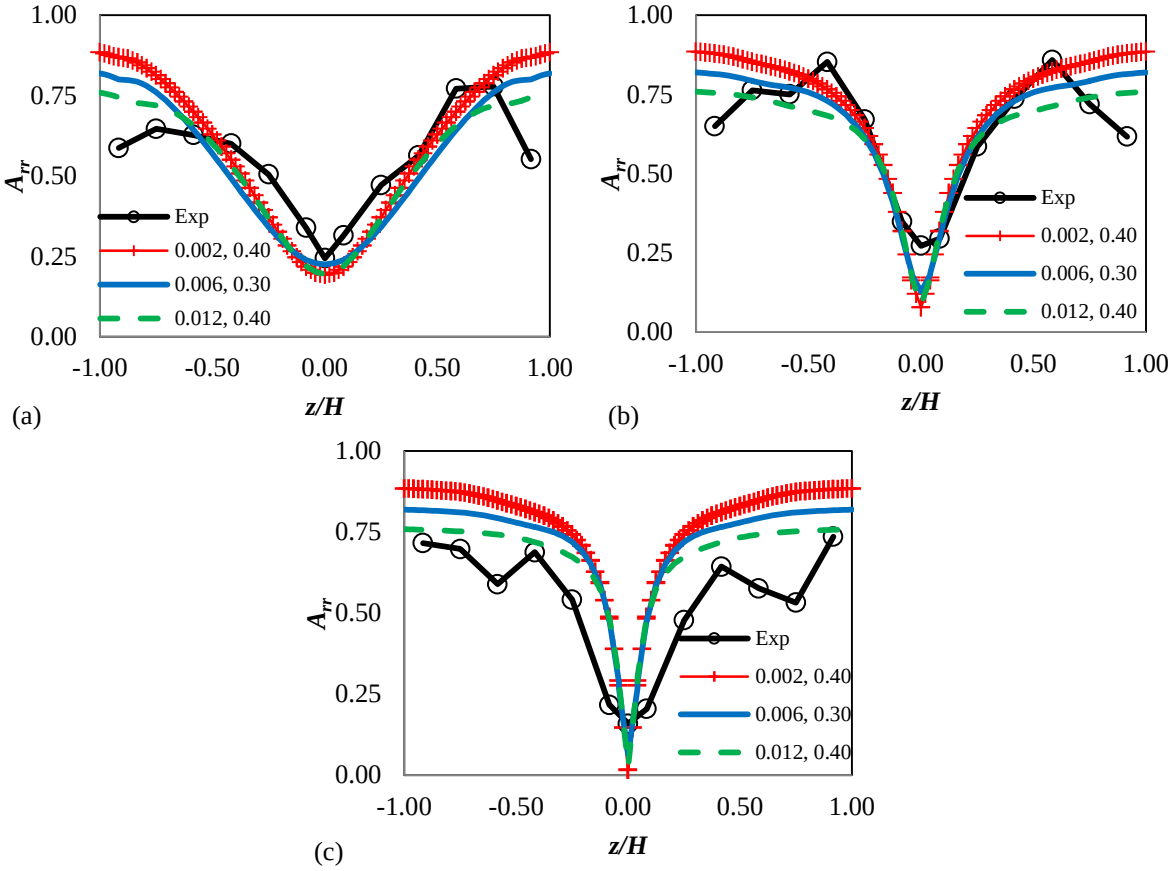

Figure 5.8 *Experimental and predicted fiber orientation represented through the A_{rr} component in a center-gated disk, evaluated at different flow regions (r/H): (a) entry (11.3), (b) lubrication (32.5), and (c) near-end-of-fill (67.5). The simulations were performed using the Folgar-Tucker model with slip correction, Eq. (5.3), with the model parameters (C_I, α) shown in the figure. Inlet orientation was assumed as random.*

layer were observed

The assessment of the inlet orientation in a center-gated disk is a significant contribution of this work. Fig. 5.9 illustrates model predictions based on the original Folgar-Tucker model and the inlet orientation experimentally determined at the gate of the center-gated disk. At the entry region, the typical orientation profile, related to the Folgar-Tucker model, suffered from considerable changes in shape and smoothness as can be observed in Fig. 5.9(a). For all of the C_I values used in the simulations, the asymmetry in inlet condition

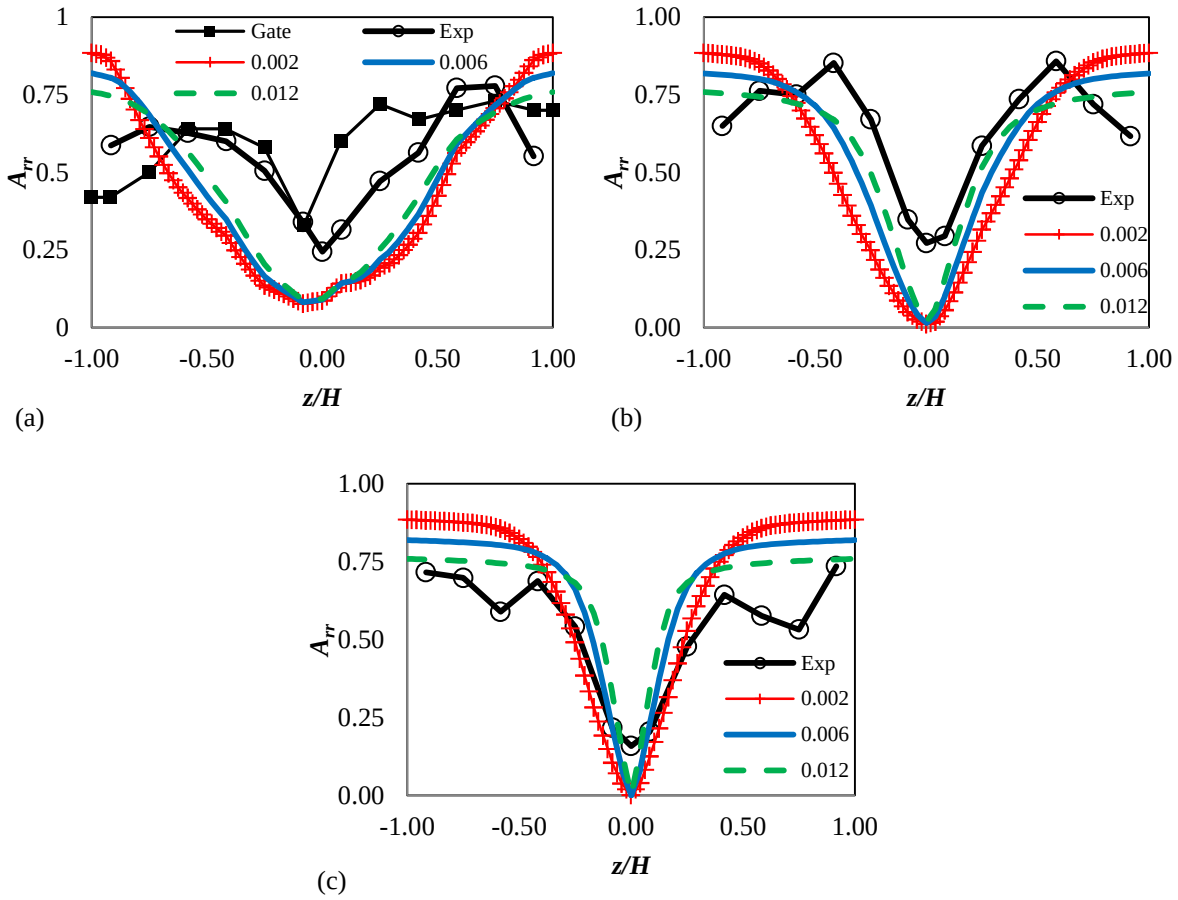

Figure 5.9 *Experimental and predicted fiber orientation represented through the A_{rr} component in a center-gated disk, evaluated at different flow regions (r/H): (a) entry (11.3), (b) lubrication (32.5), and (c) near-end-of-fill (67.5). The simulations were performed using the Folgar-Tucker model, Eq. (5.1), with the C_I values shown in the figure. Inlet orientation was experimentally determined at the gate.*

caused irregularities in the orientation profile, reduction in A_{rr} values towards the center of the sample, and larger underestimation of experimental data than observed in Fig. 5.7(a) for random inlet orientation. The irregularities in the predicted orientation profile impeded the application of the convention used to define the multilayer structure as considered in orientation profiles based on random inlet conditions. However, the core seen in Fig. 5.9(a) was much wider than the core seen in Fig. 5.7(a) and the widths of the core were slightly reduced as C_I values were increased. Near the walls, all model predictions produced A_{rr} values identical to the ones obtained at the shell layers for simulations based on random inlet orientation. It is also shown in Fig.

5.9(a) that the initial asymmetric profile imposed by the gate orientation practically washed out for all model predictions, while a strong asymmetry is observed in the experimental orientation. In the lubrication region is considered the use of measured gate orientation caused large underestimation of the experimental data towards the center of the sample not seen in Fig. 5.7(b). Qualitatively the experimental and predicted orientation towards the center of the sample showed that the asymmetry was washed out, especially for model predictions. As expected, the width of the core was reduced from the entry to the lubrication region, but separations in the model predictions for the different C_I values not seen in Fig. 5.7(b) were observed. Model predictions at the region near-end-of-fill resulted in a wider core which is in better agreement with experimental data, as observed in Fig. 5.9(c).

Fig. 5.10 illustrates the model predictions based on the combined effects of the slip parameter and gate orientation. The strong delay in evolution of the asymmetric profile of the gate orientation is evident at the entry region as seen in Fig. 5.10(a). In contrast with Fig. 5.9, the effects of the asymmetry and irregularities in the orientation profile were seen in both the entry and lubrication region. Irrespective of the C_I values used in the simulations, broad core layers can be seen in Fig. 5.10(a) which are in better agreement with the experimental data than predictions with $\alpha = 1$ in Fig. 5.9(a) were observed. The better agreement was attributed to the larger A_{rr} values and orientation profile having similar shape as the gate orientation towards the center of the sample. On the other hand, as seen in Fig. 5.9, the A_{rr} values at the shell layer for all radial locations were similar to the values seen in Fig. 5.7. When the lubrication region was considered (Fig. 5.10(b)), larger underestimation of A_{rr} values was seen at z/H locations corresponding to the transition layers seen in Fig. 5.9(b). However, reductions of discrepancies were seen towards the center of the sample, especially for model predictions based on (0.006, 0.30). The orientation profiles seen in Fig. 5.10(b) for the lubrication region have similar shape to the ones seen in the entry region seen in Fig. 5.9(a); this similarity was attributed to the delay effects introduced by the slip parameter. However, slightly thinner core layers were observed in Fig. 5.10(b) in contrast with Fig. 5.9(a). Contrarily to the observations at near-end-of-fill region seen in Figs. 5.7-9, good agreement between predicted and experimental orientation was observed, especially for simulations based on values of (0.006, 0.30). The increment in thickness of the core layers due to the combination of the slip

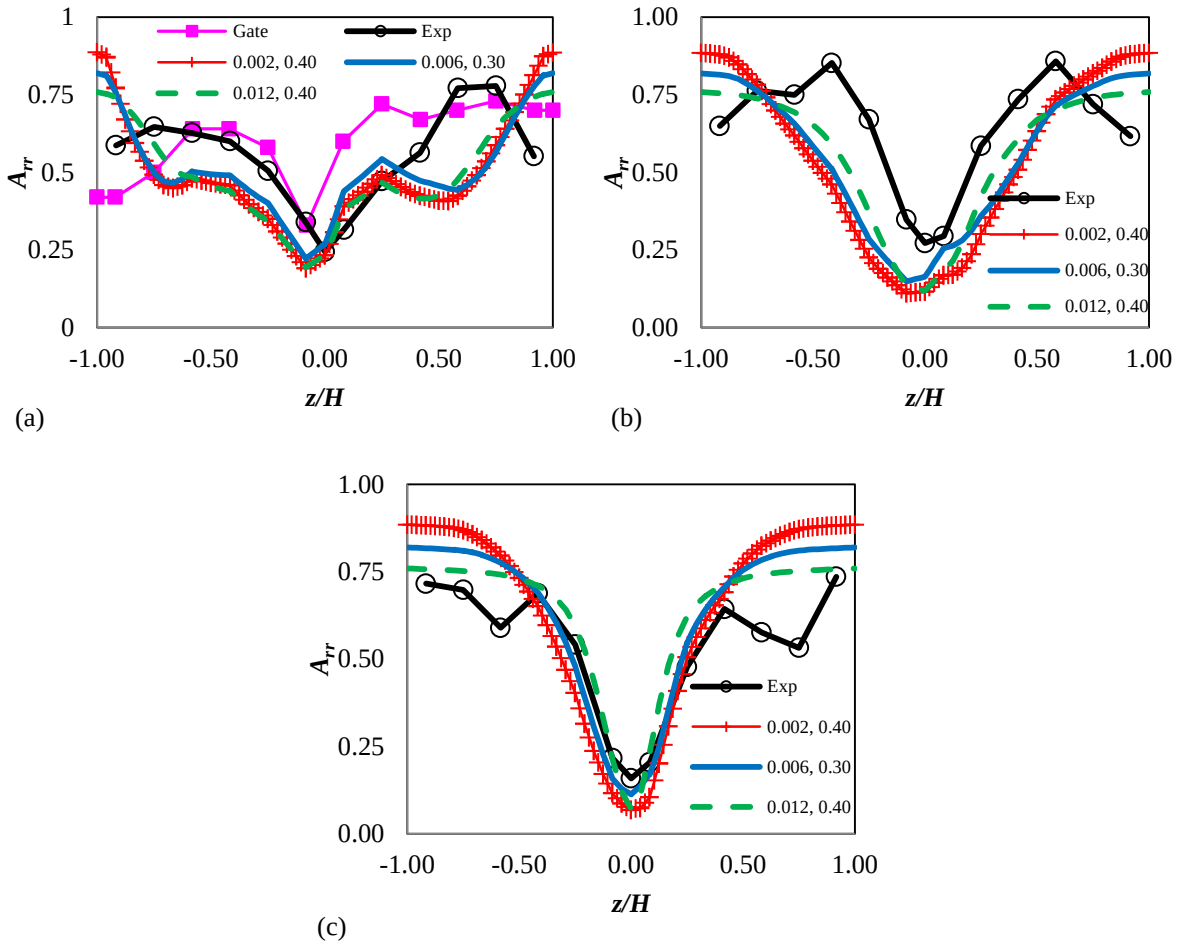

Figure 5.10 *Experimental and predicted fiber orientation represented through the A_{rr} component in a center-gated disk, evaluated at different flow regions (r/H): (a) entry (11.3), (b) lubrication (32.5), and (c) near-end-of-fill (67.5). The simulations were performed using the Folgar-Tucker model with slip correction, Eq. (5.3), with the model parameters (C_I, α) shown in the figure. Inlet orientation was experimentally determined at the gate.*

parameter and inlet orientation conditions caused an improvement of model predictions in this region.

5.6 Conclusions

The addition of the slip parameter to the Folgar-Tucker model has been proposed to delay orientation evolution and thereby reduce the differences between experimentally determined orientation in molded parts

and model predictions. However, this modified version of the Folgar-Tucker model requires an efficient method to determine the model parameters (C_I, α) to be used in the simulations. Three alternatives for obtaining model parameters in the Folgar-Tucker model with the slip correction based on fitting data from simple shear flow experiments were investigated. These model parameters were obtained from fitting to rheometrical data, steady state orientation at $\gamma = 200$, and steady state orientation at $\gamma = 50$, respectively. The model predictions based on these set of parameters were validated with experimentally determined orientation from a center-gated disk evaluated at the entry, lubrication, and near-end-of-fill regions. Both random inlet orientation and experimentally measured orientation at the gate were considered.

A single set of model parameters was incapable of reproducing the experimentally measured orientation in different flow regions for a thin center-gated disk. When the Folgar-Tucker model with random inlet orientation was assessed with different C_I values, our results showed the inability of the model predictions to validate the experimental data around the midplane. Additionally, the C_I values did not significantly affect the width of the core layers but increased the thicknesses of the shell and decreased the transition layers as functions of radial location. The previous observations give support to the speculations about the need for a variable C_I to predict the experimental orientation in a center-gated disk [33]. Model predictions based on the Folgar-Tucker model with slip correction and random inlet orientation were helpful to predict the orientation around the midplane for the entry region. Additionally, this combination caused an improvement in predicted orientation for the transition and core layers at the lubrication region. However, model predictions for the near-end-of-fill region showed a narrower core layer than seen experimentally. We also found no significant differences in model predictions based on $\alpha = 0.30$ and 0.40.

The use of inlet orientation based on the experimental determination at the gate caused strong modifications in the orientation profile for all flow regions. In contrast with experimental observations, model predictions based on the Folgar-Tucker model and gate orientation showed a fast washout of the inlet orientation which was almost completed at the entry region. More specifically, the gate orientation induced a significant reduction in A_{rr} values for the transition and core layers. Small A_{rr} values caused large discrepancies with experimental orientation for the entry and lubrication regions, but better agreement for the region near to

the end-of-fill. On the other hand, the use of slip parameter and gate orientation delayed the washout of the initial conditions up to the lubrication region, but again large discrepancies with experimental data occurred at the entry and lubrication region. However, the slip parameter and measured gate orientation produced the best agreement observed between predicted and experimental orientation for the core layers at the near-end-of-fill region.

5.7 Acknowledgements

The financial support for this work from the National Science Foundation and Department of Energy through Grant No. DMI-0521918 and National Science Foundation: CMMI-0853537 are gratefully acknowledged. Gregorio M. Vélez-García also acknowledges support from NSF-IGERT: DGE-0548783 Macromolecular Science and Infrastructure Engineering and University of Puerto Rico-Mayagüez. Syed M. Mazahir also acknowledges support from the Doctoral Scholarship program funded by the Institute for Critical Technology and Applied Science, Virginia Tech.

5.8 Nomenclature

Latin letters symbols

Symbol	Definition
$\boldsymbol{A}$	Second order orientation tensor
$\boldsymbol{A}_4$	Fourth order orientation tensor
a_r	Aspect ratio
C_I	Interaction coefficient
d	Average fiber diameter
$\boldsymbol{D}$	Rate-of-deformation tensor
H	Half gap width
$\boldsymbol{I}$	Unit tensor
II_d	Second invariant of the rate-of-deformation tensor

Chapter 5

Symbol	Definition
L_n	Number average fiber length
N_1^+	First normal stress growth function
q	Volumetric flow rate
r	Radial direction
r_{in}	Inner radius of injection molded center gated disk
r_{mold}	Outer radius of mold cavity for center-gated disk
r_{out}	Outer radius of injection molded center gated disk (short shot)
$\boldsymbol{v}$	Velocity vector
z	Gapwise direction

Greek letter symbols

Symbol	Definition
α	Slip parameter
γ	Strain
η	Steady-state shear viscosity
η^+	Shear stress growth coefficient
η^*	Complex viscosity
θ	Circumferential direction
ϕ_v	Volume fraction
ω	Angular frequency

Special character symbols

Symbol	Definition
$\partial/\partial t$	Time derivative
∇	Gradient operator
$\nabla \boldsymbol{v}$	Velocity gradient tensor
^{T}	Transpose

Acronyms

Acronym	Definition
SRF	Strain reduction factor
RSC	Reduced strain closure
PBT	Polybutylene Terephthalate
IBOF	Invariant-based optimal fitted closure approximation
DGFEM	Discontinuous Galerkin finite element method

5.9 References

[1] Folgar F, Tucker C. Orientation behavior of fibers in concentrated suspensions. J Reinf Plast Comp. 1984;3:98–119.

[2] Bay RS, Tucker CL. Fiber orientation in simple injection moldings. 2. Experimental results. Polym Composite. 1992;13:332-41.

[3] Chung S, Kwon T. Coupled analysis of injection molding filling and fiber orientation, including in-plane velocity gradient effect. Polym Composite. 1996;17(6):859-72.

[4] Neves N, Pontes A, Pouzada A. Experimental validation of morphology simulation in glass fibre reinforced polycarbonate discs. J Reinf Plast Comp. 2001;20:452-65.

Chapter 5

[5] Chung D, Kwon T. Numerical studies of fiber suspensions in an axisymmetric radial diverging flow: the effects of modeling and numerical assumptions. J Non-Newtonian Fluid Mech. 2002;107:67-96.

[6] Sepehr M, Carreau P, Grmela M, Ausias G, Lafleur P. Comparison of rheological properties of fiber suspensions with model preditions. J Polym Eng. 2004;24(6):579-607.

[7] Sepehr M, Ausias G, Carreau P. Rheological properties of short fiber filled polypropylene in transient shear flow. J Non-Newtonian Fluid Mech. 2004;123: 19-32.

[8] Eberle A, Baird D, Wapperom P, Vélez-García G. Using transient shear rheology to determine material parameters in fiber suspension theory. J Rheol. 2009;53(3):685-705.

[9] Huynh HM. Improved fiber orientation predictions for injection-molded composites: Master's Thesis, University of Illinois at Urbana-Champaign; 2001.

[10] Eberle A, Vélez-García G, Baird D, Wapperom P. Fiber orientation kinetics of a concentrated short glass fiber suspension in startup of simple shear flow. J Non-Newtonian Fluid Mech. 2010;165:110 - 9.

[11] Wang J, O'Gara J, Tucker C. An objective model for slow orientation kinetics in concentrated fiber suspensions: Theory and rheological evidence. J Rheol. 2008;52:1179-200.

[12] Tucker CL. Improved fiber orientation predictions for injection molded composites. In: Advani A, Smith, DE editor. Workshop: Future of modeling in composites molding processes. Arlington, VA: Co-Sponsored by the National Science Foundation, the United States Department of Energy and the American Plastics Council; 2004.

[13] Wang J, Silva C, Viana J, van Hattum F, Cunha A, Tucker C. Prediction of fiber orientation in a rotating compressing and expanding mold. Polym Eng Sci. 2008;48:1405-13.

[14] O'Dowd F, Levesque M, Gilchrist MD. Analysis of fibre orientation effects on injection moulded components. P I Mech Eng B-J Eng. 2006;220:1909-21.

[15] Phelps J, Tucker C. An anisotropic rotary diffusion model for fiber orientation in short- and long-fiber thermoplastics. J Non-Newtonian Fluid Mech 2009;156:165-76.

[16] Eberle A, Baird D, Wapperom P, Vélez-García G. Obtaining reliable transient rheological data on concentrated short fiber suspensions using a rotational rheometer. J Rheol. 2009;53(1049-1068).

[17] Vélez-García GM, Wapperom P, Baird DG, Anning AO, Kunc V. Unambiguous orientation in short fiber composites over small sampling area in a center-gated disk. Compos Part A-Appl. 2012;43:104-13.

[18] Vélez-García GM. Complex flow simulation of short fibers suspendend in polymeric melts. Blacksburg, VA: PhD thesis, Viginia Polytechnic Institute and State University; 2011.

[19] Jeffery GB. The motion of ellipsoidal particles immersed in a viscous fluid. Proc R Soc A. 1922;102:161-79.

[20] Larson RG. The structure and rheology of complex fluids. New York: Oxford University Press; 1999.

[21] Bay R. Fiber orientation in injection-molded composites: A comparison of theory and experiments. Urbana, Illinois: PhD thesis, University of Illinois at Urbana-Champaign; 1991.

[22] Chung D, Kwon T. Fiber orientation in the processing of polymer composites. Korea-Aust Rheol J. 2002;14(4):175-88.

[23] VerWeyst B, Tucker C, Foss P, O'Gara J. Fiber orientation in 3-D injection molded features - Prediction and experiment. Int Polym Proc. 1999;14:409-20.

[24] VerWeyst B, Tucker C. Fiber suspensions in complex geometries flow/orientation coupling. Can J Chem Eng. 2002;80:1093-106.

[25] Chung S, Kwon T. Invariant-based optimal fitting closure approximation for the numerical prediction of flow-induced fiber orientation. J Rheol. 2002;46:169-94.

[26] Eberle APR. The dynamic behavior of a concentrated composite fluid containing non-brownian glass fibers in rheometrical flows. Blacksburg: PhD Thesis, Virginia Tech; 2008.

[27] Tucker CL. Flow regimes for fiber suspensions in narrow gaps. J Non-Newtonian Fluid Mech. 1991;39:239-69.

[28] Bay R, Tucker CL. Fiber orientation in simple injection moldings .1. Theory and numerical-methods Polym Composite. 1992;13:317-31.

[29] Baird D, Collias D. Polymer processing: Principles and design: Wiley, John & Sons, Incorporated; 1995.

[30] Wu PC, Huang CF, Gogos CG. Simulation of the Mold-Filling Process. Polym Eng Sci. 1974;14:223-30.

Chapter 5

[31] Davidson N, Clarke A, Archenhold G. Large-area, high-resolution image analysis of composite materials. J Microsc-Oxford. 1997;185:233-42.

[32] Mlekusch B. Fibre orientation in short-fibre-reinforced thermoplastics - II. Quantitative measurements by image analysis. Compos Sci Technol. 1999;59(4):547-60.

[33] Chung D, Kwon T. Applications of recently proposed closure approximations to injection molding filling simulation of short-fiber reinforced plastics. Korea-Aust Rheol J. 2000;12(2):125-33.

Chapter 6 Recommendations

6.1 Sample preparation

The sample preparation procedure developed in this dissertation has demonstrated a way of producing high-quality optical micrographs having well defined footprint borders and noticeable shadows for the composites analyzed. The reason for the high-quality image is attributed to the careful sample preparation used in our experiments. Based on our experience, careful manipulation is especially recommended for the sample grinding because this step involves a manual operation which requires constant measurements of the puck height in order to avoid uneven sample dimensions. Exploring the use of an automatic polisher/grinder for the sample grinding step is a good alternative for even material removal, avoidance of repetitive measurements and ensuring even puck height.

The sample preparation procedure was tested on composites consisting of different crystalline polymer matrices and 30wt% glass fiber concentration. In all cases, the sample grinding and polishing described in Chapter 3 produced excellent polished surfaces. Similarly, the mild plasma etching process using RF plasma cleaner provided excellent surface erosion of the polished surface, producing contrast enhancement and showing the shadows of elliptical footprints. However, the hardness of the fibers or polymeric matrices in composites depends on the structure of these constituents, as indicated in Chapter 3. Therefore, testing the sample preparation procedure in other composite systems containing higher fiber concentration, or other fibers such as carbon fibers or hardened polymeric matrices, will allow assessing the actual procedure under worst case conditions.

Optical reflective microscopes are a suitable for image acquisition due to their common availability and low sample preparation cost reduction. Reliable shadow identification in optical micrographs is dependent on the depth of erosion, topographical correction and difference in color between the etched polymer matrix and the shadow. However, the use of optical microscopes is not suitable for composites having identical color of the etched polymer matrix and the shadow. Anticipating this potential problem, exploring the use of a confocal microscope for image acquisition may be of benefit to future work. Images in a confocal microscope are formed by laser detection rather than by differences in reflective index. The use of a confocal microscope is

possible with the current sample preparation procedure because the tip of the fibers is exposed to the air, otherwise the laser would be unable to penetrate the polymeric matrix [1].

6.2 Orientation measurements

The used image recognition of footprints involved both automatic and manual operations. These manual operations are time consuming and are at odds with the purpose of image analysis. Therefore, the current image analysis tool requires modifications to eliminate or reduce to a minimum the manual operation used in the image analysis tool. Therefore, subroutines for automatic fiber separation, classification and characterization of non-elliptical footprints and shadow recognition must be included in the image analysis tool. One of the most challenging subroutines is the classification and characterization of non-elliptical objects, but the approach suggested in Zhu, et al. [2] can be used to automatize these operations.

Short fibers are assumed to be cylindrical and rigid objects. However, we observed that some fibers cut longitudinally by the polished plane had bending due to interparticle interactions with other fibers. Fig. 6.1 illustrates the slight bending in rectangular footprints observed in the optical micrographs at a radial location of 11 gap widths. A rectangular shape was manually selected around such footprints to obtain an approximate characterization. The slightly bent short fiber observed in Fig. 6.1 evidences the need to introduce rectangular and elliptical shapes with bending. We performed a preliminary study for long fibers to see how flexible these fibers are. Fig. 6.2 shows the drastic curvature in some long fibers on a x_1, x_2-pulished plane for an end-gated plaque of 30wt% long fiber in PBT. The selection and characterization of these bent elliptical footprints requires other modifications in the method of ellipses capable of determining the tridimensional curvature of the long fibers.

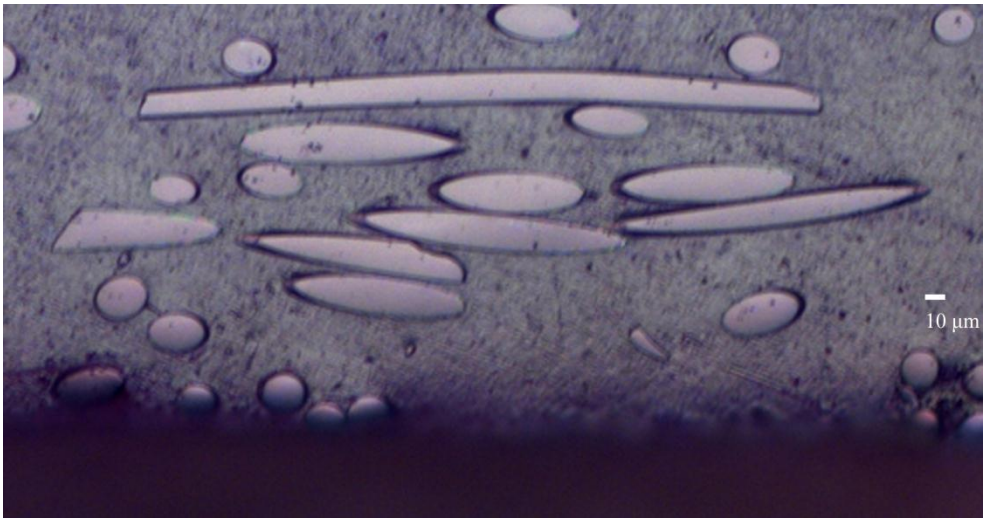

Figure 6.1 Semi-bent rectangular shape corresponding to a short fiber cut longitudinally by the polished plane. Image taken at 11 gap widths in a center-gated disk of 30wt% short fiber in PBT.

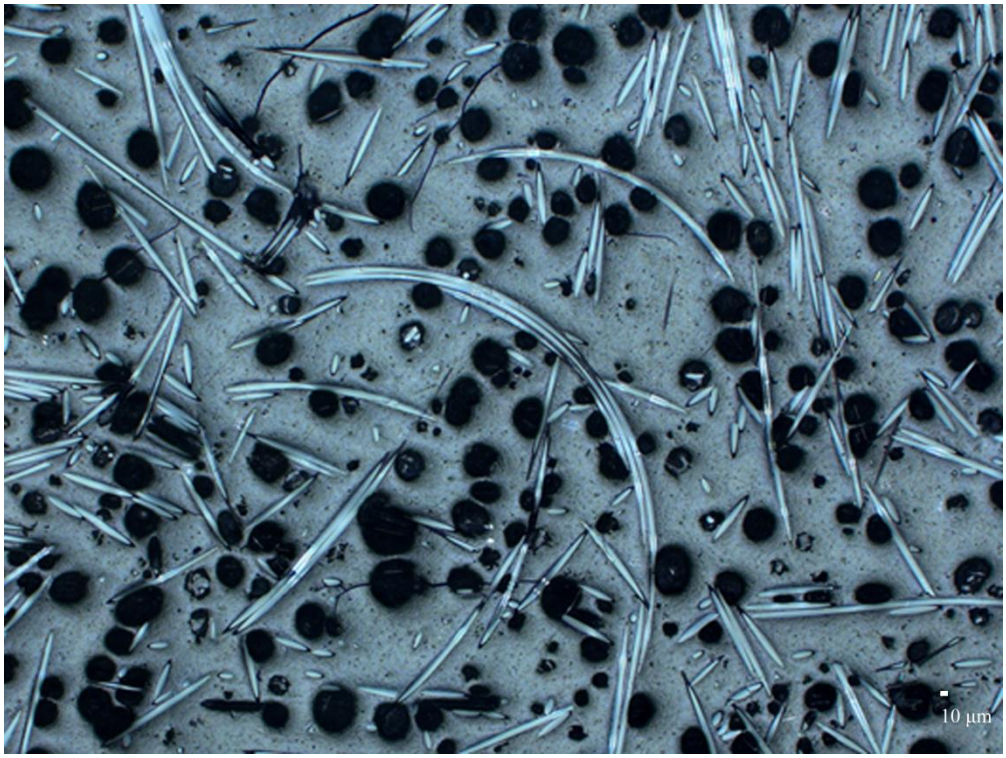

Figure 6.2 *Bent long fibers and void spaces observed in a x_1,x_2- polished plane at a radial location near the advancing front.*

Chapter 6

Study of fiber composites requires the use of test geometries where the flow field is well understood. In this dissertation, our attention was focused on center-gated disks which are axisymmetric geometries. However, the characterization of orientation can be extended to other test geometries such as the end-gated plaque. These geometries require a careful experimental design due to the complexity of the flow in the cavity. Fig. 6.3 presents an experimental design for a suitable study of fiber orientation in end-gated plaques, based on our experience with center-gated geometries. This geometry is not axisymmetric like the center-gated disks and therefore the plane of analysis must be increased. Also, this geometry shows lateral boundary effects that must be considered in the experimental design.

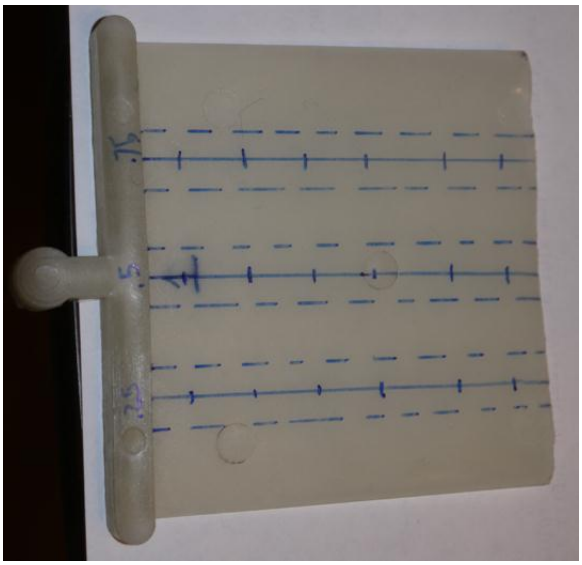

Figure 6.3 *Recommended experimental design for fiber orientation evaluation in end-gated plaques.*

One of the objectives of the modifications introduced in the method of ellipses was having the ability to measure orientation in regions with fast evolution of in orientation. This characteristic of the proposed method is suitable for performing a detailed study on critical regions such as in the advancing front or the region where the flow changes direction from the sprue to the cavity. However, our preliminary studies on these regions show a complex microtexture not observed in the cavity. The frequency and dimensions of the void spaces in these regions suggest that any study of orientation must include the characterization of void spaces frequently observed in both regions. Fig. 6.4 show many large void spaces in the change of direction

from the sprue to the cavity for a center-gated disk of 30wt% short glass fiber polypropylene. Another important microtextural aspect to be included in the characterization of orientation is the surface irregularity seen at the advancing front.

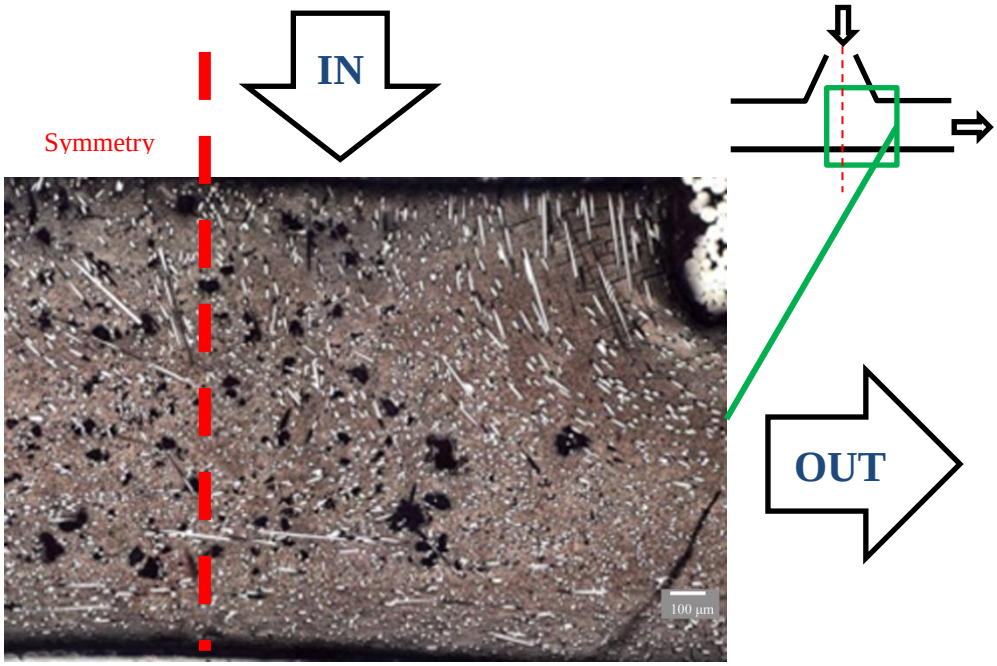

Figure 6.4 *Microtexture in the region for the change of direction from sprue to cavity in a center-gated disk of 30wt% short glass fiber polypropylene.*

6.3 Prediction of orientation

The standard model for simulating short fiber composites, the Folgar-Tucker model, predicts a faster evolution of orientation in shear flow than what is observed experimentally. Capturing the correct behavior of the orientation evolution of short fibers is essential to obtain a model capable of designing the correct molding machinery, mold, and processing conditions. The addition of a slip parameter to the Folgar-Tucker model is one of the modifications that has been proposed to slow down the orientation evolution in concentrated suspensions. However, our results indicate that the use of a slip parameter as a scaling factor may not be a good model. The use of an objective model that avoids many of the issues in regions with combined shear and extensional flow, *e.g.* center-gated disk, would be of beneficial in modeling of fiber composites. Additionally,

studying effects of the extensional flow on the slowdown of orientation would be of benefit to simulate geometries in which this kind of flow is important.

Simulations based on a decoupled flow and orientation computation are the standard approach used in the literature. In some literature considering the coupled simulations it has been found that a coupled approach may be important in the entry region for the transition and core layers. However, when compared with experimental data, the improvement in predictions of orientation due to the coupled approach is only qualitative. Some of the reasons for the discrepancies are that these simulations consider the viscous drag coefficient described by the Dinh-Armstrong model with model parameters estimated theoretically and requiring a closure approximation. Our capability to measure fiber orientation offers an area of opportunity to explore the viscous stress coefficient considering the contribution of interparticle interactions and assessing the closure approximation with experimental data.

In our simulations, the thermal effects have been neglected because of the quick filling time in the center-gated disk. An estimation of changes in temperature showed that for a filling of center-gated disk in 1 s, the changes in temperature are small. However, this is not typical in injection molded parts of commercial interest. The inclusion of thermal effects opens the opportunity to develop experiments to study the effects on orientation in the skin layer which is affected by the combination of the advancing front, thermal effects and boundary effects related to the wall. The addition of this kind of experiments and numerical simulations will help to understand the different orientation structure that is formed near the walls.

6.4 References

[1] Clarke AR, Eberhardt CN. Microscopy techniques for materials science. Boca Raton, FL, USA: CRC; 2002.

[2] Zhu YT, Blumenthal WR, Lowe TC. Determination of non-symmetric 3-D fiber-orientation distribution and average fiber length in short-fiber composites. J Compos Mater. 1997;31:1287-1301.

APPENDICES

Appendix A

APPENDIX A: CENTER-GATED DISKS' DIMENSIONS

A.1: Dimensions of for the disks used in the experimental measurements of orientation

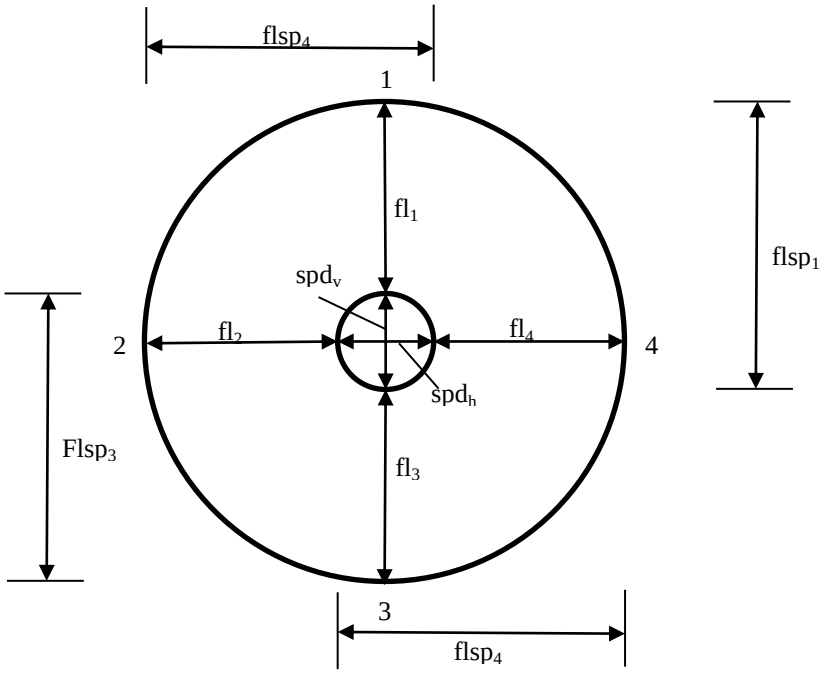

sample	Disk Mass	Disk thickness (mm)					Sprue diameter(mm)		Flow length with sprue (mm)			
	(g)	1	2	3	4	Ave	spd_v	spd_h	$flsp_1$	$flsp_2$	$flsp_3$	$flsp_4$
1	18.09	1.31	1.44	1.42	1.39	1.38	5.91	5.95	52.99	55.51	56.14	52.57
2	18.00	1.32	1.35	1.43	1.41		5.90	5.98	53.57	54.32	55.94	54.91
3	18.11	1.38	1.31	1.39	1.45		6.01	6.00	53.04	53.96	56.56	55.31

sample	Flow length					Flow length line for study	Sampling position		
	1	2	3	4	ave		10%	40%	90%
1	47.08	49.56	50.23	46.62	49.74	2	5.06	20.22	45.50
2	47.67	48.34	50.04	48.93		3	4.96	19.82	44.60
3	47.03	47.96	50.55	49.31		3	5.00	20.02	45.04

Appendix A

A.2: Average dimensions for samples 1 and 2:

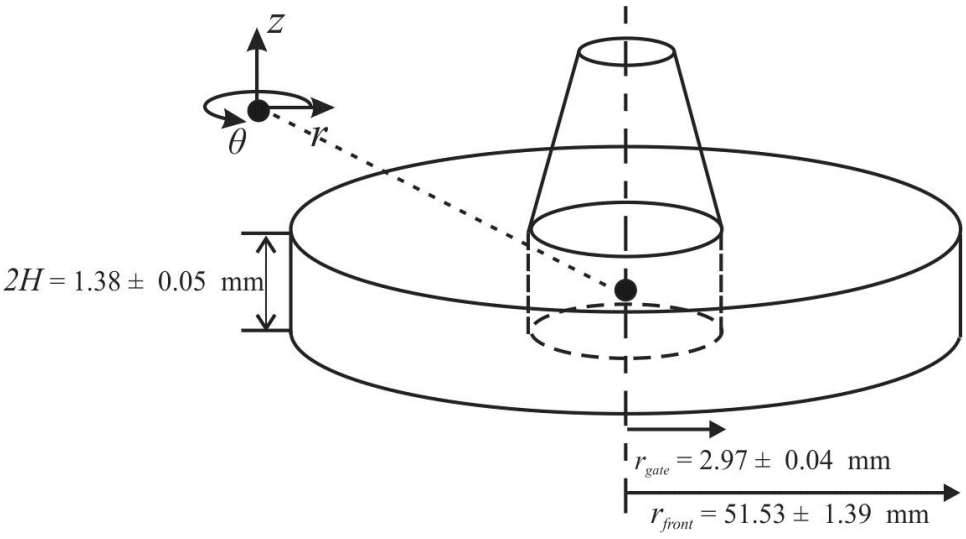

APPENDIX B: ORIENTATION ALONG THE CAVITY THICKNESS AT DIFFERENT RADIAL LOCATIONS EVALUATED BY DIFFERENT APPROACHES

Appendix B.1.1: Fiber orientation with error analysis assuming independent samples for two 1.38 mm center-gated disk made of 30 wt% glass fiber reinforced PBT (Valox 420) measured at r/H = 4.3 (1% of flow length). Measurements were evaluated by considered elliptical and partial ellipses of any size (VWB approach).

z/H	*Center-gated disk 1*									*Center-gated disk 2*								
	Orientation component						F_a	H	ϕ_v	Orientation component						F_a	H	ϕ_v
	A_{rr}	A_{zz}	$A_{\theta\theta}$	A_{rz}	$A_{r\theta}$	$A_{z\theta}$				A_{rr}	A_{zz}	$A_{\theta\theta}$	A_{rz}	$A_{r\theta}$	$A_{z\theta}$			
0.92	0.82	0.03	0.15	0.05	0.13	0.02	28.63	85.99	0.16	0.58	0.01	0.4	-0.03	-0.09	0.00	44.6	74.63	0.16
0.75	0.78	0.05	0.17	0.1	0.07	0.01	25.77	70.93	0.13	0.72	0.03	0.25	0.07	-0.09	-0.02	35.71	80.61	0.14
0.58	0.59	0.05	0.36	0.09	0.11	-0.01	37.21	65.68	0.18	0.74	0.05	0.21	0.06	-0.12	0.01	41.89	104.1	0.20
0.42	0.63	0.03	0.34	0.09	0.03	-0.01	45.52	84.46	0.15	0.75	0.03	0.22	0.03	-0.08	0.01	39.83	97.83	0.21
0.25	0.74	0.02	0.24	0.05	0.02	0.01	27.89	64.43	0.15	0.67	0.04	0.29	0.03	-0.18	-0.01	40.3	79.25	0.18
0.08	0.7	0.02	0.28	0.09	-0.11	-0.02	41.02	87.46	0.16	0.53	0.01	0.46	0.04	-0.11	-0.01	56.73	90.42	0.16
0.00	0.46	0.02	0.53	0.01	0.02	0.01	51.7	75.63	---	0.35	0.02	0.63	-0.01	-0.03	-0.02	69.84	90.83	---
-0.08	0.25	0.02	0.74	0.01	0.12	0.00	81.55	95.62	0.20	0.44	0.02	0.54	0.01	-0.06	-0.03	81.66	123.54	0.26
-0.25	0.5	0.02	0.48	0.00	0.18	0.02	50.84	80.39	0.23	0.67	0.02	0.32	-0.08	-0.05	-0.02	59.62	119.63	0.25
-0.42	0.72	0.01	0.27	0.02	0.16	-0.01	50.93	110.88	0.23	0.59	0.02	0.39	-0.02	0.05	-0.04	48.55	81.55	0.13
-0.58	0.61	0.01	0.38	0.02	0.10	0.00	40.35	71.57	0.13	0.6	0.03	0.37	0.00	0.01	-0.04	46.01	81.18	0.17
-0.75	0.43	0.03	0.54	0.01	-0.08	-0.01	46.68	64.86	0.13	0.66	0.03	0.32	-0.03	-0.05	0.00	37.06	75.27	0.17
-0.92	0.22	0.02	0.75	0.02	0.04	-0.06	32.87	37.82	0.09	0.62	0.02	0.36	-0.01	0.14	-0.02	36.8	66.39	0.15

z/H	*Average orientation and error for two independent center-gated disks*													
	Orientation component						$\langle\phi_v\rangle$	Standard Error						
	$\langle A_{rr}\rangle$	$\langle A_{zz}\rangle$	$\langle A_{\theta\theta}\rangle$	$\langle A_{rz}\rangle$	$\langle A_{r\theta}\rangle$	$\langle A_{z\theta}\rangle$		$SE_{\langle A_{rr}\rangle}$	$SE_{\langle A_{zz}\rangle}$	$SE_{\langle A_{\theta\theta}\rangle}$	$SE_{\langle A_{rz}\rangle}$	$SE_{\langle A_{r\theta}\rangle}$	$SE_{\langle A_{z\theta}\rangle}$	$SE_{\langle\phi_v\rangle}$
0.92	0.71	0.02	0.27	0.01	0.03	0.01	0.16	0.06	0.00	0.06	0.02	0.05	0.06	0.00
0.75	0.75	0.04	0.21	0.08	-0.02	-0.01	0.13	0.02	0.00	0.02	0.01	0.04	0.02	0.00
0.58	0.69	0.05	0.27	0.07	-0.03	0.00	0.19	0.04	0.00	0.04	0.01	0.06	0.04	0.00
0.42	0.69	0.03	0.28	0.06	-0.03	0.00	0.18	0.03	0.00	0.03	0.02	0.03	0.03	0.01
0.25	0.70	0.03	0.27	0.04	-0.09	0.00	0.17	0.02	0.00	0.01	0.00	0.05	0.02	0.01
0.08	0.61	0.02	0.37	0.06	-0.11	-0.02	0.16	0.04	0.00	0.04	0.01	0.00	0.04	0.00
0.00	0.40	0.02	0.58	-0.01	-0.01	-0.01	---	0.03	0.00	0.03	0.00	0.01	0.03	---
-0.08	0.36	0.02	0.63	0.01	0.02	-0.01	0.23	0.05	0.00	0.05	0.00	0.05	0.05	0.02
-0.25	0.60	0.02	0.38	-0.05	0.05	0.00	0.24	0.04	0.00	0.04	0.02	0.06	0.04	0.00
-0.42	0.67	0.02	0.32	0.00	0.11	-0.03	0.19	0.03	0.00	0.03	0.01	0.03	0.03	0.02
-0.58	0.61	0.02	0.37	0.01	0.05	-0.02	0.15	0.00	0.00	0.00	0.00	0.02	0.00	0.01
-0.75	0.55	0.03	0.42	-0.01	-0.07	-0.01	0.15	0.06	0.00	0.06	0.01	0.01	0.06	0.01
-0.92	0.48	0.02	0.50	0.00	0.10	-0.03	0.13	0.10	0.00	0.10	0.01	0.02	0.10	0.02

Appendix B.1.2: Fiber orientation with error analysis assuming independent samples for two 1.38 mm center-gated disk made of 30 wt% glass fiber reinforced PBT (Valox 420) measured at r/H = 11 (10% of flow length). Measurements were evaluated by considered elliptical and partial ellipses of any size (VWB approach).

z/H	*Center-gated disk 1*									*Center-gated disk 2*								
	Orientation component						F_a	H	ϕ_v	Orientation component						F_a	H	ϕ_v
	A_{rr}	A_{zz}	$A_{\theta\theta}$	A_{rz}	$A_{r\theta}$	$A_{z\theta}$				A_{rr}	A_{zz}	$A_{\theta\theta}$	A_{rz}	$A_{r\theta}$	$A_{z\theta}$			
0.92	0.52	0.05	0.43	0.06	0.13	0.05	49.51	78.36	0.14	0.59	0.01	0.40	0.02	0.03	0.01	49.15	82.87	0.14
0.75	0.78	0.03	0.20	0.08	0.15	0.02	32.05	84.27	0.13	0.78	0.01	0.20	0.00	0.01	0.01	30.74	76.84	0.16
0.58	0.75	0.04	0.21	0.07	0.10	0.02	48.63	118.76	0.21	0.75	0.02	0.23	0.00	-0.08	0.00	45.17	105.16	0.18
0.42	0.55	0.03	0.42	0.02	0.02	0.02	46.96	73.98	0.11	0.64	0.01	0.35	0.02	0.05	0.00	43.67	79.82	0.16
0.25	0.48	0.03	0.49	-0.02	0.01	0.00	62.52	97.41	0.16	0.46	0.02	0.53	-0.02	-0.06	0.00	56.84	81.23	0.14
0.08	0.31	0.01	0.68	-0.02	0.07	-0.01	85.08	105.08	0.18	0.38	0.02	0.61	-0.04	-0.13	0.00	79.67	107.71	0.18
0.00	0.30	0.01	0.69	-0.02	0.06	0.00	68.69	83.24	---	0.28	0.01	0.70	-0.04	-0.13	0.01	75.14	88.93	---
-0.08	0.30	0.02	0.68	-0.04	0.05	0.00	88.38	108.14	0.19	0.34	0.02	0.64	-0.06	-0.06	-0.01	88.48	110.30	0.20
-0.25	0.59	0.04	0.37	-0.06	0.09	0.00	57.90	100.77	0.16	0.44	0.04	0.52	-0.06	0.11	-0.05	56.07	78.99	0.13
-0.42	0.65	0.01	0.33	-0.04	0.01	0.00	53.90	98.07	0.16	0.60	0.02	0.38	-0.01	0.03	-0.02	37.65	61.84	0.11
-0.58	0.52	0.01	0.47	-0.03	0.03	-0.01	55.06	83.99	0.15	0.69	0.01	0.30	-0.01	0.05	-0.02	36.87	72.95	0.13
-0.75	0.61	0.01	0.38	-0.02	0.17	-0.01	46.99	81.70	0.16	0.69	0.01	0.30	0.01	-0.03	-0.02	43.82	90.51	0.17
-0.92	0.72	0.02	0.26	-0.01	0.02	0.00	37.72	86.31	0.14	0.45	0.02	0.53	-0.06	0.18	-0.04	58.75	81.41	0.14

z/H	*Average orientation and error for two independent center-gated disks*													
	Orientation component						$\langle\phi_v\rangle$	Standard Error						
	$\langle A_{rr}\rangle$	$\langle A_{zz}\rangle$	$\langle A_{\theta\theta}\rangle$	$\langle A_{rz}\rangle$	$\langle A_{r\theta}\rangle$	$\langle A_{z\theta}\rangle$		$SE_{\langle A_{rr}\rangle}$	$SE_{\langle A_{zz}\rangle}$	$SE_{\langle A_{\theta\theta}\rangle}$	$SE_{\langle A_{rz}\rangle}$	$SE_{\langle A_{r\theta}\rangle}$	$SE_{\langle A_{z\theta}\rangle}$	$SE_{\langle\phi_v\rangle}$
0.92	0.56	0.03	0.41	0.04	0.08	0.03	0.14	0.02	0.01	0.01	0.01	0.03	0.01	0.00
0.75	0.78	0.02	0.20	0.04	0.08	0.02	0.14	0.00	0.00	0.00	0.02	0.03	0.00	0.01
0.58	0.75	0.03	0.22	0.04	0.02	0.01	0.20	0.00	0.01	0.01	0.02	0.05	0.01	0.01
0.42	0.59	0.02	0.39	0.02	0.04	0.01	0.14	0.02	0.00	0.02	0.00	0.01	0.01	0.01
0.25	0.47	0.03	0.51	-0.02	-0.02	0.00	0.15	0.01	0.00	0.01	0.00	0.02	0.00	0.01
0.08	0.34	0.02	0.64	-0.03	-0.03	0.00	0.18	0.02	0.00	0.02	0.01	0.05	0.00	0.00
0.00	0.29	0.01	0.70	-0.03	-0.03	0.00	---	0.00	0.00	0.00	0.00	0.05	0.00	---
-0.08	0.32	0.02	0.66	-0.05	-0.01	-0.01	0.19	0.01	0.00	0.01	0.00	0.03	0.00	0.00
-0.25	0.52	0.04	0.44	-0.06	0.10	-0.02	0.15	0.04	0.00	0.04	0.00	0.00	0.01	0.01
-0.42	0.63	0.02	0.35	-0.03	0.02	-0.01	0.14	0.01	0.00	0.01	0.01	0.01	0.00	0.01
-0.58	0.60	0.01	0.39	-0.02	0.04	-0.02	0.14	0.04	0.00	0.04	0.00	0.00	0.00	0.00
-0.75	0.65	0.01	0.34	-0.01	0.06	-0.01	0.16	0.02	0.00	0.02	0.01	0.05	0.00	0.00
-0.92	0.59	0.02	0.39	-0.03	0.10	-0.02	0.14	0.07	0.00	0.07	0.01	0.04	0.01	0.00

Appendix B.1.3: Fiber orientation with error analysis assuming independent samples for two 1.38 mm center-gated disk made of 30 wt% glass fiber reinforced PBT (Valox 420) measured at r/H = 32 (40% of flow length). Measurements were evaluated by considered elliptical and partial ellipses of any size (VWB approach).

z/H	*Center-gated disk 1*									*Center-gated disk 2*								
	Orientation component						F_a	H	ϕ_v	Orientation component						F_a	H	ϕ_v
	A_{rr}	A_{zz}	$A_{\theta\theta}$	A_{rz}	$A_{r\theta}$	$A_{z\theta}$				A_{rr}	A_{zz}	$A_{\theta\theta}$	A_{rz}	$A_{r\theta}$	$A_{z\theta}$			
0.92	0.61	0.01	0.37	0.01	0.11	0.00	55.48	95.04	0.14	0.62	0.02	0.36	-0.02	-0.01	0.01	58.78	106.51	0.17
0.75	0.77	0.00	0.23	0.01	-0.07	0.00	49.86	118.64	0.18	0.71	0.01	0.28	-0.01	0.12	-0.01	37.56	79.24	0.14
0.58	0.85	0.01	0.15	0.00	0.03	0.00	32.70	103.02	0.21	0.85	0.01	0.15	0.01	-0.04	-0.01	34.89	115.18	0.18
0.42	0.83	0.02	0.14	0.01	-0.01	-0.02	34.64	106.11	0.18	0.72	0.04	0.24	0.05	0.00	0.00	42.03	95.85	0.16
0.25	0.61	0.04	0.35	-0.02	0.06	-0.01	59.66	104.21	0.16	0.58	0.02	0.40	0.05	0.10	-0.01	53.02	89.25	0.12
0.08	0.27	0.01	0.72	0.00	-0.13	0.00	94.44	112.00	0.17	0.31	0.02	0.67	0.02	-0.04	-0.01	90.19	109.46	0.16
0.00	0.31	0.02	0.68	-0.02	-0.17	0.01	92.76	113.84	---	0.40	0.01	0.59	-0.01	-0.07	-0.03	80.44	106.00	---
-0.08	0.27	0.02	0.71	-0.02	-0.06	-0.01	116.63	138.51	0.22	0.44	0.01	0.55	-0.02	-0.18	-0.02	94.48	127.77	0.22
-0.25	0.70	0.02	0.28	-0.04	0.10	-0.01	42.43	93.26	0.15	0.65	0.02	0.33	-0.04	0.03	-0.05	41.37	78.39	0.13
-0.42	0.87	0.03	0.11	-0.01	0.02	-0.01	35.55	136.14	0.22	0.84	0.02	0.13	-0.02	0.11	-0.01	36.88	112.90	0.17
-0.58	0.71	0.02	0.27	-0.02	0.07	0.01	31.54	66.64	0.12	0.78	0.01	0.21	0.01	0.00	0.00	40.47	99.96	0.15
-0.75	0.81	0.01	0.18	0.03	-0.01	0.00	34.48	94.16	0.14	0.72	0.02	0.26	-0.04	0.04	-0.01	37.33	82.74	0.12
-0.92	0.75	0.03	0.22	-0.08	0.07	-0.01	40.75	96.72	0.16	0.57	0.02	0.40	-0.01	0.04	-0.04	69.54	118.18	0.18

z/H	*Average orientation and error for two independent center-gated disks*													
	Orientation component						$\langle\phi_v\rangle$	Standard Error						
	$\langle A_{rr}\rangle$	$\langle A_{zz}\rangle$	$\langle A_{\theta\theta}\rangle$	$\langle A_{rz}\rangle$	$\langle A_{r\theta}\rangle$	$\langle A_{z\theta}\rangle$		$SE_{\langle A_{rr}\rangle}$	$SE_{\langle A_{zz}\rangle}$	$SE_{\langle A_{\theta\theta}\rangle}$	$SE_{\langle A_{rz}\rangle}$	$SE_{\langle A_{r\theta}\rangle}$	$SE_{\langle A_{z\theta}\rangle}$	$SE_{\langle\phi_v\rangle}$
0.92	0.62	0.01	0.37	0.00	0.05	0.01	0.15	0.02	0.01	0.01	0.01	0.03	0.01	0.01
0.75	0.74	0.01	0.25	0.00	0.01	0.00	0.16	0.00	0.00	0.00	0.02	0.03	0.00	0.01
0.58	0.85	0.01	0.15	0.01	-0.01	0.00	0.20	0.00	0.01	0.01	0.02	0.05	0.01	0.01
0.42	0.78	0.03	0.19	0.03	0.00	-0.01	0.17	0.02	0.00	0.02	0.00	0.01	0.01	0.01
0.25	0.59	0.03	0.37	0.01	0.08	-0.01	0.14	0.01	0.00	0.01	0.00	0.02	0.00	0.01
0.08	0.29	0.02	0.69	0.01	-0.09	-0.01	0.17	0.02	0.00	0.02	0.01	0.05	0.00	0.00
0.00	0.35	0.02	0.63	-0.01	-0.12	-0.01	---	0.00	0.00	0.00	0.00	0.05	0.00	---
-0.08	0.35	0.02	0.63	-0.02	-0.12	-0.01	0.22	0.01	0.00	0.01	0.00	0.03	0.00	0.00
-0.25	0.68	0.02	0.30	-0.04	0.07	-0.03	0.14	0.04	0.00	0.04	0.00	0.00	0.01	0.00
-0.42	0.86	0.03	0.12	-0.01	0.06	-0.01	0.19	0.01	0.00	0.01	0.01	0.01	0.00	0.01
-0.58	0.75	0.01	0.23	0.00	0.03	0.00	0.14	0.04	0.00	0.04	0.00	0.00	0.00	0.01
-0.75	0.77	0.02	0.22	0.00	0.01	0.00	0.13	0.02	0.00	0.02	0.01	0.05	0.00	0.00
-0.92	0.66	0.03	0.32	-0.04	0.05	-0.03	0.17	0.07	0.00	0.07	0.01	0.04	0.01	0.00

Appendix B.1.4: Fiber orientation with error analysis assuming independent samples for two 1.38 mm center-gated disk made of 30 wt% glass fiber reinforced PBT (Valox 420) measured at r/H = 68 (90% of flow length). Measurements were evaluated by considered elliptical and partial ellipses of any size (VWB approach).

z/H	*Center-gated disk 1*									*Center-gated disk 2*								
	Orientation component						F_a	H	ϕ_v	Orientation component						F_a	H	ϕ_v
	A_{rr}	A_{zz}	$A_{\theta\theta}$	A_{rz}	$A_{r\theta}$	$A_{z\theta}$				A_{rr}	A_{zz}	$A_{\theta\theta}$	A_{rz}	$A_{r\theta}$	$A_{z\theta}$			
0.92	0.77	0.01	0.22	-0.01	0.10	0.00	36.97	90.43	0.16	0.71	0.02	0.27	-0.05	0.09	0.00	39.22	81.84	0.14
0.75	0.52	0.02	0.45	-0.04	-0.07	0.01	33.34	51.29	0.08	0.55	0.03	0.42	-0.02	0.03	0.03	53.85	86.39	0.15
0.58	0.61	0.02	0.37	-0.04	0.14	-0.01	38.87	69.55	0.13	0.56	0.04	0.40	-0.06	0.10	0.01	46.52	80.54	0.13
0.42	0.63	0.04	0.34	-0.02	0.02	0.00	46.27	88.54	0.12	0.63	0.02	0.35	-0.06	0.11	0.01	44.84	82.20	0.16
0.25	0.54	0.02	0.44	0.00	0.11	0.01	47.03	74.67	0.12	0.48	0.01	0.51	-0.02	0.02	0.02	58.60	85.01	0.12
0.08	0.21	0.03	0.76	0.00	0.03	0.02	120.74	138.43	0.23	0.19	0.02	0.79	-0.02	-0.09	0.02	116.38	129.35	0.19
0.00	0.21	0.04	0.75	-0.03	-0.07	0.01	111.41	127.27	---	0.20	0.02	0.78	-0.03	-0.15	0.05	102.34	114.77	---
-0.08	0.25	0.03	0.72	-0.05	0.01	0.01	110.56	130.14	0.20	0.21	0.02	0.77	-0.05	-0.03	0.02	121.06	136.45	0.20
-0.25	0.57	0.04	0.38	-0.05	0.10	0.00	43.69	76.96	0.14	0.55	0.03	0.41	-0.03	0.04	0.01	54.90	92.30	0.12
-0.42	0.72	0.02	0.26	-0.02	-0.01	0.00	43.24	97.93	0.16	0.64	0.02	0.35	-0.03	0.00	0.00	48.45	89.82	0.17
-0.58	0.60	0.01	0.38	0.02	0.08	0.00	46.61	82.34	0.16	0.57	0.03	0.40	-0.03	0.02	-0.02	50.27	82.89	0.13
-0.75	0.66	0.02	0.32	0.04	0.14	0.02	48.07	89.77	0.13	0.77	0.01	0.22	-0.02	0.04	0.00	44.56	105.08	0.16
-0.92	0.72	0.04	0.24	0.07	0.00	0.03	46.22	108.61	0.16	0.73	0.02	0.26	-0.02	0.07	-0.01	39.52	90.97	0.17

z/H	*Average orientation and error for two independent center-gated disks*													
	Orientation component						$\langle\phi_v\rangle$	Standard Error						
	$\langle A_{rr}\rangle$	$\langle A_{zz}\rangle$	$\langle A_{\theta\theta}\rangle$	$\langle A_{rz}\rangle$	$\langle A_{r\theta}\rangle$	$\langle A_{z\theta}\rangle$		$SE_{\langle A_{rr}\rangle}$	$SE_{\langle A_{zz}\rangle}$	$SE_{\langle A_{\theta\theta}\rangle}$	$SE_{\langle A_{rz}\rangle}$	$SE_{\langle A_{r\theta}\rangle}$	$SE_{\langle A_{z\theta}\rangle}$	$SE_{\langle\phi_v\rangle}$
0.92	0.74	0.01	0.25	-0.03	0.09	0.00	0.15	0.01	0.00	0.01	0.01	0.00	0.00	0.01
0.75	0.54	0.03	0.43	-0.03	-0.01	0.02	0.12	0.01	0.00	0.01	0.01	0.02	0.00	0.02
0.58	0.58	0.03	0.39	-0.05	0.12	0.00	0.13	0.01	0.00	0.01	0.00	0.01	0.00	0.00
0.42	0.63	0.03	0.35	-0.04	0.06	0.00	0.14	0.00	0.00	0.00	0.01	0.02	0.00	0.01
0.25	0.51	0.01	0.48	-0.01	0.06	0.01	0.12	0.02	0.00	0.02	0.00	0.02	0.00	0.00
0.08	0.20	0.03	0.77	-0.01	-0.03	0.02	0.21	0.00	0.00	0.01	0.01	0.03	0.00	0.01
0.00	0.21	0.03	0.76	-0.03	-0.11	0.03	---	0.00	0.00	0.01	0.00	0.02	0.01	---
-0.08	0.23	0.02	0.75	-0.05	-0.01	0.02	0.20	0.01	0.00	0.01	0.00	0.01	0.00	0.00
-0.25	0.56	0.04	0.40	-0.04	0.06	0.01	0.13	0.00	0.00	0.01	0.01	0.02	0.00	0.01
-0.42	0.68	0.02	0.30	-0.02	-0.01	0.00	0.16	0.02	0.00	0.02	0.00	0.00	0.00	0.00
-0.58	0.59	0.02	0.39	-0.01	0.05	-0.01	0.14	0.01	0.00	0.00	0.01	0.01	0.00	0.01
-0.75	0.72	0.01	0.27	0.00	0.09	0.01	0.15	0.03	0.00	0.03	0.02	0.02	0.00	0.01
-0.92	0.72	0.03	0.25	0.03	0.03	0.01	0.17	0.00	0.01	0.00	0.02	0.02	0.01	0.00

Appendix B.2.1: Fiber orientation with error analysis assuming independent samples for two 1.38 mm center-gated disk made of 30 wt% glass fiber reinforced PBT (Valox 420) measured at r/H = 4.3 (1% of flow length). Measurements were evaluated by considering elliptical and partial ellipses having areas larger than half ellipse (BT approach).

z/H	*Center-gated disk 1*							*Center-gated disk 2*						
	Orientation component				F_a	H	ϕ_v	Orientation component				F_a	H	ϕ_v
	A_{rr}	A_{zz}	$A_{\theta\theta}$	A_{rz}				A_{rr}	A_{zz}	$A_{\theta\theta}$	A_{rz}			
0.92	0.83	0.04	0.13	-0.07	28	103.85	0.16	0.61	0.01	0.38	0.03	44	80.04	0.16
0.75	0.77	0.02	0.21	-0.06	23	57.88	0.13	0.72	0.05	0.23	-0.09	31	79.05	0.14
0.58	0.69	0.06	0.25	-0.13	36	88.23	0.18	0.76	0.04	0.20	-0.06	43	119.93	0.20
0.42	0.63	0.03	0.34	-0.09	42	83.67	0.15	0.79	0.03	0.18	0.00	35	103.68	0.21
0.25	0.80	0.02	0.18	-0.08	27	85.21	0.15	0.70	0.04	0.27	-0.08	41	93.67	0.18
0.08	0.69	0.02	0.30	-0.08	38	81.68	0.16	0.56	0.01	0.42	-0.04	52	91.89	0.16
0.00	0.68	0.02	0.30	-0.01	18	38.84	---	0.32	0.02	0.67	-0.02	28	35.50	---
-0.08	0.24	0.01	0.75	-0.01	76	89.91	0.20	0.51	0.02	0.47	-0.02	84	150.66	0.26
-0.25	0.55	0.01	0.44	-0.01	53	95.05	0.23	0.72	0.02	0.26	0.10	53	130.38	0.25
-0.42	0.73	0.01	0.26	-0.04	48	114.44	0.23	0.56	0.02	0.42	0.02	44	73.12	0.13
-0.58	0.55	0.01	0.44	0.00	38	61.34	0.13	0.66	0.02	0.32	-0.01	45	91.55	0.17
-0.75	0.38	0.03	0.59	0.00	46	62.51	0.13	0.65	0.04	0.32	0.05	40	87.56	0.17
-0.92	0.23	0.02	0.75	-0.02	32	37.65	0.09	0.65	0.02	0.33	0.01	36	72.03	0.15

z/H	*Average orientation and error for two independent center-gated disks*									
	Orientation component				$\langle \phi_v \rangle$	Standard Error				
	$\langle A_{rr} \rangle$	$\langle A_{zz} \rangle$	$\langle A_{\theta\theta} \rangle$	$\langle A_{rz} \rangle$		$SE_{\langle A_{rr} \rangle}$	$SE_{\langle A_{zz} \rangle}$	$SE_{\langle A_{\theta\theta} \rangle}$	$SE_{\langle A_{rz} \rangle}$	$SE_{\langle \phi_v \rangle}$
0.92	0.73	0.03	0.24	-0.02	0.16	0.06	0.01	0.06	0.02	0.00
0.75	0.74	0.04	0.22	-0.08	0.13	0.01	0.01	0.01	0.01	0.00
0.58	0.73	0.05	0.22	-0.09	0.19	0.02	0.00	0.01	0.02	0.00
0.42	0.72	0.03	0.25	-0.04	0.18	0.04	0.00	0.04	0.02	0.01
0.25	0.74	0.03	0.23	-0.08	0.16	0.03	0.00	0.02	0.00	0.01
0.08	0.62	0.02	0.36	-0.06	0.16	0.03	0.00	0.03	0.01	0.00
0.00	0.51	0.02	0.48	-0.02	---	0.09	0.00	0.09	0.00	---
-0.08	0.41	0.02	0.57	-0.02	0.24	0.07	0.00	0.07	0.00	0.02
-0.25	0.65	0.02	0.34	0.05	0.24	0.04	0.00	0.04	0.03	0.00
-0.42	0.66	0.01	0.32	-0.02	0.19	0.04	0.00	0.04	0.02	0.02
-0.58	0.62	0.01	0.37	0.00	0.15	0.03	0.00	0.03	0.00	0.01
-0.75	0.54	0.03	0.43	0.03	0.16	0.07	0.00	0.07	0.01	0.01
-0.92	0.50	0.02	0.48	0.00	0.13	0.10	0.00	0.10	0.01	0.02

Appendix B.2.2: Fiber orientation with error analysis assuming independent samples for two 1.38 mm center-gated disk made of 30 wt% glass fiber reinforced PBT (Valox 420) measured at r/H = 11 (10% of flow length). Measurements were evaluated by considering elliptical and partial ellipses having areas larger than half ellipse (BT approach).

z/H	*Center-gated disk 1*							*Center-gated disk 2*						
	Orientation component				F_a	H	ϕ_v	Orientation component				F_a	H	ϕ_v
	A_{rr}	A_{zz}	$A_{\theta\theta}$	A_{rz}				A_{rr}	A_{zz}	$A_{\theta\theta}$	A_{rz}			
0.92	0.57	0.03	0.40	-0.06	48	83.51	0.14	0.60	0.01	0.39	-0.02	49	86.91	0.14
0.75	0.76	0.03	0.21	-0.06	31	83.18	0.13	0.82	0.01	0.17	0.01	30	92.17	0.16
0.58	0.79	0.04	0.17	-0.10	41	125.62	0.21	0.79	0.02	0.20	0.00	38	105.86	0.18
0.42	0.52	0.01	0.46	-0.01	42	65.16	0.11	0.62	0.01	0.36	-0.02	52	98.14	0.16
0.25	0.50	0.01	0.49	0.04	59	96.41	0.16	0.59	0.01	0.40	0.01	54	102.63	0.14
0.08	0.34	0.01	0.65	0.00	85	112.55	0.18	0.30	0.02	0.68	0.03	80	100.15	0.18
0.00	0.18	0.01	0.81	0.02	37	41.35	---	0.22	0.01	0.77	0.02	42	47.95	---
-0.08	0.33	0.02	0.66	0.05	87	110.96	0.19	0.37	0.02	0.61	0.07	84	112.75	0.20
-0.25	0.58	0.03	0.38	0.03	53	93.44	0.16	0.43	0.02	0.55	0.05	57	79.93	0.13
-0.42	0.56	0.02	0.43	0.03	54	87.94	0.16	0.59	0.04	0.37	0.03	40	70.33	0.11
-0.58	0.58	0.01	0.41	0.04	49	85.51	0.15	0.72	0.01	0.27	0.01	35	78.76	0.13
-0.75	0.66	0.01	0.34	0.02	43	87.56	0.16	0.73	0.01	0.26	-0.02	43	105.55	0.17
-0.92	0.76	0.02	0.22	0.01	38	102.85	0.14	0.46	0.02	0.52	0.06	59	85.33	0.14

z/H	*Average orientation and error for two independent center-gated disks*									
	Orientation component				$\langle \phi_v \rangle$	Standard Error				
	$\langle A_{rr} \rangle$	$\langle A_{zz} \rangle$	$\langle A_{\theta\theta} \rangle$	$\langle A_{rz} \rangle$		$SE_{\langle A_{rr} \rangle}$	$SE_{\langle A_{zz} \rangle}$	$SE_{\langle A_{\theta\theta} \rangle}$	$SE_{\langle A_{rz} \rangle}$	$SE_{\langle \phi_v \rangle}$
0.92	0.58	0.02	0.40	-0.04	0.14	0.01	0.01	0.00	0.01	0.00
0.75	0.79	0.02	0.19	-0.02	0.15	0.01	0.00	0.01	0.02	0.01
0.58	0.79	0.03	0.18	-0.05	0.20	0.00	0.01	0.01	0.02	0.01
0.42	0.58	0.01	0.40	-0.01	0.14	0.02	0.00	0.02	0.00	0.01
0.25	0.54	0.01	0.44	0.02	0.15	0.02	0.00	0.02	0.01	0.01
0.08	0.32	0.01	0.67	0.01	0.18	0.01	0.00	0.01	0.01	0.00
0.00	0.20	0.01	0.79	0.02	---	0.01	0.00	0.01	0.00	---
-0.08	0.35	0.02	0.63	0.06	0.19	0.01	0.00	0.01	0.01	0.00
-0.25	0.51	0.03	0.46	0.04	0.15	0.04	0.00	0.04	0.01	0.01
-0.42	0.57	0.03	0.40	0.03	0.14	0.01	0.01	0.01	0.00	0.01
-0.58	0.65	0.01	0.34	0.02	0.14	0.03	0.00	0.03	0.01	0.00
-0.75	0.70	0.01	0.29	0.00	0.16	0.02	0.00	0.02	0.01	0.00
-0.92	0.62	0.02	0.36	0.03	0.14	0.07	0.00	0.07	0.01	0.00

Appendix B.2.3: Fiber orientation with error analysis assuming independent samples for two 1.38 mm center-gated disk made of 30 wt% glass fiber reinforced PBT (Valox 420) measured at r/H = 32 (40% of flow length). Measurements were evaluated by considering elliptical and partial ellipses having areas larger than half ellipse (BT approach).

z/H	*Center-gated disk 1*							*Center-gated disk 2*						
	Orientation component				F_a	H	ϕ_v	Orientation component				F_a	H	ϕ_v
	A_{rr}	A_{zz}	$A_{\theta\theta}$	A_{rz}				A_{rr}	A_{zz}	$A_{\theta\theta}$	A_{rz}			
0.92	0.63	0.01	0.36	-0.01	54	100.34	0.14	0.66	0.02	0.33	0.01	59	123.13	0.17
0.75	0.79	0.00	0.21	-0.01	46	122.70	0.18	0.70	0.01	0.29	0.02	37	82.85	0.14
0.58	0.89	0.01	0.11	-0.01	33	140.09	0.21	0.89	0.01	0.11	-0.02	34	152.29	0.18
0.42	0.78	0.03	0.19	0.00	37	95.47	0.18	0.74	0.04	0.22	-0.06	46	118.18	0.16
0.25	0.62	0.04	0.34	0.03	56	105.33	0.16	0.55	0.02	0.42	-0.04	48	81.47	0.12
0.08	0.27	0.01	0.72	0.00	86	104.13	0.17	0.32	0.02	0.66	-0.03	86	107.53	0.16
0.00	0.27	0.01	0.72	0.00	48	58.62	---	0.28	0.01	0.70	0.01	52	62.69	---
-0.08	0.26	0.02	0.72	0.03	123	147.75	0.22	0.44	0.01	0.55	0.02	97	135.94	0.22
-0.25	0.75	0.02	0.23	0.06	36	94.49	0.15	0.63	0.02	0.34	0.03	45	85.78	0.13
-0.42	0.90	0.02	0.07	0.00	32	179.23	0.22	0.88	0.02	0.10	0.03	34	135.14	0.17
-0.58	0.76	0.02	0.22	0.03	31	78.88	0.12	0.81	0.01	0.19	-0.01	40	116.86	0.15
-0.75	0.83	0.01	0.16	-0.04	34	110.86	0.14	0.74	0.02	0.23	0.03	38	95.98	0.12
-0.92	0.78	0.03	0.19	0.08	41	117.37	0.16	0.60	0.03	0.38	0.00	69	128.41	0.18

z/H	*Average orientation and error for two independent center-gated disks*									
	Orientation component				$\langle \phi_v \rangle$	Standard Error				
	$\langle A_{rr} \rangle$	$\langle A_{zz} \rangle$	$\langle A_{\theta\theta} \rangle$	$\langle A_{rz} \rangle$		$SE_{\langle A_{rr} \rangle}$	$SE_{\langle A_{zz} \rangle}$	$SE_{\langle A_{\theta\theta} \rangle}$	$SE_{\langle A_{rz} \rangle}$	$SE_{\langle \phi_v \rangle}$
0.92	0.65	0.01	0.34	0.01	0.15	0.01	0.00	0.01	0.01	0.01
0.75	0.75	0.01	0.24	0.00	0.16	0.02	0.00	0.02	0.01	0.01
0.58	0.89	0.01	0.11	-0.02	0.20	0.00	0.00	0.00	0.00	0.01
0.42	0.76	0.03	0.21	-0.04	0.17	0.01	0.00	0.01	0.01	0.01
0.25	0.59	0.03	0.37	0.00	0.14	0.02	0.00	0.02	0.02	0.01
0.08	0.29	0.02	0.69	-0.01	0.17	0.01	0.00	0.01	0.01	0.00
0.00	0.28	0.01	0.71	0.01	---	0.00	0.00	0.00	0.00	---
-0.08	0.34	0.02	0.64	0.02	0.22	0.04	0.00	0.04	0.00	0.00
-0.25	0.70	0.02	0.28	0.05	0.14	0.03	0.00	0.03	0.01	0.00
-0.42	0.89	0.02	0.09	0.01	0.19	0.01	0.00	0.01	0.01	0.01
-0.58	0.79	0.01	0.20	0.01	0.14	0.01	0.00	0.01	0.01	0.01
-0.75	0.79	0.02	0.19	-0.01	0.13	0.02	0.00	0.02	0.02	0.00
-0.92	0.69	0.03	0.29	0.04	0.17	0.05	0.00	0.05	0.02	0.00

Appendix B.2.4: Fiber orientation with error analysis assuming independent samples for two 1.38 mm center-gated disk made of 30 wt% glass fiber reinforced PBT (Valox 420) measured at r/H = 68 (90% of flow length). Measurements were evaluated by considering elliptical and partial ellipses having areas larger than half ellipse (BT approach).

z/H	*Center-gated disk 1*							*Center-gated disk 2*						
	Orientation component				F_a	H	ϕ_v	Orientation component				F_a	H	ϕ_v
	A_{rr}	A_{zz}	$A_{\theta\theta}$	A_{rz}				A_{rr}	A_{zz}	$A_{\theta\theta}$	A_{rz}			
0.92	0.79	0.01	0.19	0.02	36	106.39	0.16	0.74	0.02	0.25	0.05	38	88.80	0.14
0.75	0.54	0.02	0.43	0.05	33	53.12	0.08	0.55	0.04	0.41	0.03	60	102.10	0.15
0.58	0.62	0.04	0.34	0.04	38	77.09	0.13	0.62	0.03	0.35	0.06	43	87.46	0.13
0.42	0.68	0.01	0.31	-0.01	39	81.74	0.12	0.67	0.02	0.32	0.06	49	102.65	0.16
0.25	0.61	0.03	0.36	0.04	45	89.27	0.12	0.43	0.01	0.56	0.01	55	77.62	0.12
0.08	0.20	0.02	0.77	0.01	123	141.16	0.23	0.19	0.02	0.79	0.03	115	129.64	0.19
0.00	0.15	0.02	0.83	0.02	69	75.73	---	0.15	0.02	0.82	0.03	58	63.99	---
-0.08	0.22	0.03	0.76	0.05	108	125.43	0.20	0.22	0.02	0.76	0.05	116	134.10	0.20
-0.25	0.62	0.02	0.35	0.06	43	85.09	0.14	0.49	0.01	0.50	0.05	53	80.15	0.12
-0.42	0.73	0.02	0.25	-0.01	40	101.48	0.16	0.69	0.04	0.27	-0.01	53	125.86	0.17
-0.58	0.66	0.01	0.33	-0.01	49	101.90	0.16	0.60	0.03	0.37	0.03	51	91.43	0.13
-0.75	0.64	0.02	0.34	-0.03	43	81.25	0.13	0.79	0.01	0.20	0.03	44	121.77	0.16
-0.92	0.75	0.04	0.21	-0.07	45	123.83	0.16	0.76	0.02	0.22	0.01	39	109.98	0.17

z/H	*Average orientation and error for two independent center-gated disks*									
	Orientation component				$\langle\phi_v\rangle$	Standard Error				
	$\langle A_{rr}\rangle$	$\langle A_{zz}\rangle$	$\langle A_{\theta\theta}\rangle$	$\langle A_{rz}\rangle$		$SE_{\langle A_{rr}\rangle}$	$SE_{\langle A_{zz}\rangle}$	$SE_{\langle A_{\theta\theta}\rangle}$	$SE_{\langle A_{rz}\rangle}$	$SE_{\langle\phi_v\rangle}$
0.92	0.77	0.01	0.22	0.03	0.15	0.01	0.00	0.01	0.01	0.01
0.75	0.55	0.03	0.42	0.04	0.13	0.00	0.00	0.01	0.00	0.02
0.58	0.62	0.04	0.35	0.05	0.13	0.00	0.00	0.00	0.00	0.00
0.42	0.67	0.01	0.31	0.03	0.14	0.00	0.00	0.00	0.02	0.01
0.25	0.53	0.02	0.45	0.03	0.12	0.04	0.01	0.05	0.01	0.00
0.08	0.20	0.02	0.78	0.02	0.21	0.00	0.00	0.01	0.00	0.01
0.00	0.15	0.02	0.83	0.02	---	0.00	0.00	0.00	0.00	---
-0.08	0.22	0.02	0.76	0.05	0.20	0.00	0.00	0.00	0.00	0.00
-0.25	0.56	0.02	0.42	0.06	0.13	0.03	0.00	0.04	0.00	0.01
-0.42	0.71	0.03	0.26	-0.01	0.16	0.01	0.00	0.01	0.00	0.00
-0.58	0.63	0.02	0.35	0.01	0.14	0.02	0.00	0.01	0.01	0.01
-0.75	0.73	0.01	0.25	0.01	0.15	0.04	0.00	0.04	0.01	0.01
-0.92	0.76	0.03	0.22	-0.03	0.17	0.00	0.01	0.00	0.02	0.00

Appendix B.3.1: Fiber orientation with error analysis assuming independent samples for two 1.38 mm center-gated disk made of 30 wt% glass fiber reinforced PBT (Valox 420) measured at r/H = 4.3 (1% of flow length). Measurements were evaluated by considering only elliptical footprints in the polished plane (LA approach).

z/H	*Center-gated disk 1*							*Center-gated disk 2*						
	Orientation component				F_a	H	ϕ_v	Orientation component				F_a	H	ϕ_v
	A_{rr}	A_{zz}	$A_{\theta\theta}$	A_{rz}				A_{rr}	A_{zz}	$A_{\theta\theta}$	A_{rz}			
0.92	0.74	0.02	0.25	-0.03	19	45.08	0.09	0.58	0.01	0.41	0.02	37	65.10	0.13
0.75	0.75	0.02	0.23	-0.08	20	46.43	0.08	0.62	0.04	0.34	-0.07	26	50.61	0.09
0.58	0.55	0.05	0.40	-0.04	27	45.35	0.08	0.76	0.02	0.22	-0.05	33	88.41	0.16
0.42	0.53	0.02	0.44	-0.07	35	58.73	0.11	0.69	0.04	0.26	0.00	28	61.70	0.12
0.25	0.69	0.02	0.29	-0.08	22	45.92	0.10	0.68	0.04	0.28	-0.08	36	80.52	0.15
0.08	0.61	0.02	0.37	-0.07	32	58.85	0.12	0.36	0.01	0.63	-0.02	42	54.12	0.11
0.00	0.64	0.02	0.34	0.01	15	30.66	---	0.26	0.01	0.73	0.00	23	27.28	---
-0.08	0.21	0.00	0.79	-0.01	73	84.47	0.18	0.27	0.01	0.71	0.02	72	88.29	0.18
-0.25	0.48	0.01	0.51	0.01	48	78.55	0.21	0.59	0.02	0.40	0.07	46	80.24	0.16
-0.42	0.67	0.01	0.32	-0.04	40	84.99	0.18	0.51	0.02	0.47	0.02	42	64.76	0.12
-0.58	0.53	0.01	0.46	0.00	36	57.02	0.11	0.61	0.01	0.37	-0.02	38	70.94	0.14
-0.75	0.39	0.01	0.59	-0.01	42	57.21	0.12	0.49	0.01	0.50	-0.01	30	45.75	0.09
-0.92	0.19	0.02	0.79	-0.02	27	31.05	0.07	0.65	0.01	0.34	0.02	33	66.71	0.14

z/H	*Average orientation and error for two independent center-gated disks*									
	Orientation component				$\langle \phi_v \rangle$	Standard Error				
	$\langle A_{rr} \rangle$	$\langle A_{zz} \rangle$	$\langle A_{\theta\theta} \rangle$	$\langle A_{rz} \rangle$		$SE_{\langle A_{rr} \rangle}$	$SE_{\langle A_{zz} \rangle}$	$SE_{\langle A_{\theta\theta} \rangle}$	$SE_{\langle A_{rz} \rangle}$	$SE_{\langle \phi_v \rangle}$
0.92	0.65	0.01	0.34	0.00	0.11	0.04	0.00	0.04	0.01	0.01
0.75	0.68	0.03	0.29	-0.08	0.09	0.03	0.00	0.03	0.00	0.00
0.58	0.69	0.03	0.28	-0.04	0.13	0.05	0.01	0.04	0.00	0.02
0.42	0.62	0.03	0.35	-0.03	0.11	0.04	0.01	0.05	0.02	0.00
0.25	0.69	0.03	0.28	-0.08	0.13	0.00	0.01	0.00	0.00	0.01
0.08	0.49	0.01	0.50	-0.04	0.11	0.06	0.00	0.06	0.01	0.00
0.00	0.46	0.02	0.52	0.01	---	0.10	0.00	0.10	0.00	---
-0.08	0.24	0.01	0.75	0.01	0.18	0.02	0.00	0.02	0.01	0.00
-0.25	0.53	0.01	0.45	0.04	0.18	0.03	0.00	0.03	0.02	0.01
-0.42	0.60	0.01	0.39	-0.01	0.15	0.04	0.00	0.04	0.02	0.01
-0.58	0.58	0.01	0.41	-0.01	0.13	0.02	0.00	0.02	0.01	0.01
-0.75	0.44	0.01	0.55	-0.01	0.11	0.03	0.00	0.02	0.00	0.01
-0.92	0.51	0.01	0.48	0.00	0.12	0.11	0.00	0.11	0.01	0.02

Appendix B.3.2: Fiber orientation with error analysis assuming independent samples for two 1.38 mm center-gated disk made of 30 wt% glass fiber reinforced PBT (Valox 420) measured at r/H = 11 (10% of flow length). Measurements were evaluated by considering only elliptical footprints in the polished plane (LA approach).

z/H	*Center-gated disk 1*							*Center-gated disk 2*						
	Orientation component				F_a	H	ϕ_v	Orientation component				F_a	H	ϕ_v
	A_{rr}	A_{zz}	$A_{\theta\theta}$	A_{rz}				A_{rr}	A_{zz}	$A_{\theta\theta}$	A_{rz}			
0.92	0.51	0.02	0.48	-0.03	42	63.74	0.11	0.50	0.01	0.49	-0.02	42	63.79	0.11
0.75	0.71	0.01	0.29	-0.02	20	42.54	0.07	0.81	0.01	0.18	-0.01	23	67.67	0.13
0.58	0.78	0.04	0.18	-0.08	30	83.22	0.14	0.81	0.01	0.18	-0.02	34	98.75	0.15
0.42	0.48	0.01	0.51	0.01	34	49.75	0.08	0.59	0.01	0.40	-0.01	46	82.48	0.14
0.25	0.38	0.02	0.60	0.03	53	72.93	0.13	0.45	0.01	0.54	0.00	50	73.26	0.12
0.08	0.24	0.01	0.75	0.01	76	91.08	0.16	0.21	0.01	0.78	0.02	75	86.12	0.15
0.00	0.12	0.00	0.87	0.01	32	34.48	---	0.17	0.01	0.83	0.01	40	44.25	---
-0.08	0.27	0.01	0.72	0.04	75	91.29	0.15	0.32	0.02	0.66	0.07	78	100.53	0.17
-0.25	0.59	0.01	0.40	0.04	44	77.08	0.13	0.40	0.02	0.58	0.04	49	67.18	0.11
-0.42	0.55	0.01	0.44	0.02	42	67.16	0.11	0.54	0.05	0.41	0.05	33	55.06	0.09
-0.58	0.56	0.01	0.43	0.04	43	73.44	0.13	0.67	0.01	0.33	0.03	28	54.34	0.09
-0.75	0.55	0.01	0.44	0.03	38	59.74	0.10	0.66	0.01	0.33	-0.02	38	77.01	0.13
-0.92	0.75	0.01	0.24	0.00	30	76.06	0.11	0.42	0.02	0.56	0.05	54	74.66	0.13

z/H	*Average orientation and error for two independent center-gated disks*									
	Orientation component				$\langle \phi_v \rangle$	Standard Error				
	$\langle A_{rr} \rangle$	$\langle A_{zz} \rangle$	$\langle A_{\theta\theta} \rangle$	$\langle A_{rz} \rangle$		$SE_{\langle A_{rr} \rangle}$	$SE_{\langle A_{zz} \rangle}$	$SE_{\langle A_{\theta\theta} \rangle}$	$SE_{\langle A_{rz} \rangle}$	$SE_{\langle \phi_v \rangle}$
0.92	0.50	0.01	0.49	-0.03	0.11	0.00	0.00	0.00	0.00	0.00
0.75	0.77	0.01	0.22	-0.01	0.11	0.03	0.00	0.03	0.00	0.01
0.58	0.80	0.02	0.18	-0.05	0.15	0.01	0.01	0.00	0.02	0.00
0.42	0.55	0.01	0.44	0.00	0.12	0.03	0.00	0.03	0.01	0.01
0.25	0.42	0.01	0.57	0.01	0.12	0.02	0.00	0.02	0.01	0.00
0.08	0.23	0.01	0.76	0.01	0.15	0.01	0.00	0.01	0.00	0.00
0.00	0.15	0.01	0.85	0.01	---	0.01	0.00	0.01	0.00	---
-0.08	0.30	0.02	0.69	0.05	0.16	0.01	0.00	0.02	0.01	0.01
-0.25	0.50	0.02	0.48	0.04	0.12	0.05	0.00	0.05	0.00	0.00
-0.42	0.54	0.03	0.43	0.04	0.10	0.00	0.01	0.01	0.01	0.01
-0.58	0.61	0.01	0.39	0.03	0.11	0.03	0.00	0.03	0.00	0.01
-0.75	0.61	0.01	0.38	0.00	0.12	0.03	0.00	0.03	0.01	0.01
-0.92	0.59	0.01	0.40	0.03	0.12	0.08	0.00	0.08	0.01	0.00

Appendix B.3.3: Fiber orientation with error analysis assuming independent samples for two 1.38 mm center-gated disk made of 30 wt% glass fiber reinforced PBT (Valox 420) measured at r/H = 32 (40% of flow length). Measurements were evaluated by considering only elliptical footprints in the polished plane (LA approach).

z/H	*Center-gated disk 1*							*Center-gated disk 2*						
	Orientation component				F_a	H	ϕ_v	Orientation component				F_a	H	ϕ_v
	A_{rr}	A_{zz}	$A_{\theta\theta}$	A_{rz}				A_{rr}	A_{zz}	$A_{\theta\theta}$	A_{rz}			
0.92	0.64	0.01	0.34	-0.02	45	85.04	0.12	0.65	0.01	0.34	0.01	49	102.33	0.14
0.75	0.73	0.01	0.27	-0.01	39	85.99	0.13	0.63	0.01	0.36	0.01	30	55.71	0.10
0.58	0.83	0.01	0.16	-0.01	24	72.98	0.11	0.77	0.00	0.23	-0.03	24	60.48	0.09
0.42	0.68	0.03	0.29	0.05	24	49.24	0.07	0.68	0.04	0.27	-0.04	38	83.16	0.13
0.25	0.62	0.03	0.35	0.02	45	81.94	0.13	0.47	0.02	0.51	-0.04	43	64.39	0.10
0.08	0.20	0.00	0.79	-0.01	76	87.22	0.15	0.27	0.01	0.72	-0.02	75	89.95	0.14
0.00	0.19	0.00	0.81	-0.01	42	47.86	---	0.24	0.01	0.75	0.01	44	51.59	---
-0.08	0.18	0.02	0.80	0.02	109	123.02	0.19	0.43	0.01	0.56	0.02	89	123.81	0.20
-0.25	0.65	0.02	0.33	0.07	29	58.25	0.10	0.61	0.02	0.37	0.02	41	74.02	0.11
-0.42	0.83	0.01	0.16	0.00	22	74.39	0.12	0.77	0.03	0.19	0.03	23	61.77	0.09
-0.58	0.69	0.01	0.31	0.04	21	42.19	0.07	0.69	0.00	0.31	0.01	33	64.65	0.09
-0.75	0.74	0.01	0.25	0.00	27	64.42	0.09	0.65	0.03	0.32	0.03	32	65.71	0.10
-0.92	0.75	0.02	0.24	0.07	32	77.27	0.13	0.50	0.01	0.49	0.01	61	93.25	0.14

z/H	*Average orientation and error for two independent center-gated disks*									
	Orientation component				$\langle \phi_v \rangle$	Standard Error				
	$\langle A_{rr} \rangle$	$\langle A_{zz} \rangle$	$\langle A_{\theta\theta} \rangle$	$\langle A_{rz} \rangle$		$SE_{\langle A_{rr} \rangle}$	$SE_{\langle A_{zz} \rangle}$	$SE_{\langle A_{\theta\theta} \rangle}$	$SE_{\langle A_{rz} \rangle}$	$SE_{\langle \phi_v \rangle}$
0.92	0.65	0.01	0.34	0.00	0.13	0.00	0.00	0.00	0.01	0.01
0.75	0.69	0.01	0.30	0.00	0.12	0.02	0.00	0.02	0.01	0.01
0.58	0.80	0.01	0.19	-0.02	0.10	0.02	0.00	0.02	0.00	0.00
0.42	0.68	0.04	0.28	-0.01	0.11	0.00	0.00	0.00	0.02	0.01
0.25	0.56	0.02	0.42	0.00	0.12	0.04	0.00	0.04	0.02	0.01
0.08	0.24	0.01	0.76	-0.01	0.14	0.02	0.00	0.02	0.00	0.00
0.00	0.21	0.01	0.78	0.00	---	0.01	0.00	0.01	0.00	---
-0.08	0.31	0.01	0.68	0.02	0.20	0.06	0.00	0.06	0.00	0.00
-0.25	0.63	0.02	0.35	0.04	0.10	0.01	0.00	0.01	0.01	0.00
-0.42	0.81	0.02	0.17	0.01	0.11	0.01	0.01	0.01	0.01	0.01
-0.58	0.69	0.01	0.31	0.02	0.08	0.00	0.00	0.00	0.01	0.01
-0.75	0.70	0.02	0.29	0.02	0.09	0.02	0.01	0.02	0.01	0.00
-0.92	0.61	0.01	0.37	0.04	0.14	0.06	0.00	0.06	0.02	0.00

Appendix B.3.4: Fiber orientation with error analysis assuming independent samples for two 1.38 mm center-gated disk made of 30 wt% glass fiber reinforced PBT (Valox 420) measured at r/H = 68 (90% of flow length). Measurements were evaluated by considering only elliptical footprints in the polished plane (LA approach).

z/H	*Center-gated disk 1*							*Center-gated disk 2*						
	Orientation component				F_a	H	ϕ_v	Orientation component				F_a	H	ϕ_v
	A_{rr}	A_{zz}	$A_{\theta\theta}$	A_{rz}				A_{rr}	A_{zz}	$A_{\theta\theta}$	A_{rz}			
0.92	0.74	0.01	0.25	-0.01	32	77.94	0.12	0.70	0.02	0.28	0.07	26	54.54	0.08
0.75	0.55	0.03	0.42	0.06	28	45.97	0.07	0.52	0.02	0.46	0.04	49	78.13	0.12
0.58	0.49	0.04	0.47	0.00	33	51.90	0.09	0.49	0.01	0.50	0.03	37	56.47	0.08
0.42	0.67	0.01	0.32	-0.01	36	73.81	0.11	0.66	0.01	0.33	0.05	40	82.03	0.13
0.25	0.39	0.01	0.60	-0.01	38	50.39	0.08	0.38	0.01	0.61	0.00	49	65.67	0.10
0.08	0.14	0.02	0.84	0.00	112	123.32	0.20	0.13	0.01	0.86	0.01	108	117.54	0.17
0.00	0.09	0.01	0.90	0.01	64	67.53	---	0.08	0.02	0.90	0.01	52	54.85	---
-0.08	0.17	0.02	0.81	0.03	99	111.23	0.18	0.18	0.02	0.80	0.04	109	122.94	0.18
-0.25	0.63	0.01	0.37	0.03	38	73.66	0.13	0.47	0.01	0.52	0.05	46	67.94	0.10
-0.42	0.69	0.01	0.29	-0.01	35	81.13	0.13	0.55	0.02	0.43	0.06	43	71.31	0.10
-0.58	0.63	0.01	0.36	-0.03	44	87.90	0.14	0.56	0.02	0.41	0.02	42	70.85	0.10
-0.75	0.60	0.02	0.38	-0.04	41	71.33	0.11	0.68	0.01	0.30	0.03	37	74.33	0.10
-0.92	0.72	0.03	0.25	-0.07	33	80.08	0.11	0.69	0.01	0.30	0.05	34	75.32	0.13

z/H	*Average orientation and error for two independent center-gated disks*									
	Orientation component				$\langle \phi_v \rangle$	Standard Error				
	$\langle A_{rr} \rangle$	$\langle A_{zz} \rangle$	$\langle A_{\theta\theta} \rangle$	$\langle A_{rz} \rangle$		$SE_{\langle A_{rr} \rangle}$	$SE_{\langle A_{zz} \rangle}$	$SE_{\langle A_{\theta\theta} \rangle}$	$SE_{\langle A_{rz} \rangle}$	$SE_{\langle \phi_v \rangle}$
0.92	0.72	0.01	0.26	0.02	0.10	0.01	0.00	0.01	0.02	0.01
0.75	0.53	0.03	0.44	0.05	0.10	0.01	0.00	0.01	0.00	0.01
0.58	0.49	0.03	0.49	0.02	0.08	0.00	0.01	0.01	0.01	0.00
0.42	0.66	0.01	0.33	0.03	0.12	0.00	0.00	0.00	0.02	0.00
0.25	0.39	0.01	0.60	-0.01	0.09	0.00	0.00	0.00	0.00	0.00
0.08	0.14	0.01	0.85	0.00	0.19	0.00	0.00	0.00	0.00	0.01
0.00	0.08	0.01	0.90	0.01	---	0.00	0.00	0.00	0.00	---
-0.08	0.17	0.02	0.81	0.04	0.18	0.00	0.00	0.00	0.00	0.00
-0.25	0.55	0.01	0.44	0.04	0.11	0.04	0.00	0.04	0.00	0.01
-0.42	0.63	0.01	0.36	0.02	0.12	0.04	0.00	0.03	0.02	0.01
-0.58	0.60	0.02	0.38	-0.01	0.12	0.02	0.00	0.01	0.01	0.01
-0.75	0.64	0.01	0.34	0.00	0.11	0.02	0.00	0.02	0.02	0.00
-0.92	0.70	0.02	0.28	-0.01	0.12	0.01	0.00	0.01	0.03	0.00

APPENDIX C: ORIENTATION ALONG THE CAVITY THICKNESS FROM MUTUALLY PERPENDICULAR PLANES AT DIFFERENT RADIAL LOCATIONS EVALUATED BY DIFFERENT APPROACHES

Appendix C.1.1: Fiber orientation with error analysis for mutually perpendicular planes in a 1.38 mm center-gated disk made of 30 wt% glass fiber reinforced PBT (Valox 420) measured at the entry region. Measurements were evaluated by considered elliptical and partial ellipses of any size (VWB approach).

z/H	*Plane rz*									*Plane $\theta_p z$*								
	Orientation component						F_a	H	ϕ_v	Orientation component						F_a	H	ϕ_v
	A_{rr}	A_{zz}	$A_{\theta\theta}$	A_{rz}	$A_{r\theta}$	$A_{z\theta}$				A_{rr}	A_{zz}	$A_{\theta\theta}$	A_{rz}	$A_{r\theta}$	$A_{z\theta}$			
0.92	0.73	0.06	0.21	-0.15	0.05	-0.04	26.90	67.35	0.10	0.75	0.02	0.23	-0.03	0.22	-0.03	35.65	41.04	0.10
0.75	0.79	0.02	0.19	0.00	0.08	-0.03	26.25	77.75	0.09	0.71	0.02	0.27	-0.04	0.22	-0.03	41.77	49.48	0.11
0.58	0.70	0.02	0.28	0.02	0.22	-0.01	56.99	122.39	0.18	0.67	0.04	0.29	-0.02	-0.05	0.01	50.30	61.68	0.17
0.42	0.62	0.03	0.34	0.06	0.15	-0.03	56.37	103.76	0.16	0.69	0.07	0.24	-0.04	-0.09	0.00	47.73	57.77	0.15
0.25	0.67	0.03	0.31	0.05	0.09	-0.01	61.73	125.68	0.18	0.63	0.04	0.33	-0.01	0.00	0.02	69.47	89.47	0.19
0.08	0.56	0.01	0.43	0.02	0.18	-0.02	70.65	119.03	0.18	0.58	0.03	0.39	-0.02	0.03	0.01	42.96	57.94	0.15
0.00	0.40	0.01	0.58	0.00	0.16	-0.02	84.47	119.17	---	0.42	0.05	0.53	-0.01	-0.10	0.05	41.77	67.80	---
-0.08	0.23	0.02	0.75	-0.02	0.12	-0.05	109.67	127.88	0.19	0.28	0.06	0.66	-0.04	-0.18	0.06	37.74	77.01	0.19
-0.25	0.49	0.03	0.49	-0.03	0.03	-0.03	72.24	108.72	0.17	0.51	0.04	0.45	-0.01	-0.08	0.01	41.15	59.69	0.15
-0.42	0.63	0.02	0.35	-0.04	0.08	-0.03	60.82	112.11	0.17	0.60	0.03	0.36	-0.03	-0.01	0.05	50.04	64.83	0.16
-0.58	0.63	0.02	0.34	-0.03	0.10	-0.04	48.14	90.11	0.14	0.66	0.05	0.29	-0.06	0.09	0.05	44.70	55.10	0.13
-0.75	0.57	0.02	0.41	-0.03	0.00	-0.04	54.62	93.14	0.14	0.53	0.02	0.44	-0.02	0.02	0.06	38.61	58.52	0.14
-0.92	0.76	0.01	0.22	0.03	-0.18	-0.02	32.09	72.24	0.11	0.65	0.02	0.33	-0.04	0.14	0.02	57.57	73.32	0.17

z/H	*Average orientation and error for mutually perpendicular planes*													
	Orientation component						$\langle \phi_v \rangle$	Standard Error						
	$\langle A_{rr} \rangle$	$\langle A_{zz} \rangle$	$\langle A_{\theta\theta} \rangle$	$\langle A_{rz} \rangle$	$\langle A_{r\theta} \rangle$	$\langle A_{z\theta} \rangle$		$SE_{\langle A_{rr} \rangle}$	$SE_{\langle A_{zz} \rangle}$	$SE_{\langle A_{\theta\theta} \rangle}$	$SE_{\langle A_{rz} \rangle}$	$SE_{\langle A_{r\theta} \rangle}$	$SE_{\langle A_{z\theta} \rangle}$	$SE_{\langle \phi_v \rangle}$
0.92	0.73	0.05	0.22	-0.10	0.12	-0.04	0.10	0.01	0.01	0.01	0.03	0.04	0.01	0.00
0.75	0.76	0.02	0.22	-0.01	0.13	-0.03	0.09	0.02	0.00	0.02	0.01	0.04	0.02	0.02
0.58	0.69	0.03	0.28	0.01	0.13	0.00	0.17	0.01	0.01	0.00	0.01	0.07	0.01	0.01
0.42	0.65	0.05	0.31	0.02	0.06	-0.02	0.16	0.02	0.01	0.03	0.02	0.06	0.02	0.01
0.25	0.65	0.03	0.32	0.02	0.05	0.01	0.18	0.01	0.00	0.01	0.01	0.02	0.01	0.01
0.08	0.57	0.02	0.41	0.00	0.13	-0.01	0.17	0.00	0.01	0.01	0.01	0.04	0.00	0.01
0.00	0.41	0.03	0.56	-0.01	0.06	0.01	---	0.01	0.01	0.01	0.00	0.06	0.01	---
-0.08	0.25	0.04	0.72	-0.03	0.01	-0.01	0.19	0.01	0.01	0.02	0.00	0.07	0.01	0.01
-0.25	0.50	0.03	0.47	-0.02	-0.01	-0.02	0.16	0.01	0.00	0.01	0.01	0.03	0.01	0.01
-0.42	0.62	0.02	0.36	-0.03	0.05	0.00	0.17	0.01	0.00	0.00	0.00	0.02	0.01	0.00
-0.58	0.64	0.03	0.32	-0.04	0.09	0.00	0.14	0.01	0.01	0.01	0.01	0.00	0.01	0.00
-0.75	0.56	0.02	0.42	-0.03	0.00	0.00	0.14	0.01	0.00	0.01	0.00	0.01	0.01	0.00
-0.92	0.71	0.02	0.28	0.00	-0.02	0.00	0.14	0.03	0.00	0.03	0.02	0.08	0.03	0.03

Appendix C.1.2: Fiber orientation with error analysis for mutually perpendicular planes in a 1.38 mm center-gated disk made of 30 wt% glass fiber reinforced PBT (Valox 420) measured at the entry region. Measurements were evaluated by considered elliptical footprints (LA approach).

z/H	*Plane rz*							*Plane $\theta_p z$*						
	Orientation component				F_a	H	ϕ_v	Orientation component				F_a	H	ϕ_v
	A_{rr}	A_{zz}	$A_{\theta\theta}$	A_{rz}				A_{rr}	A_{zz}	$A_{\theta\theta}$	A_{rz}			
0.92	0.64	0.06	0.31	0.12	22	45.72	0.07	0.76	0.02	0.22	-0.03	36	41.95	0.10
0.75	0.65	0.03	0.32	-0.03	19	38.98	0.06	0.67	0.02	0.31	-0.05	35	43.55	0.11
0.58	0.73	0.01	0.26	-0.03	51	123.33	0.18	0.74	0.03	0.23	0.00	50	59.43	0.15
0.42	0.67	0.02	0.31	-0.05	48	99.86	0.16	0.74	0.02	0.23	0.01	47	55.48	0.14
0.25	0.64	0.02	0.34	-0.03	51	102.81	0.14	0.71	0.02	0.27	0.02	56	67.82	0.17
0.08	0.53	0.01	0.46	-0.02	55	93.89	0.15	0.51	0.03	0.46	0.02	46	72.06	0.16
0.00	0.65	0.01	0.34	-0.02	25	53.72	---	0.57	0.05	0.39	0.06	24	34.67	---
-0.08	0.22	0.01	0.76	0.02	104	122.31	0.18	0.31	0.03	0.66	0.04	26	51.02	0.13
-0.25	0.46	0.03	0.52	0.04	62	94.78	0.15	0.51	0.02	0.46	0.01	31	46.42	0.12
-0.42	0.60	0.01	0.38	0.02	53	95.49	0.14	0.59	0.03	0.38	0.03	43	57.94	0.15
-0.58	0.53	0.02	0.46	0.02	33	55.02	0.09	0.67	0.03	0.30	0.05	41	51.80	0.13
-0.75	0.54	0.01	0.45	0.03	47	78.74	0.12	0.65	0.01	0.33	0.03	36	47.99	0.12
-0.92	0.73	0.01	0.26	-0.02	26	56.73	0.09	0.72	0.02	0.27	0.03	51	61.86	0.16

z/H	*Average orientation and error for mutually perpendicular planes*									
	Orientation component				$\langle\phi_v\rangle$	Standard Error				
	$\langle A_{rr}\rangle$	$\langle A_{zz}\rangle$	$\langle A_{\theta\theta}\rangle$	$\langle A_{rz}\rangle$		$SE_{\langle A_{rr}\rangle}$	$SE_{\langle A_{zz}\rangle}$	$SE_{\langle A_{\theta\theta}\rangle}$	$SE_{\langle A_{rz}\rangle}$	$SE_{\langle\phi_v\rangle}$
0.92	0.69	0.04	0.27	0.05	0.08	0.03	0.01	0.02	0.04	0.02
0.75	0.66	0.02	0.31	-0.04	0.09	0.01	0.00	0.00	0.00	0.03
0.58	0.73	0.02	0.25	-0.02	0.16	0.00	0.00	0.01	0.01	0.01
0.42	0.69	0.02	0.28	-0.03	0.15	0.02	0.00	0.02	0.02	0.01
0.25	0.67	0.02	0.31	-0.01	0.16	0.02	0.00	0.02	0.01	0.01
0.08	0.52	0.02	0.46	-0.01	0.15	0.01	0.01	0.00	0.01	0.00
0.00	0.62	0.02	0.36	0.01	---	0.02	0.01	0.01	0.02	---
-0.08	0.25	0.02	0.73	0.02	0.16	0.02	0.00	0.02	0.01	0.03
-0.25	0.48	0.02	0.50	0.03	0.14	0.01	0.00	0.01	0.01	0.02
-0.42	0.60	0.02	0.38	0.02	0.15	0.00	0.00	0.00	0.00	0.00
-0.58	0.60	0.03	0.38	0.03	0.11	0.03	0.00	0.04	0.01	0.02
-0.75	0.58	0.01	0.40	0.03	0.12	0.03	0.00	0.03	0.00	0.00
-0.92	0.72	0.01	0.26	0.01	0.12	0.00	0.00	0.00	0.01	0.03

Appendix C.2.1: Fiber orientation with error analysis for mutually perpendicular planes in a 1.38 mm center-gated disk made of 30 wt% glass fiber reinforced PBT (Valox 420) measured at the lubrication region. Measurements were evaluated by considered elliptical and partial ellipses of any size (VWB approach).

z/H	*Plane rz*									*Plane* $\theta_p z$								
	Orientation component						F_a	H	ϕ_v	Orientation component						F_a	H	ϕ_v
	A_{rr}	A_{zz}	$A_{\theta\theta}$	A_{rz}	$A_{r\theta}$	$A_{z\theta}$				A_{rr}	A_{zz}	$A_{\theta\theta}$	A_{rz}	$A_{r\theta}$	$A_{z\theta}$			
0.92	0.73	0.02	0.26	-0.02	0.11	0.01	26.09	55.72	0.11	0.65	0.02	0.33	0.04	0.33	0.01	18	34.73	0.15
0.75	0.68	0.02	0.30	0.00	0.14	0.01	44.32	92.66	0.18	0.60	0.01	0.39	-0.01	0.27	0.00	38	70.77	0.16
0.58	0.55	0.02	0.43	0.03	0.10	-0.02	36.35	59.57	0.12	0.44	0.01	0.55	-0.01	0.34	-0.01	24	33.50	0.13
0.42	0.64	0.02	0.34	0.05	0.13	0.02	38.02	75.83	0.18	0.51	0.01	0.47	-0.01	0.28	-0.03	33	53.43	0.11
0.25	0.26	0.02	0.72	0.03	0.27	0.04	54.48	64.04	0.14	0.26	0.02	0.72	-0.04	0.29	-0.05	50	60.29	0.17
0.08	0.05	0.04	0.91	0.00	0.19	0.03	115.38	119.95	0.25	0.03	0.02	0.95	0.00	0.07	0.00	106	108.98	0.22
0.00	0.13	0.05	0.82	-0.02	0.17	0.00	98.84	110.37	---	0.02	0.04	0.93	0.00	0.07	0.00	50	51.84	---
-0.08	0.14	0.10	0.76	-0.01	0.17	0.04	119.90	140.59	0.29	0.10	0.04	0.85	0.02	0.13	0.03	104	114.04	0.24
-0.25	0.29	0.06	0.65	-0.03	0.19	0.02	78.45	100.87	0.22	0.19	0.03	0.78	0.02	0.21	0.01	67	77.56	0.16
-0.42	0.42	0.08	0.50	0.00	0.12	0.01	53.70	77.67	0.15	0.44	0.04	0.52	0.00	0.34	0.01	35	50.79	0.15
-0.58	0.65	0.04	0.31	-0.01	0.04	0.02	41.69	80.10	0.19	0.62	0.01	0.37	-0.02	0.37	-0.02	34	60.72	0.14
-0.75	0.56	0.03	0.41	0.04	0.13	0.04	44.41	71.64	0.15	0.60	0.02	0.39	-0.01	0.37	-0.03	33	56.58	0.13
-0.92	0.72	0.05	0.24	0.02	0.21	0.02	41.00	93.20	0.23	0.69	0.02	0.30	-0.04	0.29	-0.03	28	61.28	0.10

z/H	*Average orientation and error for mutually perpendicular planes*													
	Orientation component						$\langle \phi_v \rangle$	Standard Error						
	$\langle A_{rr} \rangle$	$\langle A_{zz} \rangle$	$\langle A_{\theta\theta} \rangle$	$\langle A_{rz} \rangle$	$\langle A_{r\theta} \rangle$	$\langle A_{z\theta} \rangle$		$SE_{\langle A_{rr} \rangle}$	$SE_{\langle A_{zz} \rangle}$	$SE_{\langle A_{\theta\theta} \rangle}$	$SE_{\langle A_{rz} \rangle}$	$SE_{\langle A_{r\theta} \rangle}$	$SE_{\langle A_{z\theta} \rangle}$	$SE_{\langle \phi_v \rangle}$
0.92	0.72	0.03	0.25	-0.02	0.14	0.01	0.13	0.00	0.00	0.00	0.00	0.01	0.00	0.02
0.75	0.67	0.02	0.31	-0.04	0.13	-0.01	0.17	0.01	0.00	0.01	0.02	0.00	0.01	0.01
0.58	0.56	0.02	0.42	0.02	0.09	0.00	0.12	0.00	0.00	0.00	0.01	0.01	0.01	0.00
0.42	0.60	0.02	0.38	0.01	0.09	0.01	0.14	0.02	0.00	0.02	0.02	0.02	0.01	0.04
0.25	0.27	0.03	0.70	0.00	0.02	0.06	0.15	0.00	0.00	0.01	0.02	0.11	0.01	0.01
0.08	0.08	0.04	0.88	-0.01	0.01	0.07	0.24	0.01	0.00	0.02	0.01	0.10	0.02	0.02
0.00	0.13	0.05	0.81	-0.02	0.04	0.00	---	0.00	0.00	0.00	0.00	0.09	0.01	---
-0.08	0.13	0.09	0.78	0.00	0.03	0.06	0.26	0.01	0.01	0.01	0.00	0.08	0.01	0.02
-0.25	0.31	0.06	0.63	0.01	0.12	0.04	0.19	0.01	0.00	0.01	0.02	0.05	0.01	0.03
-0.42	0.39	0.08	0.53	0.01	0.03	0.01	0.15	0.02	0.00	0.02	0.01	0.04	0.00	0.00
-0.58	0.63	0.04	0.33	-0.01	0.12	0.01	0.17	0.01	0.00	0.01	0.00	0.04	0.00	0.02
-0.75	0.61	0.03	0.36	0.04	0.15	0.02	0.14	0.03	0.00	0.02	0.00	0.01	0.01	0.01
-0.92	0.66	0.05	0.29	0.03	0.17	0.01	0.17	0.04	0.00	0.04	0.01	0.02	0.00	0.06

Appendix C.2.2: Fiber orientation with error analysis for mutually perpendicular planes in a 1.38 mm center-gated disk made of 30 wt% glass fiber reinforced PBT (Valox 420) measured at the lubrication region. Measurements were evaluated by considered elliptical footprints (LA approach).

z/H	*Plane rz*							*Plane $\theta_p z$*						
	Orientation component				F_a	H	ϕ_v	Orientation component				F_a	H	ϕ_v
	A_{rr}	A_{zz}	$A_{\theta\theta}$	A_{rz}				A_{rr}	A_{zz}	$A_{\theta\theta}$	A_{rz}			
0.92	0.65	0.02	0.33	0.04	18	34.73	0.07	0.71	0.03	0.26	0.03	53	65.78	0.14
0.75	0.60	0.01	0.39	-0.01	38	70.77	0.15	0.65	0.02	0.33	-0.04	62	81.73	0.17
0.58	0.44	0.01	0.55	-0.01	24	33.50	0.08	0.54	0.01	0.45	0.02	44	64.46	0.13
0.42	0.51	0.01	0.47	-0.01	33	53.43	0.12	0.54	0.02	0.44	0.00	38	55.48	0.10
0.25	0.26	0.02	0.72	-0.04	50	60.29	0.13	0.30	0.02	0.67	0.05	37	75.48	0.16
0.08	0.03	0.02	0.95	0.00	106	108.98	0.24	0.11	0.04	0.85	0.04	31	98.26	0.21
0.00	0.02	0.04	0.93	0.00	50	51.84	---	0.09	0.04	0.87	0.04	9	30.36	---
-0.08	0.10	0.04	0.85	0.02	104	114.04	0.24	0.09	0.06	0.85	0.02	26	99.66	0.22
-0.25	0.19	0.03	0.78	0.02	67	77.56	0.17	0.28	0.06	0.66	-0.03	32	68.21	0.15
-0.42	0.44	0.04	0.52	0.00	35	50.79	0.11	0.46	0.01	0.52	0.01	41	67.64	0.14
-0.58	0.62	0.01	0.37	-0.02	34	60.72	0.14	0.62	0.03	0.35	0.00	39	52.65	0.12
-0.75	0.60	0.02	0.39	-0.01	33	56.58	0.11	0.71	0.01	0.28	0.00	48	58.66	0.11
-0.92	0.69	0.02	0.30	-0.04	28	61.28	0.15	0.56	0.03	0.41	0.02	30	40.76	0.09

z/H	*Average orientation and error for mutually perpendicular planes*									
	Orientation component				$\langle\phi_v\rangle$	Standard Error				
	$\langle A_{rr}\rangle$	$\langle A_{zz}\rangle$	$\langle A_{\theta\theta}\rangle$	$\langle A_{rz}\rangle$		$SE_{\langle A_{rr}\rangle}$	$SE_{\langle A_{zz}\rangle}$	$SE_{\langle A_{\theta\theta}\rangle}$	$SE_{\langle A_{rz}\rangle}$	$SE_{\langle\phi_v\rangle}$
0.92	0.69	0.03	0.29	0.03	0.10	0.02	0.00	0.02	0.00	0.04
0.75	0.62	0.02	0.36	-0.03	0.16	0.01	0.00	0.02	0.01	0.01
0.58	0.50	0.01	0.49	0.01	0.10	0.02	0.00	0.03	0.01	0.03
0.42	0.53	0.02	0.46	-0.01	0.11	0.01	0.00	0.01	0.00	0.01
0.25	0.28	0.02	0.69	0.01	0.14	0.01	0.00	0.01	0.02	0.01
0.08	0.07	0.03	0.90	0.02	0.22	0.02	0.00	0.03	0.01	0.02
0.00	0.05	0.04	0.91	0.02	---	0.02	0.00	0.02	0.01	---
-0.08	0.10	0.05	0.85	0.02	0.23	0.00	0.00	0.00	0.00	0.01
-0.25	0.23	0.04	0.72	0.00	0.16	0.02	0.01	0.03	0.01	0.01
-0.42	0.45	0.02	0.52	0.00	0.13	0.00	0.01	0.00	0.00	0.01
-0.58	0.62	0.02	0.36	-0.01	0.13	0.00	0.00	0.01	0.00	0.01
-0.75	0.65	0.02	0.33	-0.01	0.11	0.03	0.00	0.03	0.00	0.00
-0.92	0.64	0.02	0.34	-0.01	0.12	0.03	0.00	0.03	0.01	0.03

APPENDIX D: ORIENTATION ALONG THE CAVITY THICKNESS FOR DIFFERENT SAMPLING WIDTH MEASURED IN THE rz-PLANE AT THE GATE REGION EVALUATED BY VWB AND LA APPROACHES

Appendix D.1: Fiber orientation for the *rz*-plane in a 1.38 mm center-gated disk made of 30 wt% glass fiber reinforced PBT (Valox 420) measured at the gate region. Measurements were evaluated by considered elliptical and partial ellipses of any size (VWB approach) in sampling regions having height *dh* = 0.1150 mm and different widths *ds*.

z/H	*ds = 0.92 mm*									*ds = 0.69 mm*								
	Orientation component						F_a	H	ϕ_v	Orientation component						F_a	H	ϕ_v
	A_{rr}	A_{zz}	$A_{\theta\theta}$	A_{rz}	$A_{r\theta}$	$A_{z\theta}$				A_{rr}	A_{zz}	$A_{\theta\theta}$	A_{rz}	$A_{r\theta}$	$A_{z\theta}$			
0.92	0.73	0.06	0.21	-0.15	0.05	-0.04	26.90	67.35	0.10	0.78	0.06	0.17	-0.14	0.10	-0.05	18.90	52.84	0.07
0.75	0.79	0.02	0.19	0.00	0.08	-0.03	26.25	77.75	0.09	0.84	0.02	0.14	0.00	0.08	-0.02	20.11	68.41	0.07
0.58	0.70	0.02	0.28	0.02	0.22	-0.01	56.99	122.39	0.18	0.72	0.02	0.27	0.02	0.21	-0.01	47.54	104.48	0.15
0.42	0.62	0.03	0.34	0.06	0.15	-0.03	56.37	103.76	0.16	0.64	0.03	0.33	0.07	0.13	-0.03	40.35	77.54	0.12
0.25	0.67	0.03	0.31	0.05	0.09	-0.01	61.73	125.68	0.18	0.69	0.03	0.29	0.05	0.08	0.00	50.32	107.63	0.15
0.08	0.56	0.01	0.43	0.02	0.18	-0.02	70.65	119.03	0.18	0.62	0.01	0.37	0.02	0.13	-0.02	45.76	86.44	0.13
0.00	0.40	0.01	0.58	0.00	0.16	-0.02	84.47	119.17	---	0.46	0.02	0.53	-0.01	0.14	-0.01	57.89	88.37	---
-0.08	0.23	0.02	0.75	-0.02	0.12	-0.05	109.67	127.88	0.19	0.27	0.02	0.71	-0.02	0.13	-0.05	75.08	90.60	0.14
-0.25	0.49	0.03	0.49	-0.03	0.03	-0.03	72.24	108.72	0.17	0.48	0.03	0.49	-0.04	0.06	-0.04	59.07	89.17	0.14
-0.42	0.63	0.02	0.35	-0.04	0.08	-0.03	60.82	112.11	0.17	0.62	0.02	0.37	-0.02	0.09	-0.03	41.95	76.48	0.12
-0.58	0.63	0.02	0.34	-0.03	0.10	-0.04	48.14	90.11	0.14	0.66	0.03	0.31	-0.02	0.10	-0.03	34.90	68.52	0.11
-0.75	0.57	0.02	0.41	-0.03	0.00	-0.04	54.62	93.14	0.14	0.65	0.01	0.35	-0.02	-0.04	-0.03	40.36	76.00	0.11
-0.92	0.76	0.01	0.22	0.03	-0.18	-0.02	32.09	72.24	0.11	0.76	0.01	0.22	0.04	-0.15	-0.03	25.61	57.75	0.08

z/H	*ds = 0.46 mm*									*ds = 0.23 mm*								
	Orientation component						F_a	H	ϕ_v	Orientation component						F_a	H	ϕ_v
	A_{rr}	A_{zz}	$A_{\theta\theta}$	A_{rz}	$A_{r\theta}$	$A_{z\theta}$				A_{rr}	A_{zz}	$A_{\theta\theta}$	A_{rz}	$A_{r\theta}$	$A_{z\theta}$			
0.92	0.85	0.06	0.09	-0.16	0.09	-0.04	11.41	40.46	0.05	0.83	0.00	0.17	-0.04	0.11	-0.01	4.21	11.58	0.01
0.75	0.88	0.01	0.11	-0.05	0.06	-0.01	10.18	39.57	0.04	0.66	0.01	0.33	0.01	0.00	-0.02	2.94	6.41	0.01
0.58	0.72	0.02	0.26	0.03	0.19	0.00	29.12	67.62	0.09	0.73	0.01	0.26	0.07	0.16	0.00	17.19	42.24	0.06
0.42	0.67	0.03	0.30	0.06	0.14	-0.02	23.84	48.72	0.08	0.61	0.03	0.36	0.08	0.14	-0.03	9.41	19.09	0.03
0.25	0.54	0.03	0.43	0.01	0.10	-0.01	33.01	54.69	0.08	0.62	0.02	0.36	-0.01	0.10	-0.05	12.43	23.36	0.03
0.08	0.71	0.01	0.27	0.02	0.14	-0.02	23.51	53.62	0.08	0.76	0.01	0.23	0.02	0.14	-0.03	11.74	30.69	0.05
0.00	0.53	0.02	0.45	-0.01	0.12	-0.01	35.42	60.84	---	0.63	0.01	0.36	-0.01	0.13	0.00	15.74	31.84	---
-0.08	0.29	0.03	0.69	-0.03	0.12	-0.05	53.65	66.02	0.10	0.24	0.02	0.74	-0.02	0.16	-0.06	26.26	30.67	0.05
-0.25	0.45	0.05	0.51	-0.05	0.07	-0.05	41.15	60.36	0.09	0.37	0.06	0.57	-0.03	0.07	-0.06	24.50	33.10	0.05
-0.42	0.62	0.02	0.35	-0.03	0.07	-0.04	24.91	45.81	0.07	0.58	0.01	0.41	0.00	-0.10	-0.04	9.09	15.50	0.02
-0.58	0.57	0.03	0.39	0.00	0.12	-0.05	26.93	45.19	0.07	0.54	0.03	0.43	0.05	0.06	-0.02	13.64	21.41	0.03
-0.75	0.69	0.01	0.30	0.00	-0.10	-0.02	21.66	43.50	0.07	0.59	0.01	0.40	0.05	-0.07	-0.01	8.90	14.55	0.02
-0.92	0.76	0.02	0.23	0.04	0.00	-0.03	14.91	35.80	0.06	0.80	0.01	0.19	0.04	0.10	-0.01	7.90	21.27	0.03

Appendix D.2: Fiber orientation for the *rz*-plane in a 1.38 mm center-gated disk made of 30 wt% glass fiber reinforced PBT (Valox 420) measured at the gate region. Measurements were evaluated by considered elliptical footprints (LA approach) in sampling regions having height *dh* = 0.1150 mm and different widths *ds*.

z/H	*ds = 0.92 mm*							*ds = 0.69 mm*						
	Orientation component				F_a	H	ϕ_v	Orientation component				F_a	H	ϕ_v
	A_{rr}	A_{zz}	$A_{\theta\theta}$	A_{rz}				A_{rr}	A_{zz}	$A_{\theta\theta}$	A_{rz}			
0.92	0.64	0.06	0.31	0.12	22	45.72	0.07	0.69	0.05	0.27	0.10	15	33.05	0.05
0.75	0.65	0.03	0.32	-0.03	19	38.98	0.06	0.69	0.02	0.29	0.00	13	26.97	0.04
0.58	0.73	0.01	0.26	-0.03	51	123.33	0.18	0.75	0.01	0.23	-0.03	42	107.74	0.15
0.42	0.67	0.02	0.31	-0.05	48	99.86	0.16	0.67	0.02	0.30	-0.05	35	75.47	0.12
0.25	0.64	0.02	0.34	-0.03	51	102.81	0.14	0.67	0.02	0.32	-0.02	41	86.61	0.12
0.08	0.53	0.01	0.46	-0.02	55	93.89	0.15	0.59	0.01	0.40	-0.03	37	70.15	0.11
0.00	0.65	0.01	0.34	-0.02	25	53.72	---	0.71	0.01	0.28	-0.02	17	42.71	---
-0.08	0.22	0.01	0.76	0.02	104	122.31	0.18	0.25	0.01	0.74	0.01	69	83.07	0.12
-0.25	0.46	0.03	0.52	0.04	62	94.78	0.15	0.46	0.03	0.51	0.05	49	76.30	0.12
-0.42	0.60	0.01	0.38	0.02	53	95.49	0.14	0.57	0.01	0.41	0.01	36	63.31	0.10
-0.58	0.53	0.02	0.46	0.02	33	55.02	0.09	0.60	0.02	0.38	0.02	23	42.78	0.07
-0.75	0.54	0.01	0.45	0.03	47	78.74	0.12	0.61	0.01	0.38	0.02	34	62.58	0.09
-0.92	0.73	0.01	0.26	-0.02	26	56.73	0.09	0.73	0.01	0.26	-0.03	21	45.40	0.07

z/H	*ds = 0.46 mm*							*ds = 0.23 mm*						
	Orientation component				F_a	H	ϕ_v	Orientation component				F_a	H	ϕ_v
	A_{rr}	A_{zz}	$A_{\theta\theta}$	A_{rz}				A_{rr}	A_{zz}	$A_{\theta\theta}$	A_{rz}			
0.92	0.80	0.04	0.15	0.11	8	22.53	0.03	0.80	0.00	0.20	0.02	4	10.35	0.01
0.75	0.70	0.02	0.29	0.02	8	17.52	0.02	0.07	0.00	0.93	0.00	2	2.07	0.00
0.58	0.78	0.01	0.21	-0.04	27	76.92	0.10	0.79	0.02	0.20	-0.07	17	52.24	0.07
0.42	0.69	0.01	0.30	-0.04	17	39.13	0.06	0.69	0.02	0.29	-0.08	7	18.95	0.03
0.25	0.54	0.03	0.43	0.00	28	48.68	0.07	0.63	0.03	0.35	0.03	10	20.60	0.03
0.08	0.72	0.01	0.27	-0.04	20	49.81	0.08	0.70	0.01	0.29	-0.02	13	31.44	0.05
0.00	0.88	0.01	0.11	-0.02	7	30.47	---	0.93	0.00	0.07	-0.05	2	11.26	---
-0.08	0.25	0.01	0.74	0.02	50	60.35	0.09	0.17	0.01	0.81	0.00	22	24.61	0.04
-0.25	0.42	0.04	0.54	0.07	36	52.82	0.08	0.25	0.06	0.69	0.06	22	27.03	0.04
-0.42	0.61	0.02	0.38	0.01	21	38.59	0.06	0.67	0.01	0.32	-0.03	8	16.69	0.03
-0.58	0.58	0.02	0.40	0.01	18	33.04	0.05	0.45	0.04	0.51	-0.02	9	13.26	0.02
-0.75	0.71	0.01	0.29	0.02	20	44.33	0.07	0.35	0.01	0.63	-0.04	7	8.90	0.01
-0.92	0.72	0.02	0.26	-0.02	13	29.60	0.05	0.72	0.01	0.28	-0.01	7	15.16	0.02

APPENDIX E: ORIENTATION ALONG THE CAVITY THICKNESS FOR DIFFERENT SAMPLING WIDTH MEASURED IN THE rz-PLANE AT THE LUBRICATION REGION EVALUATED BY VWB AND LA APPROACHES

Appendix E.1: Fiber orientation for the *rz*-plane in a 1.38 mm center-gated disk made of 30 wt% glass fiber reinforced PBT (Valox 420) measured at the lubrication region. Measurements were evaluated by considered elliptical and partial ellipses of any size (VWB approach in sampling regions having height *dh* = 0.1150 mm and different widths *ds*.

z/H	*ds = 0.59 mm*									*ds = 0.44 mm*								
	Orientation component						F_a	H	ϕ_v	Orientation component						F_a	H	ϕ_v
	A_{rr}	A_{zz}	$A_{\theta\theta}$	A_{rz}	$A_{r\theta}$	$A_{z\theta}$				A_{rr}	A_{zz}	$A_{\theta\theta}$	A_{rz}	$A_{r\theta}$	$A_{z\theta}$			
0.92	0.73	0.02	0.26	-0.02	0.11	0.01	26.09	55.72	0.11	0.76	0.01	0.22	-0.01	0.12	0.03	13.78	33.25	0.07
0.75	0.68	0.02	0.30	0.00	0.14	0.01	44.32	92.66	0.18	0.68	0.02	0.30	0.01	0.17	0.01	34.61	72.64	0.16
0.58	0.55	0.02	0.43	0.03	0.10	-0.02	36.35	59.57	0.12	0.62	0.02	0.36	0.04	0.08	-0.02	21.49	39.51	0.10
0.42	0.64	0.02	0.34	0.05	0.13	0.02	38.02	75.83	0.18	0.60	0.03	0.38	0.06	0.14	0.03	28.21	52.60	0.12
0.25	0.26	0.02	0.72	0.03	0.27	0.04	54.48	64.04	0.14	0.23	0.02	0.75	0.03	0.29	0.05	46.10	52.82	0.11
0.08	0.05	0.04	0.91	0.00	0.19	0.03	115.38	119.95	0.25	0.05	0.03	0.92	0.00	0.19	0.02	99.35	102.78	0.22
0.00	0.13	0.05	0.82	-0.02	0.17	0.00	98.84	110.37	---	0.11	0.04	0.85	-0.02	0.19	-0.02	88.19	96.00	---
-0.08	0.14	0.10	0.76	-0.01	0.17	0.04	119.90	140.59	0.29	0.11	0.10	0.79	-0.01	0.18	0.03	102.78	117.48	0.23
-0.25	0.29	0.06	0.65	-0.03	0.19	0.02	78.45	100.87	0.22	0.27	0.07	0.66	-0.03	0.16	0.03	62.85	80.25	0.19
-0.42	0.42	0.08	0.50	0.00	0.12	0.01	53.70	77.67	0.15	0.39	0.09	0.52	0.00	0.15	0.01	43.63	62.25	0.13
-0.58	0.65	0.04	0.31	-0.01	0.04	0.02	41.69	80.10	0.19	0.71	0.02	0.28	0.01	-0.02	0.01	30.99	62.89	0.15
-0.75	0.56	0.03	0.41	0.04	0.13	0.04	44.41	71.64	0.15	0.60	0.03	0.37	0.05	0.11	0.03	32.85	55.69	0.12
-0.92	0.72	0.05	0.24	0.02	0.21	0.02	41.00	93.20	0.23	0.75	0.04	0.21	0.02	0.20	0.00	34.00	81.45	0.19

z/H	*ds = 0.30 mm*									*ds = 0.15 mm*								
	Orientation component						F_a	H	ϕ_v	Orientation component						F_a	H	ϕ_v
	A_{rr}	A_{zz}	$A_{\theta\theta}$	A_{rz}	$A_{r\theta}$	$A_{z\theta}$				A_{rr}	A_{zz}	$A_{\theta\theta}$	A_{rz}	$A_{r\theta}$	$A_{z\theta}$			
0.92	0.63	0.01	0.35	0.07	0.32	0.04	7.50	13.63	0.02	0.17	0.01	0.82	0.02	0.29	0.01	3.00	3.27	0.01
0.75	0.70	0.02	0.28	0.00	0.19	0.01	22.33	47.84	0.11	0.61	0.03	0.35	0.06	0.15	0.02	10.59	20.65	0.05
0.58	0.65	0.02	0.33	0.06	0.01	-0.03	15.49	30.33	0.08	0.78	0.02	0.20	0.07	-0.06	-0.04	6.62	15.92	0.04
0.42	0.63	0.03	0.34	0.07	0.07	0.03	19.23	39.28	0.09	0.74	0.01	0.24	0.09	0.00	0.01	9.67	25.50	0.06
0.25	0.23	0.02	0.75	0.03	0.27	0.04	33.07	37.75	0.07	0.26	0.03	0.72	0.04	0.28	0.05	14.77	17.19	0.03
0.08	0.05	0.04	0.91	0.00	0.19	0.03	68.14	70.89	0.15	0.05	0.03	0.92	0.00	0.18	0.00	40.00	41.34	0.09
0.00	0.06	0.05	0.89	-0.01	0.19	-0.01	60.41	63.34	---	0.07	0.05	0.88	-0.01	0.20	-0.04	35.49	37.46	---
-0.08	0.06	0.13	0.81	0.00	0.16	0.03	73.65	82.56	0.16	0.07	0.18	0.75	0.00	0.18	-0.02	41.98	49.53	0.09
-0.25	0.27	0.08	0.64	-0.04	0.15	0.02	47.80	62.84	0.15	0.15	0.11	0.74	-0.06	0.20	0.01	27.26	31.86	0.08
-0.42	0.37	0.09	0.54	-0.01	0.18	0.00	31.79	44.52	0.09	0.39	0.06	0.55	0.05	0.15	0.04	15.42	21.68	0.04
-0.58	0.72	0.02	0.27	-0.02	0.01	0.01	19.98	42.49	0.10	0.71	0.01	0.28	-0.01	0.03	0.01	10.41	21.04	0.04
-0.75	0.57	0.03	0.40	0.03	0.11	0.02	23.85	38.56	0.08	0.49	0.03	0.48	0.03	0.25	0.00	12.79	18.47	0.04
-0.92	0.78	0.03	0.19	0.01	0.19	0.01	25.00	63.81	0.15	0.74	0.01	0.25	0.00	0.18	-0.01	9.93	20.97	0.04

Appendix E.2: Fiber orientation for the *rz*-plane in a 1.38 mm center-gated disk made of 30 wt% glass fiber reinforced PBT (Valox 420) measured at the lubrication region. Measurements were evaluated by considered elliptical footprints (LA approach) in sampling regions having height *dh* = 0.1150 mm and different widths *ds*.

z/H	*ds = 0.59 mm*							*ds = 0.44 mm*						
	Orientation component				F_a	H	ϕ_v	Orientation component				F_a	H	ϕ_v
	A_{rr}	A_{zz}	$A_{\theta\theta}$	A_{rz}				A_{rr}	A_{zz}	$A_{\theta\theta}$	A_{rz}			
0.92	0.65	0.02	0.33	0.04	18	34.73	0.07	0.65	0.02	0.34	0.01	10	19.48	0.04
0.75	0.60	0.01	0.39	-0.01	38	70.77	0.15	0.60	0.01	0.39	-0.02	29	55.11	0.12
0.58	0.44	0.01	0.55	-0.01	24	33.50	0.08	0.49	0.00	0.51	0.00	16	23.58	0.05
0.42	0.51	0.01	0.47	-0.01	33	53.43	0.12	0.45	0.02	0.53	-0.03	23	33.86	0.07
0.25	0.26	0.02	0.72	-0.04	50	60.29	0.13	0.24	0.02	0.74	-0.04	42	49.51	0.10
0.08	0.03	0.02	0.95	0.00	106	108.98	0.24	0.03	0.02	0.96	0.00	93	95.20	0.20
0.00	0.02	0.04	0.93	0.00	50	51.84	---	0.03	0.02	0.95	0.01	43	44.13	---
-0.08	0.10	0.04	0.85	0.02	104	114.04	0.24	0.05	0.04	0.91	0.01	89	93.86	0.19
-0.25	0.19	0.03	0.78	0.02	67	77.56	0.17	0.14	0.04	0.82	0.02	55	61.74	0.13
-0.42	0.44	0.04	0.52	0.00	35	50.79	0.11	0.40	0.05	0.56	0.01	28	39.16	0.08
-0.58	0.62	0.01	0.37	-0.02	34	60.72	0.14	0.66	0.01	0.32	-0.02	27	51.96	0.12
-0.75	0.60	0.02	0.39	-0.01	33	56.58	0.11	0.61	0.01	0.37	-0.02	25	44.10	0.09
-0.92	0.69	0.02	0.30	-0.04	28	61.28	0.15	0.72	0.01	0.26	-0.03	24	56.02	0.13

z/H	*ds = 0.30 mm*							*ds = 0.15 mm*						
	Orientation component				F_a	H	ϕ_v	Orientation component				F_a	H	ϕ_v
	A_{rr}	A_{zz}	$A_{\theta\theta}$	A_{rz}				A_{rr}	A_{zz}	$A_{\theta\theta}$	A_{rz}			
0.92	0.59	0.01	0.40	-0.07	6	10.84	0.02	0.17	0.01	0.82	-0.02	3	3.32	0.01
0.75	0.54	0.01	0.45	-0.01	19	31.53	0.07	0.52	0.01	0.47	-0.04	9	15.01	0.03
0.58	0.45	0.01	0.54	-0.02	10	14.02	0.03	0.63	0.01	0.36	-0.04	5	8.41	0.02
0.42	0.48	0.02	0.50	-0.05	17	26.12	0.05	0.58	0.01	0.41	-0.07	8	14.33	0.03
0.25	0.26	0.02	0.72	-0.05	29	34.73	0.07	0.24	0.02	0.74	-0.03	15	17.56	0.04
0.08	0.04	0.02	0.94	0.00	63	64.97	0.14	0.04	0.02	0.94	0.00	37	38.13	0.08
0.00	0.03	0.03	0.93	0.01	28	29.06	---	0.03	0.03	0.94	0.00	17	17.57	---
-0.08	0.04	0.05	0.91	0.01	65	68.48	0.14	0.05	0.08	0.88	0.02	33	35.34	0.07
-0.25	0.10	0.05	0.85	0.03	41	45.02	0.10	0.09	0.06	0.85	0.02	24	26.28	0.06
-0.42	0.36	0.01	0.63	0.02	20	26.27	0.06	0.40	0.01	0.59	0.00	11	15.31	0.03
-0.58	0.69	0.01	0.30	0.01	18	36.00	0.08	0.71	0.01	0.28	0.01	11	23.67	0.05
-0.75	0.63	0.01	0.36	0.00	19	34.30	0.07	0.48	0.02	0.50	-0.03	8	11.84	0.02
-0.92	0.74	0.01	0.24	-0.04	18	44.17	0.11	0.66	0.01	0.33	-0.04	8	15.20	0.03

APPENDIX F: ORIENTATION ALONG CONSTANT HEIGHTS AND MULTIPLE RADIAL LOCATIONS EVALUATED BY THE VWB APPROACH

Appendix F.1: Fiber orientation in radial direction with error analysis assuming independent samples for two 1.38 mm center-gated disk made of 30 wt% glass fiber reinforced PBT (Valox 420) measured at z/H=0.75 (Shell layer). Measurements were evaluated by considered elliptical and partial ellipses of any size (VWB approach).

	Center-gated disk 1								*Center-gated disk 2*							
r/H	Orientation components						$F_{a,Tot}$	H_{Tot}	Orientation components						$F_{a,Tot}$	H_{Tot}
	A_{rr}	A_{zz}	$A_{\theta\theta}$	A_{rz}	$A_{r\theta}$	$A_{z\theta}$			A_{rr}	A_{zz}	$A_{\theta\theta}$	A_{rz}	$A_{r\theta}$	$A_{z\theta}$		
4.8	0.76	0.03	0.21	0.08	0.09	0.02	23.94	65.83	0.70	0.04	0.26	0.07	-0.04	-0.02	30.80	76.37
7.8	0.57	0.07	0.36	0.06	0.13	0.05	38.81	77.58	0.57	0.02	0.41	-0.04	0.00	0.01	38.20	68.44
11.3	0.76	0.03	0.21	0.07	0.18	0.02	31.15	90.39	0.80	0.01	0.19	0.00	-0.01	0.01	29.88	90.30
14.9	0.60	0.02	0.38	0.02	0.17	0.03	32.37	64.90	0.72	0.02	0.26	-0.01	-0.04	0.02	38.84	102.56
18.4	0.60	0.04	0.37	0.03	0.04	-0.01	63.40	125.69	0.56	0.02	0.42	0.05	-0.04	-0.03	47.21	78.53
25.4	0.69	0.02	0.29	0.02	0.05	0.01	41.32	97.87	0.72	0.01	0.27	0.02	0.03	0.00	35.75	85.67
32.5	0.76	0.00	0.23	0.01	-0.08	0.01	45.36	118.47	0.68	0.01	0.31	-0.02	0.15	-0.01	37.12	82.27
39.5	0.69	0.03	0.27	0.06	0.06	-0.03	43.85	116.47	0.77	0.01	0.22	0.00	-0.01	0.00	41.49	125.83
53.6	0.59	0.04	0.37	0.03	0.14	0.05	46.36	80.97	0.65	0.05	0.30	-0.03	0.06	0.00	48.10	103.48
67.6	0.52	0.02	0.46	-0.05	-0.09	0.02	32.44	51.21	0.55	0.04	0.42	-0.03	0.04	0.02	58.21	99.95
71.2	0.40	0.08	0.52	0.06	0.00	0.00	53.64	81.11	0.69	0.03	0.28	0.09	0.06	0.03	47.27	113.11

	Average orientation and error for two independent center-gated disks											
r/H	Orientation components						Absolute error in independent samples					
	A_{rr}	A_{zz}	$A_{\theta\theta}$	A_{rz}	$A_{r\theta}$	$A_{z\theta}$	A_{rr}	A_{zz}	$A_{\theta\theta}$	A_{rz}	$A_{r\theta}$	$A_{z\theta}$
4.8	0.73	0.04	0.24	0.07	0.03	0.00	0.08	0.00	0.08	0.02	0.09	0.01
7.8	0.57	0.05	0.38	0.01	0.06	0.03	0.04	0.04	0.00	0.04	0.03	0.04
11.3	0.78	0.02	0.20	0.03	0.09	0.01	0.03	0.03	0.00	0.06	0.02	0.03
14.9	0.66	0.02	0.32	0.01	0.07	0.02	0.03	0.03	0.00	0.05	0.03	0.03
18.4	0.58	0.03	0.39	0.04	0.00	-0.02	0.03	0.03	0.00	0.03	0.02	0.02
25.4	0.71	0.01	0.28	0.02	0.04	0.00	0.02	0.02	0.00	0.04	0.01	0.02
32.5	0.72	0.01	0.27	0.00	0.03	0.00	0.02	0.02	0.00	0.05	0.01	0.03
39.5	0.73	0.02	0.25	0.03	0.03	-0.02	0.03	0.03	0.00	0.05	0.03	0.03
53.6	0.62	0.05	0.34	0.00	0.10	0.03	0.05	0.03	0.04	0.02	0.05	0.02
67.6	0.53	0.03	0.44	-0.04	-0.03	0.02	0.03	0.03	0.01	0.04	0.02	0.03
71.2	0.55	0.05	0.40	0.08	0.03	0.01	0.04	0.04	0.00	0.05	0.05	0.03

Appendix F.2: Fiber orientation in radial direction with error analysis assuming independent samples for two 1.38 mm center-gated disk made of 30 wt% glass fiber reinforced PBT (Valox 420) measured at z/H=0.42 (Transition layer). Measurements were evaluated by considered elliptical and partial ellipses of any size (VWB approach).

	Center-gated disk 1								*Center-gated disk 2*							
r/H	Orientation components						$F_{a,Tot}$	H_{Tot}	Orientation components						$F_{a,Tot}$	H_{Tot}
	A_{rr}	A_{zz}	$A_{\theta\theta}$	A_{rz}	$A_{r\theta}$	$A_{z\theta}$			A_{rr}	A_{zz}	$A_{\theta\theta}$	A_{rz}	$A_{r\theta}$	$A_{z\theta}$		
4.8	0.61	0.03	0.36	0.08	0.01	-0.01	42.80	84.84	0.73	0.04	0.23	0.01	-0.09	0.02	36.43	100.25
7.8	0.52	0.02	0.47	0.04	0.05	0.01	54.72	87.39	0.47	0.09	0.44	-0.01	0.04	0.00	48.22	83.41
11.3	0.52	0.03	0.45	0.02	0.04	0.03	46.05	73.63	0.61	0.01	0.38	0.01	0.07	0.00	50.90	96.70
14.9	0.60	0.05	0.35	0.04	0.06	0.02	43.23	90.52	0.67	0.02	0.30	0.02	0.02	0.01	41.63	98.48
18.4	0.66	0.03	0.32	0.00	0.01	-0.01	47.27	105.29	0.65	0.04	0.32	0.06	-0.11	-0.01	42.17	85.43
25.4	0.75	0.02	0.23	0.05	0.06	-0.01	37.14	102.62	0.69	0.03	0.28	0.00	0.01	-0.01	54.81	126.52
32.5	0.78	0.03	0.19	0.00	-0.02	-0.02	34.50	83.95	0.72	0.04	0.24	0.06	0.03	0.01	45.72	117.92
39.5	0.80	0.03	0.17	0.08	0.00	0.00	36.54	150.27	0.79	0.02	0.19	-0.01	0.00	0.01	41.72	141.58
53.6	0.69	0.04	0.27	0.01	0.07	0.00	38.10	84.41	0.72	0.02	0.26	-0.01	0.17	0.01	33.98	103.39
67.6	0.64	0.02	0.34	-0.01	0.01	0.00	40.49	86.04	0.64	0.02	0.34	-0.06	0.11	0.01	49.14	102.61
71.2	0.15	0.09	0.76	0.00	0.02	-0.04	104.14	122.74	0.19	0.06	0.75	0.05	-0.01	0.01	101.56	120.85

	Average orientation and error for two independent center-gated disks											
r/H	Orientation components						Absolute error in independent samples					
	A_{rr}	A_{zz}	$A_{\theta\theta}$	A_{rz}	$A_{r\theta}$	$A_{z\theta}$	A_{rr}	A_{zz}	$A_{\theta\theta}$	A_{rz}	$A_{r\theta}$	$A_{z\theta}$
4.8	0.67	0.04	0.30	0.05	-0.04	0.01	0.09	0.01	0.09	0.01	0.10	0.01
7.8	0.49	0.05	0.45	0.01	0.05	0.00	0.03	0.03	0.00	0.04	0.06	0.03
11.3	0.56	0.02	0.41	0.01	0.06	0.01	0.02	0.02	0.00	0.03	0.01	0.03
14.9	0.64	0.04	0.33	0.03	0.04	0.02	0.04	0.04	0.00	0.07	0.06	0.03
18.4	0.65	0.03	0.32	0.03	-0.05	-0.01	0.03	0.03	0.00	0.04	0.02	0.03
25.4	0.72	0.02	0.25	0.03	0.03	-0.01	0.04	0.04	0.00	0.05	0.04	0.03
32.5	0.75	0.03	0.22	0.03	0.00	0.00	0.04	0.04	0.00	0.06	0.02	0.03
39.5	0.79	0.03	0.18	0.04	0.00	0.00	0.04	0.04	0.00	0.05	0.04	0.03
53.6	0.71	0.03	0.26	0.00	0.12	0.01	0.06	0.04	0.05	0.03	0.05	0.03
67.6	0.64	0.02	0.34	-0.03	0.06	0.00	0.03	0.03	0.00	0.05	0.02	0.03
71.2	0.17	0.07	0.75	0.03	0.00	-0.02	0.03	0.03	0.00	0.02	0.03	0.02

Appendix F.3: Fiber orientation in radial direction with error analysis assuming independent samples for two 1.38 mm center-gated disk made of 30 wt% glass fiber reinforced PBT (Valox 420) measured at z/H=0.08 (Core layer). Measurements were evaluated by considered elliptical and partial ellipses of any size (VWB approach).

	Center-gated disk 1								*Center-gated disk 2*							
r/H	Orientation components						$F_{a,Tot}$	H_{Tot}	Orientation components						$F_{a,Tot}$	H_{Tot}
	A_{rr}	A_{zz}	$A_{\theta\theta}$	A_{rz}	$A_{r\theta}$	$A_{z\theta}$			A_{rr}	A_{zz}	$A_{\theta\theta}$	A_{rz}	$A_{r\theta}$	$A_{z\theta}$		
4.8	0.68	0.02	0.30	0.08	-0.11	-0.02	39.00	88.91	0.52	0.01	0.47	0.03	-0.12	-0.01	51.25	88.50
7.8	0.48	0.03	0.49	0.01	0.12	-0.01	58.64	90.37	0.35	0.05	0.61	-0.02	0.06	-0.03	74.55	100.51
11.3	0.32	0.01	0.67	-0.01	0.07	-0.01	83.88	111.16	0.31	0.02	0.67	-0.03	-0.15	0.00	80.24	104.27
14.9	0.25	0.06	0.69	-0.05	-0.02	0.03	93.01	116.30	0.32	0.02	0.66	0.03	-0.04	-0.01	77.46	104.17
18.4	0.26	0.06	0.68	-0.03	-0.04	0.02	98.90	125.46	0.40	0.03	0.57	0.07	-0.07	-0.03	66.14	95.75
25.4	0.15	0.03	0.83	0.03	-0.06	-0.07	122.62	137.28	0.42	0.03	0.55	0.01	-0.14	-0.04	82.56	121.16
32.5	0.28	0.02	0.71	0.01	-0.13	0.00	92.18	112.95	0.31	0.02	0.66	0.03	-0.07	-0.01	84.61	105.94
39.5	0.28	0.05	0.67	0.05	-0.03	-0.06	84.59	107.87	0.35	0.04	0.62	-0.06	-0.12	0.04	99.42	125.17
53.6	0.28	0.03	0.68	0.02	0.14	-0.01	88.41	112.88	0.24	0.04	0.72	-0.03	-0.09	0.10	78.84	95.07
67.6	0.22	0.03	0.75	0.00	0.05	0.02	122.92	145.20	0.19	0.02	0.79	-0.02	-0.10	0.02	114.42	129.52
71.2	0.05	0.09	0.85	0.03	0.08	0.02	129.99	143.65	0.08	0.06	0.86	-0.02	0.02	0.03	130.50	141.49

	Average orientation and error for two independent center-gated disks											
r/H	Orientation components						Absolute error in independent samples					
	A_{rr}	A_{zz}	$A_{\theta\theta}$	A_{rz}	$A_{r\theta}$	$A_{z\theta}$	A_{rr}	A_{zz}	$A_{\theta\theta}$	A_{rz}	$A_{r\theta}$	$A_{z\theta}$
4.8	0.60	0.02	0.38	0.06	-0.12	-0.02	0.10	0.00	0.10	0.01	0.11	0.01
7.8	0.41	0.04	0.55	-0.01	0.09	-0.02	0.03	0.03	0.00	0.02	0.03	0.03
11.3	0.32	0.01	0.67	-0.02	-0.04	-0.01	0.01	0.01	0.00	0.02	0.02	0.02
14.9	0.28	0.04	0.67	-0.01	-0.03	0.01	0.02	0.02	0.00	0.02	0.03	0.03
18.4	0.33	0.05	0.62	0.02	-0.05	-0.01	0.03	0.03	0.00	0.03	0.04	0.03
25.4	0.28	0.03	0.69	0.02	-0.10	-0.05	0.02	0.02	0.00	0.02	0.02	0.02
32.5	0.29	0.02	0.69	0.02	-0.10	0.00	0.01	0.01	0.00	0.02	0.01	0.02
39.5	0.31	0.05	0.64	0.00	-0.07	-0.01	0.03	0.03	0.00	0.04	0.04	0.02
53.6	0.26	0.04	0.70	-0.01	0.03	0.05	0.03	0.01	0.02	0.01	0.04	0.02
67.6	0.20	0.03	0.77	-0.01	-0.03	0.02	0.01	0.01	0.00	0.01	0.01	0.01
71.2	0.07	0.07	0.86	0.00	0.05	0.03	0.03	0.03	0.00	0.06	0.05	0.02

APPENDIX G: PROBABILITIES OF DETECTING A FOOTPRINT WHEN A FIBER IS CUT BY A PLANE AT A RANDOM HEIGHT

G.1: Probability of detecting a footprint with area of any size when the fiber is cut by a plane at a random height

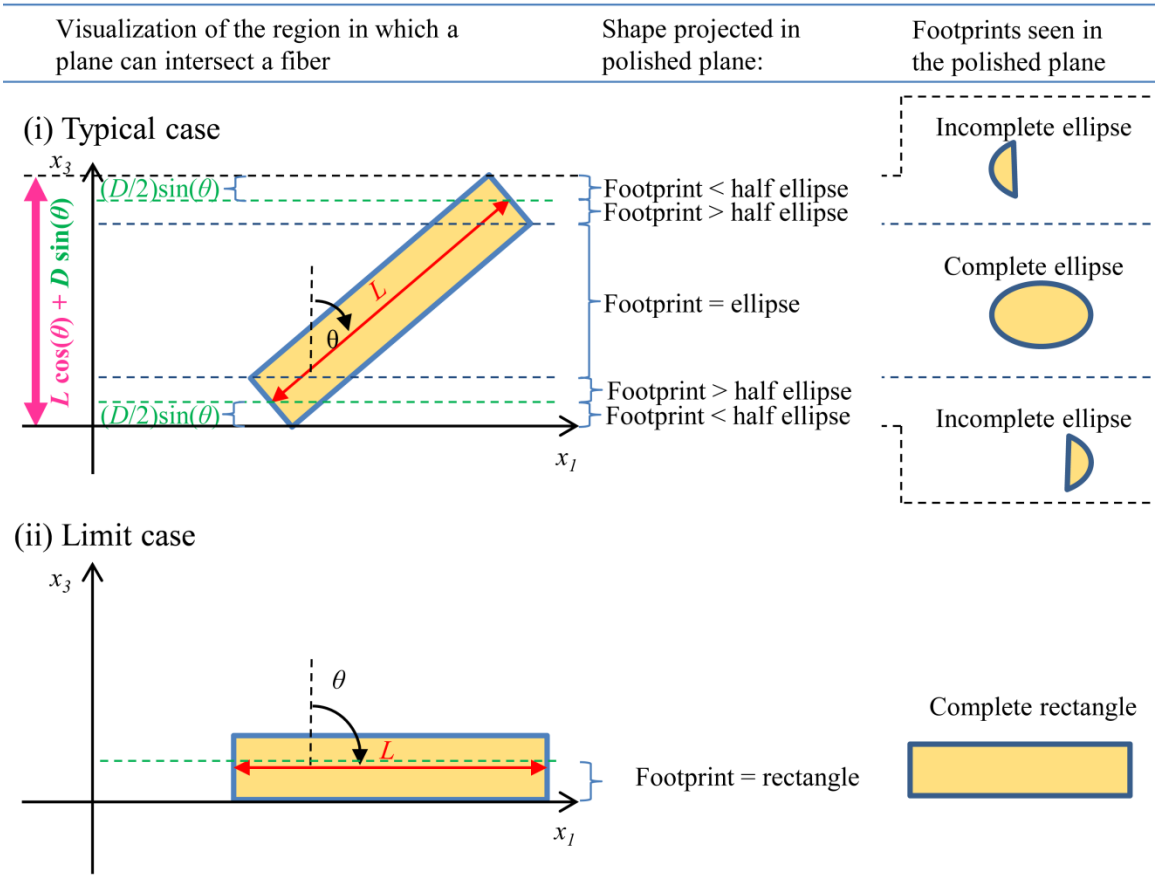

Probability: $P(\theta) = L * \cos(\theta) + D * \sin(\theta)$

Appendix G

G.2: Probability of detecting a footprint with area greater than half ellipse when the fiber is cut by a plane at a random height

Visualization of the region in which a plane can intersect a fiber	Shape projected in polished plane:	Footprints seen in the polished plane

(i) Typical case

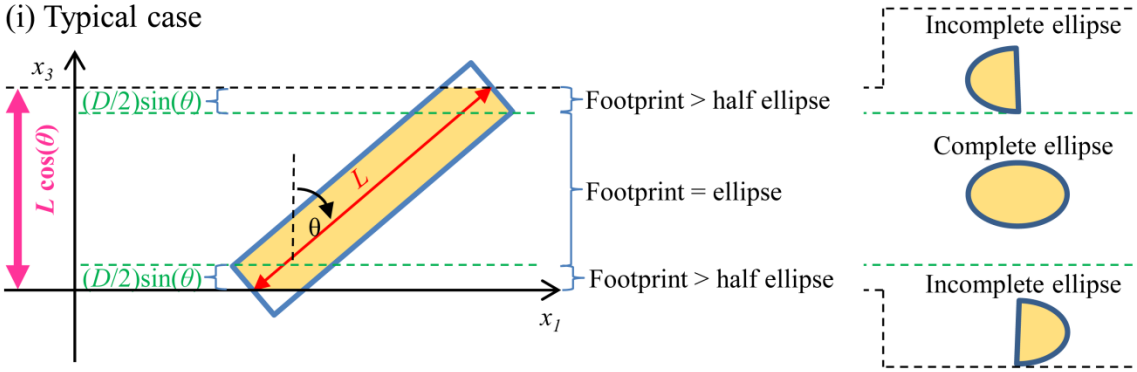

(ii) Limit case

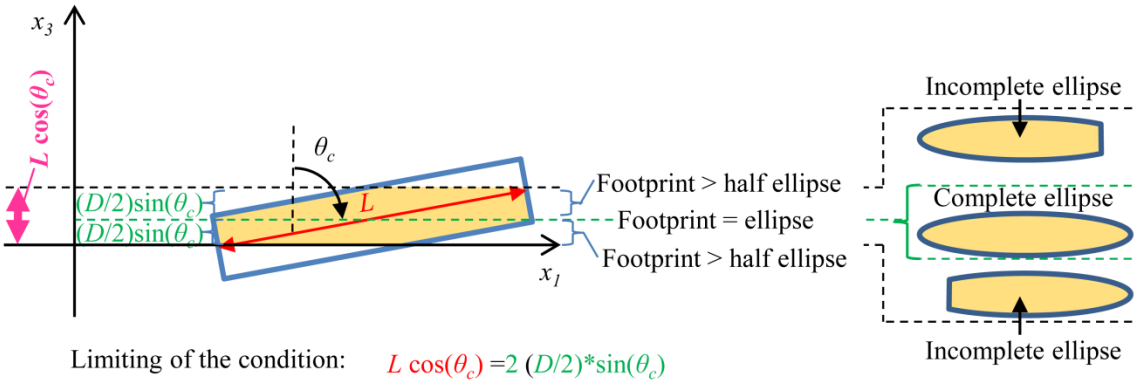

Limiting of the condition: $L\cos(\theta_c) = 2\,(D/2)*\sin(\theta_c)$

Simplification: $\sin(\theta_c) \approx 1$

Cutoff angle : $\cos(\theta_c) = D/L$

$\boldsymbol{\theta_c = \arccos(D/L)}$

Probability: $P(\theta) = L * \cos(\theta)$

G.3: Probability of detecting a footprint with area equal to a complete ellipse when the fiber is cut by a plane at a random height

Visualization of the region in which a plane can intersect a fiber	Shape projected in polished plane:	Footprints seen in the polished plane

(i) Typical case

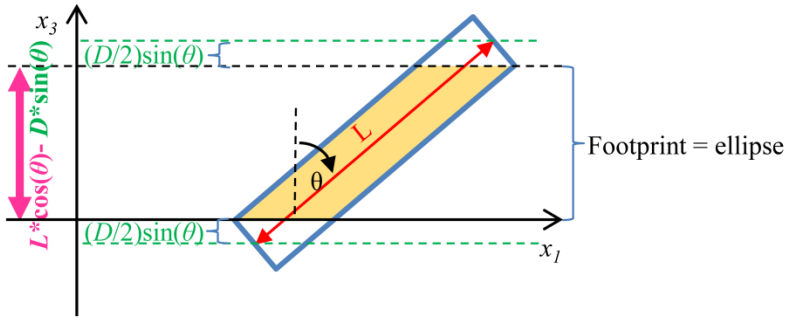

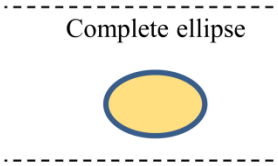

(ii) Limit case

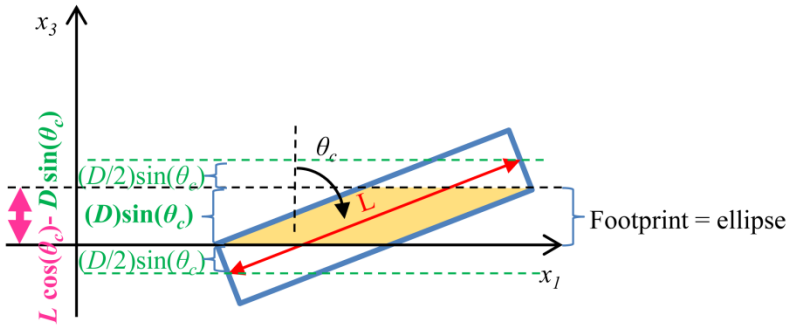

Limiting of the condition: $L\cos(\theta_c) - D\sin(\theta_c) = D\sin(\theta_c)$

Simplification: $\sin(\theta_c) \approx 1$

Cutoff angle : $\cos(\theta_c) = 2D/L$

$\boldsymbol{\theta_c = \arccos(2D/L)}$

Probability: $P(\theta) = L * \cos(\theta) - D * \sin(\theta)$

Appendix H

APPENDIX H: ELECTRONIC APPENDICES ARE AVAILABLE AT THE WEBPAGE:

http://www.math.vt.edu/people/pwappero